Nanostructured Metal Borides: Synthesis and Their Applications

KRISHNA KUMAR YADAV

A thesis submitted for the partial fulfillment of the degree of Doctor of Philosophy

Institute of Nano Science and Technology,
Knowledge City, Sector-81, SAS Nagar, Manauli PO, Mohali, 140306, Punjab, India.

Indian Institute of Science Education and Research Mohali
Knowledge city, Sector 81, SAS Nagar, Manauli PO, Mohali, 140306, Punjab, India.

March 2021

Dedicated to

My Family

Declaration

The work presented in this thesis has been carried out by me under the guidance of Dr. Menaka Jha, Dr. Indranil Sarkar and Prof. Ashok K. Ganguli at the Institute of nano science and technology, Mohali, India. This work has not been submitted in part or in full for a degree, a diploma, or a fellowship to any other university or institute. Whenever contributions of others are involved, every effort is made to indicate this clearly, with due acknowledgement of collaborative research and discussions. This thesis is a bonafide record of original work done by me and all sources listed.

Krishna Kumar Yadav

In my capacity as the supervisor of the candidate's thesis work, I certify that the above statements made by the candidate are true to the best of my knowledge.

Dr. Menaka Jha Prof. Ashok K. Ganguli Dr. Indranil Sarkar

Acknowledgment

कर्मण्ये वाधिका रस्ते मा फलेषु कदाचन।

मा कर्म फल हेतु र्भूर्मा ते सङ्गोऽस्त्व कर्मणि॥

It is a wonderful and inspiring journey of my life. I thanks and very grateful, what I have received throughout these years. The journey shaped my carrier as well as me as a person. The complication of this thesis could not have been possible without the participation and assistance of so many people whose name may not all enumerated. Their contributions are sincerely appreciated and acknowledged. And here, I take this opportunity to express my gratitude to all those who helped me during this odyssey of my PhD and curated my life to come.

First and foremost, I would like to extend my heartfelt gratitude to my thesis supervisor, **Dr. Menaka Jha**. She is the most energetic and vibrant person I have ever met in my life with a perpetual passion and dedication to science and research. Her view to see the positive thing in negative outcome encourage me more and more. I joined the PhD with a motive to contribute towards science, which can give a better future to the human being, but this motivation was given a real direction by Dr. Menaka Jha. Her command of the subject, clear vision to execute research ideas, positive and energetic attitude helped me to solve every single problem of work very easily. With her eagerness, motivation, great efforts and excellent guidance, I am fortunate to avail myself of the right opportunities to grow as a researcher as well as a person. I am privileged that I was the first PhD students of her. Throughout my entire PhD duration, she always motivated sound advice, good teaching, good company, and lots of good ideas. She has always brought out the best in me, and this period of working with her has been a wonderful learning experience and hence I am very thankful for all she has done for me. By investing her time and experience with me makes a strong work ethic and a collaborative spirit and she prepared me for all-round professional and scholarly work. She not only helped us grow professionally but also the pep talks from her helped me in my personal growth. Sometimes she scolded me but only for my betterment. I thank her for being the architect of my research career. I would not have imagined a better mentor than her for my PhD.

I am thankful to **Prof. Ashok K. Ganguli**, who was the founding director of our institute as well as my supervisor. He has always enlightened me through his wide knowledge and

his deep intuitions about where it should go and what is necessary to get there. He is a great personality, and I am very blessed that he guides me as my mentor. His valuable input and unparalleled encouragement had been a dependable force to arrive at the conclusions of my PhD work. I thank Prof. Ganguli for their suggestion and constant support. I am also grateful to **Dr. Indranil Sarkar** as one of my supervisors. His vast knowledge of physics is always helpful to shape the thesis.

I am grateful to The Director, INST, Mohali, for making a great working atmosphere and all the facilities required to complete our tasks during the PhD tenure. I would extend my gratitude to our former acting director Prof. H. N. Ghosh. I am also grateful to all the supporting staff of the institute for their kind help and cooperation.

I am very much grateful to **CSIR-India** for providing the fellowship to carry out my research. It would be a great opportunity to express my sincere thanks to Prof. Shantanu Ghosh, Department of Physics, IIT Delhi for field emission measurements. I am also thankful to Dr. M. Sreekanth, Department of Physics, IIT Delhi and Mr. Gulsan Kumar, Department of Physics, IIT Delhi for his help in carrying out field emission measurements and their continuous support. I would like to express my gratitude to Prof. S. E. Lofland, Rowan University, Glassboro, USA and Prof. Kandalam V Ramanujachary, Rowan University, Glassboro, USA with whom I got the opportunity to work for the magnetic measurements. I would extend my gratitude to Dr. Suvankar Chakraverty, INST, Mohali for their help in magnetic measurements. I would like to extend my thanks to Dr S. T. Nishanthi, CSIR- CECRI Karaikudi, Tamilnadu for the XPS measurement. I learn several instrumental techniques when she was the Postdoc within the group. I want to thank Prof. Avtar S. Matharu, York University, UK and Dr Ranjana Yadav, IPIRTI, Mohali for their support in bio-board work.

Also, I am grateful to my thesis and annual review committee members: Dr. Vivek Bagchi (INST, Mohali) and Dr. Kiran S. Hazra (INST, Mohali), for their time, ideas, insightful comments, and inspiration. I would like to extend my gratitude to Prof. S. K. Mehta, Punjab University, who was the external member of my SRF presentation. His suggestion was helpful to the shape of my thesis. I would also like to take this opportunity to thank the INST-Administrative staff, Ms. Reena, Mrs. Gurveen, Mrs. Suman, Dr. Mukesh, Mrs. Shweta, Mr. Rohit, Mr. Rajeev, Mr. Dhanjeet, Mrs. Kamini, Miss Vandna, Mrs. Arti, Mr. Nitin for all the help, love and care they have given to me which made my stay in INST comfortable. My acknowledgement would be incomplete without mentioning the non-administrative staff of INST. My heartfelt thanks to our driver uncle *Ravinder Ji* who

always carries us from one lab to another lab, INST cook Vikram Ji, Mr. Deepak and INST gardeners. Regardless of our constant troubles, they always helped us and made our stay in INST relaxed and safe. In all the INST staff, I would like to acknowledge Mr. Bharat, who always cleaned the lab (specially INST Basement) without asking and their helping nature to transport gas cylinder from one lab to another lab.

I also want to thank Dr. Kamalakannan Kailasam, Dr. Sharmistha Sinha, Dr. Kaushik Ghosh, Dr. Rahul K. Verma, Dr. Tapasi Sen, Dr. Sanyasinaidu Boddu, Mr. Bhanu, Dr. Sonalika Vaidya, Dr. Vijay and all other INST Faculty for helping me during my PhD and allowing me easy access of facilities and teaching me the basics about the instruments during course work. I want to extend my thanks to **IISER-Mohali**, who provide the basic facility to us.

My sincerest gratitude also goes to **Dr. Manu Sharma** with whom I started my research work in the lab from zero. She was the first who showed me how to do work in the chemical lab. I would like thanks to **Ritu** ma'am for their helpful nature as I started the instrument learning from her. In this name, **Dr. Vishwajit Gaikwad** is a constant supporter of mine as well as a good friend. He was a former INST postdoc and one of my dear friends. His approach towards his subject, positive attitude and immense knowledge inspired me a lot. PhD journey is many times overloaded with work and friends are the ones who can take up all your burden and fill you with fresh energy. I am blessed that I have always got great friends during my stay in INST who made my PhD journey even more enjoyable. In all of them, my deepest gratitude to my colleague and my best friend **Ms. Sunaina** for being my companion for most of my journey. She always motivated me during my PhD tenure, and I started my 1st thesis work with her. Her thinking spirit always shows me a path, I learnt a lot from her. I am fortunate to have a friend like her. In all of my group member, **Dr. Sujit Guchhait** was the 1st person with whom I started electrochemistry work. Without his help, It might be very hard to start the electrochemical work. As a human being, he is a great personality. I am thankful to **Paramita Bhabhi** for the lovely food, and thoughts beyond the research. I thank **Dr. Ruchi Tomar** and **Dr. Neha Wadera** as my seniors as well as my dear friend. I am grateful to both. If I have any problem related to physics and anything, I discussed it with them and got the solutions. It was a very grateful journey to share the common institute with **Mr. Nand Kumar**. He is a great personality. I would also extend my gratitude to **Dr. Renu Rani**, who always helped me when in need.

I would also like to thank my roommates **Mr. Venu** and **Dr. Naimat**. They always support and take care of the room and created a healthy environment in the room. Both are very

good cook (especially chicken). I cannot go further without acknowledging **Mr Danish** and **Mr Ankush** (my roommates). We all are good friends and knows the secret of each other. I thank them for a lot of memories that we made during our stay in Mohali. I have also been fortunate to have the company of great lab members. I want to thank **Ms. Supriya Rana** for being my colleague for most of my journey. Her lively and humorous nature is commendable and makes tense situations also feel light. I would like thanks to **Ms Ritika Wadhwa** and **Mr Ankush**. The helping and Joyful nature of **Ritika** and **Ankush** always make the situation light and enjoyable. I would also like to thank my group members, **Nausad Khan, Kritika Sood, Sapna Devi** and **Arushi Arora** for their common understanding and helping in the lab. All of our collective efforts always made work enjoyable. In the journey of my PhD, I would like to thank our former group member **Harish Singh, Heena, Priyanka, Debanjan,** and **Pankaj**. I would extend my deep gratitude to **Navneet Samra** a member of our group without being a group member. She has a very helpful nature and cheerful person. I am thankful to **Dr. Tania Purkait** and **Mr. Zubair Ahmad** for their constant motivation and support. I thank to my dear friend **Rajinder Chaudhary**, **Babita**, **Kalpesh,** and **Taru**. I am grateful to **Sushil** and **Aashish Bhatt** for their support. Sunday is always special due to their cooking skills.

I am very fortunate to have a friend like **Abhay Malviya** and **Mithilesh**. Both are my source of energy from childhood. I thanks them for always being there when I needed them. I also extend my thanks to **Mr. Madan**, **Mr. Saurabh** and **Mr. Ambrish** for their support during my Delhi stay.

I also want to thank Post-Doc who joined INST during my PhD. A special thank **Dr. Vijay Tomar, Dr. Bhagwati Sharma, Dr. Radha Manohar Aperu, Dr. Soumen Mondal, Dr. Sachin, Dr. Lenin, Dr. Bilal** for their valuable guidance and support. I want to extend my gratitude to INST researcher scholars including Anirban, Harman, Munish, Nitya, Pulkit, Ankur, Anup, Swati, Rashmi, Harsimran, Soumen, Preeti, Antara, Deepak, Aashima, Parbhaleen, Deepika Rani, Saumadri, Tanmay, Rejaul, Neha, Puspendra, Pranjali Yadav, Ankush Garg, Anas, Aditi, Vaibhav, Rashmika, Ashmeet, Chirag, Arti, Deepika, Riyaj, Vibhav, Ajit, Mujeeb, Rohit, Mayank, Jasveer, Hitasha, Rimple Kalia, Gurpreet, Anamika, Mansi throughout our journey. I take this opportunity to especially thank my friends Anish, Saurabh, Sarad, MN, Vaishali, Snehil, Mithilesh, Monu, Kanchan, and Manmohan. I am lucky enough to have friends like Imtiyaz Hussain, Sunil Singh, Jyotsana, Parvez, Asjad, Atul Dubey, Atul Jaiswal, Ayush and Parmod.

I am thankful to **Arif, Ravi** and **Novbhar**, who was my former roommate and batchmate but friends forever. I also want to extend my gratitude to **Guratinder** and **Shabi**. I have always motivated by them. I would also like to thank the ***chai group*** and ***cycle group*** members. I would also thank our TEM operator, **Mr. Vaibhav**, who always clicked the best micrograph. The PhD journal is difficult without chemicals. I am very glad to thank Mr Gaurav, Mr Ankush, Mr Sarad, Mr Varun and Mr Surjit. I would also thank PXRD engineer Mr Kailash. I want to extend my gratitude to my college day professors especially *Dr R. K. Verma, Dr Sarita, Dr Sanjay* and *Dr Piyush*.

Last but not the least, I would like to thank my whole family for making me the person I am today. I am blessed to be born in a family full of people to be inspired by. Whether it is the elders like my Baba, Chacha (Doctor Chacha), bade papa, Dinesh, Bhola, Aman, Arun, Amarnath or my cousins, everyone has their own role to play. I don't have words to thank my parents, **Mr Rambriksh Yadav** and **Mrs Shobha Devi** who nurtured me, to become thoughtful and independent human beings. What I am right now because of them. I learn the dedication towards the work from my father. My parent managed a life between work and family taught me greatly to manage all my works well. ***I can rightly say that I owe my entire life to them***. Finally, I want to extend heartfelt gratitude to the best gift of my life, my sister **Preeti** and my brother **Abhay**. Both have their individuality, and I learnt a lot from them. I am extremely lucky that they always believe in me. Lastly, I thank one and all involved in the completion of this work.

Krishna Kumar Yadav

Abbreviations

E_g	*Bandgap*
VB	*Valence band*
CB	*Conduction band*
SEM	*Scanning electron microscopy*
FESEM	*Field emission scanning electron microscopy*
TEM	*Transmission electron microscopy*
SAED	*Selected area electron diffraction pattern*
EDX	*Energy-dispersive X-ray spectroscopy*
HRTEM	*High resolution transmission electron microscopy*
STEM	*Scanning transmission electron microscopy*
XPS	*X-ray photoelectron spectroscopy*
UV-vis	*Ultraviolet-visible*
Ω	*Ohm*
CPE	*Constant phase element*
Y_0	*CPE constant*
ω	*Angular frequency*
n	*Exponent of CPE*
$PE_{(j)}$	*Protective efficiency*
RHE	*Revirsible hydrogen electrode*
PXRD	*Powder X-ray diffraction*
GIXRD	*Grazing incident X-ray diffraction*
HTXRD	*High-temperature X-ray diffraction*
2θ	*Bragg's angle*
d	*Interplanar distances*
(hkl)	*Miller indices*
SAXS	*Small angle X ray scattering*
AFM	*Atomic force microscopy*
KPFM	*Kelvin probe force microscopy*
MFM	*Magnetic force microscopy*
CPD	*Contact potential difference*

TGA	***Thermogravimetric analysis***
DTA	***Diffrantial thermogravimetric analysis***
BET	***Brunauer-Emmett-Teller***
BJH	***Barrett-Joyner-Halenda***
nm	***Nanometer***
mm	***Millimetre***
TX 100	***Triton X-100***
min	***Minutes***
eV	***Electronvolt***
IR	***Infrared***
mA	***Milliampere***
μA	***Microampere***
cm	***Centimeter***
λ	***Wavelength***
Å	***Angstrom***
v	***Wavenumber***
h	***Plank's constant***
μ	***Micro***
J	***Current density***
J_E	***Field emission current density***
J_T	***Temperature-dependent current density***
E	***Electric field***
A_R	***Richardson constant***
k	***Boltzmann constant***
nA	***Nanoampear***
ϕ	***Work function***
β	***Field enhancement factor***
c_f	***Temporal stability***
mL	***Milliliter***
LSV	***Linear sweep voltammetry***
CV	***Cyclic voltammetry***
MS	***Mott- schottkey***
EIS	***Electrochemical impedance spectroscopy***

HER	***Hydrogen evolution reaction***
OER	***Oxygen evolution reaction***
$NaBH_4$	***Sodium borohydride***
E_{CB}	***Conduction band edge***
E_{VB}	***Valence band edge***
Wt %	***Weight percentage***
V/V %	***Volume percentage***
w/w	***Weight by weight***
t	***Time***
JCPDS	***Joint Committee on Powder Diffraction Standards***
mA	***Milliampere***
V	***Voltage***
w. r. t.	***with respect to***
ln	***Natural logarithm***
Log	***Logarithm***
i. e.	***That is***
T	***Temperature***
h	***Hours***
s	***Seconds***
M	***Molar***
g	***Gram***
mg	***Milligram***
VESTA	***Visualization of electronic and structural analysis***
PPT	***Part per trillion***
PPM	***Part per million***
Si	***Silicone***
$NaBH_4$	***Sodium borohydride***
LaB_6	***Lanthanum hexaboride***
NdB_6	***Neodymium hexaboride***
GdB_6	***Gadolinium hexaboride***
$La_xNd_{1-x}B_6$	***Lanthanum doped neodymium hexaboride***
$La_xGd_{1-x}B_6$	***Lanthanum doped gadolinium hexaboride***
ZrB_2	***Zirconium diboride***

ZrO_2	*Zirconia*
$m\text{-}ZrO_2$	*Monoclinic zirconia*
CG	*Graphene oxide*
SG	*Sulphur doped graphene oxide*
UG	*Nitrogen-doped graphene oxide*
KOH	*Potassium hydroxide*
EDLC	*Electric double-layer capacitance*
GCD	*Galvanic charge-discharge*
CA	*Contact angle*
MS	*Mott-Schottky*
R_{ct}	*Charge transfer resistance*
j_{corr}	*Corrosion current density*

ABSTRACT

Nanostructured metal borides have attracted lots of researcher attention due to their wide application such as field emitters, scratchless/ultrahard coating, superconductivity, catalysis, anticorrosive coatings and ceramics materials. These exciting properties of metal borides generally arise due to the complex metal borides structure. In general, metal borides are generally synthesized via a solid-state borothermal reduction route. Based on a detailed literature survey, it has been observed that metal boride nanostructures have been synthesized in very adverse condition (either high temperature or under high vacuum). Therefore, in the present thesis, we focused on the new strategies to obtain binary as well as ternary nanostructured metal borides using chemical routes and investigate their properties at the nanoscale. Metal boride comprises boron with the less electronegative atom. Metal borides are classified into two main types: (a) boron rich borides (B: M>= to 4:1) and (b) metal-rich boride (B: M< to 4:1). Among the wide variety of metal boride, here we have attempted to stabilize metal borides of type AB_2 (A=3d-transition metals) and AB_6 (A=Rare earth metals). Further, we have explored the corrosion and field emission properties of these metal borides. The main aim of the present thesis is to design a new low-temperature synthesis process for the stabilization of metal diboride and metal hexaboride at ambient pressure.

In the present thesis, metal hexaborides such as NdB_6, GdB_6, $La_xNd_{1-x}B_6$ and $La_xGd_{1-x}B_6$ (x=0.1, 0.2, 0.3, 0.4, and 0.5) has been synthesised. For the synthesis of these metal hexaboride, first their metal hydroxide has been synthesised using hydrothermal route. The as synthesised metal hydroxide precursors have been heated with sodium borohydride to obtained various composition of rare earth hexaboride. Further, the synthesised rare earth hexaboride has been coated over a silicon substrate and their field emission and air oxidation study properties have been explored.

Further, an important material of metal-rich boride *i.e.* ZrB_2 has been synthesised. Here, for the synthesis ZrB_2, first nanostructured zirconia of size 10-15 nm has been synthesised using the hydrothermal route. Further, zirconia nanoparticles heated with elemental boron to obtained pure ZrB_2. The synthesised ZrB_2 has been coated over stainless steel substrate and their anticorrosive properties have been done studied.

Table of Contents

Annexure

Appendix

List of Figures

List of tables

Chapter 1

Introduction

1.1 Metal borides

Metal borides are formed by the reaction of boron with the less electronegative atom. The complex bonding of the metal boride family results in interesting properties of materials such as high melting point, low work function, low vapour pressure, high mechanical and chemical strength, broad neutron capture cross-section,[1] good oxidation resistance,[1] high strength-to-weight ratio, excellent thermal shock resistance,[2] and nonbrittle fracture behaviour, superconductivity,[3] high catalytic performance,[4] optical, electronic and refractory properties.[5] Due to these properties, metal boride finds tremendous application technological application as field emitter, thermal neutron detectors, corrosion-resistant materials, cutting tools and nose cone of aerospace.[6] Metal borides possess excellent electrical conductivity, low work function and high chemical stability and therefore these metal diborides are quite popular in flat plane display and electron emission nanodevices. The properties of metal boride are strongly dependent on the arrangement of boron in metal boride as well as the crystal structure of metal boride. Various arrangement of boron in metal boride has been shown in Figure 1.1. The boron can be arranged in isolated form, paired boron, zigzag, sp^2 type and so on.

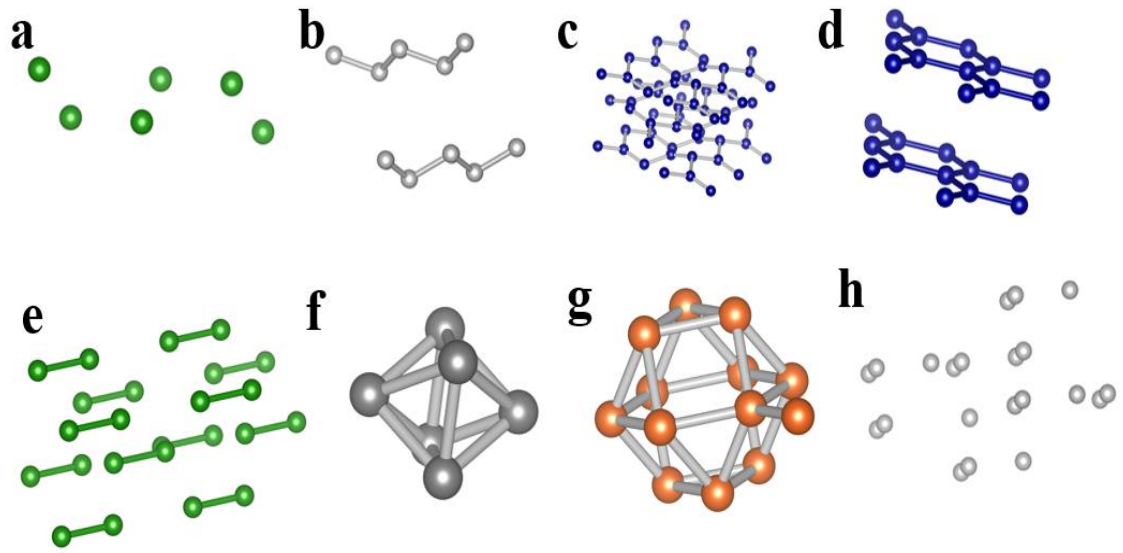

Figure 1.1. *Possible boron arrangement in various metal boride crystal. (a) Isolated boron atoms. (b) zig-zag boron chains. (c) puckered boron layers with "chair" configuration. (d) graphene-like flat boron layers. (e) paired boron atoms. (f) B12 cuboctahedra. (g) B_6 octahedron. (h) double boron.*

A survey suggests that around 1253 inorganic crystal structure database present for binary boron compounds; however, very few application of borides have been explored due to limited fundamental research on borides.[5] It is interesting to note that in the early year of

1950, metal borides have been studied only for structural determination by physicist, materials scientist and chemist. Recently, theoretical reports of silver boride and gold boride have been investigated for high-temperature superconductors. In earlier days metal borides have been used for their mechanical and electrical properties (Thermionic emission). However, the properties of metal borides strongly dependent on the structure of metal borides.

1.2 Types of metal borides

Metal borides show a range of properties based on their crystal structures. The metal diboride especially ZrB_2, HfB_2 and TiB_2 are known for their high-temperature application; however, at the same time metal hexaboride such as LaB_6, CaB_6 are used for their electronic properties. Here, it is worth to mention that "boride" refers to the ordered intermetallic boride with a well-defined structure. Inorganic Crystal Structure Database (ICSD) shows that ~55 % of metal borides are transition metals borides and ~25 % is covered by intermetallic borides of lanthanides.[7] At the same time, 80 % of metal boride is in the form of 3:1 (M_3B) to 1:12 (MB_{12}) except few borides of alkali-earth metals and lanthanides such as Be_4B, Mg_2B_{25}, YB_{66}. The arrangement of boron atoms in the crystal structure plays an important role in determining the physical and chemical properties of borides. Kiessling *et al.* suggested borides can be classified based on the boron atom arrangement in borides such as isolated boron atoms, pairs of boron atoms, chains of boron atoms, double chains of boron atoms, networks of boron atoms, and skeletons/backbones of boron atoms.[8] Generally, boron rich borides contain 3-dimensional frameworks of boron atoms that can include boron polyhedral. The structures of boron in metal boride are single boron atoms, B_2 units, boron chains, boron clusters or boron sheets/layers (Figure 1.1). The details of metal borides crystal structures are as follows.

1.2.1 Metal-rich boride

In metal-rich boride the ratio of B: M is < 4:1. The common example of metal-rich borides is Mn_4B, Ni_2B, Be_2B, V_3B_2, Ta_3B_4, Cr_3B_4, $Fe_{23}B_6$, and $Co_{23}B_6$ (Figure 1.2).[5] In metal-rich borides, metal atoms are connected to form a 3D skeleton and boron atoms are distributed in the metal skeleton to form metal–boron bonds.[9]

Monoborides

When boron reacts with transition metals with B: M in an equal molar ratio then the mono borides (MB) are formed. The different crystal structures of mono-borides have been shown in Figure 1.3, which includes WC-type, anti-NiAs-type, NaCl-type, and MoB-type crystal structures.

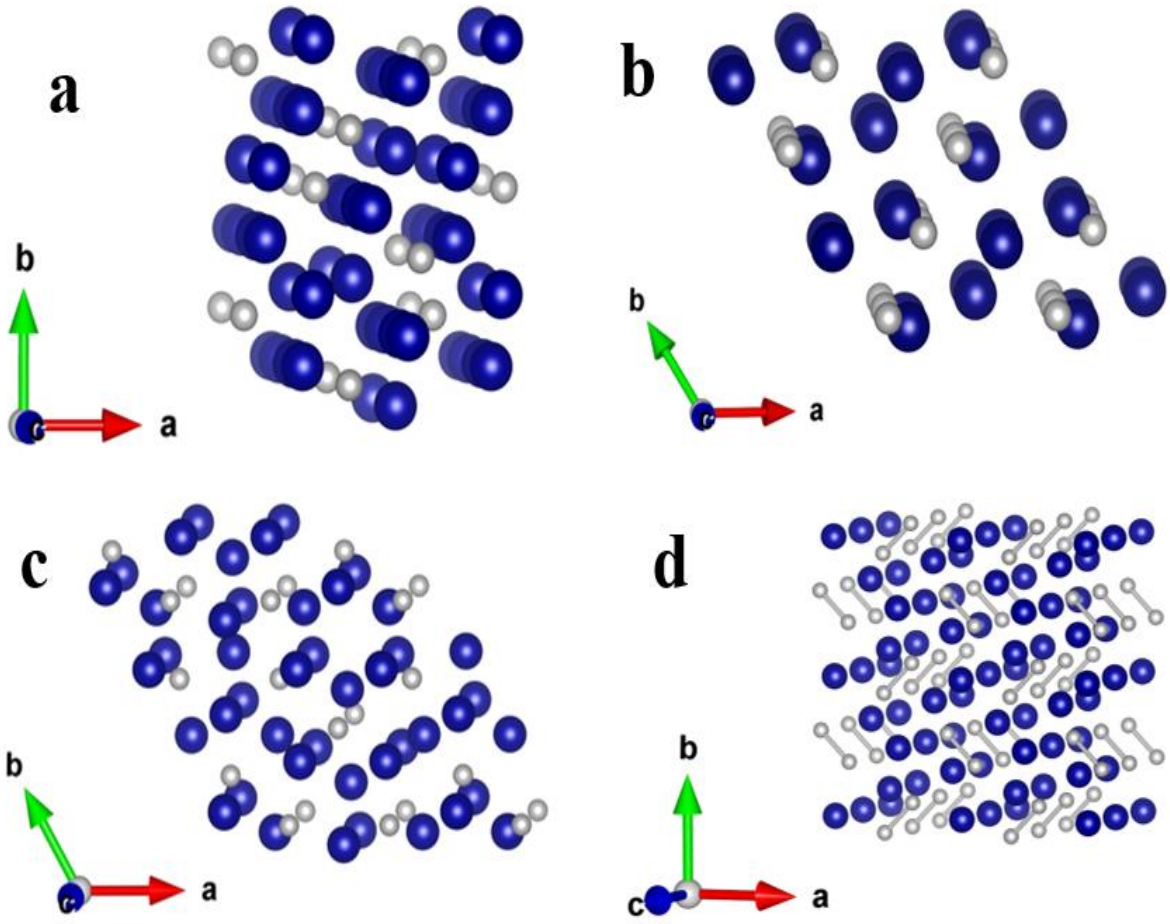

Figure 1.2. *Representative crystal structures of (a) M_3B (M=Co/Ni/Pd). (b) M_2B (M=Cr/Mo/W/Ta/Mn/Fe/Co/Ni). (c) M_7B_3 (M=Re/Tc/Ru/Rh/Ni) (d) M_3B_2 (M=V/Nb/Ta). Metal atoms and boron atoms are in blue and grey, respectively.*

Diborides

In metal diboride structure one metal atom covalently bonded reacts with two units of boron. In metal-rich boride, IVth group elements form metal diboride such as ZrB_2, HfB_2 and TiB_2, which is used widely for the high-temperature material-based application. These diborides have graphene-like boron layers in which metal ions embedded homogeneously. The covalent bond and sp^2 type hybridization of the boron layer results in high mechanical strength and high melting point. The melting point of selected metal diborides has been

included in Figure 1.4. These metal diborides have high melting points (> 3000 ℃), high hardness and also high electric conductivity.[10,11] These properties are essential for making the material for super hard coatings, electron emitters and anticorrosive. It is known that IVth group metal diboride has an AlB_2-type hexagonal structure.[12]

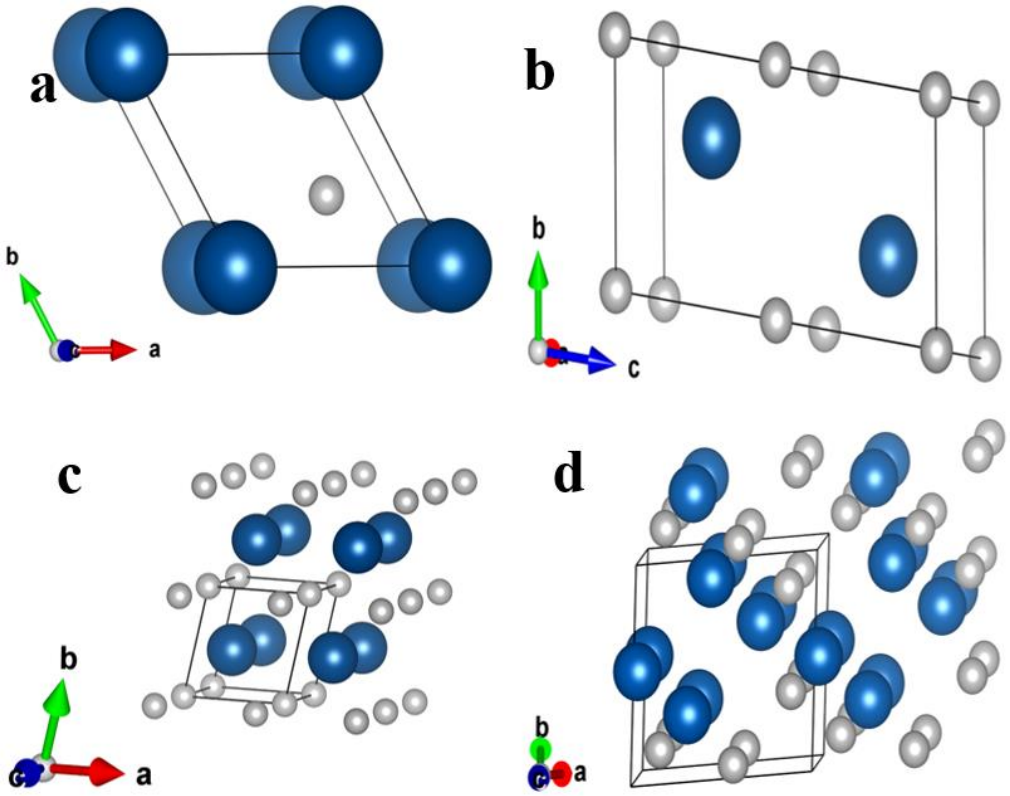

Figure. 1.3. *Crystal structures of (a) WC-type monoboride (IrB, ReB, RhB, OsB). (b) anti-NiAs type monoboride (PdB, RhB, PtB). (c) NaCl-type monoboride (ZrB, HfB) (d) MoB-type monoboride (CrB. MoB, WB). Metal atoms and boron atoms are in blue and grey, respectively.*

These excellent properties arise from its robust crystal structure (hexagonal AlB_2 type), where boron atoms form honeycomb layers and metal atom (Zr, Al, Mg) located at the centre of the hexagonal ring formed by B sheets (Figure 1.5a).[13,14] Apart from AlB_2 crystal structures metal diboride can also be crystallized in ReB_2 and RuB_2 type lattice structure (Figure 1.5b-c).[15] The hypersonic flight mostly runs at greater than 5 Mach (1715 ms^{-1}) and due to this high speed, materials that can bear temperatures upto 3000 °C, high heat flux, rapid heating and disassociated reactive oxygen in the extreme environment of space during re-entry should be needed. The materials, which withstand over 2000 ℃ classified as ultra-high-temperature ceramics (UHTCs). Among the family of UHTCs, ZrB_2, TiB_2 and HfB_2 are reported as the most promising candidates for thermal protection systems (TPS), which can be used in the nose tip and sharp leading edges in space vehicles. These metal borides

have melting points higher than 3000 °C. Also, these materials have excellent thermal conductivity from low temperature to over 2500 °C, good chemical, and ablation stability at high temperatures. However, metal diborides of the IVth group, the formation of corresponding oxides at elevated temperature, leads to a volume change that results in cracking of the formed oxide scale.[16]

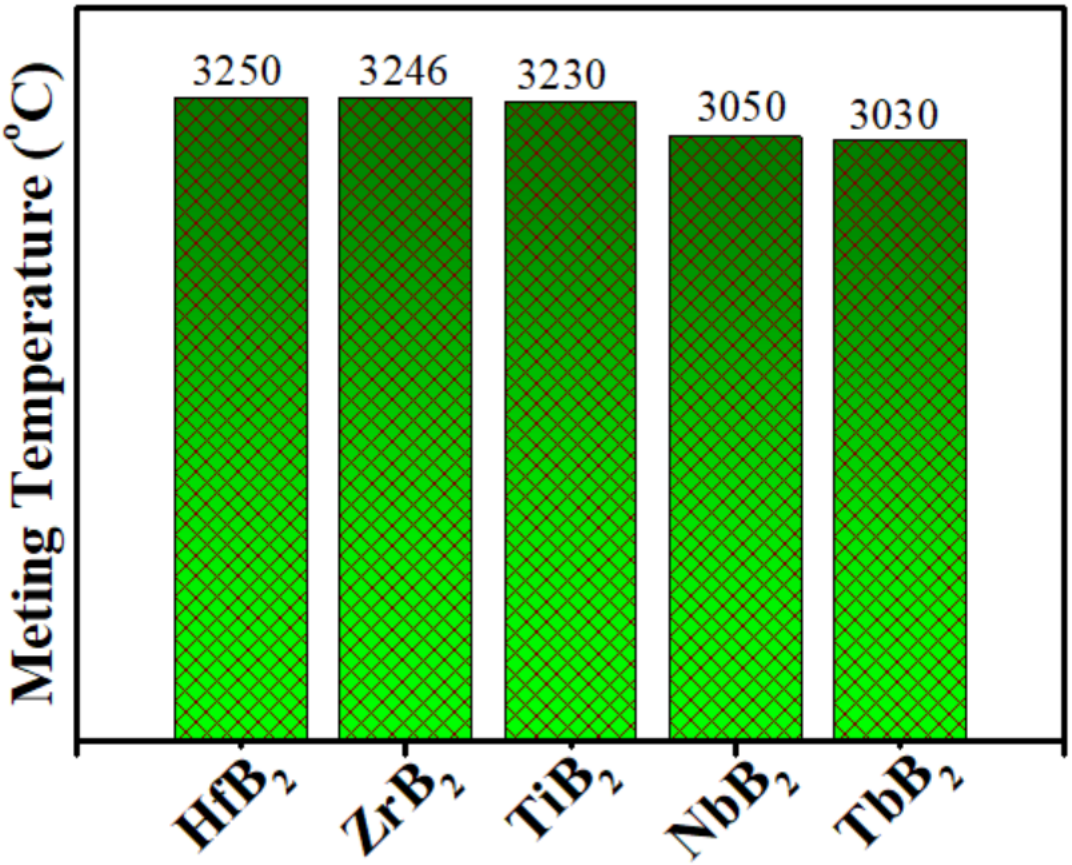

Figure 1.4. *Melting point of the transition metal diboride.*

In all the metal diborides of IVth group, ZrB_2 has exciting properties such as high hardness (9–22 GPa), high wear resistance, relatively low density (6.09 g cm^{-3}) and low electrical resistivity (7-24 μΩcm).[17] It has a high bulk modulus (410–500 GPa), good flexural strength (200–375MPa) and low coefficient of thermal expansion (about 7.5×10^{-6} °C^{-1}). However, its poor fracture toughness (around 2–3 Mpa m$^{1/2}$) limits its reliability for many applications.[18] Due to these properties make ZrB_2 is used as an anticorrosive coating to protect the metallic surface from various type of corrosion.

1.2.2 Boron-rich borides

The boron rich metal borides are consisting of boron and metal, where the boron to metal ratio is equal to or more than 4 (B: M ≥ 4:1), this ratio can be upto 66 in the case of

YB_{66}. In boron rich metal boride, covalently bonded boron makes structural units of boron cages/clusters and again linked together to generate a 3D boron skeleton. In the case of MB_4 (M=Cr, Fe, Mn), the structural boron unit is B_4 (Figure 1.6a). The MB_4 lattice structures of rare-earth metal borides have different crystal structures than transition metal diboride form (Figure 1.6b). Apart from MB_4, MB_6 and MB_{12} are two other main metal borides, which mainly occur in lanthanides–boron, actinides–boron systems and few alkaline earth metals. The structural boron unit is B_6 octahedra and B_{12} cuboctahedra for MB_6 and MB_{12} metal borides respectively (Figure 1.6c-d).

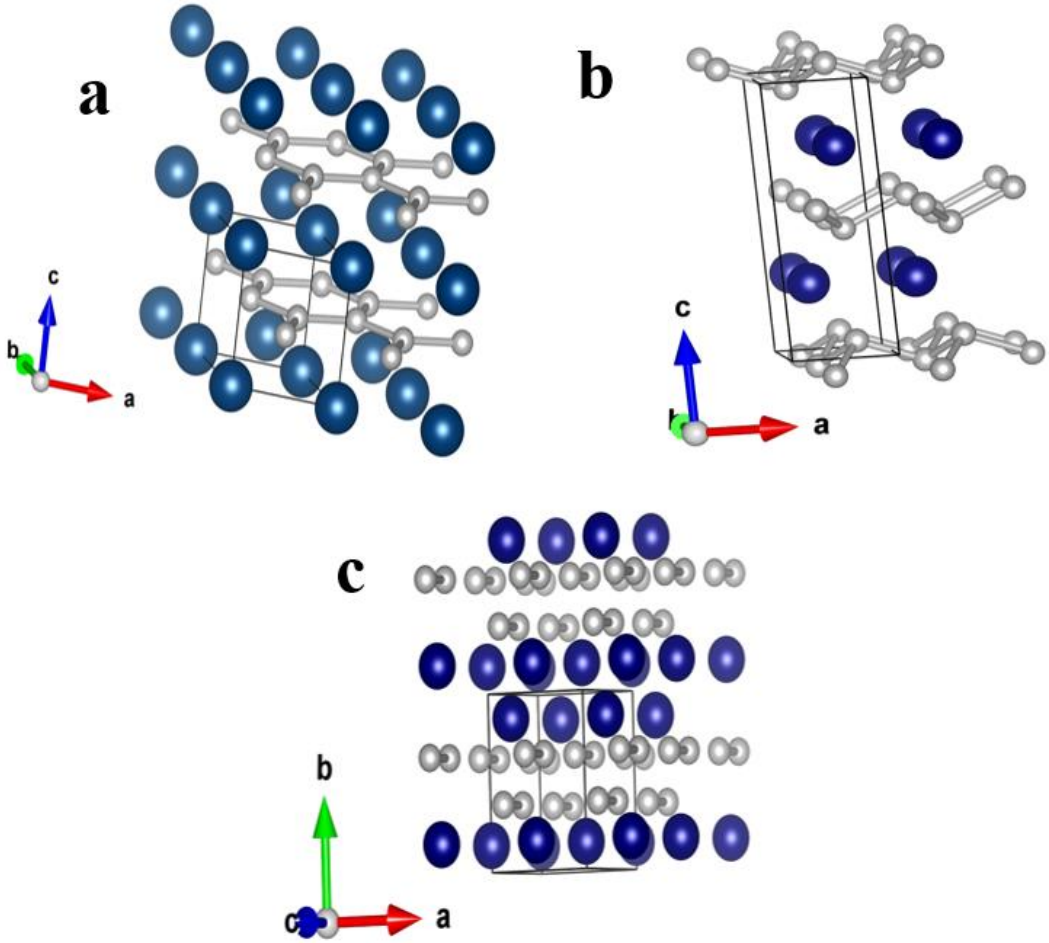

Figure 1.5. *Crystal structures of (a) AlB_2-type diboride (ZrB_2, MgB_2). (b) ReB_2-type metal diboride. (c) RuB_2-type metal diboride. Metal atoms and boron atoms are in dark blue and grey, respectively.*

Some rare-earth and alkaline-earth metals form metal borides having a higher ratio of B/M (>12,) such as Na_2B_{29}, YB_{66}, where the basic structural unit is a 3D boron framework consisting of B_{12} icosahedra. In boron rich boride, metal hexaborides are recently gain much attention due to their application in cold filed emission. Rare earth hexaboride crystallises in CsCl-type structure (Cubic structure) with $Pm3m/O_h^1$ space group,[19] metal

atom embedded at the centre of the cube at Cs site, whereas boron forms octahedra and at making their presence at all the corner of cube at Cl^- site (Figure 1.6c).

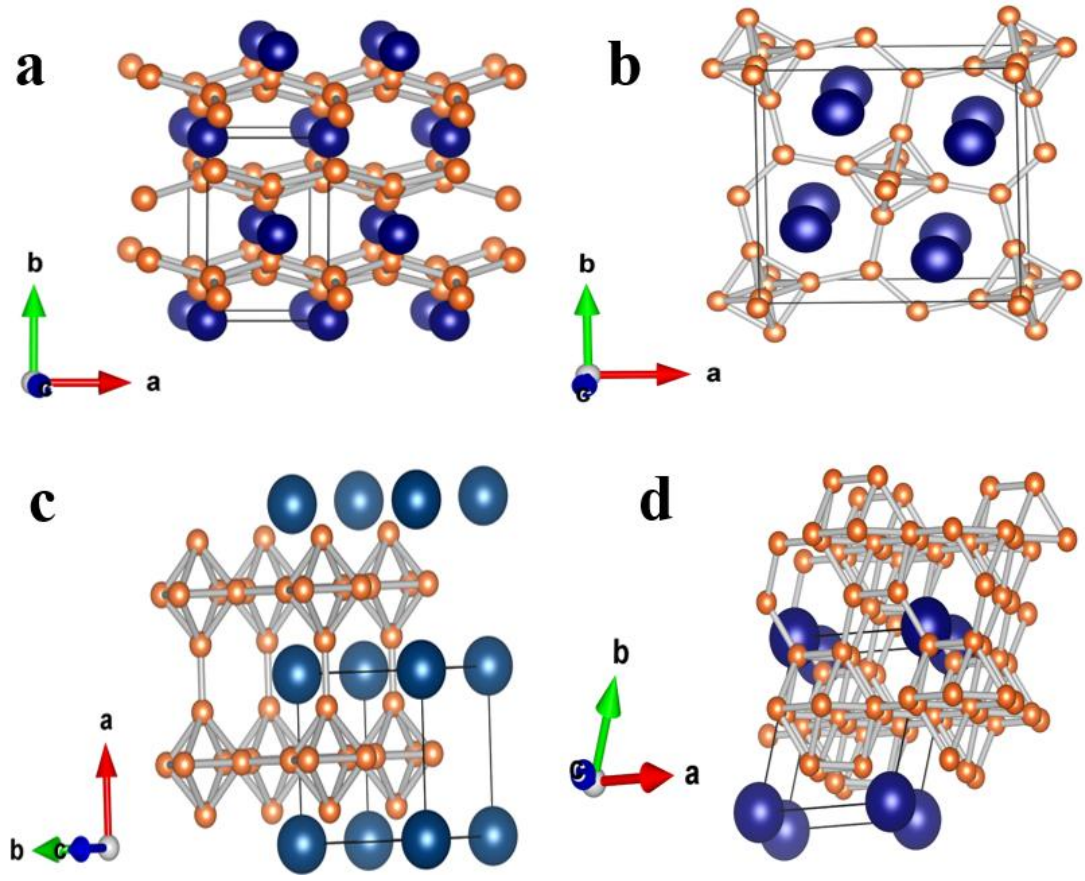

Figure 1.6. *Crystal structures of (a) MB_4 (M = Cr, Fe, Mn). (b) MB_4 (M = Y, La, Ce, Pr, Nd, Sm, Gd, Tb, Dy, Ho, Er, Tm, Yb, Lu, Th, U and Pu). (c) MB_6 (M = K, Ca, Sr, Ba, Y, La, Ce, Pr, Nd, Sm, Eu, Gd, Tb, Dy, Ho, Er and Tm). (d) MB_{12} (M = Zr, Hf, Y, Gd, Tb, Dy, Ho, Er, Tm, Yb, Lu, Th, U and Pu). Metal atoms and boron atoms are in dark blue and dark orange colour, respectively.*

1.3 Application of metal borides

1.3.1 Metal boride as energy harvesting materials

Transition metal borides can be used for electrochemical water splitting.[20] Interestingly, amorphous boride such as Fe-B, Co-B, Cu-B, Mo-B, Ni-B shows excellent electrocatalytic properties toward water splitting.[21,22] Here, the reported electrochemical reaction parameter for selected metal boride have been included in Table 1.1. It is interesting to note that FeB_2 shows very low overpotential, which might be arises due to the higher conductivity of hexagonal FeB_2, where B atom arranged in sp^2 type hybridization.[23] The full water-splitting involves two steps and the detailed reaction mechanism of the anode and cathode are as follows.

In an acidic medium (*e.g.* sulphuric acid)

Cathode: $4H^+ + 4e^- = 2H_2$ 1.1

Anode: $2H_2O = O_2 + 4H^+ + 4e^-$ 1.2

In an alkaline medium (*e.g.* Potassium hydroxide)

Cathode: $4H_2O + 4e^- = 2H_2 + 4OH^-$ 1.3

Anode: $4OH^- = 2H_2O + 4e^- + O_2$ 1.4

In a neutral medium (*e.g.* potassium phosphate buffer)

Cathode: $2H_2O + 4e^- = 2H_2 + 4OH^-$ 1.5

Anode: $2H_2O = O_2 + 4H^+ + 4e^-$ 1.6

Irrespective of the medium, a good catalyst should have some specific properties such as a large number of active sites with optimum electron density, low charge transfer resistance across the interface as well as with bottom lying electrode material and stability in the electrolyte medium.[24]

The metal borides can also be used as corrosion protection in different pH, which will be discussed later.[25] As mentioned earlier, the properties of metal borides are mostly dependent on their crystal structures and boron arrangement. The metal hexaboride (rare earth hexaboride and alkaline earth hexaboride) has the cubic crystal structure, in which boron atom forms the framework of B_6 octahedra which presents at all the corner of cubes and metal atom at the centre at cubes. The metal hexaboride, including rare earth hexaboride and alkaline earth hexaboride, has a high melting point, high chemical stability, high hardness, low work function and the ability to absorb neutron radiation.[26,27] These properties attracted the attention of researchers and related industry for their practical application. A recent report suggests that low function materials such as LaB_6 and CeB_6 can also be used as a material for solar energy converter.[36,37] However, a great number of study has been done for solar energy conversion, but current solar technologies are still expensive, which require high maintenance and a large collection area of solar heat. The thermionic energy conversion can directly transform the heat into electricity using phenomena of thermionic emission.[38]

Table 1.1. State of art boride materials for the overall water splitting in different electrolyte

Catalyst	Electrolyte	Overpotential (mV) (@10 mV/cm^2)		Stability (h)		Crystal Structure	Ref.
		HER	OER	HER	OER		
Mo-B	1M H_2SO_4	225 (20 mV/cm^2)	-	48 h	-	α-form (tetragonal)	[28]
Co-B	0.5 m KPi	251		40		Amorphous	[29]
Ni-B	1 m $HClO_4$	132 (20 mA cm^{-2})		8h		Amorphous	[30]
Co_2B	0.1 m KOH	328	380	-	60	Crystalline	[31]
MoB_2	0.5 m H_2SO_4	230 (2.5 mA cm^{-2})		-		Hexagonal	[32]
Co_3B	0.1 m KOH		312			orthorhombic	[33]
FeB_2	1 m KOH	61	296	24	48	Hexagonal	[23]
MoB_2	0.5 m H_2SO_4	154		-		Hexagonal	[34]
Ni_3B	0.5 m H_2SO_4	79		20		Crystalline	[35]

1.3.2 Superconductor

If any materials show the transportation of electricity from one atom to another atom without any resistance, known as superconducting materials. It has been observed that at a certain temperature (certain temperature, T_c) several materials can behave like superconducting materials. The temperature at which any materials show its superconductor behaviour defined as critical temperature (T_c). In the superconducting materials, there is no loss of heat, sound or any other form of energy when reached "critical temperature" (T_c). However, most of the materials show their T_c at extremely low temperature. Scientists are working to develop materials having high-temperature T_c. There was a belief that copper-based materials can show high-temperature superconductivity; however, J. Nagamatsu *et al*. show that layer metal boride (MgB_2) has a high critical temperature (39 K), which was a great achievement at that time.[3] MgB_2 has P6/mmm space group (no.191). MgB_2 have a similar crystal structure as AlB_2, where boron atoms are arranged in graphene-like layers and Mg interleaved between them. Each boron atom is here equidistant from three other boron atoms (Figure 1.5a).[3] Thereafter several metal borides such as W_2B_3, RuB_2 have been studied for the superconducting nature.[39,40]

Recently, a theoretical study shows that high T_c for AgB_2 and AuB_2 can be obtained which are 59 and 72 K respectively.[41] Therefore, layered metal boride will be a possible high-temperature superconductor.

1.3.3 Thermoelectric properties of metal boride

One of the other promising application for boron rich borides is high-temperature thermoelectric (TE) properties.[42–45] From the thermoelectric (TE) effects, electric power can be generated from waste heat and also for cooling devices, which operate without using any refrigeration medium. The type of semiconductor materials (n-type or p-type) greatly affect the efficiency of a TE. The inherent efficiency of any TE material is determined by a dimensionless parameter ZT given by equation 1.7.

$$ZT = \frac{\alpha^2 \sigma}{\kappa} T \qquad 1.7$$

where α, σ,κ, and T are the Seebeck coefficient, electrical conductivity, thermal conductivity, and absolute temperature, respectively. High Seebeck coefficient and enhanced electrical conductivity with reduced thermal conductivity should be needed for improved TE performance.[42,46,47] In all the metal hexaboride, alkaline earth hexaborides specially CaB_6 shows outstanding n-type thermoelectric properties due to higher or comparable power factor of CaB_6 than common TE materials such as Bi_2Te_3, PbTe, $Si_{1-x}Ge_x$.[42,48] Calcium hexaboride (CaB_6), is a divalent alkaline earth cubic hexaborides, having low density (2.45 g/cm^3), high melting point (2235 ℃), high hardness (Knoop: 2600 kg/mm^2), high Young's modulus (379 GPa), high electrical conductivity (Bandgap: 0.8± 0.1 eV) and high chemical stability.[49,50]

1.3.4 Anticorrosive properties of metal boride

Corrosion of metal is a serious problem, which causes the failure of the equipment made from metallic materials. This will bring economic losses and problems for the protection, durability, and safety of various resources. To address this issue a clear mechanism understanding is utmost required. It is known that for steel-based materials, reinforcement leads to the formation of rust, cracking, delamination, and degradation of structures. These issues arise mostly in construction (bridge, buildings) equipemnet.[51] The are various type of corrosion occurs such as atmospheric corrosion, galvanic corrosion and stress corrosion, which can reduce the performance of the materials. Therefore, the global research community oriented towards developing methods or materials to prevent this corrosion of steel. The corrosion can be protected by surface treatment procedure, which

will also improve the hardness, corrosion resistance, thermal stability and wear resistance of steel.[52,53] The application of steel or medium where they are going to use decide the coating materials. It is believed that stainless steel (SS) is anticorrosive in several media; however, enhancement in anticorrosive nature will be appreciable. The SS is an alloy of iron, carbon and mixture of chromium, nickel, molybdenum, and magnesium, which is one of the primary components of construction material in buildings, weapons, aircraft, marine, medical tools, and industrials equipment. Depending upon the end-user requirement, various grades of SS are available in markets. Air oxidation of stainless steel can be prevented by the metal coating of Zn, Mo, Sn, or Cu.[54] Whereas, for preventing the corrosion of stainless steel in acidic and alkaline media use of transition metal-based borides.[55,56] In high-temperature environments such as aeroplane or missiles required the anticorrosive coating, which can protect the outer surface by erosion and able to sustain that high temperature and thermal gradients. Earlier, various types of metal borides such as ZrB_2, TiB_2, FeB, Fe_2B, CrB_2, and HfB_2 has been used as an anti-corrosive coating in harsh media for a longer time.[57] Depending on the potential of the medium and the chemical composition of the base materials, single or duplex (FeB+Fe_2B) boride coatings may be formed. These type of coating materials mostly used in industrial applications.[52,58–60] To explore the possibility of making the highly anticorrosive stainless steel anti-corrosive nature of ZrB_2 deposited on stainless have been studied in the present thesis. Earlier, the corrosion behaviour of D.C. magnetron sputtered zirconium boride (ZrB_2) and zirconium boron nitride (Zr-B-N) on carbon steel have been investigated by M.Urgen *et al.* in neutral and acidic media.[61] C. Monticellia and co-workers also reported anticorrosive properties of ZrB_2 sintered with Si_3N_4 and ZrB_2/SiC composite in different aqueous solution.[62] The strong interatomic bonding of B-B and Zr-B atoms of the B-B rings and the covalent bond between zirconium with boron, gives very high hardness, high strength, chemical inertness and high-temperature stability.[63] These properties meet the requirement for making components of space vehicles such as sharp wing leading edges (in space shuttle), nose cones and propulsion components in future thermal protection systems of the hypersonic vehicles.[64] The metal borides can be used in several strategic application as anticorrosive coating such as in submarines.

1.3.5 Thermionic emission

In most of the display devices, the electrons used to make an image by using electron, emitted through thermionic emission**.** It has been observed 1st time in 1883

by Thomas A. Edison that passage of electricity from a filament to a plate of metal inside an incandescent lamp. In thermionic emission, at least a minimum energy has been acquired by the surface electrons of metal from the heat so that electron can remove from the metal surface. This minimum energy called the work function, which is one of the main characteristics of the electron-emitting material. Metal hexaboride (rare earth hexaboride) such as LaB_6, CeB_6 shows excellent performance towards cathode materials for thermionic emission.[65,66] These rare earth metal hexaborides have high melting point (beyond 2500 °C) excellent chemical and thermal stability, constant electrical conductivity and low work function (2.5- 2.7 eV).[38,67–70] The low work function materials give very high electron emission at a given temperature as compared to materials having high work function. Rare-earth hexaborides have been recognised as ideal electron emitter materials due to their low work function and high stability. In other words, electron emission from the outer surface of the atom by applying heat. The ejection of electron governed by the Richerdsen-Dusmen formula, which is given bellow.

$$J_s = AT^2\, e^{\frac{-\emptyset}{kT}} \qquad 1.8$$

Where j_s is the current density, A is Richardson's constant, T is temperature, ϕ is the work function of the cathode material, k is the Boltzmann constant. The most used metal hexaboride as the thermionic emitter is boron rich borides, where boron atom bonded covalently and generally there two- or three-dimensional boron cage or boron network are electron-deficient; however, can be stabilized by gaining electrons from metal atoms.

1.3.6 Field Emission

The discovery of anisotropic carbon nanotubes in 1991 by Iijima *et al.* gain extensive scientific support due to the hollow tube configuration, very tiny size, and almost perfect crystallinity. In the field of electronics, carbon nanotubes have shown a potential candidate for a long time as an electron field emission source with high emission current density due to a very sharp tip. The emission of electrons from metal or semiconductor (cathode material) to vacuum level can be done via thermionic emission, photoelectric emission, and field emission. The electrons emission from a cathode material into a vacuum can be achieved at less potential as compared to thermionic emission under the influence of a strong electric field. The field emission mechanism can be explained by quantum-mechanical tunnelling. Theoretically, the probability of an electron to be found beside the barrier is finite; however, the total energy of electrons is less the barrier potential. The

electrons will cross the potential barrier through tunnelling the potential barrier, unlike thermionic emission or photoemission case, where electron escaping over the potential barrier.[71] The process of electron emission through various mechanism has been illustrated in **Figure 1.7.**

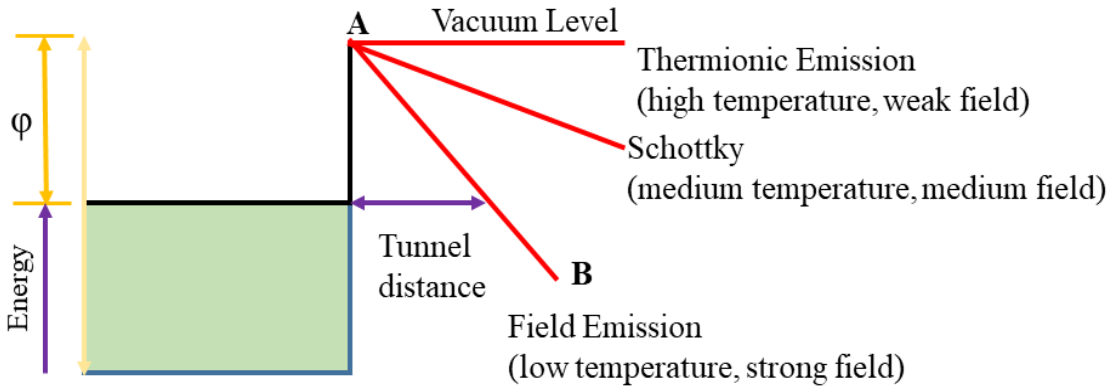

Figure 1.7. *Energy level diagram for electron emission at absolute zero temperature and comparison between different types of electron emission.*

The Fermi level of metal is filled with electrons and the energy required to reach at vacuum level from the Fermi level by an electron is known as work function (ϕ). Earlier, refractory metals such as W, Mo, and rare-earth hexaborides, such as LaB_6, CeB_6 and some metal oxides conventionally used for the field emission. Like carbon nanotubes, metal oxides also have a wide bandgap with a high work function, which creates joule heating and quickly damages the emitter when operating at high current density. Rare-earth hexaborides are superior to refractory metals, metal oxide and carbon nanotubes because of their low work functions, which is nearly 2-3 times less than that of refractory metals and carbon nanotubes. Figure 1.8 indicates the work function of several rare-earth hexaborides.[72–76] In Figure 1.7, the triangular barrier will be formed when a strong electric field applied across the cathode materials by deformation of the potential barrier along the line ***AB***. The position, where the Fermi level barrier is thinnest most of the emission occurs from the vicinity of that place. In other words, the withdrawal of electrons from any solid by tunnelling through the rounded triangular potential barrier is known as the field emission. The Fowler–Nordheim first explained this theory by the famous F-N.

$$J = \frac{A\beta^2 E^2}{\varphi} \exp\left(-\frac{B\varphi^{\frac{3}{2}}}{\beta E}\right) \qquad 1.9$$

$$ln\frac{J}{E^2} = \ln\frac{A\beta^2}{\varphi} - \frac{B\varphi^{\frac{3}{2}}}{\beta E} \qquad 1.10$$

Where A= 1.54 X $10^{-6}\, eVV^{-2}$, B= 6.83 X $10^3\, VeV^{\frac{3}{2}}\mu m^{-1}$, J, β, E and φ are the current density, field enhancement factor, applied field and work function of emitting materials, respectively. A plot of ln (J/E^2) versus 1/E is Fowler–Nordheim plot is approximately a linear curve. From the above observation, the material having low function with a high

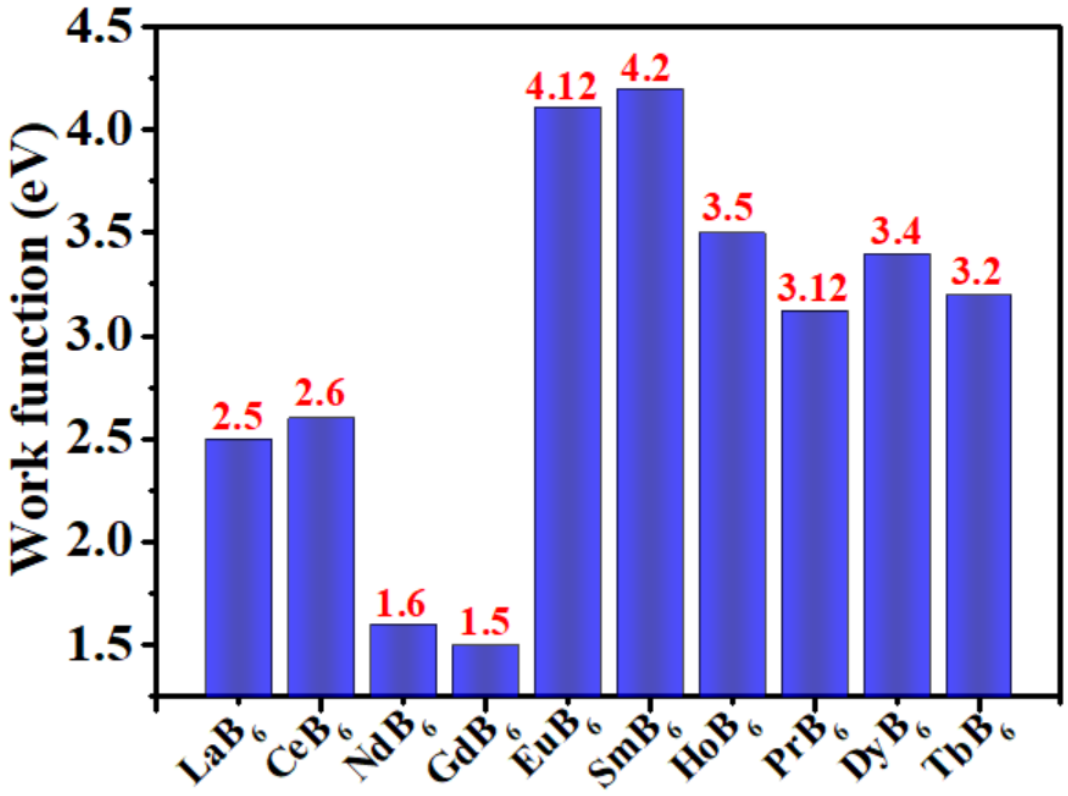

Figure 1.8. *Work-function of some rare earth hexaboride.*

the aspect ratio will serve as a good field emitting material. The rare earth hexaboride will be a good choice for the use of cathode materials in field emitter. Metal hexaborides show their unique range of properties when we talk about their electronic conductivity due to their unique bonding.[77] The covalently bonded boron atoms (B_6 framework) "encapsulate" the metal atoms by the electron-deficient B_6 framework, which enables the low work function of earth hexaborides. Theoretical and experimental evidence indicates the semiconductor nature of divalent metal hexaborides[78] and trivalent metal hexaborides are metallic in nature.[66,79] Lafferty's studied the thermionic emission properties of various several metal hexaboride materials such as ThB_6, BaB_6, SrB_6, CaB_6, LaB_6 and CeB_6.[66] The low work function (2.5 eV) and high current emission from lanthanum hexaboride makes

LaB_6 a promising thermionic emission source till that date. The electrochemically etched polycrystalline LaB_6 rod was used as the field emitter, and ~2 mA emission current was obtained and remain almost the same for more than 1000 h. In the present thesis, NdB_6, GdB_6, $La_xNd_{1-x}B_6$ and $La_xGd_{1-x}B_6$ was used as the cathode material. Earlier, to the best of our knowledge, there are only two reports of NdB_6 and only one report for anisotropic Gdb_6 based on field emission. In 1980's, M. Futamoto was first time used NdB_6 as cathode material for thermionic emission, which shows the comparable current density to LaB_6.[80] Also, mixed metal hexaboride shows a higher current density than the binary hexaboride.[80] Zhai *et al.* first time used the NdB_6 nanoneedles with sharp tips, which shows low turn-on (2.71 V/μm) and threshold (3.60 V/μm) electric fields, as well as a high current density (5.37 mA/cm^2) at a field of 4.32 V/μm.[75] A single crystalline GdB_6 nanorod was first time used as a tip emitter in 2005 by Han Zhang, and 10 nA current was obtained at a voltage of 650 V, and the emission current reached 200 nA.[74] It was observed that the temperature during emission was increased upto 400 °C.[74] Here, it is worth to mention there are no reports of field emission for mixed hexaboride ($La_xNd_{1-x}B_6$ and $La_xGd_{1-x}B_6$). Earlier, the theoretical report suggests that materials having low work function shows an exponential increase in current and shows excellent field emission, field-induced ballistic emission and thermionic emission current density.[81] The strong bonds between the boron atoms in the B_6 framework result in high thermal and chemical stability, which would be an ideal property for the material to be used in field emission display (FED) devices.[5] In the crystal structure of rare-earth hexaboride, rare earth metal has a total 24 coordination number and five coordination number of boron, including four B atoms in their octahedra cage and one B is in the direction to the adjacent octahedra cage.[66] The high conductivity in rare-earth hexaboride arises due to metallic bonding inside the rare-earth hexaboride; however, the covalent bond between B-B gives high stability such as high melting point, and high mechanical strength. The boron octahedra cage is electron deficient thus electron move over low energy barrier from rare-earth hexaboride surface, which is terminated with rare-earth atoms. The transport of electron from rare-earth atom maintains the metal atom layer through diffusion, which makes low work function of rare earth hexaborides.

Apart from the field emission, rare-earth hexaboride can also be used in modern application such as plasma/ion sources, optical coatings, thermionic converters, electron beam welders and free-electron lasers, sensors for photon detectors, electrical coatings for resistors, topological insulator, and used as additives to improve the oxidation resistance of ZrB_2 based UHTC.[82–85]

1.4 Synthesis of metal borides

As stated above, the low work function and anisotropic structure significantly increase the field emission properties; however, due to the covalent bond between the boron octahedra, synthesis of rare earth hexaboride requires high temperature as well as expensive instruments. The details of the synthesis condition will be discussed as follows.

1.4.1 Chemical vapour deposition

Earlier, rare earth hexaborides have been synthesised using the floating zone method, solid-state reaction, autoclave, thermal evaporation, pulsed laser deposition (PLD), and selective area laser-induced deposition.[86–91] CVD method has been developed to fabricate thin films. In this process, precursor gas passes through the reaction chamber (in most cases, several temperature zone tubular furnace) where the precursor gas either reacts with the sample deposited on substrate or deposits onto the substrate after decomposition. The CVD process can be modified as per the requirement. For example, MoS_2 film deposition, sulphur and molybdenum precursors have been placed at different temperature zone, and substrate was placed at the centre of the horizontal chamber.[92] In this process, argon gas was selected as a carrier gas, when the temperature rises in the different zone, the precursors evaporate and deposited to the surface of the substrate.[93] The various properties of the fabricated film such as thickness, uniformity, crystallinity and crystallographic orientation can be controlled by manipulating reaction parameters such as the flow rate, pressure, substrate temperature, catalyst, reaction time, and nature of substrate materials. Uniform, smooth film as well as epitaxial atomic layers can be grown via From CVD process. However, in the CVD process, the boron precursors are either BCl_3 or B_2H_6, these precursors of boron are toxic.[44] The anisotropic synthesis of rare earth hexaboride (NdB_6 and GdB_6) has been done using catalysed and self-catalysed (without catalyst) CVD process.[75,94–96] In a typical catalysed CVD process, first Pd, Pt or Au has been drop costed over the substrate followed by loading of corresponding rare earth metal on which rare earth hexaboride will grow. The as loaded rare earth metal and catalyst (Pd, Pt or Au) on the substrate has been placed in a horizontal tube of CVD and gaseous boron precursors allowed to flow during the heating process.[95,97] In the catalysed CVD process, gaseous boron precursors decomposed onto catalytic seeds (noble metal nanoparticles) and these catalytic seeds also used as "concentrators" to collect the chemicals needed for the "precipitation" of nanowires from these supersaturated particles. This reaction falls in vapour-liquid-solid (VLS) or vapour-solid-solid (VSS) mechanism depending on whether

the supersaturated metal particles are liquid or solid during the reaction. The anisotropic synthesis of rare earth hexaboride via CVD process follow the VLS mechanism because there are no metal particle was found on the tip of prepared nanorods.[98] For the synthesis of nanorods of metal hexaboride, CVD approach is mostly adopted by the researcher.

1.4.2 Solid-state reaction route

In solid-state reaction, the metal precursors and boron precursor were mixed and annealed in inert or vacuum to get the desire metal borides. In the solid-state reaction, high purity precursors with the high temperature often needed, which is higher than 900 ℃, where the metal boride formation occurs by the reaction of all the reactants. The excess lighter elements such as H, C, O, or N converts into gaseous product. Borothermal and carbothermal reductions reaction are the two well know used solid-state methods for synthesizing hexaborides.[99–102] The metal oxide or metal and excess boron will be needed during the borothermal reductions, while carbothermal reductions utilize carbon or organometallic compounds and boron oxide during the synthesis of rare earth hexaboride. The recent, report suggests that metal nitrate, metal chloride, metal oxides, or metal hydroxide with $NaBH_4$ or elemental boron can also be used for borothermal reduction synthesis metal boride.[103,104] The utilization of $NaBH_4$ as a boron precursor significantly reduced the synthesis temperature. It has been observed that the addition of reducing metal atom such as Mg can also reduce the synthesis temperature. Boron-carbon reductions, where B_4C utilized as both the reducing agent (carbon) as well as a source of boron.[105] The outcome metal boride can be affected by several ways such as initial precursors, the used ratio of precursors, mixing of precursors and their mixing medium, the particle size of precursor, and reduction temperature and duration. The annealing of the mixture of high purity metal precursors with boron precursors in inert or argon gas for several hours gives the metal borides.[66,106] The other solid-state route such as the floating zone method, molten salt method, mechanochemical synthesis can also be used for metal boride synthesis. In the floating zone method, pure metal, or metal oxide precursors with an excess amount of boron melted under argon to obtained crystallized phase of metal boride. Apart from the above methods, metal borides can be also synthesised using mechanochemical synthesis.[107] Other methods such as spark plasma sintering (SPS), aluminium flux, electrochemical synthesis, hot press and plasma sintering method can also be used for the synthesis of metal boride. In summary, the metal boride can be synthesised using various methods such as chemical routes,[108–110] reduction processes,[111,112] hot pressing,[63,113] spark plasma sintering,[114]

pressureless sintering,[115] chemical vapour deposition,[116] self-propagating high-temperature synthesis,[19] magnesiothermic reductions,[104] and borothermal reduction.[117]

1.5 Fabrication of film

Various properties of metal boride such as catalytic, field emission, corrosion can be verified via the making of the film over the desired substrate. Earlier, sol-gel, plasma spraying, plasma electrolytic deposition, sputtering, PECVD, CVD have been used for the fabrication of metal boride films.[74,75,90,118–122] However, these techniques require high-end equipment as well as the toxic precursor. Earlier, the doctor blade and spin coating technique has been used for the fabrication of thick and thin coating, which was mostly used for making a variety of low cast electronic devices.[123] In the electrodeposition technique, the thickness can be tuned as a function of temperature and applied potential, which is an energy-intensive process. In the present thesis, we have used a doctor blade technique and spin coating process. These processes are economical, and film of controlled thickness can be easily fabricated.

1.5.1 Doctor blade technique

The doctor blade technique (tape casting) is a large area surface deposition method and widely used for producing films over the substrate.[124,125] Earlier, several decades doctor blade method is used to fabricate the sheets of piezoelectric materials and capacitors.[126] In the doctor blade method, a well-mixed slurry of the coating materials with additives (such as binders, dispersants or plasticizers) is placed on a substrate and a constant relative motion with constant force applied between the blade and the substrate. Due to the motion and force between blade and substrate a thin sheet has been formed and dried to get the thin film of desire materials. The doctor blading can operate at the required speed on a commercial scale. This method is suitable to coat the substrate with a very wide range of wet film have thicknesses ranging from 20 nm to several hundred microns. A typical process of doctor blade has been given in Figure 1.9.

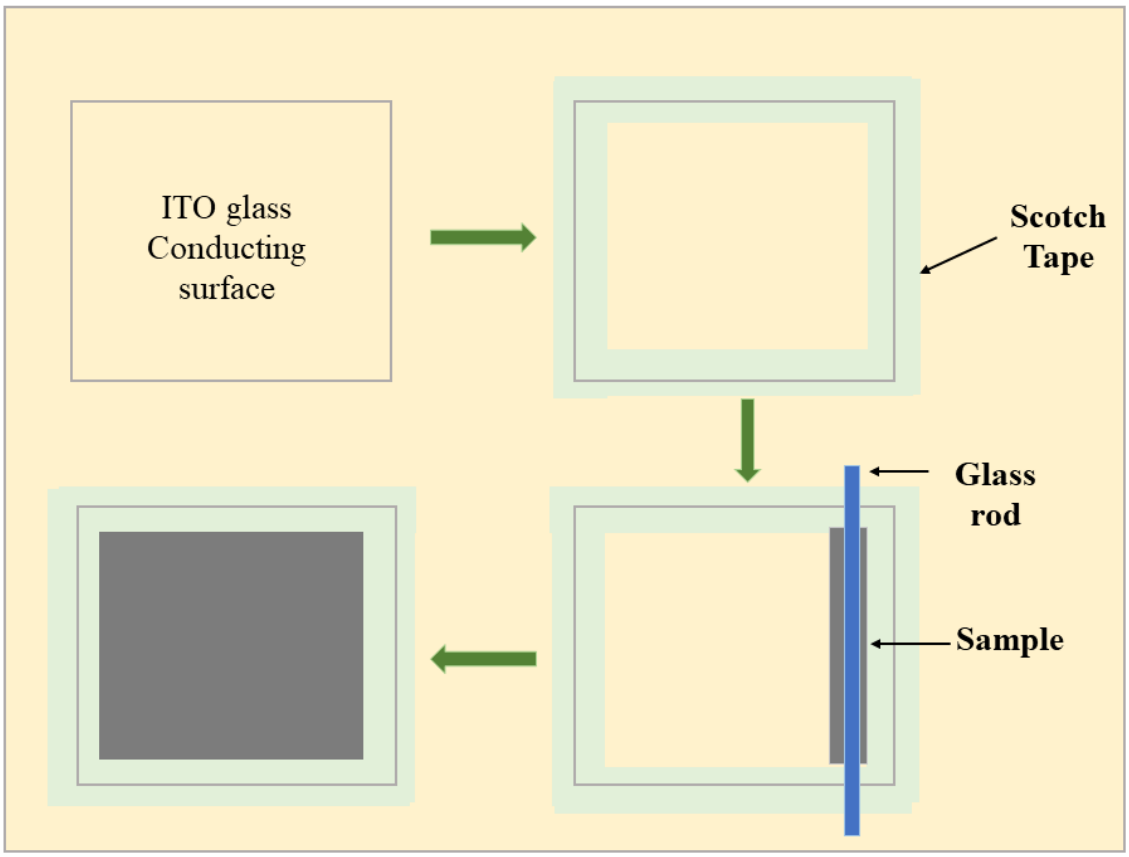

Figure 1.9. *A typical coating procedure via doctor blade coating procedure.*

1.5.2 Spin Coating

Spin coating is the easiest and economical process for the fabrication of the film over the solid substrate. For fabrication of the film, first, the dispersion of the desired sample in a suitable solvent is usually attempted. Then the solution is dispensed at the centre of the substrate surface followed by rotating the substrate at the desire rotation. The film thickness can be controlled by controlling the spinning speed, surface tension, and viscosity of the dispersion. After the spin-coating process film is cured by drying the sample at the desired condition. The spin coating process uses the principle of centrifugal force to disperse the liquid over the substrate (Figure 1.10). The centrifugal force of the rotation causes the liquid to spread into a film and coat the surface. This technique can be used for the deposition of various ceramic materials, such as lead zirconate titanate (PZT), CeO_2, ZrB_2.[14]

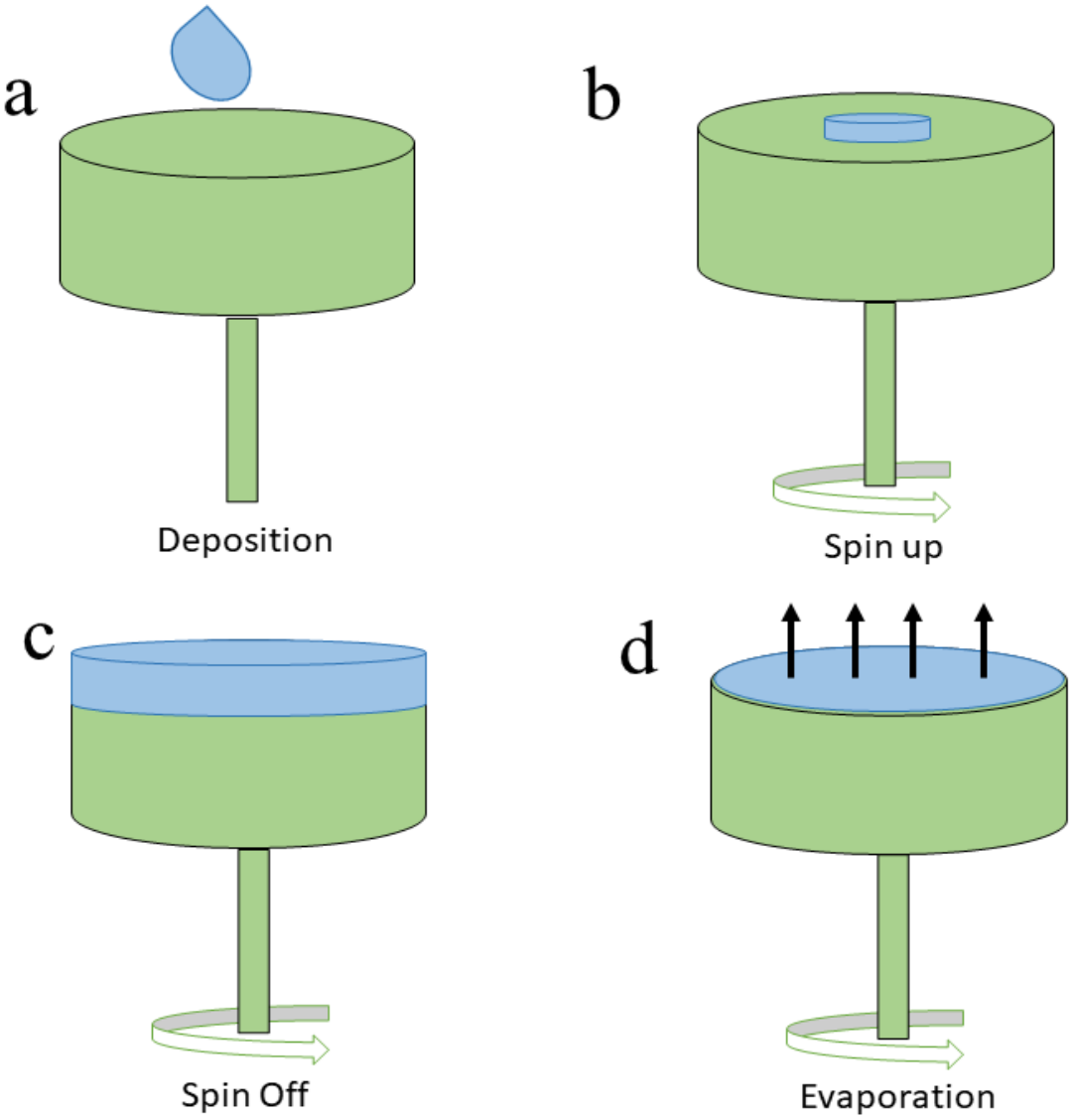

Figure 1.10. *A typical spin coating procedure.*

1.6 Characterization techniques for the metal borides film and powder

1.6.1 Powder X-ray diffraction

German physicist Röntgen has discovered X-rays in 1895 and named "X-ray" because of their unknown nature. These rays are invisible, moving in a straight line and photographic plate can be affected by these rays somehow like the light. These rays have a remarkably high intensity to penetrate thick objects such as the human body, metal plate, and other opaque objects. If an X-ray can be placed on one side of an object a shadow picture can be obtained on other ends by placing a photographic film. Earlier, X-ray is used in the medical imaginary system for diagnosis purpose. In 1912, the phenomenon of constrictive x-ray diffraction by crystals was discovered and the latter X-rays was used to

investigate the structure of materials. X-ray diffraction can indirectly reveal the crystallographic structure of any materials upto 10^{-7} mm in size. The wavelength of the X-ray is ~ 0.5-2.5 Å. Two types of X-rays spectrum generated when the electrically charged particle (mostly electrons) of sufficient kinetic energy rapidly decelerates. The first one is the continuous spectrum and the second one is the characteristic spectrum**.** For the structure analysis, the characteristic spectrum has been used. The characteristic spectrum defined as K, L, M and so on. There are set of K spectra such as $K\alpha_1$, $K\alpha_2$, and $K\beta_2$; however, mostly strong diffraction observed in PXRD data and additional higher wavelength line easily adsorbs. These characteristic x-ray lines were discovered by W. H. Bragg and systematized by H. G. Moseley. The latter found that as the emitter atomic number increases the wavelength decreased and give a liner relation (Moseley's law) between the square root of the line frequency ν and the atomic number Z:

$$\sqrt{\nu} = C(Z - \sigma) \qquad 1.11$$

C and σ are constant. In modern time, Powder x-ray diffraction (PXRD) is a very essential tool to characterize crystalline materials. From this method, the crystallographic structure, the crystallite size (grain size), stress, strain (due to doping or any other reason) and preferred orientation in polycrystalline or powdered solid samples can be obtained. PXRD is used to get the identification of the unknown substance, characterize heterogeneous solid mixtures, and determine the relative abundance of crystalline compounds. The Rietveld refinement of data obtained from PXRD can give information such as lattice parameters, space group. X-ray diffraction is based on the principle of constructive diffraction, which was the first time proposed by Bragg's and defined as Bragg's law:

$$n\lambda = 2d\sin\theta \qquad 1.12$$

where λ is the wavelength of X-rays (1.5418 Å for Cu Kα), d is the interplanar distance. Though it is a challenge to solve a structure from powder diffraction data, there are cases where structures have been solved using powder diffraction data. A typical image of PXRD has been given in Figure 1.11a. A simple X-ray geometry has been represented by the ray diagram in Figure 1.11b.

1.6.1.1 High-temperature x-ray diffraction

The X-ray diffraction study at the variable high temperature has been used to get the information about crystallinity and phase change of materials in the desired temperature range. The *in-situ* high-temperature X-ray diffraction works on the same Bragg's diffraction method. *In-situ* high-temperature X-ray diffraction provides additional unique

information such as temperature-dependent phase transformations, the thermal changes of structural parameters and changes of the real structural parameters with temperature. The high-temperature X-ray sample assembly has been shown in Figure 1.11b.

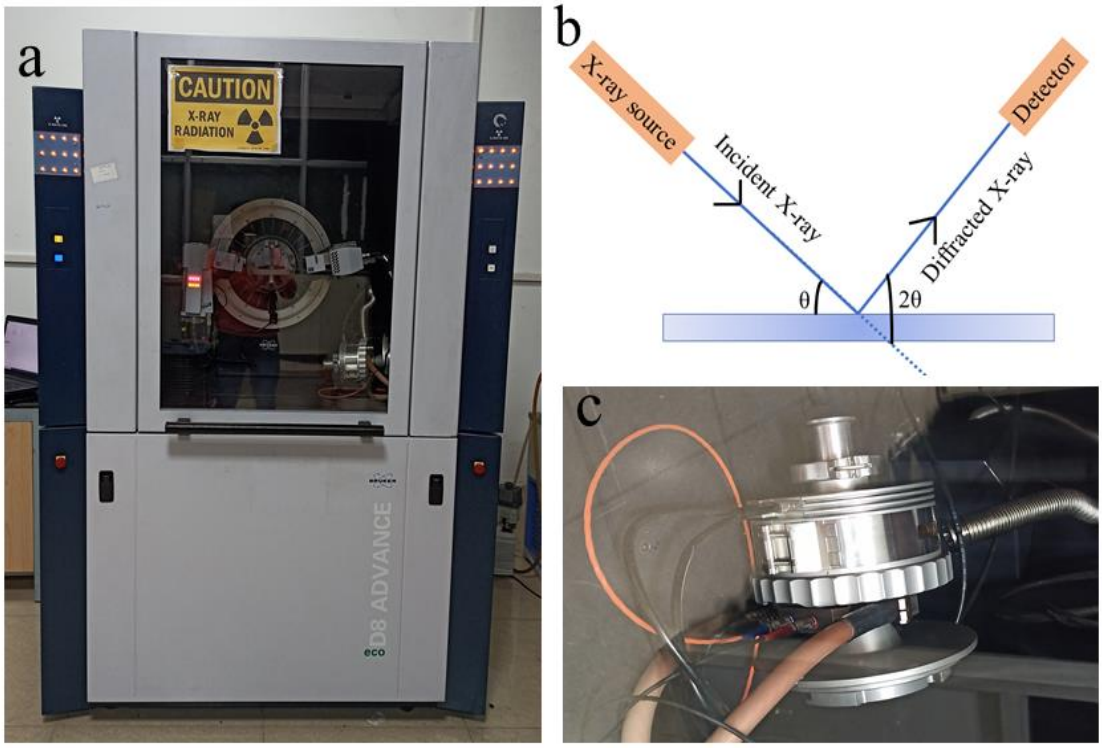

Figure 1.11. *(a) A typical view of PXRD instrument. (b) High-temperature X-ray sample holder. (c) X-ray generation geometry.*

1.6.1.2 Grazing incident X-Ray diffraction

It has been observed that X-ray diffraction of thin film using the conventional method results in a strong intense peak of the substrate and week diffraction peak for the film sample. One can avoid the high intense signal from the substrate by performing 2θ scan with a fixed grazing angle of incidence, popularly known as GIXRD. Mostly the fixed angle is just above the critical angle of the total reflection of the substrate. The GIXRD can be used to determine the phase of crystalline surface (Film) or layers pattern because. In GIXRD, the arises diffraction signal is strong due to the four-time enhancement of the electric field at the critical angle. A disadvantage is the limited in-plane spatial resolution (beam footprint). The typical image of the GIXRD has been shown in Figure 1.12.

Figure 1.12. *A typical view of grazing incident X-ray diffractometer.*

1.6.2 Thermogravimetric analysis

In thermogravimetric analysis (TGA) the weight or mass of the sample can be measured as the function of temperature or time. During the TGA measurement sample is typically heated at a particular heating rate or placed at a constant temperature (isothermal measurement). The temperature choice depends upon the type of information required

about the sample. The atmosphere used in the TGA will play an important role. In TGA curve the weight or mass or percentage mass obtained against temperature or time. For the analysis of TGA, 1st derivative of the TGA curve concerning temperature or time has been used, which represent the mass change rate and known as differential thermogravimetric (DTA) curve. The following types of information can be obtained from the TGA/DTA.

- Get the knowledge of volatile constituents, desorption and adsorption of gases, moisture removal, loss of water of crystallization and other volatile substances
- Oxidation temperature of the metal in the air or any atmosphere
- Thermal decomposition with the formation of gaseous products
- With organic compounds, the decomposition process is known as pyrolysis or carbonization
- Production of synthetic temperature for new materials
- Prediction of change in magnetic properties (Curie transition)

It has been seen that there will be TGA signal observed if heated in an inhomogeneous magnetic field. The modern thermo-balances are designed in such a manner that they can record the DTA (differential thermal analysis) signal during the actual thermogravimetric measurement (TGA). In DTA not only the nature of weight loss events can be observed the DTA signal can also reveal the thermal effects which cannot be predicted by a mass loss such as melting, crystallisation or a glass transition. These properties can be predicted using endothermic and exothermic peaks. The endothermic peak related to the adsorption of energy and exothermic refers to the release of energy during the thermal treatment. A typical view of TGA/DTA has been shown in Figure 1.13.

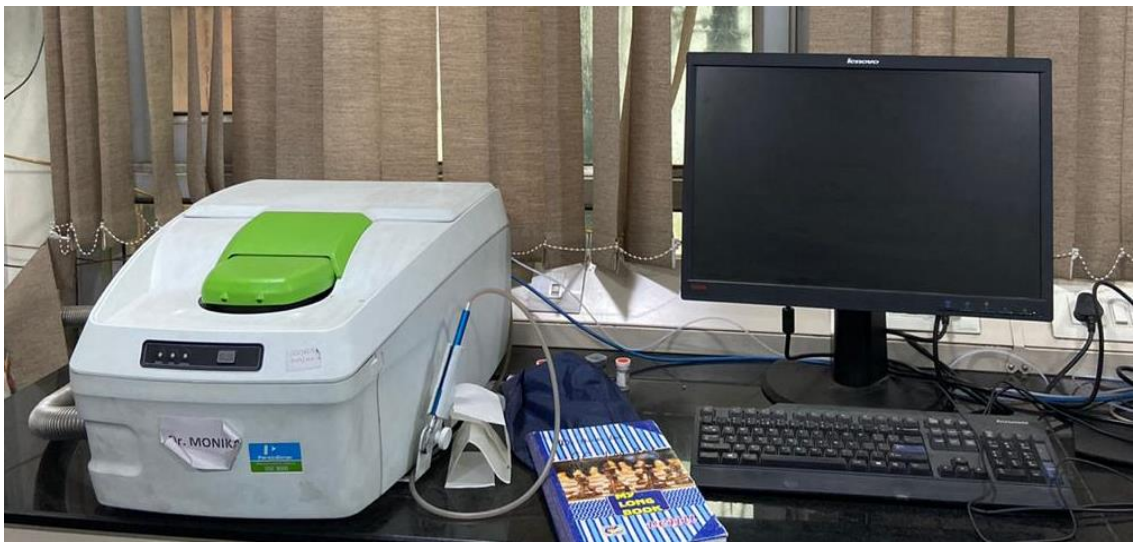

Figure 1.13. *TGA system for studying the thermal stability of compounds.*

1.6.3 Inductively coupled plasma- mass spectroscopy

In the field of analytical chemistry, precise measurement in term of qualitative, as well as quantitative elemental analysis is important for metal borides. There is various instrumentation technique available such as a flame photometer, inductively coupled plasma- atomic emission spectroscopy (ICP-AES), atomic absorption spectroscopy (AAS) and inductively coupled plasma- mass spectroscopy (ICP-MS). ICP-MS is widely used to measure the quantitative elements presented in the field of chemical and material science. In ICP-MS, extremely low concentration can be measured, which will be in a range from ppb (parts per billion = µg/l) to ultra-low-concentrations of elements (ppt = parts per trillion = µg/l). In ICP-MS, atomic elements are lead through a plasma source where they become ionized. Then, the type of elements has been detected through the mass of the ions. A typical view of ICP-MS instrument has been shown in Figure 1.14.

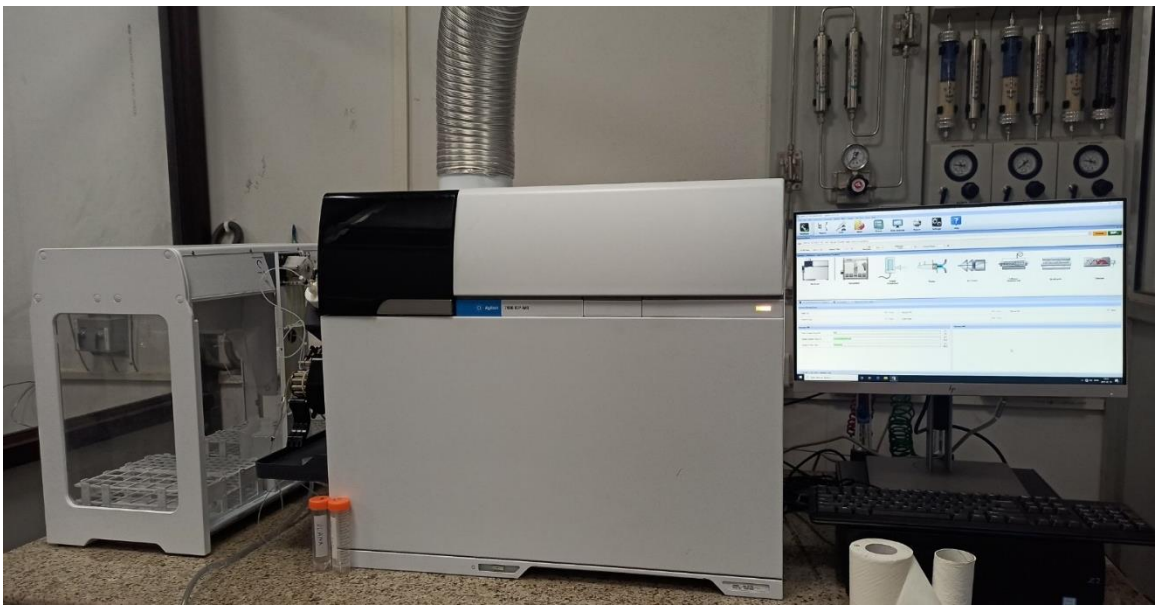

Figure 1.14. *Typical view of inductively coupled plasma- mass spectroscopy.*

The ICP-MS technique has advanced technique over AAS or ICP-OES (inductively coupled plasma optical emission spectrometry) due to;

- Extremely low detection limits
- A large linear range
- Possibilities to detect isotope composition of elements

For the elemental detection through the ICP-MS technique, first sample solution has been injected into the device through the peristaltic pump. The injected sample is further nebulized in a spray chamber and the resulting aerosol introduced into high temperature (5500 -7500 ℃ and up to 10000 ℃ for refractory materials) argon-plasma chamber.

Further, the solution has been removed from the sample followed by atomization and ionization inside the plasma torch. Only a small amount of the ions introduced in the plasma, which further reached the mass-spectrometer part. A small amount of ion generated by plasma has been transmitted by an interface into "sampler cone" and a skimmer cone followed by migration of ions into extremely high temperature and atmospheric pressure environment.

1.6.4 Surface Area Measurements

The knowledge of the surface area of nanostructured materials is an important criterion to predict possible applications in the field of semiconductors, heterogeneous catalysts as well as in biological research. The surface area is the highly desirable tool used by catalyst manufacturers and users to monitor the activity and stability of a catalyst. The various surface area measurement technique has been used. The widely used methods are based on the adsorption-desorption of inert gasses (mostly nitrogen, which will be physically adsorbed on the material surface). The adsorption-desorption methods for measuring the surface area are sensitive to outermost atomic layers (depth of 2-3 atomic layers) of the bulk solids. Many techniques to characterize the surface area and pores of materials have been available such as mercury porosimetry, thermoporometry, and BET surface area method. The theory developed by Langmuir and by Brunauer, Emmett and Teller (BET) is used to measure the pores and surface area of materials. A typical view of the surface area instrument has been shown in Figure 1.15.

The BET theory is the extension of the Langmuir theory which applied only to a monolayer and it is developed by Stephen Brunauer, Paul Emmett, and Edward Teller in 1938. Brunauer–Emmett–Teller (BET) method is associated with the adsorption of gas molecules on a solid surface and serves as the basis for the measurement of the specific surface area. The gas can be physical or chemical adsorption on the surface of materials. In the physical adsorption process, energetic molecules overlay on the first sites at low relative pressure. The chemical adsorption process is a result of the chemical reaction between the solid and the adsorbate. The concept of the BET theory is based on the following hypotheses.

1. Gas molecules physically adsorb on a solid in infinite layers
2. Gas molecules only interact with adjacent layers
3. The Langmuir theory can be applied to each layer
4. The enthalpy of adsorption for the first gas molecular layer is constant and higher than the second gas molecular

5. The enthalpy of adsorption for the second gas molecular layers is the same as the enthalpy of liquefaction

Figure 1.15. *A typical view of surface area analyser.*

1.6.5 Scanning electron microscopy

Scanning Electron Microscope works similarly to the optical microscope, however; here beam of electrons has been used rather than light to get the micrograph. Light microscopy uses visible light (400- 700 nm) and transparent lenses to see entities. It can see the tiny object up to one micrometre, such as a red blood cell (7 μm) or a human hair (100 μm). The light microscope can be zoom up to 1000 x and can distinguish the object separated from each other by 200 nm. However, fundamental science research needs a more resolving microscope, therefore scientist looked for electron microscopes. Electron microscopes have high resolving power and can capture the micrograph up to the atomic level.

In SEM, the beam of electrons generated through the cathode and travel towards the specimen using a positive electrode (anode) in an extremely high vacuum. The beam

can be confined into monochromatic and focus on sample using magnetic lenses and metal apparatus. The electron beam interacts with the atoms of the specimen and generates a signal which contains information on surface topography, composition, and other electrical properties. The information was collected via a detector and processed the image. During the collision of high energy electrons with atoms, several types of signals generated such as secondary electrons, backscattered electrons (BSE), characteristic x-rays and transmitted electrons. To collect the specialized signal, a specialized detector should be needed. Secondary electron imaging or SEI is the most common or standard detection mode in SEM. Figure 1.16 represent the generation of the various type of electron source.

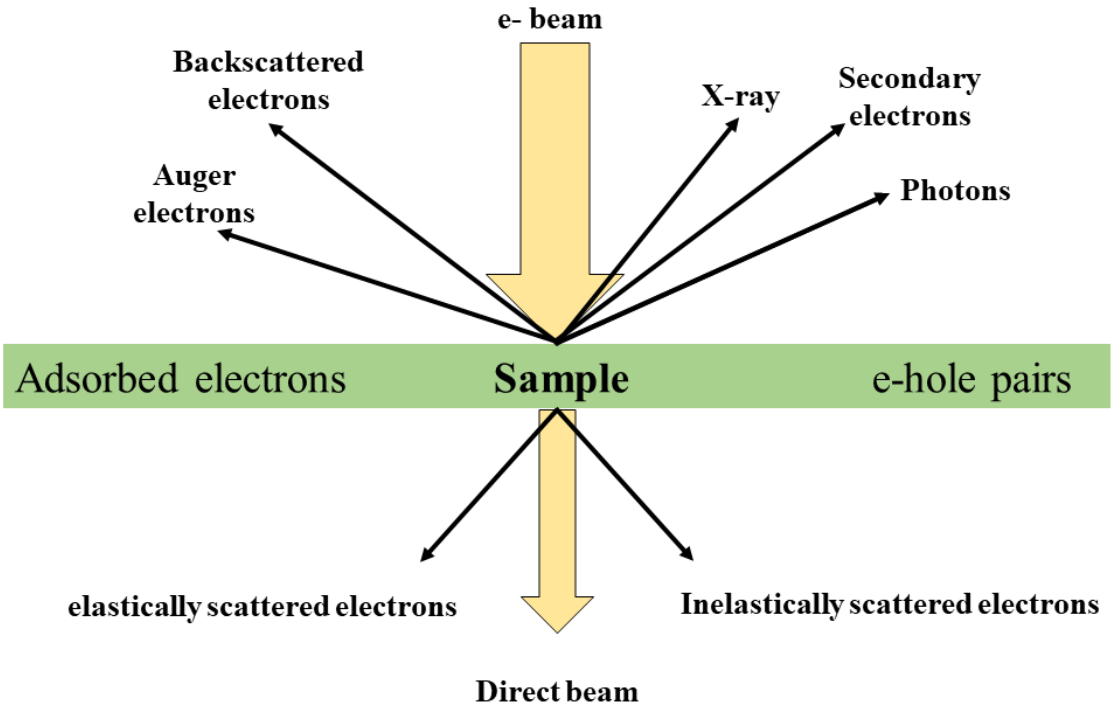

Figure 1.16. *Nature of transmitted and reflected electrons.*

In 1931, electron microscope was first developed by Ernst Ruska and Max Knoll having a resolution of 100 nm, which was enhanced up to 0.05 nm by using electromagnetic lenses. The beam of electrons produced when cathode (tungsten, copper) heated by current accelerated towards the anode. The produced beam moves in the vertical vacuum column via electromagnetic lenses, which concentrate the beam down toward the sample. When the incident beam touches the surface of the sample and produces signals of various type such as secondary electrons (SE), Auger electrons, Backscattered electrons (BSE), Characteristic X – Rays, Cathodoluminescence. The obtained signal has been captured by the detectors and converts the obtained information into digital images. The low

acceleration voltage has been used to avoid beam penetration into the surface as we require only secondary electrons from the true surface structure of a sample. A schematic representation of the SEM has been shown in Figure 1.17.

Figure 1.17. *(a) A typical view of SEM column. (b) The EDX detector (backside of column). (c) Gold coater unit.*

Major advantages of SEM-imaging are as follows.

- 3D and topographical imaging can be generated
- Processing to get images are very fast
- SEM requires very less sample preparation
- Cross-sectional SEM can result in the thickness of the film

Therefore, due to their advantage it is wide acceptable for capturing the surface morphology and surface structures of materials or film.

1.6.5.1 Energy-dispersive X-ray spectroscopy and elemental mapping

The information of atomic constituents can be also obtained from EDX coupled with SEM spectroscopy. In SEM-EDX the elements having an atomic number higher than boron (boron can also be detected using some modification) can be detected at 0.1 concentration. The EDX can be used in numerous application such as material evaluation and identification, determination of contamination, quality control screening, and others. When the electron beam collides onto the SEM specimen and generate characteristic X-rays and it is well known that no two or more atoms have the same X-ray wavelength consequently different energy. The detector collects the X-ray spectrum and measured its concentration in the sample.[127] In principle, X-ray production is the result of the primary electron beam collides with the nucleus of the specimens atom and will excite the electrons in the nucleus of an atom, which leaves that particular shell and shift to a different shell. The vacant electron position of an atom will replace the missing ejected electron and releases the superfluous X-ray. The emitted X-ray have both types of electron (X-ray continuum and characteristic X-ray). However, the energy dispersive spectrometer uses the characteristic X-ray for the measurement of elemental composition. Apart from the elemental percentage in the specimen and the micrograph, electron microscopy can produce the information of elemental distribution in the specimen in a form of an image. The elemental distribution image formed by collecting characteristic X-rays from elements by a raster scan across the specimen. The first, compositional image was obtained nearly 50 years back from the electron-beam instrument and after that extraordinary progress has been incorporated. A schematic representation of the EDX detector attached with SEM has been shown in Figure 1.17b. EDX setup also includes elemental mapping. In EDX-mapping mode the atoms presented in the sample has been shown in form of various colour. EDX-mapping can give an overview of the position of the atom presented at the specimen.

1.6.6 Transmission electron microscopy

In a conventional transmission electron microscope, a thin layer of the sample has been exposed to an electron beam of identical current density. The routine acceleration voltage for an instrument is 100–200 kV. The electrons have been emitted from the cathode in various ways such as thermionic, Schottky, or field emission. Out of these emission methods, the field emission is provided with remarkably high brightness and coherent beam in microscopic operation. Condenser and electromagnetic lenses have been used to focus and select the aperture of the incident electron beam on the specimen. After the interaction

of sample to electron beam, the transmitted beam is used to create the image of the sample on the fluorescent screen coupled with a CCD camera. For the transmission electron microscopy, specimen thickness should be extremely low. For a crystalline sample, diffraction contrast arises between the Bragg-reflected beam on-axis (dark field) and the primary beam (bright field), which is important for the imaging of crystal defects. The projection of atomic rows in the crystal structure can be obtained by passing the Bragg-diffracted beams. A typical image of TEM instrument has been shown in Figure 1.18.

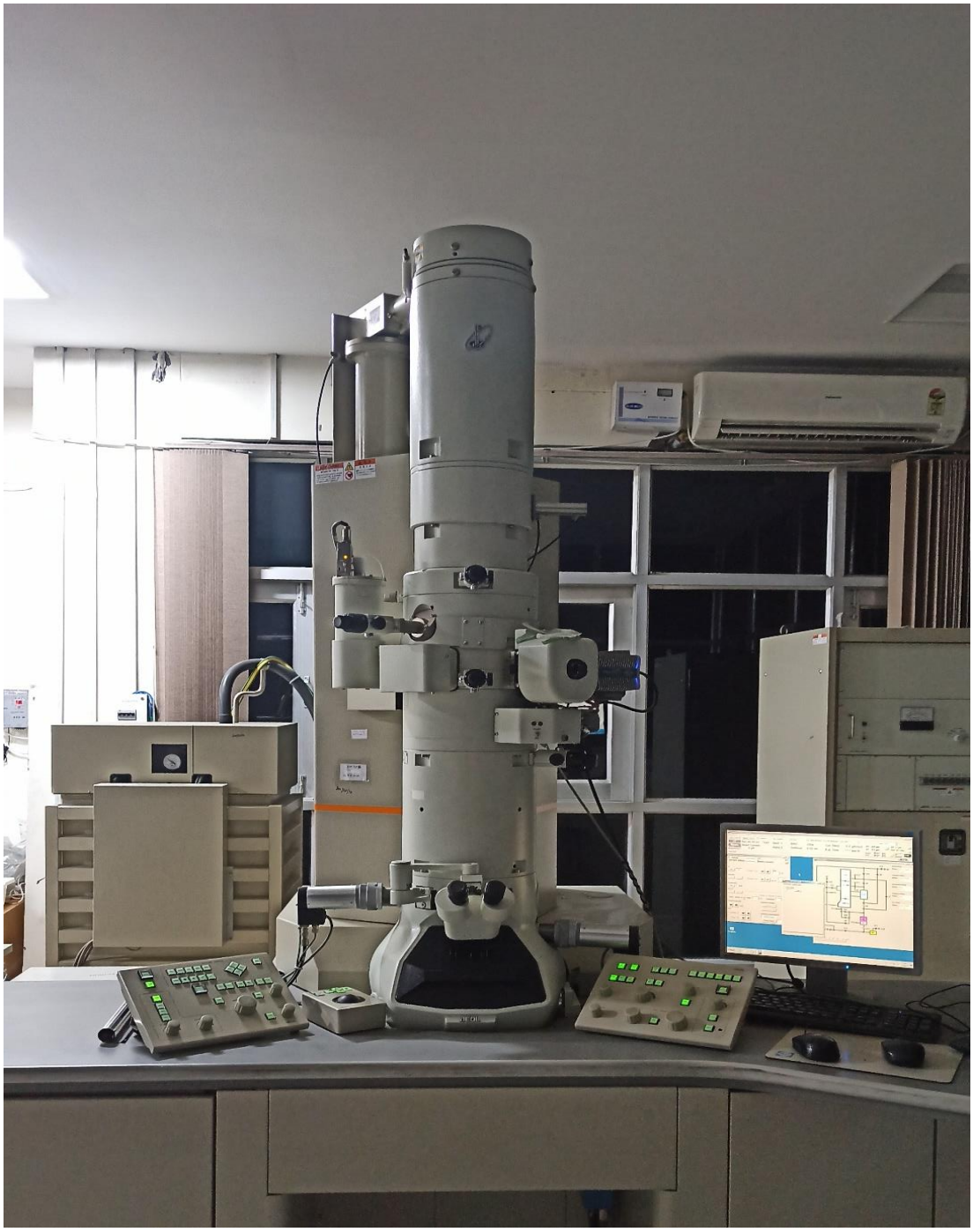

Figure 1.18. *A typical image of **t**ransmission electron microscopic.*

In a TEM, an electron gun produces a beam of monochromatic electrons which is focused on a small, thin, coherent beam by condenser lenses. The spot size (beam diameter which strike on a sample) has been determined by the first lens, however; at the same time movement of the spot can be defined by the second lens. The high angle electron beam filtered by the condenser aperture. The beam strikes the specimen and a small portion through the specimen. The objective lens has been used to focus the transmitted portion of the beam to form an image on the fluorescent screen. The obtained image is passed down the column through the intermediate and projector lenses, which is magnified by lenses. The image strikes the phosphor screen where we can see the image. When the samples have been very thin then the electron beam easily transferred through it and form an image; however, sometimes the image is very dark which represent the thicker layer of samples.

1.6.6.1 High-resolution electron microscopy

The TEM and High-Resolution Electron Microscopy (HRTEM) used the same principle to create an image on the fluorescent screen by the signal acquired by the detector. However, using high-resolution microscopy, we can do imaging at atomic level. Transmitted and scattered electron beams have been used to create an interference image in high-resolution transmission electron microscopy (HRTEM). HRTEM can even identify the unit cell of the crystal. At an extremely low angle, the outgoing modulated electron waves interfere with themself during propagation across the objective lens and electrons rising from the sample combined at a point in the image plane. In HRTEM, if the low-index direction is exactly perpendicular to the electron beam in a tilted thin slice of crystal, all lattice planes will be parallel to the electron beam and will be close to the Bragg position and diffract the primary beam. All the diffracted beams (diffraction pattern is the Fourier Transform of the periodic potential in 2D) and the primary beam brought together by the objective lens and their interference offers a back-transformation and leads to an expanded picture of the periodic potential.

Selected area electron diffraction

The selected area electron diffraction **(**SAED) is a diffraction pattern obtained at the luminescence screen on TEM. In SAED, a parallel beam (plane wave travelling in one direction) interacts with the sample. An aperture can be used for the selection of area (few hundred nanometres) where diffraction pattern is to be recorded. SAED diffraction patterns are either simple spot patterns corresponding to single-crystal diffraction or ring patterns

corresponding to powder diffraction from multiple crystals with variable orientation. It can use for phase identification, determination of structural intergrowth, determination of growth directions.

1.6.7 Profilometry

The topography of the surface can be extracted from the profilometry via a single point or line scan or three-dimensional scan. Most of the time profilometry is to find out the thickness of the film; however, it can be also used to get the data from surface morphology, step heights and surface roughness. The detector and sample stage are the two main part of the profilometers. Few systems allow the stage to move and few allow the detector for measurement. Stylus profilometers and optical profilometers are the two main type of profilometers. A probe has been used in stylus profilometers to detect the surface and the probe moves with the surface to acquire the surface height via force feedback mechanically in the z-direction. The changes in the Z position of the arm holder will be used to reconstruct the surface. The resolution of the stylus profilometer is lower than the non-contact technique due to the involvement of physical movements in X, Y and Z at the same time maintaining contact with the surface. Figure 1.19 shows the typical instrument image of profilometry used for the analysis of metal borides.

Figure 1.19. *Typical view of the profilometer.*

1.6.8 Ellipsometry

The ellipsometry technique based on the optical properties of light. The change in polarization has been measured when the light reflects from or transmits through a material structure. The polarization-change is represented as an amplitude ratio (Ψ) and a phase difference(Δ). The optical properties and thickness of each material are responsible for the

change in polarization. The film thickness and optical constant can be determined by ellipsometry; however, one can predict the change in composition, crystallinity, roughness, doping concentration, and other material properties associated with a change in optical response. From the ellipsometry data, we can calculate various parameter such as the refractive index of film, the thickness of film based on an appropriate model. Luckily, light reflection physics from surfaces is well understood therefore the selection of accurate models can be made based on classical electromagnetic theory. Here, first, metal boride dispersion has been made using appropriate dispersion media. The prepared dispersion has been uniformly spin coated over cleaned Si-substrate and used for ellipsometry study. Figure 1.20 shows the typical image of Ellipsometry.

Figure 1.20. *A typical view of ellipsometry.*

1.6.9 Electrochemical corrosion study

Corrosion can be measured by various technologies such as mass loss, surface degradation study by SEM and electrochemical corrosion test. In the electrochemical corrosion test, the flow of current through the working electrode is measure with time. During the corrosion test, low current flow indicates the superiority of the materials and vice versa. The electrochemical corrosion test can be studied using standard three-electrode cell by linear sweep voltammetry (LSV) and electrochemical impedance spectroscopy (EIS) measurements. In the three-electrode cell, a working electrode, the reference electrode and the counter electrode are necessary to perform the corrosion test. Here, 3M Ag/AgCl used as a reference electrode with 304 stainless steel modified with the

synthesised materials used as the working electrode and platinum as an auxiliary electrode. The linear sweep voltammetry was carried out after 30 min, 2 days and 14 days of immersion in different electrolytes with a scan rate 1 mV/s in the potential window – 1 V to + 1 V. Apart from the corrosion potential and corrosion current, the protective efficiency PE(j) of the coated material was also calculated by using the following equation 1.13;

$$PE_{(j)} = \left(1 - \frac{J_{corr}}{J^0_{corr}}\right) \times 100 \qquad 1.13$$

where j_{corr} is the current density of coated stainless steel and j^0_{corr} corresponds to the uncoated stainless steel. All the EIS measurements were carried out under sinusoidal AC potential at the frequency range from 0.01 to 100 kHz. The working electrode has been made in 1 cm^2 and our anticorrosive materials have been deposited over it. Various electrolyte media can be used for the electrochemical corrosion study. A typical image of an electrochemical setup has been shown in Figure 1.21.

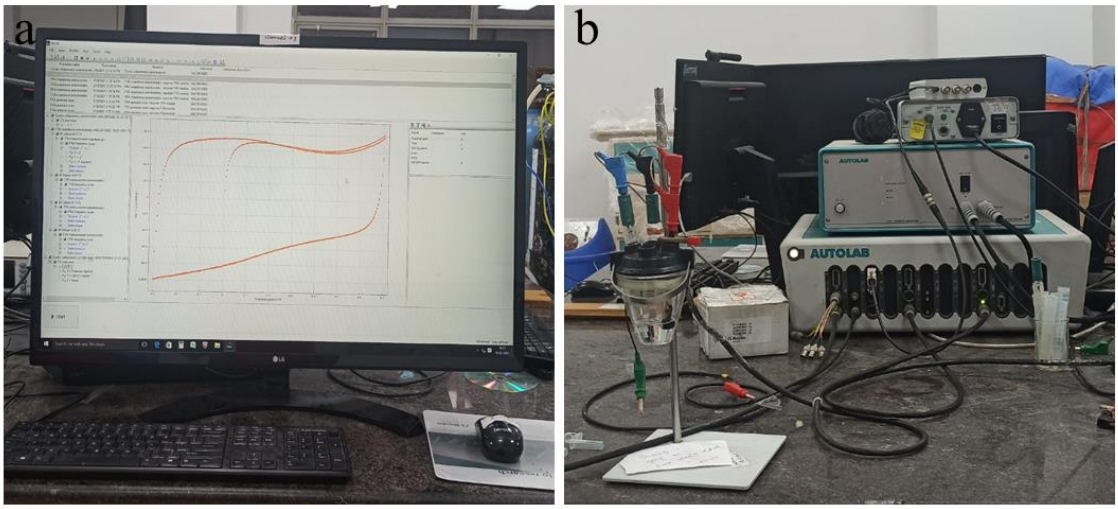

Figure 1.21. (a) Computer setup for electrochemical setup. (b) conventional 3 electrode setup to Autolab.

1.6.10 Field emission

Field emission property is the emission of electrons in presence of electric field. The emission current can be measured by F-N equation. To measure the field emission current, a self-assembled parallel plate anode-cathode configuration (diode configuration) in a high vacuum (7×10^{-7} mbar) is used (Figure 1.22). The metal hexaboride samples deposited over a conducting substrate are used as a cathode substrate in all the field emission experiments. The steel substrate is used as an anode. The distance between the cathode and anode was kept at 300 μm. A high voltage DC power supply (Stanford Model PS350) was used for generating an electric field between electrodes, and an electrometer

(Keithley 2000 DMM) was used to measure the field emission current. The applied electric field was calculated by dividing the applied voltage by the inter-electrode gap. All field emission measurements were performed for four cycles to see the repeatability field emission result obtained for all the samples and reading were recorded automatically for every 10 s through a computer interfaced with field emission system using LabVIEW program.

Figure 1.22. (a) The vacuum chamber of field emission set-up. (b) open chamber of field emission setup. (c) electrometer to measure the field emission current.

1.6.11 Raman spectroscopy

The Raman spectroscopy used as fingerprints to identify the chemical structure of materials. and physical forms and to determine quantitatively the amount of a substance in a sample. In this process, samples can be characterized in solids or liquid. The Raman scattering is an inelastic scattering phenomenon of light first postulated by Smekal[128] in 1923 and first observed experimentally in 1928 by Raman and Krishnan.[129] In the original Raman scattering experiment, sunlight was focussed by a telescope onto a sample which was either a purified liquid or a dust-free vapour. A second lens was placed by the sample to collect the scattered radiation. A system of optical filters was used to show the existence of scattered radiation with an altered frequency from the incident light. It is observed that when a beam of light passes through a substance, a small amount of radiation scattered. If instead of a beam of light, radiation of narrow frequency or monochromatic beam will be used, the scattered beam is the almost same frequency of incident (called Rayleigh

scattering) with very few scatterings below and above to the Rayleigh scattering is known as Raman scattering.

The Raman scattering may be understood by quantum theory. When the photons of the energy of hν collide with molecules and if the collision is elastic then the incident photon deflected without any loss of energy, which can be detected through the detector placed right angle to the incident beam. However, it has been seen that during the collision energy exchange between the incident photons and molecules and referred to as an inelastic collision. During the inelastic collision, the exchange of energy can be defined in form of quantum. The change in energy ΔE, will be the difference in the allowed energy state. If the molecules gain energy from the incident photon then deflected photons will have the energy $(h\nu - \Delta E)$ with frequency $(\nu - \frac{\Delta E}{h})$. In the same manner, if incident photons acquire energy from molecules then the deflected photons will be scattered with energy $h\nu + \Delta E$ and frequency $\nu + \frac{\Delta E}{h}$). Radiation scattered with a higher frequency called anti-stokes radiation and radiation having a lower frequency referred to as stokes lines. Stokes' lines are more intense than the anti-stokes line. The typical image of the Raman Spectrometer has been given in Figure 1.23.

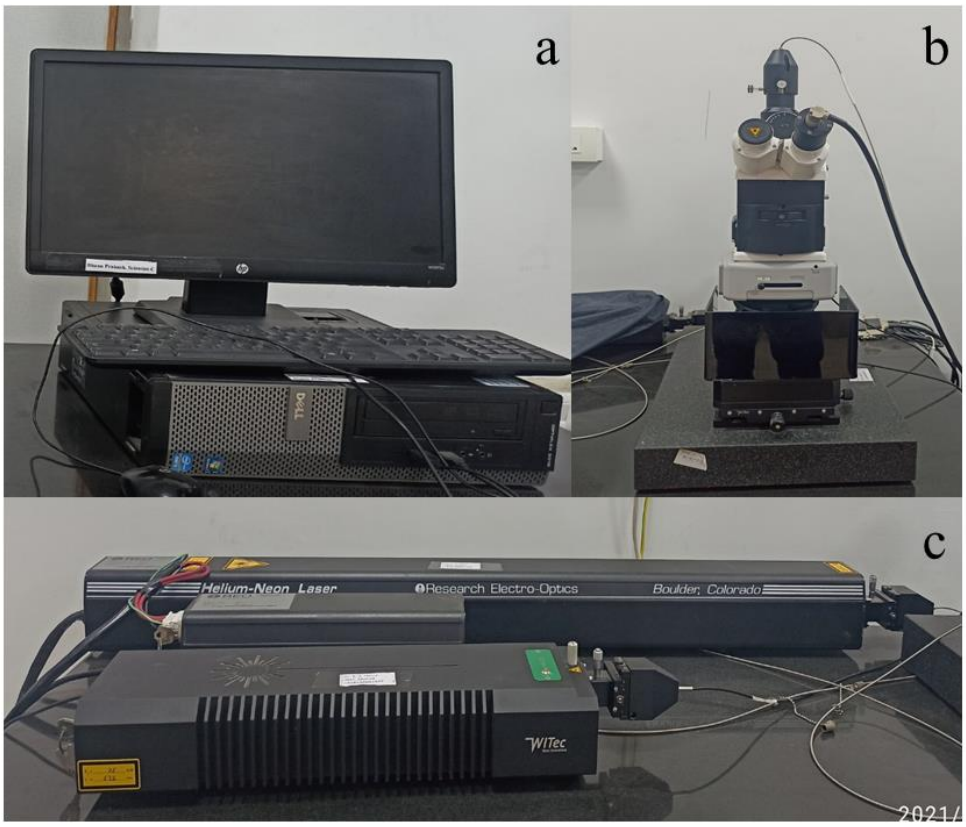

Figure 1.23. *(a) Computer of Raman setup. (b) spectrometer. (c) lesser source.*

1.6.12 Atomic Force Microscopy

Atomic force microscopy technique enables us to measure the surface morphology with high resolution and accuracy. This technique is helpful for surface understanding. The distribution of materials at the surface of any substrate can be measured using AFM.[130] Resolution of AFM is very high as it contains 40-50 individual atoms in 5 nm and can measure the crystallographic structure of materials.[131] In AFM, we can analyze various types of materials surface such as very hard, ceramic material, dispersion of metallic nanoparticles, very soft, highly flexible polymers, human cells. AFM has invented in the 1980s, can be used in all fields of science, such as chemistry, biology, physics, materials science, nanotechnology, astronomy, medicine, and more. The AFM is based on the three basic concepts which are piezoelectric transducers (commonly known as piezoelectric scanners), force transducers (force sensors), and feedback control. The piezoelectric scanner moves the tip throughout the surface of the sample, the force sensors sense the force between the tip and the surface, and the feedback controller, feeds the signal from the force sensors back into the piezoelectric, to maintain a fixed force between the tip and the surface of the sample. AFM has also various 'spectroscopic' modes and measured the properties of the sample at the nanometre scale. There is a wide range of AFM modes are possible now-a-days, which makes AFM is a very versatile and powerful tool. A typical image of AFM has been shown in Figure 1.24.

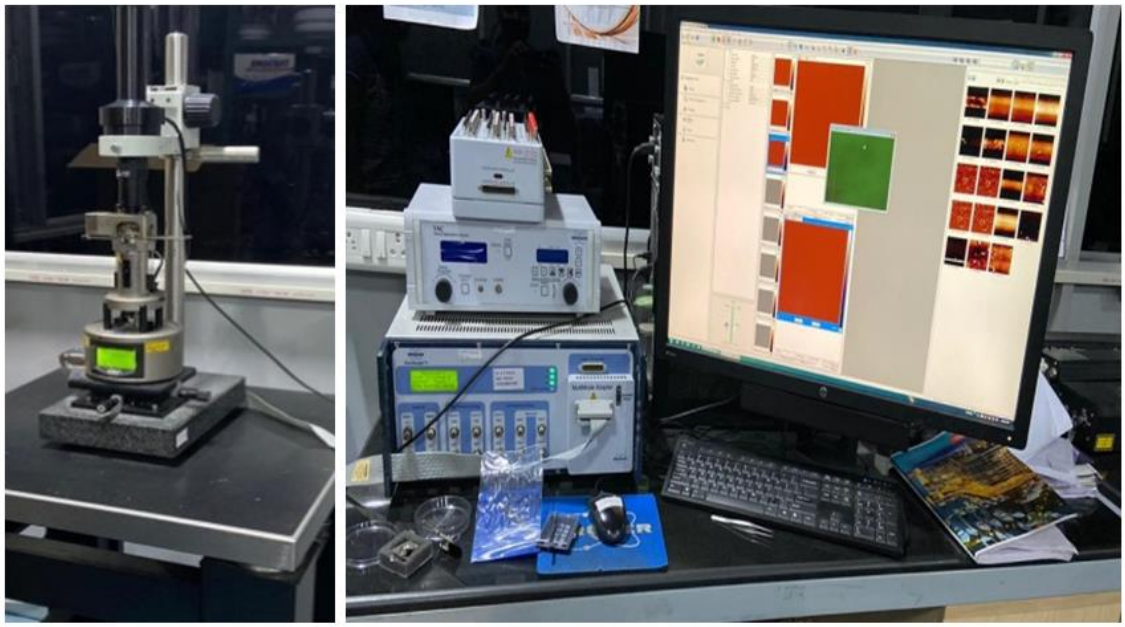

Figure 1.24. *The typical Atomic force microscope setup.*

Topography mode

As a microscopic technique, AFM will do topography the sample. AFM measure the mismatch of height and transformed it into a more naturalistic image with light shading. The differences between various mode lead not only to different experimental procedures, however; they depend on the information available, differing suitability for samples, and even to differences in the interpretation of the data.

Contact mode

This mode is one of the simplest forms and basic for all other modes. Therefore, knowledge of contact mode is very necessary to understand other advance modes. Several limitations occur in this mode such as different information gathers for the same sample in different environments. However, still, contact mode is an extremely powerful and useful technique as it can acquire very high-resolution images. In all the topography mode is the fastest modes, as the cantilever directly deflect which leads to the generation of the topography of the sample (Figure 1.25).

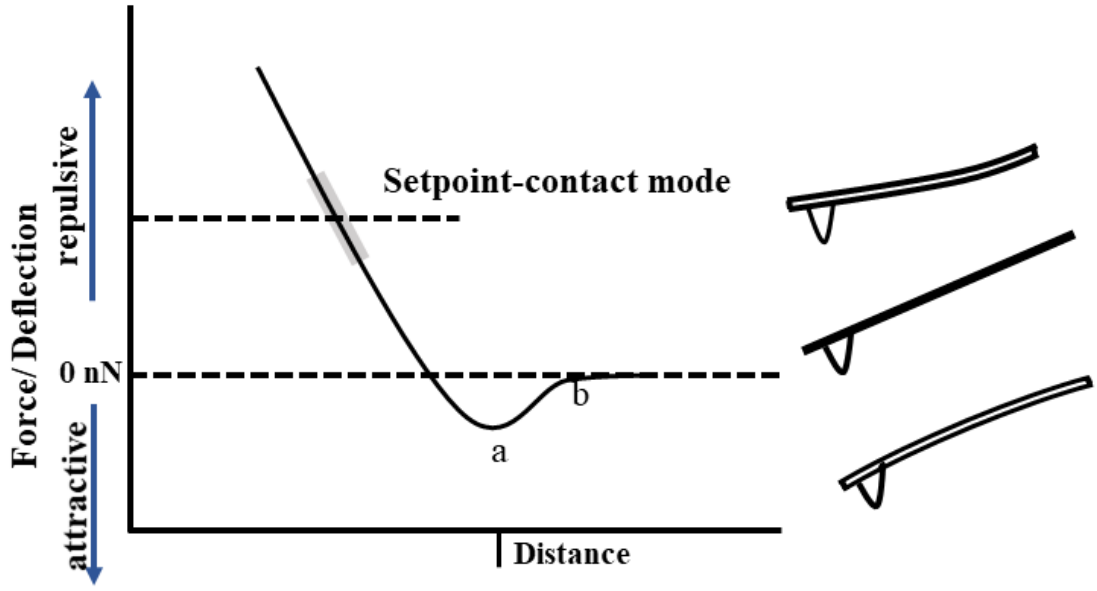

Figure 1.25. *Force–distance curve showing contact (repulsive region) scanning regime.*

Since the Tip is in always contact mode with the sample surface therefore there are certain things may happen:

1. Due to the repulsive force between the tip and the sample, the sample may be damaged or conversely, the tip could also be damaged during the scanning process.

2. Since both tip and sample are always in contact with each other the normal forces they apply to each other, the probe and sample lateral forces are experienced by both probe and sample

3. The nature of the surface of the sample may affect the results obtained, which implies that the technique is sensitive to the nature of the sample

The forces applied to the surface by the probe in contact mode are given by Hooke's law:

$$F=-k \times D \qquad 1.14$$

where F force (N), k probe force constant (N/m) and D deflection distance (m).

In contact-mode AFM the cantilever deflected by the feedback system to keep the tip at a certain value determined by the operator known as set-point. This parameter is very important to get the optimized image. Contact mode gives the highest resolution in all other modes.

Non-topography mode

Earlier, non-topography AFM (known as scanning-tunnelling spectroscopy), tunnelling voltage ramped and monitored the tunnelling current with the tip, which has been fixed over a particular distance to the sample surface. Here the 'spectroscopic' techniques probe the sample properties rather than just giving topography. Several modes have been invented into a non-topography mode such as force microscopy.

Magnetic force microscopy

The application of AFM to study the magnetic properties of materials in form of the film has gained lots of researcher interest.[132] It is well known that the magnetic fields lines decay very rapidly as we move away from the magnetic surface, while magnetic properties measurement and to avoid this the tip should be very close to the surface. The most conventional AFM experiment for measuring the magnetic properties of magnetic force microscopy (MFM) is one of the common non-topography modes.[133] The MFM, the distribution of the magnetic field can be measured directly by using a magnetic probe. The magnetic forces are few magnitudes lower than tip-sample forces when in contact with the sample surface, which enables us to measure them at a certain distance from the surface (5–50 nm) from the surface and lowers the interference from short-range forces.[134] Bard *et al*. shows that the first topography can be recorded by uplifting the probe and measure the long-range force. At the same time it considers the shape of the topography but at a certain

'lift height'.[135] Whatever the method is used, lifting the tip from the surface reduces resolution, and resolution in MFM is typically no greater than 30 nm laterally.

Electric force microscopy and scanning Kelvin probe microscopy

Here, electric force microscopy (EFM) is analogous to MFF; however, in this mode electrical signal has been measured rather than magnetic fields. The technique can be used in lighting mode without a magnetic coating on the cantilever (Tip). In EFM mode, a standard silicon cantilever may be used although conductive (metal-coated) tips are required for read/write applications and more sophisticated electrical modes. The force equation governing the AFM in this mode:

$$F_{electrostatic} = -\frac{1}{2} V^2 \frac{dC}{dz} \quad 1.15$$

The tip-sample potential can be scan through scanning Kelvin probe microscopy (SKPM)[136]. SKPM measure the forces between two surfaces and if there is no potential difference then there is no force between them. To implement the technique, a DC potential bias (V_{DC}) is applied to a conductive probe, which is further modulated by an AC signal (V_{AC}) and oscillate at the resonant frequency of the cantilever frequency. From this method, the absolute values of the work function of a sample can be obtained if the tip is first calibrated against the known work function of the sample.

$$V_{bias} = V_{DC} + V_{AC} \sin t \quad 1.16$$

1.6.13 X-ray photoelectron spectroscopy

The constituent elements and how they are bonded to each other in the materials define the physical properties of matter. It is known that most of the materials are in the solid or liquid, which exhibit a surface layer and several dissimilarities occur between them. It could be chemical, structure or both. The physical properties of the surface may vary due to the forces acting on them such as External Forces (Adsorption and/or Corrosion of the Outer Surface) and Internal Forces (*i.e.*, Those Relayed through Surface Free Energy). Due to these forces, various physical properties will affect such as adhesion, adsorption, biocompatibility, corrosion, desorption, interfacial electrical properties, texture, visible properties, tribological, wettability. TEM being microscopy only exposes the physical structure of the object. To uncover the chemistry a spectroscopy technique will be more useful. However, in all the available spectroscopies very few such that X-ray photoelectron spectroscopy (XPS) are capable to give the information (chemistry active over the outermost surface) of most out surface (~10 nm of the solid).

X-ray photoelectron spectroscopy (XPS) is a versatile tool among all the known electron spectroscopic technique to evaluate the elemental compositions, empirical formula and chemical state of materials over the most outer layer.

These are the following application of XPS.

- XPS identify a wide atomic number range (Z=3 to Z=92) and compute the elemental composition of the outer solid surface
- Reveal the chemical environment such as oxidation state
- Uniformity of elemental composition across the top surface
- Elemental composition as a function of ion beam etching (depth profiling)
- The above information can be obtained with relative ease and minimal sample preparation

In XPS studies, the sample is bombarded by X-ray under ultrahigh vacuum and during this process, the ejected electrons and associated kinetic energy has been analyzed. In XPS, electrons are ejected from the core-levels of the elements from the sample by an X-ray photon of energy $h\nu$. The kinetic energy (E_k) of the emitted photoelectrons is measured and is related to the binding energy of materials by the following equation.

$$E_B = h\nu - E_k - \Phi \qquad 1.17$$

Where, E_B = Binding energy of the electron, $h\nu$ = photon energy, E_k = kinetic energy of the photoelectrons, Φ = spectrometer work function

The binding energy of the samples has been plotted as a function of the number of electrons (counts). Since the binding energy, any elements are their characteristic feature therefore it can be used to get the elemental composition. The characteristic peaks correspond to the electron configuration of the atoms, e.g., 1s, 2s, 2p, 3s, etc. The number of detected electrons in each of the characteristic peaks is related to the quantity of the element within the (volume) irradiated. A typical image of XPS has been shown in Figure 1.26.

Figure 1.26. *A typical XPS instrument.*

1.7. Motivation of thesis

The family of metal borides divide into two categories: (1) metal-rich boride and (2) boron rich boride. Most metal-rich metal borides are known for their high hardness, thermal and electrical conductivity. These properties make them find application in immense scientific and industrial applications. The boron rich metal borides such as LaB_6, GdB_6, NdB_6 are known for their electronic properties and can be used in flat panel display and cold electron emitter. Despite exotic structure and tremendous application of metal boride, the major issue researcher has faced is metal boride adverse synthetic conditions. Also, due to this issues, till date there is very few studies have been done on nanostructured metal borides. Metal borides are generally synthesized using a solid-state route which tends to occur at high temperature (1500 °C-2500 °C) and results in large particles. Earlier, anisotropic nanostructured metal boride has been grown by chemical vapour deposition method. However, in most cases, it requires toxic boron precursors such as BCl_3 or B_2H_6 or complex boranes [113]. In view of this, the present thesis deals with the synthesis of nanostructured rare earth hexaboride (NdB_6, GdB_6, $La_xNd_{1-x}B_6$ and $La_xGd_{1-x}B_6$) and transition metal diboride (ZrB_2) at low temperature without using any toxic precursors. In the case of metal hexaborides, we have been successfully able to stabilize the cubes and rod like morphology

at low temperature (1000 °C). The as obtained metal hexaboride rods have been dispersed in a mixture of ethanol and ethylene glycol via ultrasonication method. The above dispersion has been utilized to fabricate metal hexaboride films over silicon substrate using spin coating process. Further, curing of the film have been done through the slow evaporation of metal hexaboride films. The obtained metal hexaboride powder and film have been characterized by advanced analytical technique. Interestingly, AFM studies of all the composition of metal hexaboride nanorods show that the rods are vertically oriented. Further, field emission of metal hexaboride shows that the vertically oriented rods have better field emission properties as compare the previous reports of bulk and nanostructured metal hexaboride counterparts.

We have also worked on stabilization of nanostructured metal diboride (zirconium diboride) via borothermal reaction of nanostructured zirconia and boron in presence of argon. The ZrB_2 has interesting properties such as high chemical, mechanical, and thermal stability, high melting point, good oxidation resistance, excellent thermal shock resistance, and refractory properties. These properties make them to find application in corrosion-resistant materials, cutting tools and the nose cone of aerospace. These properties arise due to the strong interatomic bonding of B-B and Zr-B atoms of the B-B rings and the covalent bond between zirconium with boron, respectively.

In the present thesis, the adopted synthesis route can be further used for other metal borides such as HfB_2, TiB_2, CrB_2. Here, the process for the development of metal hexaboride nanorods can be extended to many other complex metal borides, metal oxide and metal chalcogenides which are known for their optical and electrical properties.

1.8 Summary

Metal borides have attracted lots of researcher interest due to their interesting properties such as high melting point, high thermal and electrical conductivity, low function, and high chemical inertness. In the present thesis, two types of metal borides (rare earth hexaboride and IVth group transition metal boride) have been studied. Rare earth hexaborides (NdB_6, GdB_6, $La_xNd_{1-x}B_6$ and $La_xGd_{1-x}B_6$) have been used for field emission, and transition metal boride (ZrB_2 and TiB_2) were used as anticorrosive materials for the different electrolyte.

The second chapter deals with the synthesis of the anisotropic nanostructure of NdB_6. First, $Nd(OH)_3$ nanorods has been synthesised, which was used as Nd-precursor for

NdB_6 synthesis. $Nd(OH)_3$ nanorods of size 10 nm X 120 nm with an aspect ratio of 12 has been synthesis via hydrothermal route at 120 ℃. The synthesis $Nd(OH)_3$ nanorods annealed at 1000 ℃ with different heating in the presence of $NaBH_4$ as a boron precursor for the synthesis of NdB_6 nanorods. It was observed that different heating rate could tune the end product. The slow heating (40 ℃/h) leads to the formation of 10 nm X 100 nm NdB_6; however, at 250 ℃/h heating rate enables the formation of nanocubes up to 15-20 nm. The NdB_6 nanorods show the < 4.5 V/μm turn field and highest field enhancement factor (β = 2263).

In the third chapter, the material having the lowest work function in hexaborides, *i.e.* GdB_6 has been synthesized and used as a field emitter. The $Gd(OH)_3$ nanorods of dia ~10 nm, length ~ 120 nm and aspect ratio ~12 has been synthesised at 120 ℃ via hydrothermal route. The as-prepared $Gd(OH)_3$ nanorods with $NaBH_4$ as precursors of Gd and B respectively has been annealed in argon at 1000 ℃ with the different heating rate. The slow heating (40 ℃/h) leads to the formation of 40 nm X 150 nm nanorods, whereas a higher heating rate (250 ℃/h) indicates the formation of cubes of ~40 nm. Further, the field emission study of different GdB_6 nanostructures fabricated on Si-substrate via spin coating has been used and the anisotropic structures indicate the low turn-on field (4.4 V/μm) and the high enhancement factor (β = 1490).

As discussed above that doping of lanthanum ion can reduce the work function. Therefore, the fourth chapter deals with the synthesis and field emission application of lanthanum doped neodymium hexaboride ($La_xNd_{1-x}B_6$), where x=0.1, 0.2, 0.3, 0.4 and 0.5. The lanthanum doped neodymium hydroxide [$La_xNd_{1-x}(OH)_3$] with different concentration of lanthanum has been prepared via hydrothermal route at 120 ℃. $NaBH_4$ with $La_xNd_{1-x}(OH)_3$ mixed and annealed in the presence of argon at 1000 ℃ with 40 ℃/h. Further, TEM study shows the formation of nanorods of $La_xNd_{1-x}B_6$, and after deposition used for the field emission study. The field emission study has been done and it has found that 30 % lanthanum doped NdB_6 ($La_{0.3}Nd_{0.7}B_6$) gives the lowest turn-on field (3.6 V/μm) and highest field enhancement factor (β=2459).

We believed that the lanthanum doping in GdB_6 would certainly enhance their field emission properties. Therefore, in the fifth chapter, lanthanum doped gadolinium hexaboride has been synthesized and studied the impact on field emission current by lanthanum doping. The $La_xGd_{1-x}B_6$ (x=0.1, 0.2, 0.3, 0.4 and 0.5) has been synthesized by annealing of $La_xGd_{1-x}(OH)_3$ with $NaBH_4$ in presence of argon at 1000 ℃ with 40 ℃/h. The $La_xGd_{1-x}(OH)_3$ is synthesis via a hydrothermal route at 120 ℃. In the present work, first-

time $La_xGd_{1-x}B_6$ rods have been synthesized via a chemical route. Earlier, there is only one report for the synthesis of $La_xGd_{1-x}B_6$. It has been observed that the enhancement factor is much not affected by the La ion concentration. The field enhancement factor is ~1568 for $La_{0.5}Gd_{0.5}B_6$ with turn-on field ~5(V/μm).

The sixth chapter deals with the low-temperature stabilization of transition metal boride (ZrB_2) and its utilization for protecting the 304 stainless steel in various sulphate containing corrosive environment. First, ZrO_2 nanostructures of 10-15 nm particles as a precursor of Zr has been synthesised at 120 ℃. The ZrO_2 has been thermally reduced with elemental boron by annealing at 1200 ℃ in the presence of argon leads to the formation of pure ZrB_2 of ~150 nm particles. The as-prepared ZrB_2 has been fabricated on 304 stainless steel using the doctor blade technique. The electrochemical performance, viz linear sweep voltammetry (LSV) and electrochemical impedance spectroscopy (EIS) studies of ZrB_2 on 304-grade stainless steel (SS) show highly anticorrosive behaviour with excellent protection efficiency (up to 98% in acidic media) as compared to bare 304SS in sulphate containing neutral, acidic and alkaline media. The 7^{th} chapter deals with the main conclusions of the thesis as well as their prospect.

1.9 References

1 J. Zhang, J. Liu, H. Liao, M. Zeng and S. Ma, *J. Mater. Res. Technol.*, 2019, **8**, 6308–6320.

2 L. Li, H. Li, Y. Li, X. Yin, Q. Shen and Q. Fu, *Appl. Surf. Sci.*, 2015, **349**, 465–471.

3 J. Nagamatsu, N. Nakagawa, T. Muranaka, Y. Zenitani and J. Akimitsu, *Nature*, 2001, **410**, 63–64.

4 X. Wang, G. Tai, Z. Wu, T. Hu and R. Wang, *J. Mater. Chem. A*, 2017, **5**, 23471–23475.

5 G. Akopov, M. T. Yeung and R. B. Kaner, *Adv. Mater.*, 2017, **29**, 1604506.

6 J. Barcena, J. Coleto, S. C. Zhang, G. E. Hilmas and W. G. Fahrenholtz, *Adv. Eng. Mater.*, 2010, **12**, 623–626.

7 G. Akopov, L. E. Pangilinan, R. Mohammadi and R. B. Kaner, *APL Mater.*, 2018, **6**, 070901-8.

8 R. Kiessling, O. Samuelson, G. Lindstedt and P.-O. Kinell, *Acta Chem. Scand.*, 1950, **4**, 146–159.

9 H. Chen and X. Zou, *Inorg. Chem. Front.*, 2020, 7, 2248–2264.

10 L. Chen, Y. Gu, L. Shi, Z. Yang, J. Ma and Y. Qian, *J. Alloys Compd.*, 2004, **368**, 353–356.

11 F. Monteverde and A. Bellosi, *Adv. Eng. Mater.*, 2003, **5**, 508–512.

12 D. S. Wuu, M. L. Lee, T. Y. Lin and R. H. Horng, *Mater. Chem. Phys.*, 1996, **45**, 163–166.

13 H. Kinoshita, S. Otani, S. Kamiyama, H. Amano, I. Akasaki, J. Suda and H. Matsunami, *Japanese J. Appl. Physics, Part 2 Lett.*, 2001, **40**, 10–13.

14 K. K. Yadav, S. K. Guchhait, Sunaina, Ankush, C. M. Hussain, A. K. Ganguli and M. Jha, *J. Solid State Electrochem.*, 2019, **23**, 3243–3253.

15 H. Zhang, L. Zeng, X. Wu, L. Lian and M. Wei, *J. Alloys Compd.*, 2013, **580**, 358–362.

16 Q. Li, X. Zou, X. Ai, H. Chen, L. Sun and X. Zou, *Adv. Energy Mater.*, 2018, **9**, 1803369-8.

17 M. Mallik, A. J. Kailath, K. K. Ray and R. Mitra, *J. Eur. Ceram. Soc.*, 2012, **32**, 2545–2555.

18 C. Monticelli, F. Zucchi, A. Pagnoni and M. Dal Colle, *Electrochim. Acta*, 2005, **50**, 3461–3469.

19 V. G. Pol, S. V. Pol and A. Gedanken, *Adv. Mater.*, 2011, **23**, 1179–1190.

20 H. Sun, J. Meng, L. Jiao, F. Cheng and J. Chen, *Inorg. Chem. Front.*, 2018, **5**, 760–772.

21 S. Gupta, M. K. Patel, A. Miotello and N. Patel, *Adv. Funct. Mater.*, 2020, **30**, 1906481.

22 J. M. V. Nsanzimana, Y. Peng, Y. Y. Xu, L. Thia, C. Wang, B. Y. Xia and X. Wang, *Adv. Energy Mater.*, 2018, **8**, 1–7.

23 H. Li, P. Wen, Q. Li, C. Dun, J. Xing, C. Lu, S. Adhikari, L. Jiang, D. L. Carroll and S. M. Geyer, *Adv. Energy Mater.*, 2017, **7**, 1–12.

24 P. Sabatier, *Berichte der Dtsch. Chem. Gesellschaft*, 1911, **44**, 1984–2001.

25 X. H. Shi, L. Yang, L. H. Qi, N. N. Yan, C. C. Wang and H. R. Zhang, *Ceram. Int.*, 2018, **44**, 22318–22328.

26 L. Wang, L. Xu, Z. Ju and Y. Qian, *CrystEngComm*, 2010, **12**, 3923–3928.

27 D. Yilmaz Çakta, N. Koç and S. Turan, *J. Ceram. Sci. Technol.*, 2016, **7**, 349–356.

28 H. Vrubel and X. Hu, *Angew. Chemie - Int. Ed.*, 2012, **51**, 12703–12706.

29 S. Gupta, N. Patel, A. Miotello and D. C. Kothari, *J. Power Sources*, 2015, **279**, 620–625.

30 M. Zeng, H. Wang, C. Zhao, J. Wei, K. Qi, W. Wang and X. Bai, *ChemCatChem*, 2016, **8**, 708–712.

31 J. Masa, P. Weide, D. Peeters, I. Sinev, W. Xia, Z. Sun, C. Somsen, M. Muhler and W. Schuhmann, *Adv. Energy Mater.*, 2016, **6**, 1–10.

32 H. Park, A. Encinas, J. P. Scheifers, Y. Zhang and B. P. T. Fokwa, *Angew. Chemie Int. Ed.*, 2017, **56**, 5575–5578.

33 X. Ma, J. Wen, S. Zhang, H. Yuan, K. Li, F. Yan, X. Zhang and Y. Chen, *ACS Sustain. Chem. Eng.*, 2017, **5**, 10266–10274.

34 P. R. Jothi, Y. Zhang, J. P. Scheifers, H. Park and B. P. T. Fokwa, *Sustain. Energy Fuels*, 2017, **1**, 1928–1934.

35 X. Xu, Y. Deng, M. Gu, B. Sun, Z. Liang, Y. Xue, Y. Guo, J. Tian and H. Cui, *Appl. Surf. Sci.*, 2019, **470**, 591–595.

36 E. Sani, L. Mercatelli, M. Meucci, L. Zoli and D. Sciti, *Sci. Rep.*, 2017, **7**, 1–7.

37 C. M. Zimmer, J. Schubert, S. Hamann, U. Kunze and T. Doll, *Phys. Status Solidi Appl. Mater. Sci.*, 2011, **208**, 1241–1245.

38 K. Ebihara and S. Hiramatsu, *Rev. Sci. Instrum.*, 1996, **67**, 2765–2769.

39 L. Yan, T. Bo, W. Zhang, P. F. Liu, Z. Lu, Y. G. Xiao, M. H. Tang and B. T.

Wang, *Phys. Chem. Chem. Phys.*, 2019, **21**, 15327–15338.

40 J. Singh, A. Jayaraj, D. Srivastava, S. Gayen, A. Thamizhavel and Y. Singh, *Phys. Rev. B*, 2018, 97, 054506-7.

41 S. K. Kwon, B. I. Min, S. J. Youn and K. S. Kim, *J. Korean Phys. Soc.*, 2005, **46**, 1295–1298.

42 M. Takeda, T. Fukuda, F. Domingo and T. Miura, in *J Solid State Chem*, Academic Press Inc., 2004, **177**, 471–475.

43 M. Takeda, M. Terui, N. Takahashi and N. Ueda, *J. Solid State Chem.*, 2006, **179**, 2823–2826.

44 T. T. Xu, J. G. Zheng, A. W. Nicholls, S. Stankovich, R. D. Piner and R. S. Ruoff, *Nano Lett.*, 2004, **4**, 2051–2055.

45 K. Giannò, A. V. Sologubenko, H. R. Ott, A. D. Bianchi and Z. Fisk, *J. Phys. Condens. Matter*, 2002, **14**, 1035–1043.

46 U. Kuhlmann, H. Werheit, T. Dose and T. Lundström, *J. Alloys Compd.*, 1992, **186**, 187–200.

47 Y. Kumashiro, T. Enomoto, K. Sato, Y. Abe, K. Hirata and T. Yokoyama, *J. Solid State Chem.*, 2004, **177**, 529–532.

48 Y. Imai, M. Mukaida, M. Ueda and A. Watanabe, *Intermetallics*, 2001, **9**, 721–734.

49 H. J. Tromp, P. Van Gelderen, P. J. Kelly, G. Brocks and P. A. Bobbert, *Phys. Rev. Lett.*, 2001, **87**, 016401-4.

50 D. P. Young, D. Hall, M. E. Torelli, Z. Fisk, J. L. Sarrao, J. D. Thompson, H. R. Otto, S. B. Oseroff, R. G. Goodrich and R. Zysler, *Nature*, 1999, **397**, 412–414.

51 A. Goyal, H. S. Pouya, E. Ganjian and P. Claisse, *Arab. J. Sci. Eng.*, 2018, 43, 5035–5055.

52 J. Jiang, Y. Wang, Q. Zhong, Q. Zhou and L. Zhang, *Surf. Coatings Technol.*, 2011, **206**, 473–478.

53 D. Mu, B. luo Shen, C. Yang and X. Zhao, *Vacuum*, 2009, **83**, 1481–1484.

54 E. Budman and D. Stevens, *Anti-Corrosion Methods Mater.*, 1998, **45**, 327–332.

55 J. Tedim, S. K. Poznyak, A. Kuznetsova, D. Raps, T. Hack, M. L. Zheludkevich and M. G. S. Ferreira, *ACS Appl. Mater. Interfaces*, 2010, **2**, 1528–1535.

56 C.-T. Kao, S.-J. Ding, Y.-C. Chen and T.-H. Huang, *J. Biomed. Mater. Res.*, 2002, **63**, 786–792.

57 W. Liang, G. Zhang, H. Sun, P. Chen, Z. Zhu and A. Li, *Sol. Energy Mater. Sol.*

Cells, 2014, **132**, 425–430.

58 Z. Wang, Q. Zhao, L. Jing, Z. Wu and X. Sun, *Ceram. Int.*, 2016, **42**, 2926–2932.

59 S. J. Sitler, I. Charit and K. S. Raja, *Electrochim. Acta*, 2017, **246**, 173–189.

60 C. S. Choi, *J. Electrochem. Soc.*, 1991, **138**, 3062.

61 M. Ürgen, A. F. Çakir, O. L. Eryilmaz and C. Mitterer, *Surf. Coatings Technol.*, 1995, **71**, 60–66.

62 C. Monticelli, A. Bellosi and M. Dal Colle, *J. Electrochem. Soc.*, 2004, **151**, B331-B339.

63 A. L. Chamberlain, W. G. Fahrenholtz and G. E. Hilmas, 2004, **1172**, 1170–1172.

64 Y. Xin, H. Qizhong, S. Zhean, C. Xin, X. Liang, Z. Ping and L. Jun, *Corros. Sci.*, 2016, **107**, 9–20.

65 K. Tsuchida, T. Nagata, H. Nakata and A. Kato, *J. Mater. Sci.*, 1998, **33**, 755–762.

66 J. M. Lafferty, *J. Appl. Phys.*, 1951, **22**, 299–309.

67 H. Zhang, J. Tang, Q. Zhang, G. Zhao, G. Yang, J. Zhang, O. Zhou and L.-C. Qin, *Adv. Mater.*, 2006, **18**, 87–91.

68 H. Zhang, J. Tang, J. Yuan, J. Ma, N. Shinya, K. Nakajima, H. Murakami, T. Ohkubo and L. C. Qin, *Nano Lett.*, 2010, **10**, 3539–3544.

69 Y. Yu, S. Wang, W. Li and Z. Chen, *Powder Technol.*, 2018, **323**, 203–207.

70 C. Y. Zou, Y. M. Zhao and J. Q. Xu, *J. Cryst. Growth*, 2006, **291**, 112–116.

71 M. H. M. O. Hamanaka, V. P. Mammana and P. J. Tatsch, in *NanoCarbon*, Springer International Publishing, **2013**, 3,1–32.

72 P. H. Schmidt and D. C. Joy, *J Vac Sci Technol*, 1978, **15**, 1809–1810.

73 J. R. Brewer, R. M. Jacobberger, D. R. Diercks and C. Li Cheung, *Chem. Mater.*, 2011, **23**, 2606–2610.

74 H. Zhang, Q. Zhang, G. Zhao, J. Tang, O. Zhou and L. C. Qin, *J. Am. Chem. Soc.*, 2005, **127**, 13120–13121.

75 J. Xu, G. Hou, T. Mori, H. Li, Y. Wang, Y. Chang, Y. Luo, B. Yu, Y. Ma and T. Zhai, *Adv. Funct. Mater.*, 2013, **23**, 5038–5048.

76 L. Wang, G. Luo, D. Valencia, C. H. Sierra Llavina, R. F. Sabirianov, J. Lu, J. Q. Lu, W. N. Mei and C. Li Cheung, *J. Appl. Phys.*, 2013, **114**, 143709.

77 Q. Gu, G. Krauss and W. Steurer, *Adv. Mater.*, 2008, **20**, 3620–3626.

78 R. W. Johnson and A. H. Daane, *J. Chem. Phys.*, 1963, **38**, 425–432.

79 J. P. Mercurio, J. Etourneau, R. Naslain and P. Hagenmuller, *J. Less-Common Met.*, 1976, **47**, 175–180.

80 M. Futamoto, M. Nakazawa and U. Kawabe, *Surf. Sci.*, 1980, **100**, 470–480.

81 V. T. Petrashov, R. S. Shaikhaidarov, I. A. Sosnin, P. Delsing, T. Claeson and A. Volkov, *Phys. Rev. B*, 1998, **58**, 15088–15093.

82 F. Monteverde, D. Alfano and R. Savino, *Corros. Sci.*, 2013, **75**, 443–453.

83 D. M. Goebel and R. M. Watkins, *Rev. Sci. Instrum.*, 2010, **81**, 083504.

84 K. Leung, *Vacuum*, 1986, **36**, 865–867.

85 V. G. Pol, S. V. Pol and A. Gedanken, *Adv. Mater.*, 2011, **23**, 1179–1190.

86 C. H. Chen, T. Aizawa, N. Iyi, A. Sato and S. Otani, *J. Alloys Compd.*, 2004, **366**, 2003–2005.

87 R. K. Selvan, I. Genish, I. Perelshtein, J. M. Calderon Moreno and A. Gedanken, *J. Phys. Chem. C*, 2008, **112**, 1795–1802.

88 X. H. Ji, Q. Y. Zhang, J. Q. Xu and Y. M. Zhao, *Prog. Solid State Chem.*, 2011, **39**, 51–69.

89 H. Zhang, Q. Zhang, G. Zhao, J. Tang, O. Zhou and L. Qin, *J. Am. Chem. Soc.*, 2005, **127**, 13120–13121.

90 Z. C. Zhong, P. A. Dowben and D. J. Sellmyer, *Mater. Lett.*, 1998, **37**, 320–324.

91 M. Zhang, Y. Jia, G. Xu, P. Wang, X. Wang, S. Xiong, X. Wang and Y. Qian, *Eur. J. Inorg. Chem.*, 2010, **2010**, 1289–1294.

92 N. Kumar, R. Tomar, N. Wadehra, M. M. Devi, B. Prakash and S. Chakraverty, *Cryst. Res. Technol.*, 2018, **53**, 1800002.

93 S. T. Nishanthi, A. Baruah, K. K. Yadav, D. Sarker, S. Ghosh, A. K. Ganguli and M. Jha, *Appl. Surf. Sci.*, 2019, **467**–**468**, 1148–1156.

94 Q. Fan, Q. Zhang, Y. Zhao and Q. Ding, *J. Rare Earths*, 2013, **31**, 145–148.

95 G. Wang, J. R. Brewer, J. Y. Chan, D. R. Diercks and C. L. Cheung, *J. Phys. Chem. C*, 2009, **113**, 10446–10451.

96 Q. Wang, Y. L. Wang, H. J. Liu and C. L. Zeng, *J. Electrochem. Soc.*, 2016, **163**, D636–D644.

97 X. Duan and C. M. Lieber, *Adv. Mater.*, 2000, **12**, 298–302.

98 Dang H Y, Wang J and Fan S S, *Nanotechnology*, 2003, **14**, 738.

99 Y. Liu, W. J. Lu, J. N. Qin and D. Zhang, *J. Alloys Compd.*, 2007, **431**, 337–341.

100 G. V Samsonov, Y. B. Paderno and V. S. Fomenko, *Sov. powder Metall. Met. Ceram.*, 1963, **2**, 449–454.

101 A. Latini, F. Di Pascasio and D. Gozzi, *J. Alloys Compd.*, 2002, **346**, 311–313.

102 M. Hasan, H. Sugo and E. Kisi, *J. Alloys Compd.*, 2013, **578**, 176–182.

103 L. Wang, L. Xu, Z. Ju and Y. Qian, *CrystEngComm*, 2010, **12**, 3923–3928.

104 S. Zhang, M. Khangkhamano, H. Zhang and H. A. Yeprem, *J. Am. Ceram. Soc.*, 2014, **97**, 1686–1688.

105 S. Carenco, D. Portehault, C. Boissière, N. Mézailles and C. Sanchez, *Chem. Rev.*, 2013, 113, 7981–8065.

106 Y. Katsura, A. Yamamoto, H. Ogino, S. Horii, J. I. Shimoyama, K. Kishio and H. Takagi, *Phys. C Supercond. its Appl.*, 2010, **470**, S633–S634.

107 Ö. Balci, D. Ağaoğullari, I. Duman and M. L. Öveçoğlu, *Powder Technol.*, 2012, **225**, 136–142.

108 Y. Zhang, R. Li, Y. Jiang, B. Zhao, H. Duan, J. Li and Z. Feng, *J. Solid State Chem.*, 2011, **184**, 2047–2052.

109 S. K. Mishra, S. Das and L. C. Pathak, *Mater. Sci. Eng. A*, 2004, **364**, 249–255.

110 L. Chen, Y. Gu, Z. Yang, L. Shi, J. Ma and Y. Qian, *Scr. Mater.*, 2004, **50**, 959–961.

111 H. Zhao, Y. He and Z. Jin, *J. Am. Ceram. Soc.*, 1995, **78**, 2534–2536.

112 R. Li, H. Lou, S. Yin, Y. Zhang, Y. Jiang, B. Zhao, J. Li, Z. Feng and T. Sato, *J. Alloys Compd.*, 2011, **509**, 8581–8583.

113 C. Tian, D. Gao, Y. Zhang, C. Xu, Y. Song and X. Shi, *Corros. Sci.*, 2011, **53**, 3742–3746.

114 J. K. Sonber and A. K. Suri, *Adv. Appl. Ceram.*, 2011, **110**, 321–334.

115 S. C. Zhang, G. E. Hilmas and W. G. Fahrenholtz, *J. Am. Ceram. Soc.*, 2006, **89**, 1544–1550.

116 P. Wang, Y. Qi, S. Zhou, P. Hu, G. Chen, X. Zhang and W. Han, *Phys. status solidi*, 2016, **253**, 1590–1595.

117 S. Ran, O. Van Der Biest and J. Vleugels, *J. Am. Ceram. Soc.*, 2010, **93**, 1586–1590.

118 C. Viazzi, J. P. Bonino, F. Ansart and A. Barnabé, *J. Alloys Compd.*, 2008, **452**, 377–383.

119 H. Luo, Q. Cai, B. Wei, B. Yu, J. He and D. Li, *J. Alloys Compd.*, 2009, **474**, 551–556.

120 T. Tsai and S. A. Barnett, *J. Electrochem. Soc.*, 1995, **142**, 3084–3087.

121 Y. W. Song, D. Y. Shan and E. H. Han, *Electrochim. Acta*, 2008, **53**, 2135–2143.

122 D. M. Stewart, R. W. Meulenberg and R. J. Lad, *Thin Solid Films*, 2015, **596**, 155–159.

123 Z. Bi, X. Rodríguez-Martínez, C. Aranda, E. Pascual-San-José, A. R. Goñi, M. Campoy-Quiles, X. Xu and A. Guerrero, *J. Mater. Chem. A*, 2018, **6**, 19085–19093.

124 Y. Deng, E. Peng, Y. Shao, Z. Xiao, Q. Dong and J. Huang, *Energy Environ. Sci.*, 2015, **8**, 1544–1550.

125 K. Zhang, Z. Chen, A. Armin, S. Dong, R. Xia, H.-L. Yip, S. Shoaee, F. Huang and Y. Cao, *Sol. RRL*, 2018, **2**, 1700169-9.

126 T. Allison, in *Sol-Gel Technologies for Glass Producers and Users*, Springer, Boston, MA, Boston, MA, 2007, 21, 89–92.

127 J. I. Goldstein, D. E. Newbury, P. Echlin, D. C. Joy, C. E. Lyman, E. Lifshin, L. Sawyer and J. R. Michael, *Scanning Electron Microscopy and X-ray Microanalysis*, Springer US, Boston, MA, 2003.

128 A. Smekal, *Naturwissenschaften*, 1923, **11**, 873–875.

129 C. V. Raman and K. S. Krishnan, *Nature*, 1928, 121, 501–502.

130 N. Crampton, M. Yokokawa, D. T. F. Dryden, J. M. Edwardson, D. N. Rao, K. Takeyasu, S. H. Yoshimura and R. M. Henderson, *Proc. Natl. Acad. Sci. U. S. A.*, 2007, **104**, 12755–12760.

131 Y. Sugimoto, P. Pou, M. Abe, P. Jelinek, R. Pérez, S. Morita and Ó. Custance, *Nature*, 2007, **446**, 64–67.

132 Y. Martin and H. K. Wickramasinghe, *Appl. Phys. Lett.*, 1987, **50**, 1455–1457.

133 U. Hartmann, *Annu. Rev. Mater. Sci.*, 1999, **29**, 53–87.

134 S. Porthun, L. Abelmann and C. Lodder, *J. Magn. Magn. Mater.*, 1998, 182, 238–273.

135 C. W. Lin, F. F. Fan and A. J. Bard, *J. Electrochem. Soc.*, 1987, **134**, 1038–1039.

136 M. Nonnenmacher, M. P. O'Boyle and H. K. Wickramasinghe, *Appl. Phys. Lett.*, 1991, **58**, 2921–2923.

Chapter 2

Nanostructured neodymium hexaborides and their field emission

2.1 Introduction

One–dimensional (1D) nanostructured materials have attracted lots of researcher's interest because of their exciting morphology dependent physical properties,[1–5] which enables them to find applications in next-generation electronic devices.[6–11] Among the wide variety of 1D materials, rare-earth hexaborides (RB_6) such as NdB_6, CeB_6, LaB_6 have been widely used for the fabrication of electronic devices such as field emission displays (FEDs) because of their low work function, high melting point, chemical inertness and high mechanical strength.[12] Apart from the field emission application, various rare earth hexaboride including neodymium hexaboride show a broad range of applications such as MRI,[13] high energy optical systems,[14] as sensors for photon detectors,[15] and as electrical coatings for resistors. Neodymium hexaboride crystallises in CsCl-type structure having a space group of $Pm\bar{3}m$.[14] In this structure, neodymium occupies Cs- site, whereas boron occupies an octahedral position as B_6 of Cl^- site (Figure 2.1). The strong bonds between the boron atoms in the B_6 framework result in high thermal and chemical stability as desired for FED devices.[16] Earlier theoretical studies indicate that materials having a work function less than 2 eV show excellent field emission, field-induced ballistic emission and thermionic emission.[17]

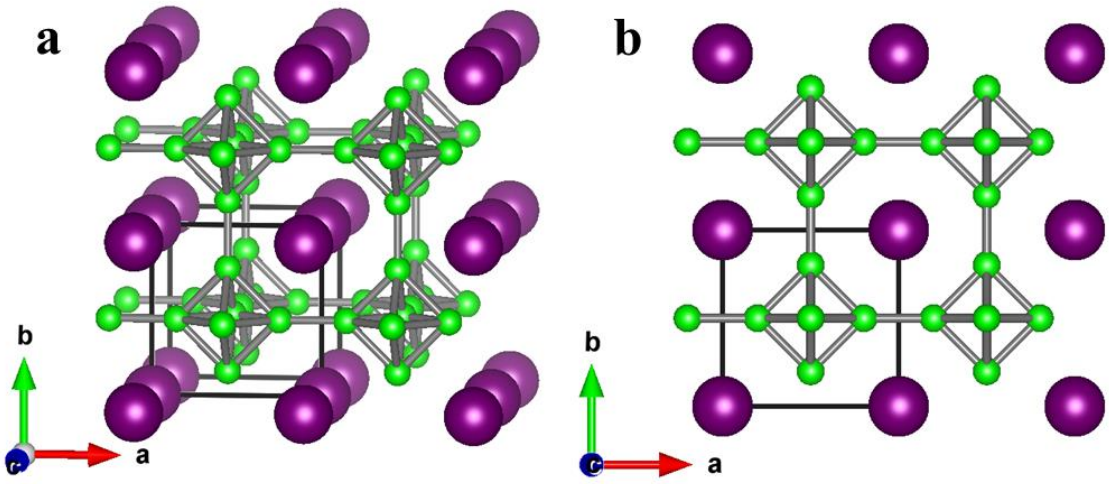

Figure 2.1. *(a) Crystal structure of NdB_6 in 3D. (b) 2D view of NdB_6.*

Among various metal hexaboride, NdB_6 shows very low work function (1.6 eV) and their utilization in the fabrication of display devices would certainly need low operational voltage.[8,18–21] Despite these facts, the synthesis of NdB_6 requires an adverse synthetic condition, where a lot of toxic gaseous precursor is utilized for stabilization ofNdB_6.[2] Earlier, synthesis of bulk NdB_6 has been carried out by floating zone method,[22] solid-state

reactions,[23] borothermal reductions,[24] and combustion synthesis.[25] However, the synthesis of anisotropic nanostructured neodymium hexaboride has been reported only via the chemical vapour deposition (CVD) process, where BCl_3 or B_2H_6 gases were used as boron precursors.[26] In the present work, we have developed a new process for the synthesis of ultrafine nanocubes and ultrafine nanorods of NdB_6 using a precursor mediated route. The as-obtained NdB_6 nanostructures have been deposited on Si-substrate via spin coating process. Surface analysis of the film indicates that the NdB_6 rods are vertically aligned and their field emission properties have been studied. Field emission properties of NdB_6 nanorods shows low turn-on voltage (< 4.5 V/μm) and the highest field enhancement factor β (2263) compared to the highest reported β factor (1037). Further, the oxidation behaviour of synthesised NdB_6 has been studied using *in-situ* high-temperature X-ray.

2.2 Experimental

2.2.1 Materials

Neodymium chloride ($NdCl_3.xH_2O$, 99.99 %, CDH, India), Triton^{TM} X-100 (Sigma- Aldrich), acetone (C_3H_6O, Merck, 99 %), Methanol (CH_3OH, Merck, 99 %), Hydrochloric Acid (HCl, 99 %, Merck) and Sodium borohydride ($NaBH_4$, 99.99 %, CDH, India) were used for the synthesis of neodymium hexaboride. All the chemicals were used as received.

2.2.2 Process of silicon substrate cleaning

The Si- substrate which was used to prepare the film was cleaned by the standard RCA method, which was firstly developed by Werner Kern in Radio Corporation of America. For cleaning Si-substrate, small pieces of substrates were immersed in acetone (heated at 50 ºC) and after 30 min Si-substrate was cleaned with water followed by isopropanol. During the acetone heating, around 10-20 % acetone was lost due to the low boiling point (56 ℃) of the acetone. In the second step, the substrate was treated with piranha solution for 10 min. The above substrate was rinsed with water followed by 5 % HF solution treatment. After HF treatment, substrate was again washed with water and isopropyl alcohol followed by drying in a vacuum desiccator.

2.2.3 Synthesis method of $Nd(OH)_3$ and NdB_6

For the synthesis of neodymium hydroxide, first 3.5 ml of TX-100 was added to 35 ml of 0.1 M of $NdCl_3.xH_2O$. To this solution, 35 ml of 0.1 M NaOH containing 3.5 ml TX-100 was added. The resultant mixture was stirred continuously for 1 h and then transferred

into Teflon lined stainless steel autoclave and heated at 120 ℃ for 24 h. The resultant solution after hydrothermal treatment was washed with methanol and dried in air at 80 ℃ overnight. The as-obtained neodymium hydroxide has been used as a source of neodymium while sodium borohydride has been used as a source of boron for the synthesis of neodymium hexaboride. For the synthesis of NdB_6, neodymium and boron source was grinded in a mole ratio of 1:10 and 1:20 (Table 2.1). The obtained homogeneous mixture was transferred to a recrystallized alumina boat and annealed at 1000 ºC in an argon atmosphere for 8 h at a heating rate of 250 ℃/h and 40 ℃/h. After completion of the reaction, the sample was allowed to cool to room temperature naturally. Further, the as-obtained product was washed with dilute hydrochloric acid. The sample after washing was vacuum dried at 80 ℃. Table 2.1 gives details of the precursor's and their sample codes, which will be used throughout the chapter.

For the preparation of NdB_6 dispersion, 50 mg of synthesised NdB_6 (S1, S2 and S3) was mixed with 2 ml of ethanol and ethylene glycol mixture (1: 1 V:V ratio) using ultrasonication. The resulting dispersion was spin-coated on the cleaned Si- substrate at a speed of 3000 rpm for 60 seconds. This process of coating was repeated 4 times to get the homogeneous film.

Table 2.1. Experimental condition for the stabilization of nanostructured neodymium hexaboride

Nd- Source	**Boron Source**	**Mole ratio of Nd to Boron**	**Heating rate [℃/h]**	**Annealing Temperature [℃]**	**Sample Code**
$Nd(OH)_3$	$NaBH_4$	1:10	250	1000	S1
$Nd(OH)_3$	$NaBH_4$	1:20	250	1000	S2
$Nd(OH)_3$	$NaBH_4$	1:20	40	1000	S3

2.3 Results and discussion

The present study deals with the process of stabilization of ultrafine neodymium hexaboride nanorods and nanocubes at ambient pressure. The process of stabilization of ultrafine nanorods involves three steps. The first step deals with the synthesis of $Nd(OH)_3$ nanorods using hydrothermal process. In the second step, $Nd(OH)_3$ ultrafine nanorods and sodium borohydride have been heated together at 1000 ℃ for the stabilization of NdB_6. Finally, for the fabrication of NdB_6 film, as synthesised NdB_6 nanostructures were deposited on Si- substrate via spin coating process and their field emission properties study have been studied.

The powder X-ray diffraction pattern of the precipitates obtained after hydrothermal treatment, confirms the formation of hexagonal neodymium hydroxide [$Nd(OH)_3$] having space group P63/m (a=0.641 nm, c= 0.374 nm) (Figure 2.2a). All the reflection pattern have been matched with JCPDS card no. 01-070-0214 of neodymium hydroxide. Further, transmission electron microscopy studies of as obtained $Nd(OH)_3$ show the formation of rods (10 nm X 120 nm) (Figure 2.2b). Figure 2.2c displays the high-resolution transmission electron micrographs of $Nd(OH)_3$. The HRTEM patterns indicate the presence of (101) plane corresponding to interplanar d spacing of ~3.01 Å. Further, the selected area electron diffraction pattern shows the presence of (101), (201) and (211) planes of $Nd(OH)_3$ (Figure 2.2d). The PXRD and TEM result confirms the formation of high purity ultrafine $Nd(OH)_3$ nanorods. Further, the as synthesised $Nd(OH)_3$ was reacted with sodium borohydride at 1000 °C.

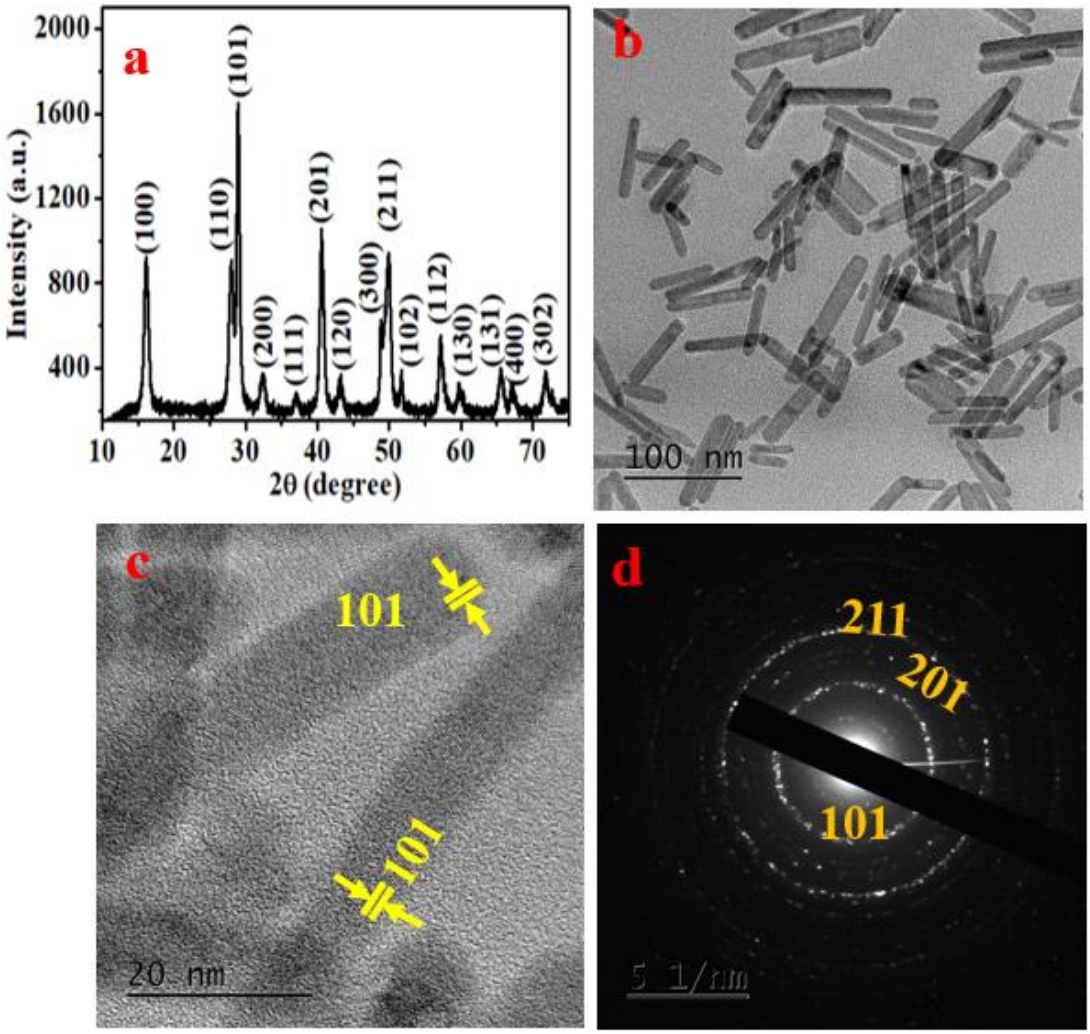

Figure 2.2. *Neodymium precursor synthesised by hydrothermal method, (a) PXRD of $Nd(OH)_3$. (b) Transmission electron microscopy of $Nd(OH)_3$. (c) HRTEM of $Nd(OH)_3$. (d) corresponding selected electron diffraction pattern of $Nd(OH)_3$.*

The optimization condition for the synthesis of NdB_6 has been analysed by the thermogravimetric analysis (TGA) of precursors mixture [$Nd(OH)_3$ and $NaBH_4$.[27] First, the TGA of $Nd(OH)_3$ has been carried upto 1000 ℃ (Figure 2.3).

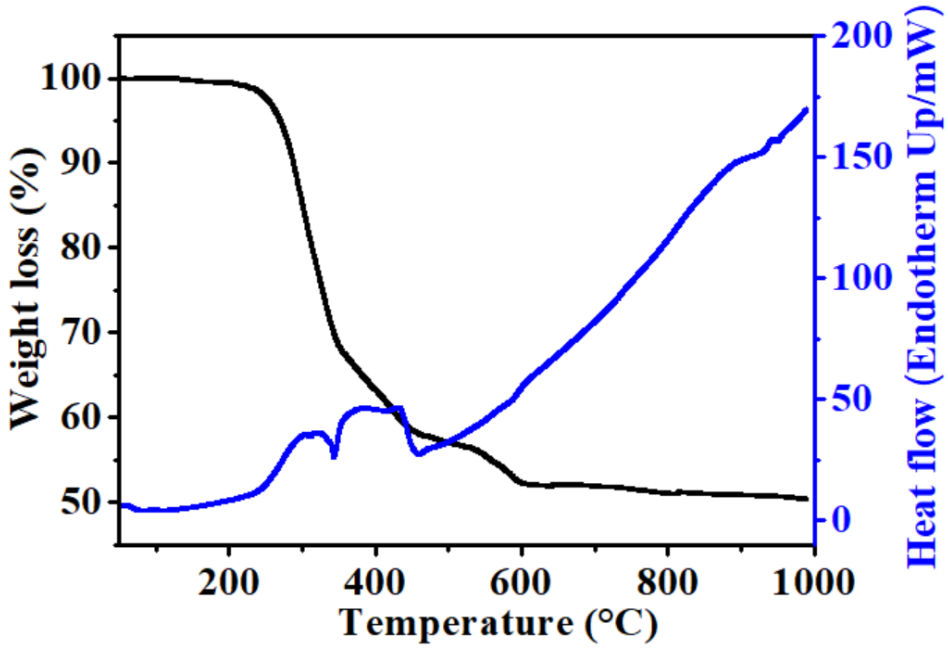

Figure 2.3. *TGA/DTA plot of $Nd(OH)_3$.*

The TGA plot confirms steep weight loss started from ~ 200 ℃- 340 ℃, which could be ascribed as the loss of surface water molecules. Further, there is slight weight loss in the temperature range 340 ℃- 420 ℃, due to the transition of $Nd(OH)_3$ to NdOOH.[28,29] Again as the temperature increases, another weight loss can be assigned as the transformation of NdOOH to Nd_2O_3 at 600 ℃. Further, the mechanism of NdB_6 formation is investigated using TGA/DTA of the prepared homogeneous mixture of $Nd(OH)_3$ and $NaBH_4$ in an argon atmosphere. In Figure 2.4a-b the presence of a weak exothermic peak in 305 - 370 ℃ corresponds to the evaporation of water from the surface of precursors molecules. The surface water removal can be seen in the TGA curve (Figure 2.4a-b). The exothermic peak around ~450-501 ºC corresponds to the decomposition of $NaBH_4$ in NaH and BH_3 as well as the formation of NdOOH by the decomposition of $Nd(OH)_3$.[27] It is known that BH_3 is highly unstable, which further decomposes to B and H_2 gas at around 530 ℃.[27,30] There is an increase in weight of precursors mixture due to the formation of intermediates compounds such as NdOOH, NaH, BH_3 and Nd_2O_3. There are exothermic peaks around 850 ºC - 980 ℃, which might be due to intermediates. The endothermic peaks around 850 ºC - 980 ℃ are found to be suitable temperatures for the formation of NdB_6. Based on the above observation, the annealing of the mixture of $Nd(OH)_3$ and $NaBH_4$ precursors was

carried out at 1000 ℃. Different ramping rate of the temperature of annealing has been used and their effect on the final product has been studied.

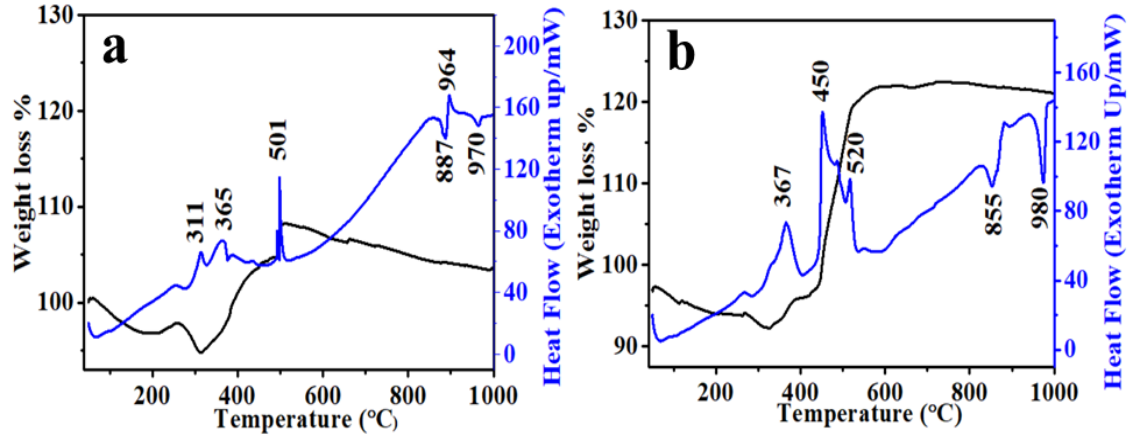

Figure 2.4. *Differential temperature analysis (DTA) and TGA of; (**a**) neodymium hydroxide with sodium borohydride in 1:10 molar ratio. (**b**) neodymium hydroxide with sodium borohydride in 1:20 molar ratio.*

The powder X-ray diffraction pattern of the product obtained after the reaction of neodymium hydroxide with sodium borohydride in a different mole ratio at the heating rate 250 ℃/h and 40 ℃/h shows the formation of pure NdB_6 (Figure 2.5a). The as-obtained pure NdB_6 at various condition crystallized in a simple cubic crystal structure with $Pm\bar{3}m$ space group. All the diffraction peaks are well-matched with the reported JCPDS card no 03-065-1828. Further, the FullProf software has been used for the Rietveld refinement of obtained PXRD pattern. Rietveld-refined data were consistent with an earlier reported single phase of cubic ($Pm\bar{3}m$) structure. The Wyckoff site for Nd and B are 1a and 6f respectively.

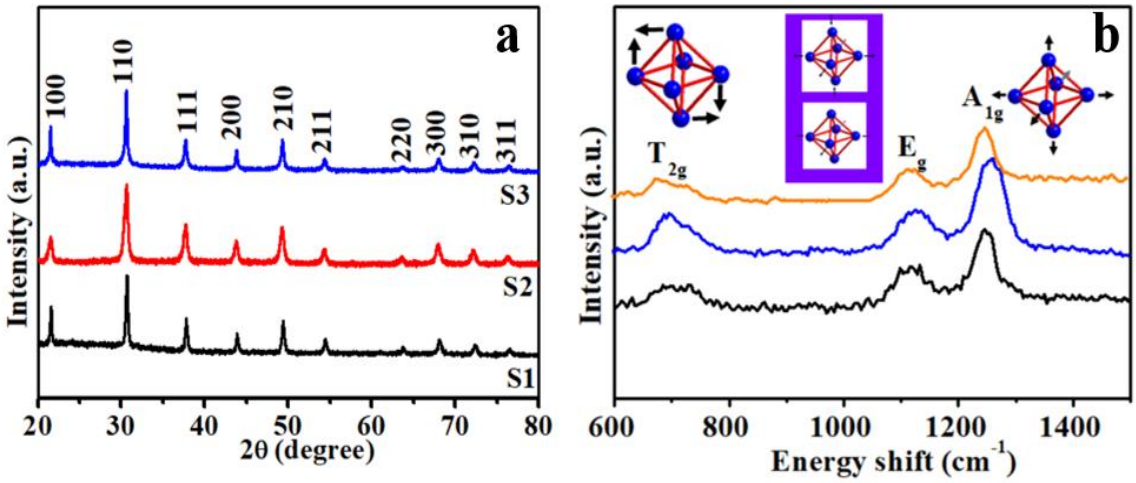

Figure 2.5. *Powder X-ray diffraction pattern of synthesised NdB_6. (b) Raman spectra of NdB_6.*

The goodness of fit for S1, S2 and S3 are 1.43, 1.83, and 1.33, respectively. The refined lattice cell parameter for S1, S2 and S3 are 4.139 (6), 4.132 (11), and 4.144 (9) Å respectively. It can be also observed that the volume of ultrafine nanocubes for sample S1 and S2 are 70.907 $Å^3$ and 70.547 $Å^3$ respectively, which are shorter than ultrafine rods [71.172 $Å^3$] and in good agreement with the previous report.[23,31] The Rietveld refined X-ray data of NdB_6 nanocubes and ultrafine nanorods (S1, S2, and S3) have been represented in Figure 2.6a-c. Table 2.2 include all the Rietveld refined parameter.

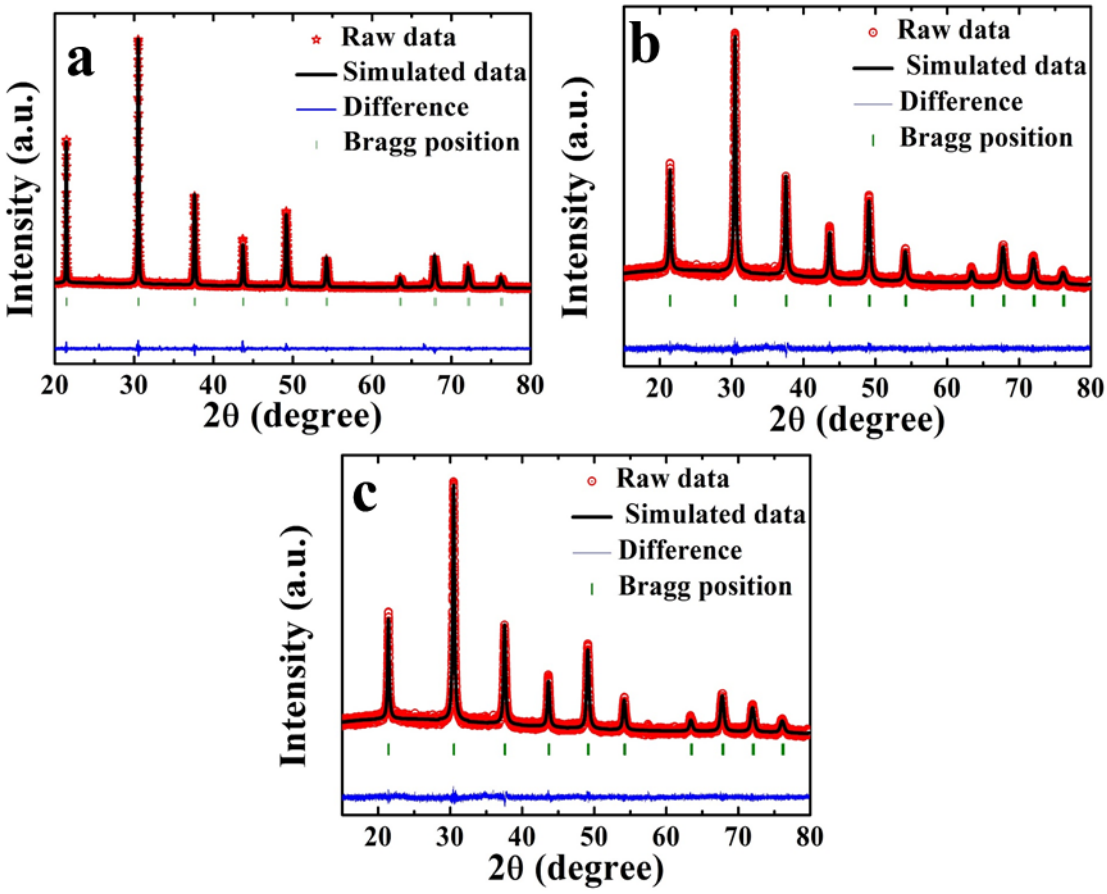

Figure 2.6. *Rietveld refined of (a) S1. (b) S2. (c) S3.*

The data generated from the Rietveld refinement has been used for the construction of crystal structure Diamond 3.2 software. It can be seen from the unit cell model that trivalent neodymium ion presents at the centre of cubes, and boron octahedron cage present at the corner of the cube (Figure 2.1). Raman microscopy is a very important tool to understand the deposited film on the silicon substrate. It is reported that $\Gamma = A_{1g} + E_g + T_{1g} + T_{2g} + 2T_{1u} + T_{2u}$ are the allowed vibrational modes for cubic $Pm\bar{3}m$ symmetry of rare earth hexaboride,

where E_g and T_{2g} are due to Raman active phonons, $2T_{1u}$ is infrared active, T_{1g} and T_{1u} are optically inactive.[32] The A_{1g} and E_g mode was observed for the stretching vibrations

Table 2.2. Rietveld refined the diffraction parameter

(a) Sample: S1, a: 4.139 (6) Å, R_{exp}:5.69, R_p:4.76, χ^2: 1.43					
Atoms	**Position**			**B_{iso} (Å^2)**	**Occupancy**
	X	**Y**	**Z**		
Nd	0	0	0	0.009 (11)	1
B	0.203 (10)	0.5	0.5	0.019 (3)	0.167
B	0.5	0.5	0.790 (6)	0.232 (5)	0.167
B	0.5	0.5	0.201 (4)	0.157 (9)	0.167
B	0.5	0.203 (5)	0.5	0.345 (5)	0.167
B	0.5	0.796 (4)	0.5	0.131 (2)	0.167
B	0.793 (5)	0.5	0.5	0.099 (6)	0.167

(b) Sample: S2, a: 4.132(11)Å, R_{exp}:6.75, R_p:4.99, χ^2: 1.83					
Atoms	**Position**			**B_{iso} (Å^2)**	**Occupancy**
	X	**Y**	**Z**		
Nd	0	0	0	0.060 (11)	1
B	0.206 (3)	0.5	0.5	0.115 (3)	0.167
B	0.5	0.5	0.801 (2)	0.239 (2)	0.167
B	0.5	0.5	0.205 (2)	0.131 (12)	0.167
B	0.5	0.202 (3)	0.5	0.233 (4)	0.167
B	0.5	0.799 (4)	0.5	0.139 (2)	0.167
B	0.801 (4)	0.5	0.5	0.267 (4)	0.167

(c) Sample: S3, a: 4.144 (9)Å, R_{exp}:5.41, R_p:4.70, χ^2: 1.33					
Atoms	**Position**			**B_{iso} (Å^2)**	**Occupancy**
	X	**Y**	**Z**		
Nd	0	0	0	0.156 (4)	1
B	0.195 (7)	0.5	0.5	0.234 (9)	0.167
B	0.5	0.5	0.795 (1)	0.229 (11)	0.167
B	0.5	0.5	0.198 (5)	0.150 (4)	0.167
B	0.5	0.199 (5)	0.5	0.098 (11)	0.167
B	0.5	0.794 (6)	0.5	0.165 (7)	0.167
B	0.798 (2)	0.5	0.5	0.067 (11)	0.167

corresponding to the octahedral boron cluster whereas the T_{2g} mode is due to the bending mode of B-B in the boron cluster. The Raman spectra for the S1, S2 and S3 samples are shown in Figure 2.5b. In all three samples, the presence of T_{2g} (680-700 cm^{-1}), E_g (1115 cm^{-1}) and A_{1g} (1250 cm^{-1}) indicates the formation of pure cubic NdB_6. All the result of the Raman studied are in good agreement with the previous reported Raman study of NdB_6.[2,7,33]

The morphology of neodymium hexaboride was investigated by transmission electron microscopy (TEM). TEM micrograph of NdB_6 obtained after annealing neodymium and boron precursors mixture in the ratio of 1:10 (S1) shows the formation of 15-20 nm nanocubes (Figure 2.7a). Interestingly, it has been observed that when the ratio of neodymium and boron was increased to 1:20 (S2), the formation of a mixture of rods (10 nm X 30 nm) and cubes (25 nm) takes place (Figure 2.7b).

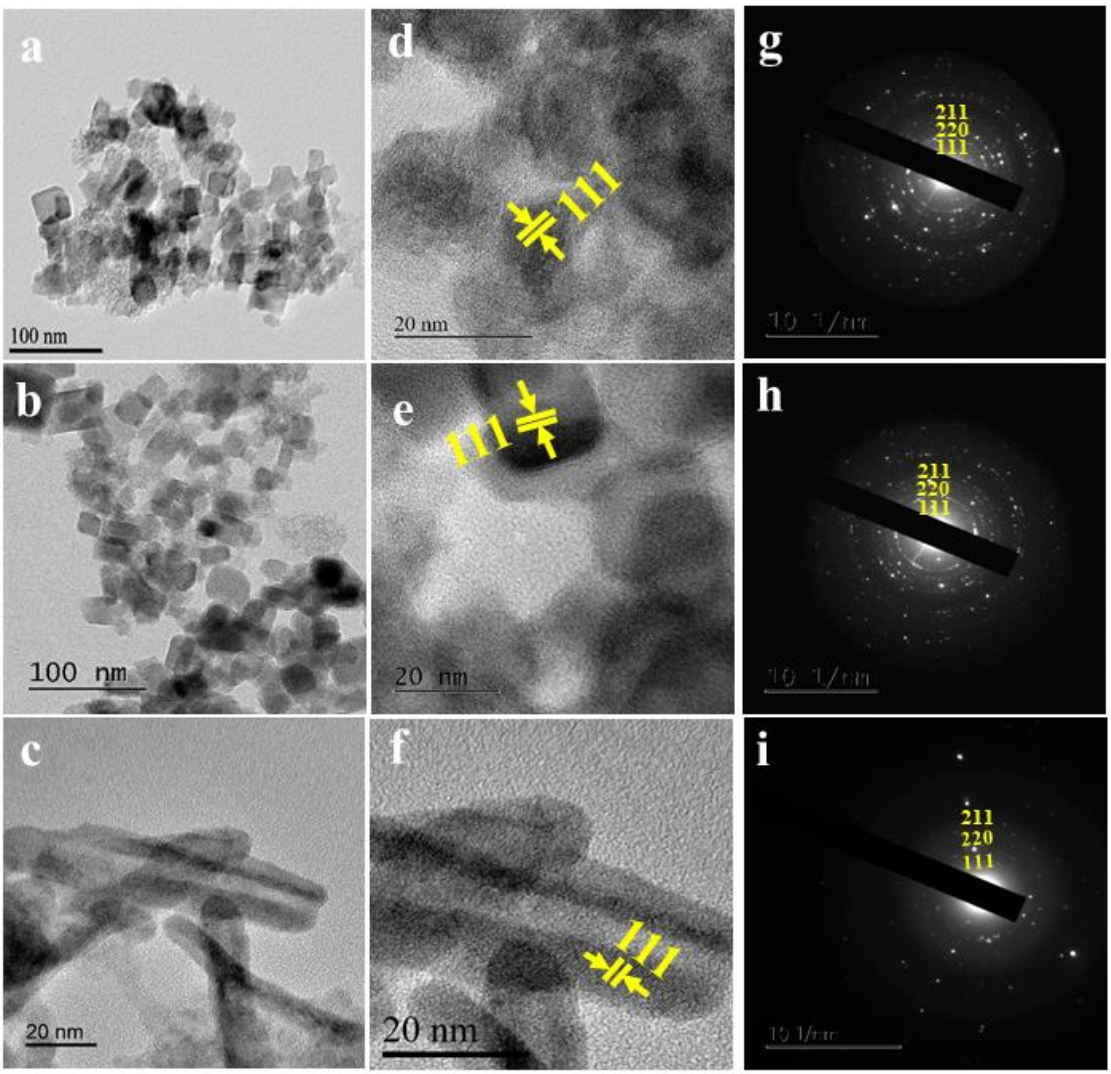

Figure 2.7. *(a-c) Transmission electron microscopy of sample S1, S2 and S3. (d-f) HRTEM of sample S1, S2 and S3. (g-i) selected area electron diffraction pattern of samples S1, S2 and S3.*

As discussed earlier, Nd- precursor and sodium borohydride mixture have also been heated at a slower heating rate (40 °C/h).[34] TEM micrographs of synthesised NdB_6 sample at the heating rate 40 °C/h show the formation of ultrafine rods of size 10 nm X 100 nm (Figure 2.7c). It may be noted that earlier submicron size cubes (200-300 nm) and nanocubes (~40 nm) have been synthesised using a high-temperature hydrothermal route.[23,35,36] To the best

of our knowledge, there is no report on NdB_6 nanorod synthesis via chemical route at ambient pressure; however, the chemical vapour deposition process leads to the formation of large nanorods. Besides this, here we have shown the possibility of stabilization of ultrafine NdB_6 nanocubes (15-20 nm) and ultrafine rods (10 nm X 100 nm) via a simple solid-state route. The possible reason behind the stabilization of the nanocube and nanorods of NdB_6 is the utilization of ultrafine starting neodymium hydroxide precursor. At the slow heating rate, $Nd(OH)_3$ and $NaBH_4$ were heated together to form NdB_6. It may be noted that earlier using CVD process, NdB_6 nanorods of diameter 50-300 nm diameter have been achieved till now.[2,24,33,37] However, in the present study, we have successfully stabilized NdB_6 ultrafine rods of 10 nm diameter. The high-resolution TEM studies of all the above samples show the presence of (111) plane for sample S1, S2 and S3, which corresponds to interplanar distance $d \sim 2.35$ l Å (Figure 2.7d-f). Electron diffraction study confirms the presence of 111, 220 and 221 diffraction planes for the samples S1, S2 and S3 (Figure 7g-i).

Further, synthesised samples (S1, S2 and S3) were used to fabricate NdB_6 films using the spin coating process. For fabrication of NdB_6 films, NdB_6 dispersion formulation was prepared by ultrasonic mixing of 50 mg of NdB_6 powder (S1, S2, and S3) in 2 ml mixture of ethanol and ethylene glycol (1:1 V/V). For the field emission study, the dispersion was coated on a silicon substrate via spin-coating. NdB_6 coated substrate was annealed in argon at 200 ℃ for 12 h to remove organic molecules. To the best of our knowledge, the *in-situ* synthesis of NdB_6 nanorods on Si-substrate has only been reported by the chemical vapour deposition (CVD) method.[2,33] The fabricated NdB_6 films on Si-substrate was analysed by GIXRD, which confirms the presence of pure NdB_6 at the Si substrate (Figure 2.8a). Further, using the ellipsometry technique the refractive index of NdB_6 film fabricated using S1, S2 and S3 samples have been measured. The refractive index for sample S1, S2 and S3 were found to be 1.18, 1.16 and 1.08 respectively (Figure 2.8b). It was observed that as the precursor ratio increases the refractive index decreases, which is in good agreement with previous reports of other rare-earth hexaborides.[20] The result indicates that the S3 sample has the lowest refractive index compared to the S1 and S2 samples. The viscosity of prepared dispersion was measured using Rheometer. The plot of shear stress vs shear rate for S1, S2 and S3 samples are shown in (Figure 2.8c). It has been observed that S1 and S2 behave as Newtonian fluid while S3 behaves as Bingham plastic fluid. The dispersion made using sample S1, S2 and S3 have viscosity 5.22, 5.55 and 6.25 mPa respectively.

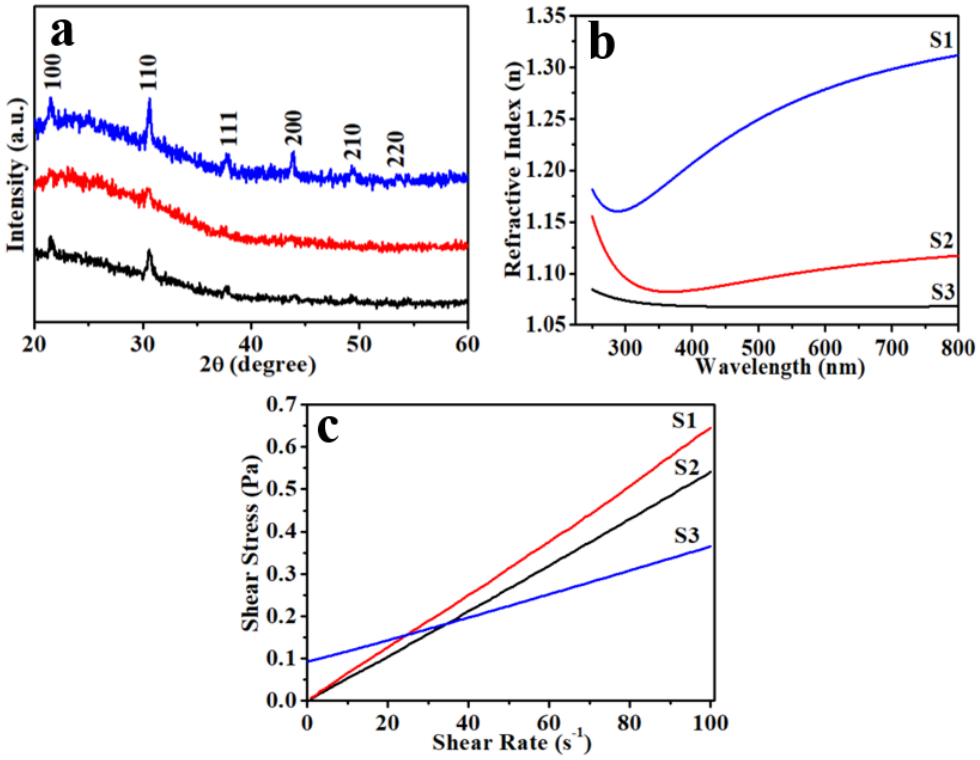

Figure 2.8. *(a) GIXRD of fabricated S1, S2 and S3 sample on Si- substrate. (b) Refractive index of as-fabricated films. (c) Viscosity of prepared dispersion.*

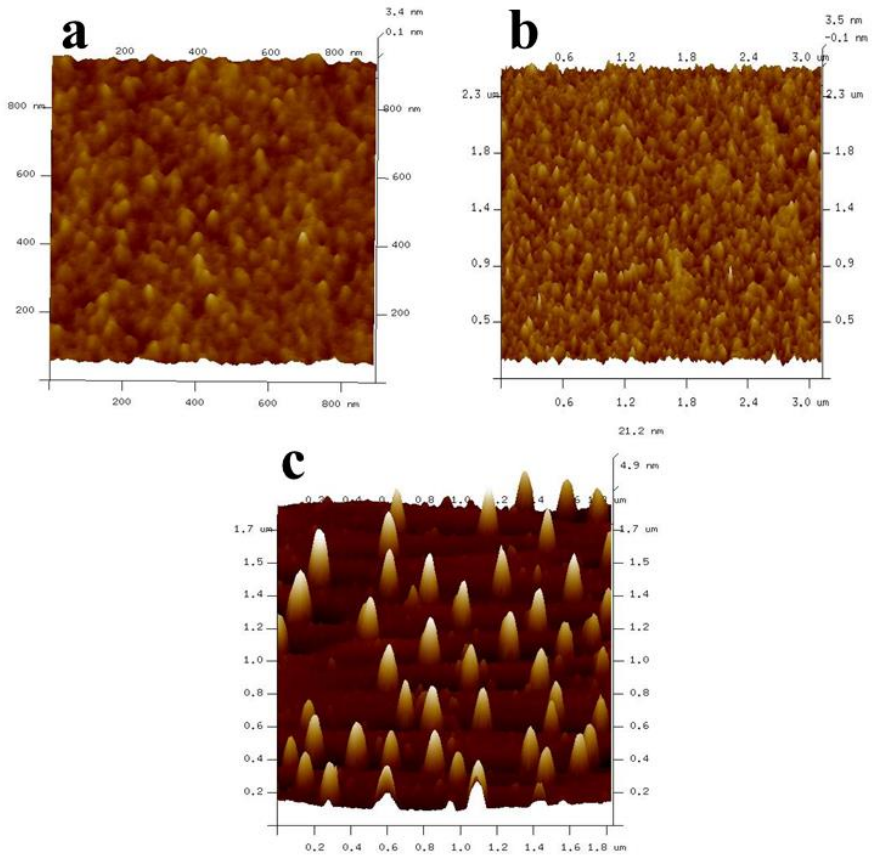

Figure 2.9. *3D view of AFM topography (a) S1. (b) S2. (c) S3.*

The surface properties of NdB_6 film of all the samples (S1, S2 and S3) were investigated using tapping mode AFM studies. The AFM study indicates that the nanoparticles (S1 and S2) are uniformly distributed over the substrate (Figure 2.9a-b) and nanorods (S3) of NdB_6 are vertically oriented over the Si- substrate (Figure 2.9c). However, there are no reports available for vertically aligned nanorods for NdB_6. It has been known that vertically oriented nanorods show better field emission properties compared to randomly oriented nanorods.[38]

2.3.1 Field emission study

The emission of electrons from the surface of a metal or semiconductor takes place in several ways such as heating the source (thermionic emission), exposure of light on the source (photo-electric) and applying a voltage across the emitter source (field emission). Field emission phenomenon was first explained by Fowler and Nordheim, which was based on Fermi-Dirac and Sommerfield's free-electron theory.[39] As per Fowler-Nordheim theory, the field emission current density (J) can be express as:

$$J_E = \frac{A\beta^2E^2}{\varphi}\exp\left(-\frac{B\varphi^{\frac{3}{2}}}{\beta E}\right) \quad 2.1$$

$$ln\frac{J}{E^2} = \ln\frac{A\beta^2}{\varphi} - \frac{B\varphi^{\frac{3}{2}}}{\beta E} \quad 2.2$$

Where A= 1.54 X $10^{-6}\, eVV^{-2}$, B= 6.83 X $10^3\, eV^{\frac{3}{2}}\mu m^{-1}$

J_E is field emission current density, β is field enhancement factor, E is applied field and φ is the work function of emitting materials.

The current density and applied electric field (J-E) characteristic plots for samples S1, S2 and S3 have been shown in Figure 2.10a-c. Here, the turn-on field is defined as the electric field required to generate a field emission current density of 500 nA/cm^2. The turn-on fields for S1, S2 and S3 are 6.6, 6.7 and < 4.5 V/μm respectively (Figure 2.10a-c), which is in close agreement with earlier reports.[2,33] It may be noted that the initial field emission current density of S3 is itself higher than the maximum current density achieved for samples S1 and S2. Also, the earlier reported turn-on field for NdB_6 nanowires such as curve nanowire, short nanowire, and long nanowires are 5.6, 3.85 and 3.01 V/μm at a current density 10 μA/cm^2.[2] However, the earlier reported NdB_6 nanowires have been fabricated using the CVD approach, which requires expensive and toxic boron source such as B_2H_6 or BCl_3.[2,33] Interestingly, it has been observed that the vertically aligned nanorods

(S3) offer much higher current density at each field compared to NdB_6 nanoparticles (S1 and S2). The higher current density of S3 is due to its anisotropic and vertically aligned structure.

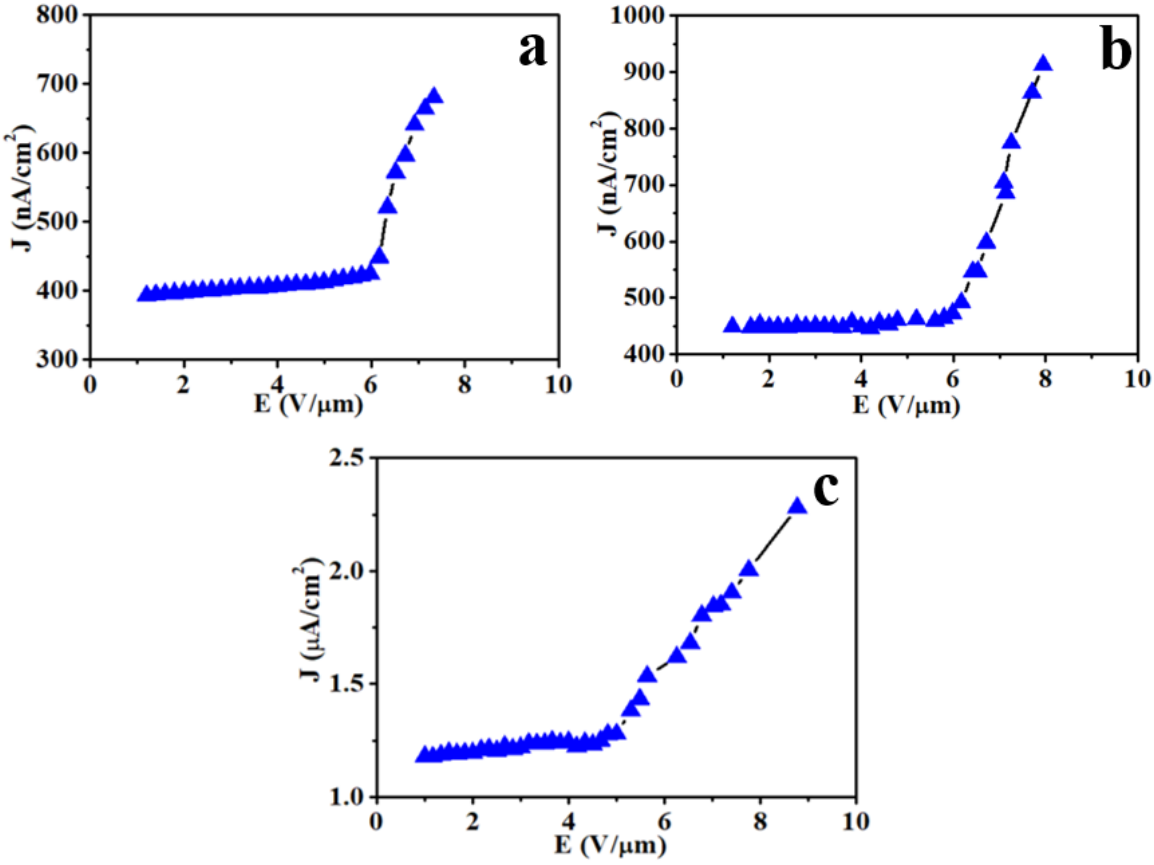

Figure 2.10. *J-E plot of samples (a) S1. (b) S2. (c) S3.*

The F-N curve ($\ln(J/E^2)$ vs 1/E) plotted in high electric field region are straight line having negative slope *i.e.,* linear behaviour, suggests that the obtained current is due to the field emission unlike thermionic or ionic behaviour, which was explained by F-N theory (Figure 2.11). The estimated slopes of FN-plots are -9.39, -8.57 and -6.10 for S1, S2 and S3 respectively, which was fitted with a straight line (Figure 2.11a-c). Further, the field enhancement factor (β) can be calculated from F-N equation, by evaluating β as $-B\phi^{3/2}$/slope, where B is a constant with value 6.83 X 10^3 $VeV^{-3/2,}$ and ϕ is the work function (1.6 eV) of cathode materials. The obtained β value for samples S1, S2, and S3 are 1471, 1611 and 2263 respectively. The observed enhancement factor reported in the present study is ~2.2 fold higher than the maximum reported field emission factor (1037) for NdB_6 nanostructures.[33] The probable reason for ~2.2 fold high field enhancement factor is due to a smaller diameter (10 nm) compared to earlier reported nanostructured where the much

wider dimension of NdB_6 being used. Field emission properties of all the sample have been included in Table 2.3.

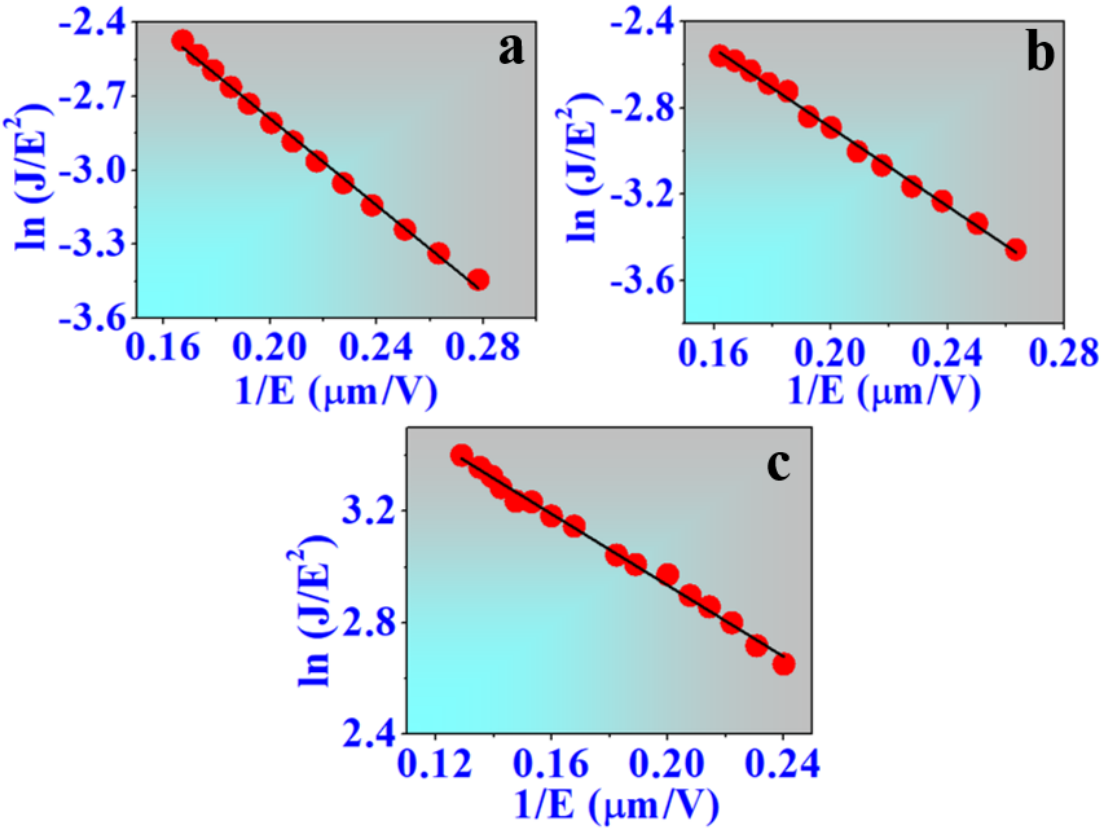

Figure 2.11. *F-N plot of (a) S1. (b) S2. (c) S3.*

Table 2.3. Various field emission parameters of samples S1, S2 and S3.

Samples	Turn-on field [V/μm]	slope	β-factor	Max. FE current density [nA/cm^2] @ E_{Max}
S1	6.6	-9.39	1471	680
S2	6.7	-8.57	1611	910
S3	<4.5	-6.10	2263	2263

2.3.2 Air oxidation of NdB_6 nanorods

It is known that as the temperature of metal hexaboride increases there will be a tendency to form surface oxidation of cathode material occurs. The oxidation of NdB_6 may deteriorate field emission performance. The high-temperature PXRD study at various temperature has been investigated in the atmospheric condition (in the air) at 10 ℃/h heating rate. Oxidation study of NdB_6 nanorods has been investigated till 800 ℃. It has

been observed there is no new diffraction peak appears till 400 ℃ and all the peaks well-matched with cubic NdB_6 (JCPDS no. 03-065-1828) and high-intensity peaks around Bragg's angle 39.09 and 45.62 matched with platinum, which was utilized as a substrate for PXRD measurement (Figure 2.12a-b). Further, enhancement in temperature (600 ℃ and 800 ℃) leads to the oxidation of NdB_6 as there are arise of neodymium borate peak (Figure 2.12a-b).

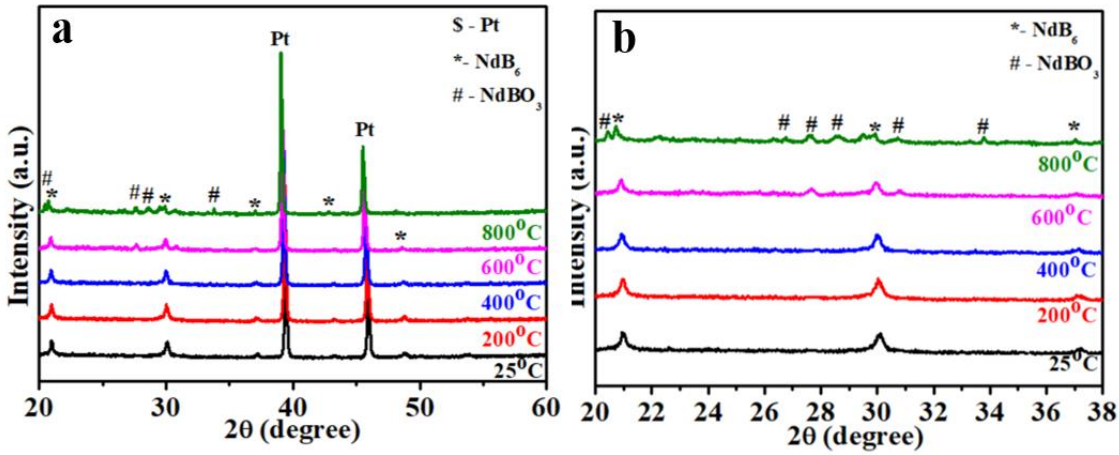

Figure 2.12. *(a) High-temperature XRD of NdB_6 nanorods. (b) Zoom view of HT-XRD in 2θ range 20-38º.*

2.4 Conclusions

The present study deals with the low-temperature stabilisation of anisotropic neodymium hexaboride and their field emission properties. It was observed that the precursor's ratio, as well as the heating rate, affect the final morphology of synthesised neodymium hexaboride. TEM study showed the formation of ultrafine NdB_6 nanocube of size 15-20 nm at the higher heating rate (250 ℃/h), while at the slow heating rate (40 ℃/h) leads to the formation of ultra-fine NdB_6 nanorods (10 nm X 100 nm). The synthesised powder has been dispersed in ethanol and ethylene glycol mixture. The prepared dispersion was coated on Si-substrate via the spin coating method followed by slow heating at 200 ℃ for 12 h. The field emission study shows that ultrafine nanorods provide the highest current density (2.3 μA /cm^2) and the lowest turn-on field (<4.5 V/μm). Apart from the lowest turn-on field, the highest enhancement factor (2263) was also achieved from ultrafine NdB_6 nanorod (S3). The observed enhancement factor is nearly two-fold higher than the previously reported field enhancement factor (β=1037). Further, the oxidation study of NdB_6 nanorods shows that the retention of NdB_6 phase up to 400 ℃ in the air.

2.5 References

1 R. Zou, G. He, K. Xu, Q. Liu, Z. Zhang and J. Hu, *J. Mater. Chem. A*, 2013, **1**, 8445–8452.

2 J. Xu, G. Hou, T. Mori, H. Li, Y. Wang, Y. Chang, Y. Luo, B. Yu, Y. Ma and T. Zhai, *Adv. Funct. Mater.*, 2013, **23**, 5038–5048.

3 H. Zhang, J. Tang, Q. Zhang, G. Zhao, G. Yang, J. Zhang, O. Zhou and L. C. Qin, *Adv. Mater.*, 2006, **18**, 87–91.

4 J. Zhou, N.-S. Xu, S.-Z. Deng, J. Chen, J.-C. She and Z.-L. Wang, *Adv. Mater.*, 2003, **15**, 1835–1840.

5 L. Zhang, X. Liu, Z. Lian, X. Wang, G. Shen, D. Shen and Q. Yan, *J. Mater. Chem. C*, 2014, **2**, 3965–3971.

6 T. H. Yang, K. C. Chiu, Y. W. Harn, H. Y. Chen, R. F. Cai, J. J. Shyue, S. C. Lo, J. M. Wu and Y. H. Lee, *Adv. Funct. Mater.*, 2018, **28**, 1–8.

7 T. Zhai, L. Li, Y. Ma, M. Liao, X. Wang, X. Fang, J. Yao, Y. Bando and D. Golberg, *Chem. Soc. Rev.*, 2011, **40**, 2986–3004.

8 Q. Y. Zhang, J. Q. Xu, Y. M. Zhao, X. H. Ji and S. P. Lau, *Adv. Funct. Mater.*, 2009, **19**, 742–747.

9 S. T. Nishanthi, A. Baruah, K. K. Yadav, D. Sarker, S. Ghosh, A. K. Ganguli and M. Jha, *Appl. Surf. Sci.*, 2019, **467**–**468**, 1148–1156.

10 S. Zhou, K. Chen, M. T. Cole, Z. Li, J. Chen, C. Li and Q. Dai, *Adv. Mater.*, 2019, 1805845.

11 Z. J. Li, K. H. Li, G. Y. Song, G. H. Qiu, L. N. Yang and A. L. Meng, *J. Mater. Chem. C*, 2018, **6**, 6565–6574.

12 Y. Tian, Z. Guo, T. Zhang, H. Lin, Z. Li, J. Chen, S. Deng and F. Liu, *Nanomaterials*, 2019, **9**, 538-560.

13 M. A. Anisimov, A. V. Bogach, V. V. Glushkov, S. V. Demishev, N. A. Samarin, V. B. Filipov, N. Y. Shitsevalova, A. V. Levchenko, V. N. Gurin and N. E. Sluchanko, *Solid State Sci.*, 2012, **14**, 1601–1603.

14 V. G. Pol, S. V. Pol and A. Gedanken, *Adv. Mater.*, 2011, **23**, 1179–1190.

15 V. A. Petrosyan, *J. Contemp. Phys.*, 2011, **46**, 125–129.

16 G. Akopov, M. T. Yeung and R. B. Kaner, *Adv. Mater.*, 2017, **29**, 1604506-29.

17 V. T. Petrashov, R. S. Shaikhaidarov, I. A. Sosnin, P. Delsing, T. Claeson and A. Volkov, *Phys. Rev. B*, 1998, **58**, 15088–15093.

18 R. Patra, S. Ghosh, E. Sheremet, M. Jha, R. D. Rodriguez, D. Lehmann, A. K.

Ganguli, H. Schmidt, S. Schulze, M. Hietschold, D. R. T. Zahn and O. G. Schmidt, *J. Appl. Phys.*, 2014, **116**, 164309-7.

19 J. Xu, G. Hou, H. Li, T. Zhai, B. Dong, H. Yan, Y. Wang, B. Yu, Y. Bando and D. Golberg, *NPG Asia Mater.*, 2013, **5**, e53-9.

20 M. Jha, R. Patra, S. Ghosh and A. K. Ganguli, *J. Mater. Chem.*, 2012, **22**, 6356–6366.

21 H. Zhang, J. Tang, Q. Zhang, G. Zhao, G. Yang, J. Zhang, O. Zhou and L.-C. Qin, *Adv. Mater.*, 2006, **18**, 87–91.

22 C. H. Chen, T. Aizawa, N. Iyi, A. Sato and S. Otani, *J. Alloys Compd.*, 2004, **366**, 2003–2005.

23 R. K. Selvan, I. Genish, I. Perelshtein, J. M. Calderon Moreno and A. Gedanken, *J. Phys. Chem. C*, 2008, **112**, 1795–1802.

24 X. H. Ji, Q. Y. Zhang, J. Q. Xu and Y. M. Zhao, *Prog. Solid State Chem.*, 2011, **39**, 51–69.

25 Z. H. Dou, T. A. Zhang, M. Wen, G. Y. Shi and J. C. He, *J. Inorg. Mater.*, 2014, **29**, 711–716.

26 W. Han, Y. Zhao, Q. Fan and Q. Li, *RSC Adv.*, 2016, **6**, 41891–41896.

27 L. Bao, X. Qi, Tana, L. Chao and O. Tegus, *CrystEngComm*, 2016, **18**, 1223–1229.

28 S. H. Jeon, K. Nam, H. J. Yoon, Y.-I. Kim, D. W. Cho and Y. Sohn, *Ceram. Int.*, 2017, **43**, 1193–1199.

29 W. Zhu, J. Ma, L. Xu, W. Zhang and Y. Chen, *Mater. Chem. Phys.*, 2010, **122**, 362–367.

30 J. Ma, J. Li, G. Li, Y. Tian, J. Zhang, J. Wu, J. Zheng, H. Zhuang and T. Pan, *Mater. Res. Bull.*, 2007, **42**, 982–988.

31 V. M. Gaikwad, K. K. Yadav, Sunaina, S. Chakraverty, S. E. Lofland, K. V. Ramanujachary, S. T. Nishanthi, A. K. Ganguli and M. Jha, *J. Magn. Magn. Mater.*, 2019, **492**, 165652-7.

32 W. Han, H. Zhang, J. Chen, Y. Zhao, Q. Fan, Q. Li, X. Liu and X. Lin, *Ceram. Int.*, 2016, **42**, 6236–6243.

33 Q. Fan, Q. Zhang, Y. Zhao and Q. Ding, *J. Rare Earths*, 2013, **31**, 145–148.

34 Sunaina, M. Sreekanth, S. Ghosh, S. K. Mehta, A. K. Ganguli and M. Jha, *CrystEngComm*, 2017, **19**, 2264–2270.

35 A. Aprea, A. Maspero, N. Masciocchi, A. Guagliardi, A. F. Albisetti and G. Giunchi, *Solid State Sci.*, 2013, **21**, 32–36.

36 Y. Zhu, Q. Li, T. Mei and Y. Qian, *J. Mater. Chem.*, 2011, **21**, 13756–13764.

37 W. Han, H. Zhang, J. Chen, Y. Zhao, Q. Fan and Q. Li, *RSC Adv.*, 2015, **5**, 12605–12612.

38 A. Datta, P. G. Chavan, F. J. Sheini, M. A. More, D. S. Joag and A. Patra, *Cryst. Growth Des.*, 2009, **9**, 4157–4162.

39 R. H. Fowler and L. Nordheim, *Proc. R. Soc. A Math. Phys. Eng. Sci.*, 1928, **119**, 173–181.

Chapter 3

Nanostructured gadolinium hexaborides and their Field Emission Properties

3.1 Introduction

Metal borides have attracted lots of research interest because of their electronic and chemical properties.[1,2] Among all the metal borides, rare earth hexaborides (REB_6) have attracted a lot of researchers' attention due to their low work function, high ionic conductivity, mono-energetic beam, high melting point, high mechanical strength, high chemical resistance, and low vapour pressure.[3,4] These properties make REB_6 useful in various application such as field emission, high energy optical systems,[5] photon detectors sensor,[6] and coatings in resistors.[7] It is known that the field emitter has been widely used in X-ray sources, cathode-ray tube, display devices and as a source of electrons in electron microscopy instruments.[8–11] It has been well studied that materials morphology could alter the emission properties of a cold cathode and anisotropic nanostructure yield better emission properties compared to other morphology having the same chemical composition.[12] Earlier, 1-dimensional REB_6 such as EuB_6, LaB_6, CeB_6, NdB_6, PrB_6 and SmB_6 being used for cold cathode.[13–17] It is known that materials with low work function offer better emission properties and the work function for GdB_6 is 1.5 eV (lowest among all the known rare earth hexaborides).[18] Apart from the low work function, good electrical conductivity (less resistive) of an emitter can also enhance the electron emission.[19] The resistivity of GdB_6 single crystal is 2.7×10^{-7} Ωcm^{-1}, which is nearly close to the electrical resistivity of the same morphology CeB_6.[20] GdB_6 crystallises in a simple cubic structure analogous to CsCl-type structure having $Pm\bar{3}m$ space group.[21] In GdB_6 structure gadolinium is present at Cs site and boron (B_6 polyhedra) is presented at Cl^- site. The covalent bonds in B_6 framework make the GdB_6 structure more robust (high thermal and chemical) and favourable for their utilization in the making of field emission display (FED) devices.[22] These facts motivated us to choose GdB_6 system for further study. Despite their exotic properties, the synthesis of GdB_6 requires adverse synthetic conditions such as high pressure, toxic gaseous precursor and high temperature.[23] Earlier, GdB_6 has been synthesised by solid-state borothermal reduction,[7] carbo-thermal reduction,[24] autoclave,[4,25] thermal evaporation,[26] chemical vapour deposition (CVD),[9,23] pulsed laser deposition (PLD),[27] selective area laser-induced deposition,[28] and aluminium flux reduction.[29] Interestingly, the detailed literature study indicates the cubes-like structure formation in most of the above synthesis process except CVD process. The CVD process leads to the formation of higher dimension rods of 50-70 nm in diameter with several micron in length;[23] however, at the same time, CVD process requires toxic boron compounds (BCl_3

and B_2H_6) with expensive equipment, which limits this process utilization in large scale. Here, we have designed a synthetic process of GdB_6 nanorods synthesis via reaction of $Gd(OH)_3$ nanorods and $NaBH_4$ as precursors at 1000 ℃.

Further, it has been observed that during the field emission study the temperature near the cathode enhanced due to local Joule heating. This local temperature may be up to 300 ℃-400 ℃, which can cause the oxidation of hexaboride materials. It has been observed that when the temperature increases the turn-on and threshold field decreases. The temperature-dependent field emission study governed by the addition of current density obtained from F-N equation and Richardson equation as.[30]

$$J = J_E + J_T \tag{3.1}$$

$$J = \frac{A\beta^2 E^2}{\varphi} \exp\left(-\frac{B\varphi^{\frac{3}{2}}}{\beta E}\right)\left[\frac{\theta}{\sin\theta}\right] + A_R T^2 \exp\left(\frac{-\varphi}{kT}\right) \tag{3.2}$$

Where A= 1.54 X $10^{-6}\, eVV^{-2}$, B= 6.83 X $10^3\, eV^{\frac{3}{2}}\mu m^{-1}$

J_E is field emission current density, β is field enhancement factor, E is applied field and φ is the work function, J_T is thermionic current density, A_R is Richardson constant with a theoretical value of 120 A $Vm^{-2}K^{-2}$, T is the emitter temperature, k is the Boltzmann constant, and θ is the temperature correction factor. The value of $\frac{\theta}{\sin\theta}$ will be always 1, below 800 ℃ with work function ~1.5 eV.

3.2 Experimental

3.2.1 Materials and Methods

Gadolinium nitrate hexahydrate ($Gd(NO_3)_3.6H_2O$, 99.99 %, CDH, India), Triton™ X-100 (Sigma- Aldrich), Acetone (C_3H_6O, Merck, 99 %), Methanol (CH_3OH, Merck, 99 %), Hydrochloric Acid (HCl, 99 %, Merck) and Sodium Borohydride ($NaBH_4$, 99.99 %, CDH, India) were used for the synthesis of gadolinium hexaboride. All the chemicals were used as received.

In the present study, the gadolinium hydroxide precursor was synthesised via the hydrothermal process. In a typical synthesis process, 35 ml of 0.1 M $Gd(NO_3)_3.6H_2O$ containing 10 % V/V TX-100 was mixed with 35 ml of 0.1 M aqueous NaOH capped with 10 % V/V TX-100. The resultant solution was stirred continuously for an hour and then transferred into a Teflon lined stainless steel hydrothermal vessel. Further, the

hydrothermal vessel was heated at 120 ℃ for 24 h and allowed to cool naturally. The obtained mixture was centrifuged, and washed with methanol and water, followed by drying in air. The resulting white $Gd(OH)_3$ and $NaBH_4$ were grinded together. The mole ratio of gadolinium hydroxide to sodium borohydride was kept at 1: 10 and 1: 20 (Table 3.1). The obtained homogeneous mixture was transferred into the recrystallized Almunia boat and annealed at 1000 ºC in Ar atmosphere for eight hours at different heating (250 ℃/h and 40 ℃/h). After completion of the heating process, the sample was allowed to cool down naturally. The as-obtained powder was washed with dilute hydrochloric acid and finally with distilled water till the sample pH reached neutral. After washing the sample was vacuum dried at 80 ℃. Table 3.1 gives details of the precursor's and their sample codes, which will be used throughout the chapter.

Table 3.1. Synthesis condition for GdB_6

Gd- Source	Boron Source	Mole ratio of Gd to B	Temperature ramp [℃/h]	Sample Code
$Gd(OH)_3$	$NaBH_4$	1:10	250	S1
$Gd(OH)_3$	$NaBH_4$	1:20	250	S2
$Gd(OH)_3$	$NaBH_4$	1:20	40	S3

3.2.2 Substrate cleaning procedure

The Si- substrate utilized for the GdB_6 film fabrication was cleaned with acetone, water, isopropanol, HF and Piranha solutions. First, Si-substrate introduced in preheated acetone at 50 ºC for 30 min and then cleaned with water and isopropanol. In the second step, piranha solution (3:1 volume ratio of 98 % H_2SO_4 and 30 % H_2O_2) was heated at 80 ºC and cleaned substrate introduced in the solution for 10 min followed by cleaned with water. In the last step, the substrate has been cleaned with HF and then washed with water, followed by isopropanol.

3.2.3 Fabrication of GdB_6 film

100 mg of pure GdB_6 powder obtained from the above process was dispersed in 2 ml of ethanol and ethylene glycol (1:1 v/v ratio) solution via ultrasonication. The as dispersed powder was drop casted on cleaned Si- substrate via spin-coating method. To get the homogeneous and uniform film of GdB_6 using a spin coating process, the acceleration time, control time and rotation per minute were kept at 20 sec, 60 sec and 3000 rpm, respectively. All the coated samples were cured at 200 ℃ for 4 h in an argon atmosphere.

This process helps in the evaporation of organic moiety (ethanol and ethylene glycol) and simultaneously enhance the adhesion of GdB_6 powder onto the silicon substrate.

3.2.4 Field emission measurements

Indigenously fabricated parallel plate diode configuration (anode-cathode) in 7 X 10^{-7} mbar vacuum with 300 μm separation between anode and cathode for I-V measurement have been utilized. The GdB_6 film on Si- substrate used as a cathode, and a circular steel plate was used as an anode. An electric field was applied using high voltage DC source (Stanford Model PS350) between electrodes (anode-cathode) and an electrometer (Keithley 2000 DMM) measures the field emission current generates from the cathode. The applied electric field was calculated by dividing the applied voltage by the inter-electrode gap. All field emission measurements were performed for three cycles for the reproducibility of field emission result for all samples and reading were recorded through the computer interfaced field emission system using the LabVIEW program.

3.3 Results and discussion

The present work deals with the design of a new method for the stabilization of ultrafine nanocubes and nanorods of GdB_6 via a solid-state borothermal reduction route. For the synthesis of gadolinium hexaboride, nanorods of $Gd(OH)_3$ and $NaBH_4$ were used as gadolinium and boron precursors respectively. Powder X-ray diffraction pattern of the sample obtained after hydrothermal reaction indicates the formation of pure $Gd(OH)_3$. The PXRD pattern well-matched with JCPDS no 01-083-2037 reported for hexagonal space group (P63/m) of pure $Gd(OH)_3$ (Figure 3.1a). The microstructure analysis of $Gd(OH)_3$ has been carried out via the TEM study (Figure 3.1b). TEM study of the sample obtained at 120 ℃ shows the formation of nanorods of dia ~10 nm, length ~ 120 nm and aspect ratio ~12. The HRTEM study has been carried out for the determination of interplanar distance "d" between two consecutive planes and HRTEM micrograph indicates the presence of (101) plane corresponds to the d value 0.32 nm (Figure 3.1c). Further, the electron diffraction of $Gd(OH)_3$ nanorods shows the presence of 100, 101, 201 and 211 planes with interplanar spacing 0.54, 0.30, 0.21 and 0.17 nm respectively (Figure 3.1d). The compositional analysis of $Gd(OH)_3$ nanorods has been done by the EDX study**.** The EDX study confirms the presence of Gd and O. The presence of Cu peak was due to the utilization of the carbon-coated copper grid (inset Figure 3.1b).

As discussed in the experimental section, the synthesised $Gd(OH)_3$ sample was mixed with $NaBH_4$ in different mole ratio and thermogravimetric analysis (TGA) of the above mixture has been done for the stabilization of GdB_6.[31] The TGA of pure $Gd(OH)_3$ has been carried out in 50-1000 ℃ temperature (Figure 3.2a). A continuous weight loss is observed until ~250 ℃ is due to the removal of water molecules adsorbed at the surface of $Gd(OH)_3$. Further, a steep reduction in weight from ~250 ℃ to 332 ℃ is due to the transition of $Gd(OH)_3$ to GdOOH.[32,33] Further, a weight loss in the temperature range of 315 ℃ to 580 ℃ indicates the conversion of Gd-O-OH to Gd_2O_3 (Figure 3.2a).

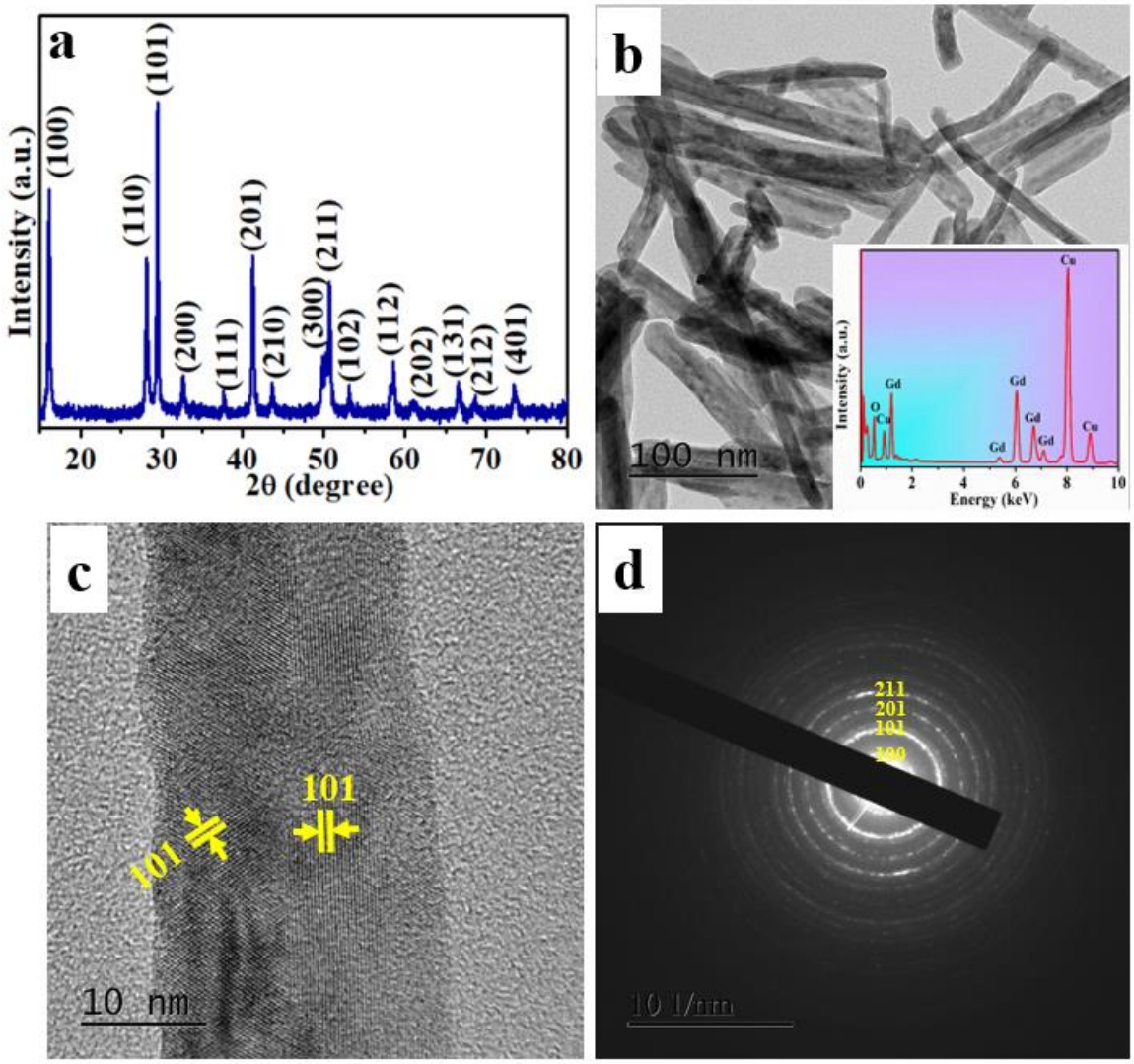

Figure 3.1. *Gadolinium precursor synthesised by hydrothermal method. (a) PXRD of $Gd(OH)_3$. (b) Transmission electron microscopy of $Gd(OH)_3$ and inset is EDX of the corresponding sample. (c) HRTEM of $Gd(OH)_3$. (d) Corresponding selected electron diffraction pattern of $Gd(OH)_3$.*

The thermal behaviour of $NaBH_4$ was shown in Figure 3.2b. It has been observed that up to 400 ℃ and no significant change in weight was observed. As the temperature

increased beyond 400 ℃, there was an increase in weight due to the formation of NaH and BH_3.[31] Further, as discussed earlier, we would like to stabilize gadolinium hexaboride using gadolinium hydroxide nanorods and sodium borohydride. The TGA/DTA of the mixture of $Gd(OH)_3$ and $NaBH_4$ in 1:10 and 1:20 argon atmosphere in the temperature range 50-1000 ℃ was carried for the getting precise temperature range for the stabilization of GdB_6 (Figure 3.2c-d).

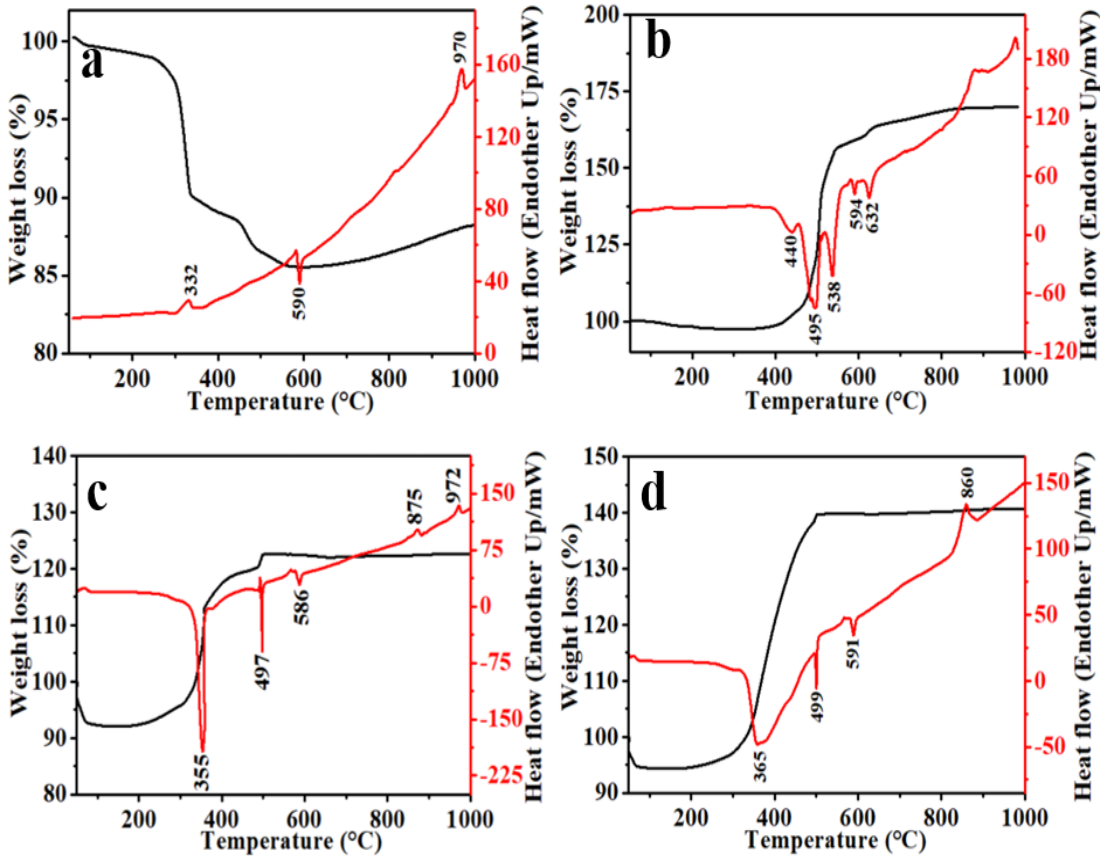

Figure 3.2. *Differential temperature analysis (DTA) and TGA of; (a) Gadolinium hydroxide. (b) Sodium borohydride. (c) Gadolinium hydroxide with sodium borohydride in 1:10 mole ratio. (d) Gadolinium hydroxide with sodium borohydride in 1:20 mole ratio.*

In Figure 3.2c, the presence of a steep exothermic peak around 355 ℃ corresponds to the removal of surface water from the precursors' molecules and the transformation of $Gd(OH)_3$ into GdOOH and exothermic peak around ~497 ºC corresponds to the decomposition of $NaBH_4$ into NaH and BH_3.[31] It might be possible that the as-obtained GdOOH further reacts with BH_3 gas generated during the decomposition of sodium borohydride, which can be seen as at 586 ℃.[31] Further, the endothermic peaks at ~875 ℃ and 972 ℃ suggest that GdB_6 can be stabilized beyond this temperature (Figure 3.2c). Further, $Gd(OH)_3$ and $NaBH_4$ were mixed in 1:20 mole ratio and TGA/DTA has been performed. The peaks around 365 ℃, 499 ℃ and 591 ℃ in the case of 1:20 ratio is in close agreement with the

1:10 ratio; however, there is a broadening in the peak, which might be due to the high amount of precursors. Further, an endothermic peak ~860 ℃ was also observed (Figure 3.2d). From the above observation, the temperature for GdB_6 stabilization was found to be in the temperature range of 800 ºC - 900 ℃. Hence, for stabilization of GdB_6, the mixture of $Gd(OH)_3$ and $NaBH_4$ has been annealed at a little higher temperature (1000 ℃) for 8 h in Ar atmosphere.

The powder X-ray diffraction pattern of samples obtained by heating $Gd(OH)_3$ and $NaBH_4$ at the heating rate of 250 ºC/h and 40 ºC/h in an inert atmosphere for 8 h is shown in Figure 3.3a.

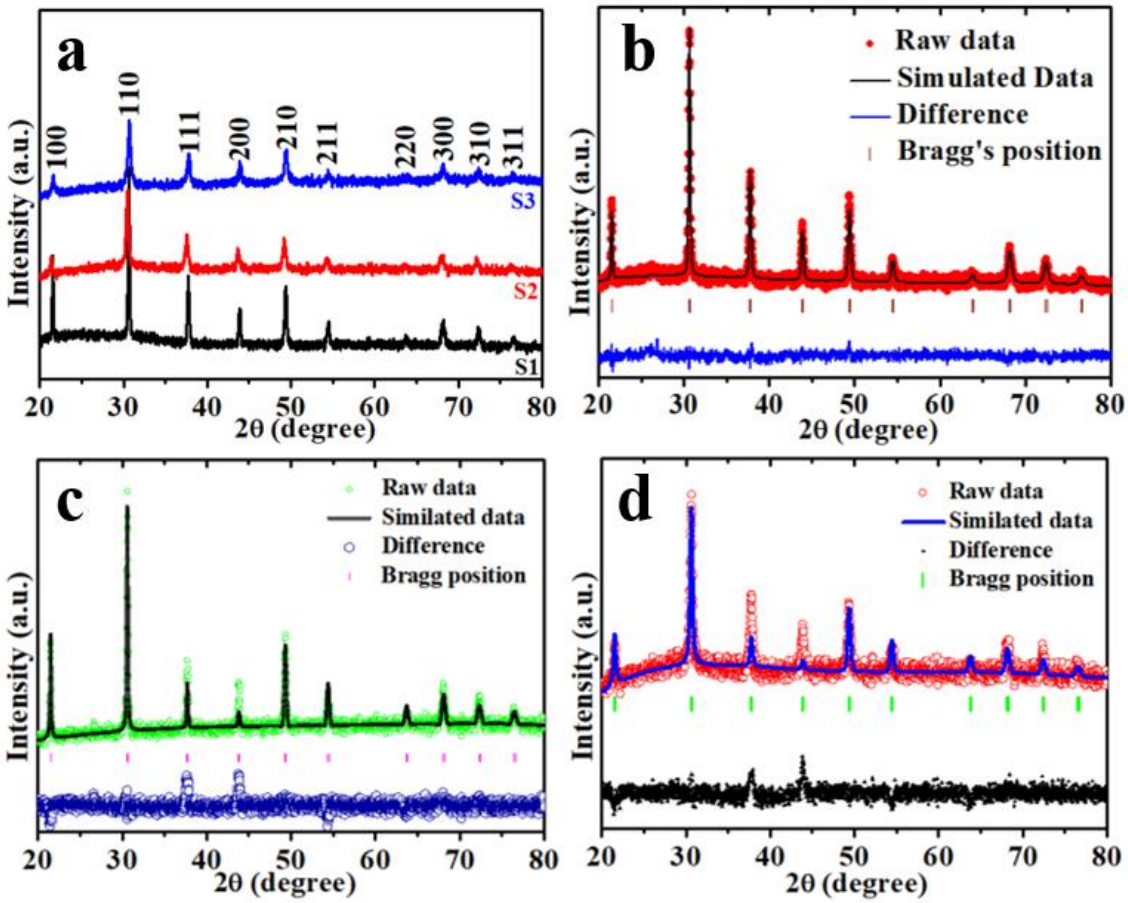

Figure 3.3. *(a) Powder X-ray diffraction pattern of synthesised GdB_6 (S1, S2 and S3). (b) Rietveld refined PXRD of S1. (c) Rietveld refined PXRD of S2. (d) Rietveld refined PXRD of S3.*

The diffraction pattern of as synthesised samples (S1, S2 and S3) matched with the JCPDS card number 03-065-1826 having cubic space group ($Pm\bar{3}m$), which confirms the formation of pure GdB_6. Further, Rietveld refinement by FullProf software of as-prepared samples (S1, S2 and S3) has been carried out to get structural information (Figure 3.3b-d). The goodness of fit for S1, S2 and S3 are 1.07, 1.21, and 1.10 with refined lattice cell

parameter 4.128 (8), 4.132 (4), and 4.135 (9) Å respectively. It was observed that the volume of ultrafine cubes [70.330 (2) for S1 and 70.514 (11) for S2 $Å^3$] is shorter than ultrafine rods [70.71 (3) $Å^3$], which is in good agreement with the previous report of reduced volume of nanorods.[7,34] The unit cell of S3 sample obtained from the Rietveld refinement method using VESTA software has been displayed in the inset of Figure 3.4.[35] All the structural parameter generated from Rietveld-refinement has been given in Table 3.2. Wyckoff sites are 1a and 6f for Gd and B respectively.

Table 3.2. Rietveld refined parameter

(a) Sample: S1, a: 4.128 (8) Å, R_{exp}:4.69, R_p:4.53, χ^2: 1.07					
Atoms	**Position**			**B_{iso} ($Å^2$)**	**Occupancy**
	X	**Y**	**Z**		
Gd	0	0	0	0.006 (8)	1
B	0.260 (3)	0.5	0.5	0.334 (7)	0.167
B	0.5	0.5	0.790 (3)	0.329 (2)	0.167
B	0.5	0.5	0.197 (2)	0.350 (7)	0.167
B	0.5	0.199 (5)	0.5	0.337 (11)	0.167
B	0.5	0.794 (6)	0.5	0.331 (2)	0.167
B	0.798 (4)	0.5	0.5	0.67 (6)	0.167

(b) Sample: S2, a: 4.132 (4) Å, R_{exp}: 4.71, R_p: 4.27, χ^2: 1.21					
Atoms	**Position**			**B_{iso} ($Å^2$)**	**Occupancy**
	X	**Y**	**Z**		
Gd	0	0	0	0.029 (15)	1
B	0.207 (4)	0.5	0.5	0.042 (4)	0.165
B	0.5	0.5	0.796 (4)	0.002 (15)	0.167
B	0.5	0.5	0.202 (3)	0.003 (5)	0.167
B	0.5	0.201 (2)	0.5	0.001 (12)	0.167
B	0.5	0.799 (6)	0.5	0.001 (11)	0.166
B	0.781 (3)	0.5	0.5	0.001 (4)	0.166

(c) Sample: S3, a: 4.135 (9) Å, R_{exp}: 4.65, R_p: 4.43, χ^2: 1.11					
Atoms	**Position**			**B_{iso} ($Å^2$)**	**Occupancy**
	X	**Y**	**Z**		
La	0	0	0	0.029 (15)	1
Nd	0	0	0	0.410 (4)	0.167
B	0.198 (5)	0.5	0.5	0.312 (7)	0.167
B	0.5	0.5	0.781	0.276 (5)	0.167
B	0.5	0.5	0.257 (7)	0.167 (5)	0.167
B	0.5	0.236 (3)	0.5	0.234 (2)	0.167
B	0.5	0.812 (2)	0.5	0.127 (1)	0.167
B	0.779 (3)	0.5	0.5	0.029 (15)	0.167

Further, Raman spectroscopic study of synthesis samples (S1, S2 and S3) has been also carried out for the confirmation of purity of GdB_6. The reported vibration mode for the cubic space group is $\Gamma = A_{1g} + E_g + T_{1g} + T_{2g} + 2T_{1u} + T_{2u}$, where the rare earth metal embedded at the centre of cubes and octahedron boron cage presented at the corner of cubes. The E_g and T_{2g} are due to Raman active phonons, $2T_{1u}$ is infrared active, T_{1g} and T_{1u} are optically inactive.[36] Apart from the allowed Raman active phonons, $\Gamma = A_{1g} + E_g + T_{2g}$ is considered to be allowed Raman active phonons for B_6 cage in the first-order Raman scattering.[37,38] Shift in spectra of A_{1g} towards higher wavenumber is observed in S2 and S3, which confirms the S2 and S3 is higher nanocrystalline nature than S1 (Figure. 3.4).[39]

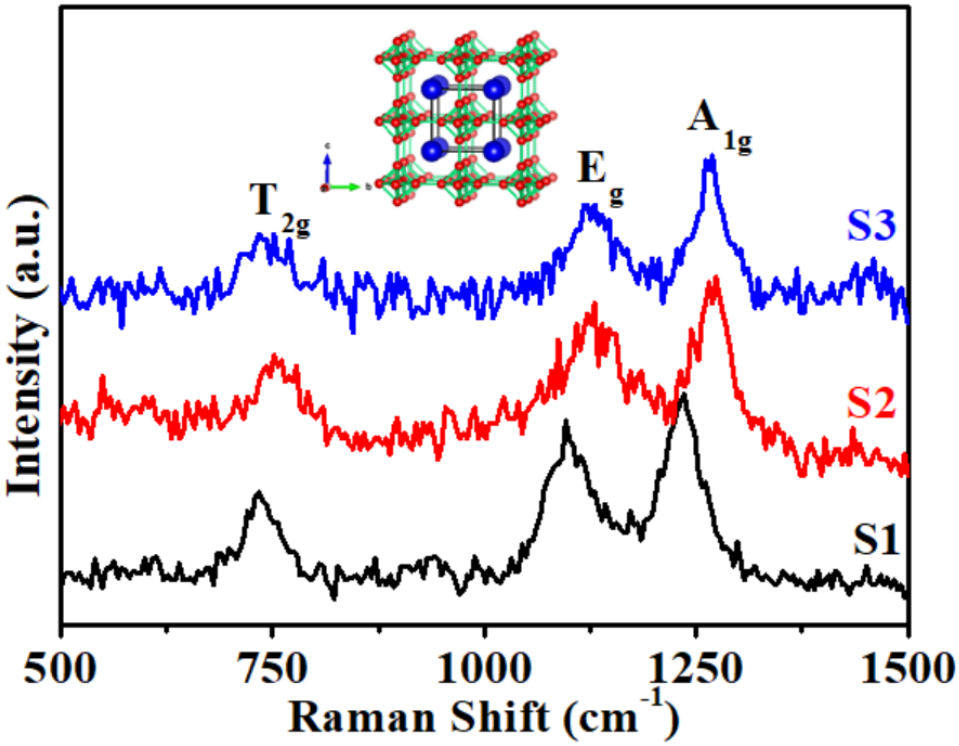

Figure 3.4. *Raman spectra of as-prepared GdB_6.*

The intensity of T_{2g} and A_{1g} is reduced as the particle size tends towards the nano regime.[39] The increase in strain and spring constants leads to shifting the Raman spectra to higher energies.[40] The presence of T_{2g}, E_g and A_{1g} at peak position observed at ~740, 1100 and 1250 cm^{-1} respectively, confirms the formation of the pure phase of GdB_6 (Figure 3.4). The microstructural analysis of prepared metal hexaboride samples has been carried out using TEM. It was observed that annealing of the precursor's mixture at 250 °C/h heating rate with 1:10 ratio, results in the formation of average nanocubes of size ~ 40 nm for sample S1 (Figure 3.5a) Further, the ratio of precursors increases up to 1:20; however, at the same heating rate during the annealed process, which leads to the formation of nanocubes of

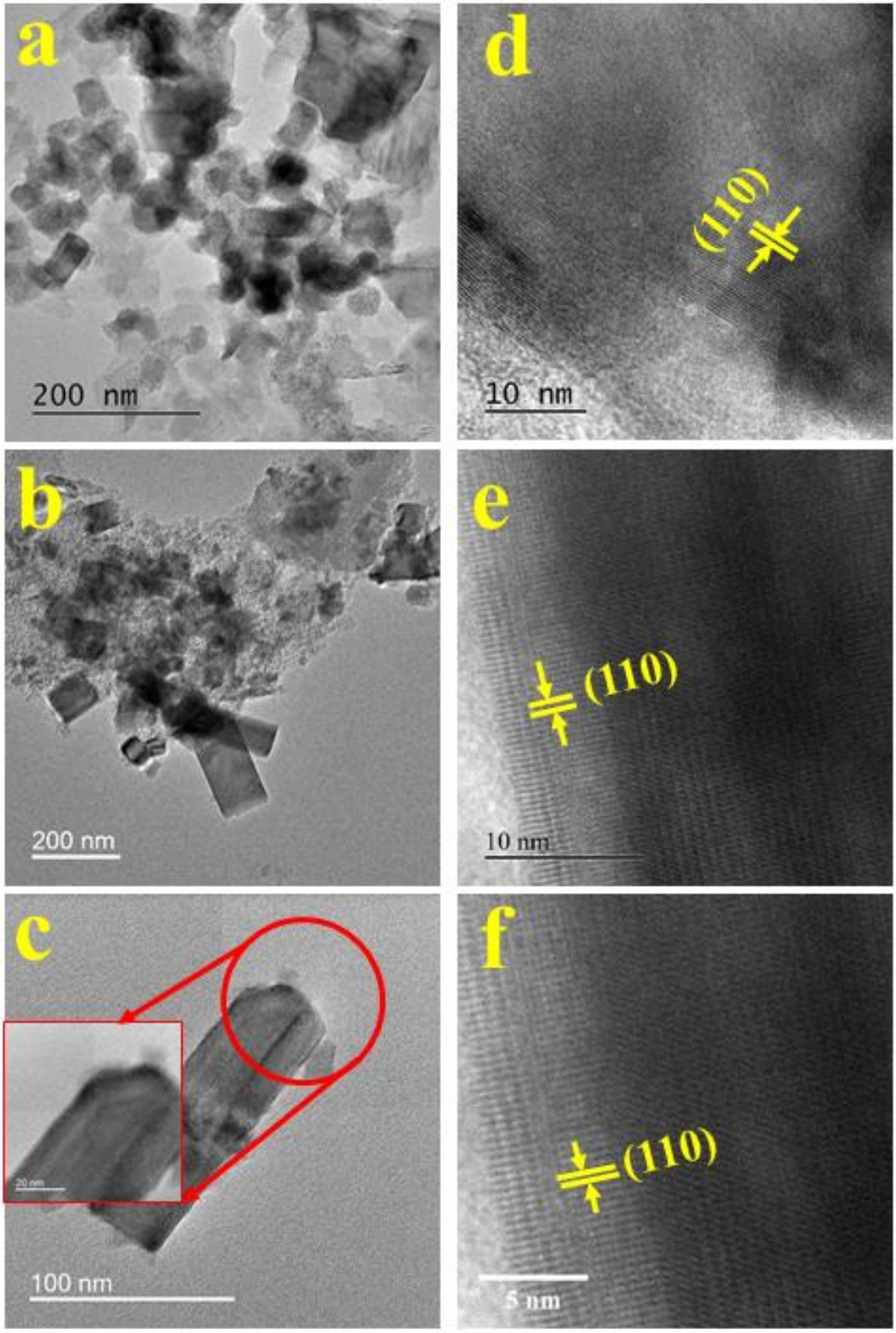

Figure 3.5. *Transmission electron microscopy. (a) S1. (b) S2. (c) S3. High resolution transmission electron microscopy (d) S1. (e) S2. (f) S3.*

40-50 nm with few nanorods of size 50 × 150 nm for sample S2 (Figure 3.5b). It has been observed that when the heating rate decreased to 40 °C/h with a precursors ratio of 1:20 results in the formation of nanorods of size 40 × 150 nm (Figure 3.5c). The possible reason for the retention of morphology while during the heating process is the slow heating rate of 40 °C/h. It appears that when $Gd(OH)_3$ nanorods were grinded with $NaBH_4$, the $NaBH_4$ might have adhered to the surface of $Gd(OH)_3$. On slow heating, the transition of $Gd(OH)_3$ to GdOOH and $NaBH_4$ to BH_3 takes place simultaneous. The evolved BH_3 gaseous moiety get adsorbed to the surface of GdOOH and form an internal structure in the temperature range of up to 500 °C. The intermediate stage was further subjected to heating up to 1000 °C, which results in the formation of GdB_6 nanorods and the scheme of the nanorods synthesis has been shown in Figure 3.6.

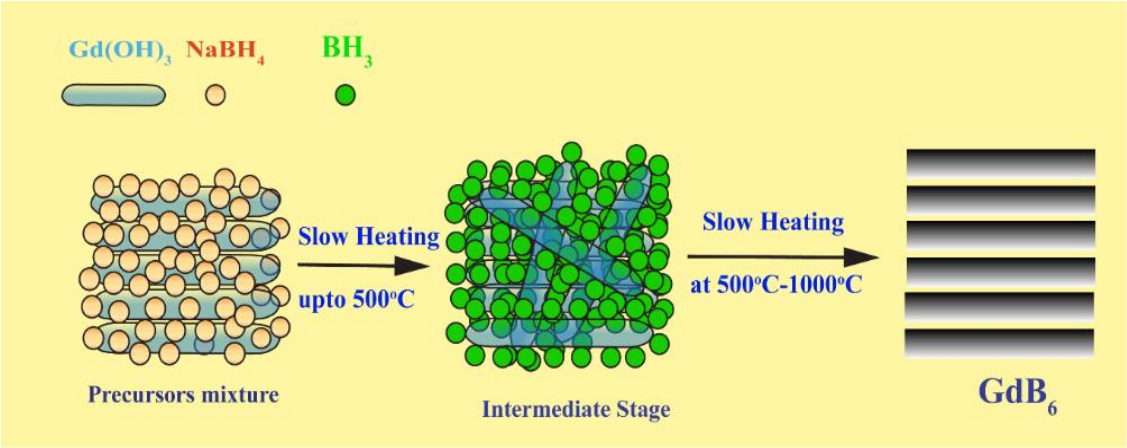

Figure 3.6. *Schematic of GdB_6 nanorods synthesis.*

The observed fact of retention of morphology at a slow heating rate is in close agreement with previous reports.[12,34] Further, the EDX study of S3 show the presence of gadolinium and there are no other elements present, which confirms the pure phase of GdB_6 (Figure 3.7). To the best of our knowledge, there is only one report for the synthesis of GdB_6 nanorods via CVD approach using BCl_3 as boron precursors with H_2 as the carrier gas.[23] However, the expensiveness and toxicity of BCl_3 limit the large scale production of GdB_6. Here, for the first-time GdB_6 nanorods have been synthesised using borothermal reduction route at ambient pressure at 1000 °C. The low-temperature heating process yields average ultrafine nanorods of 40 nm X 150 nm dimension, which is nearly 10 times shorter in length than earlier reported nanorods (50-60 nm in diameter and several micrometres in length).[23] Further, the HRTEM study confirms the (110) plane growth of GdB_6 sample, which corresponds to the 2.90 Å interplanar spacing (Figure 3.5d-f). As discussed in the

experimental section, the dispersion of GdB_6 was prepared using ultrasonic mixing of 100 mg of GdB_6 in 2 ml of ethanol and ethylene glycol (1:1 V/V).

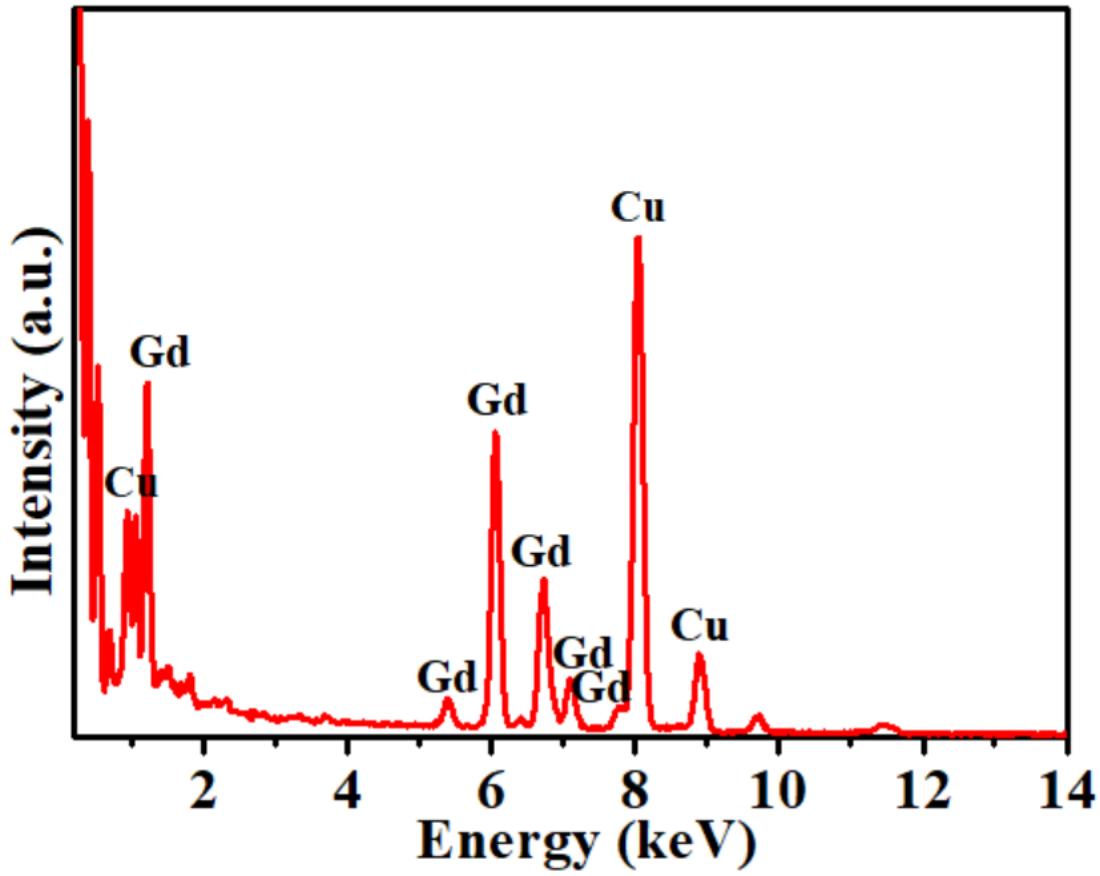

Figure 3.7. *EDX of GdB_6 nanorods.*

The as-prepared dispersion was spin-coated on the silicon substrate. The spin-coated film of GdB_6 was heated for 4 h at 200 ℃ with a slow heating rate (20 ℃/h) in the flow of argon to remove organic molecules. Further, using the ellipsometry technique the refractive index of GdB_6 film fabricated using S1, S2 and S3 samples have been measured. The refractive index for sample S1, S2 and S3 were found to be 1.00, 1.16 and 1.34 respectively at ~300 nm, which is in close agreement with the earlier report (Figure 3.8a).[41] It was observed that as the precursor ratio increases the refractive index decreases, which is in good agreement with previous reports of the rare earth hexaboride family.[41] The result indicates that the S3 sample has the highest refractive index compared to the S1 and S2 samples. The viscosity of prepared dispersion was measured using Rheometer. The plot of shear stress vs shear rate for S1, S2 and S3 samples are shown in (Figure 3.8b). It has been observed that S1 and S2 behave as a Newtonian fluid with little deviation while S3 behaves as Bingham plastic fluid (Figure 3.8b).

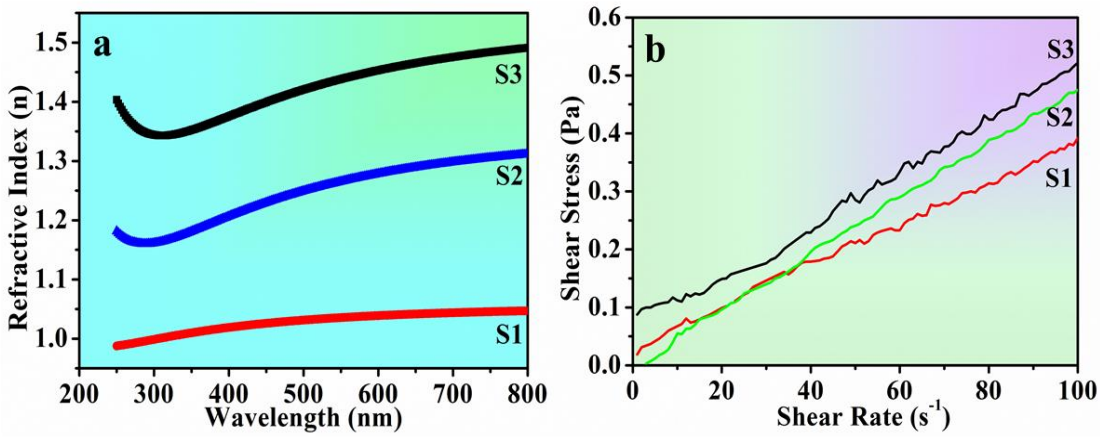

Figure 3.8. *(a) Refractive index of the synthesised sample. (b) Viscosity plot of prepared dispersion.*

3.3.1 Field emission study

The surface properties (alignment and roughness) of GdB_6 film of all the samples (S1, S2 and S3) were investigated using tapping mode AFM studies. The AFM study indicates that the particles are uniformly distributed over the substrate and few rods have been also vertically oriented on Si-substrate (Figure 3.9a-b). However, the nanorods of GdB_6 are vertically oriented over the Si- substrate (Figure 3.9c). There are no reports available for vertically aligned nanorods for GdB_6. It has been known that vertically oriented nanorods show better field emission properties compared to randomly oriented nanorods.[42] The film of GdB_6 on the silicon substrate was used for field emission measurement as a cold cathode. The emission of electrons from the surface can occur in several ways, such as thermionic emission, photoemission, field emission, thermal assisted field emission and photo-induced field emission. However, in the case of thermionic and photoemission, high power is required to induce electron emission and also the generated current density is very low, which limits their uses as a high-end application. However, at the same time by applying a small amount of electric field across the cathode and anode can generate a lot of field emission electrons. The field emission factors such as turn-on field, field enhancement factor and field emission current are dependent on the aspect ratio (shape and size) and work function of cathode materials. The phenomenon of field emission was explained in 1928 by Fowler *et al.* and known as Fowler–Nordheim equation (F-N equation).[43] In the F-N equation, the observed current density (J) is given by:

$$J = \frac{A\beta^2 E^2}{\varphi} \exp\left(-\frac{B\varphi^{\frac{3}{2}}}{\beta E}\right) \qquad 3.3$$

$$ln\frac{J}{E^2} = \ln\frac{A\beta^2}{\varphi} - \frac{B\varphi^{\frac{3}{2}}}{\beta E} \qquad 3.4$$

Where A= 1.54 X $10^{-6}\, eVV^{-2}$, B= 6.83 X $10^3\, eV^{\frac{-3}{2}}Vm^{-1}$

J, β, E and φ are the current density, field enhancement factor, applied field and work function of emitting materials, respectively.

The J-E plot has been shown in Figure 3.9d-f. Here, the lowest required field to generate a current density of 3.2 μA/cm^2 is defined as the turn-on field. The turn-on field for S1, S2 and S3 are 5.56 V/μm, 5.36 V/μm and 4.35 V/μm respectively. The lower turn-on field for S3 sample is due to the vertical alignment of nanorods of GdB_6. However, earlier, 10 nA current can be achieved at 650 V.[23] The maximum current density J_{max} (4.1 μA/cm^2) can be achieved for S3 sample and at the same time, J_{max} for S1 and S2 are 3.57 and 3.6 μA/cm^2 respectively (Figure 3.9d-f). Further, F-N plot (ln(J/E^2) vs 1/E) in high electric field region suggests that the current emission is due to the applied electric field (inset Figure 3.9d-f). The FN-plot was fitted with a single straight line, and the slope for S1, S2 and S3 are was -9.61, -9.19 and -8.39 respectively (Figure 3.9d-f).

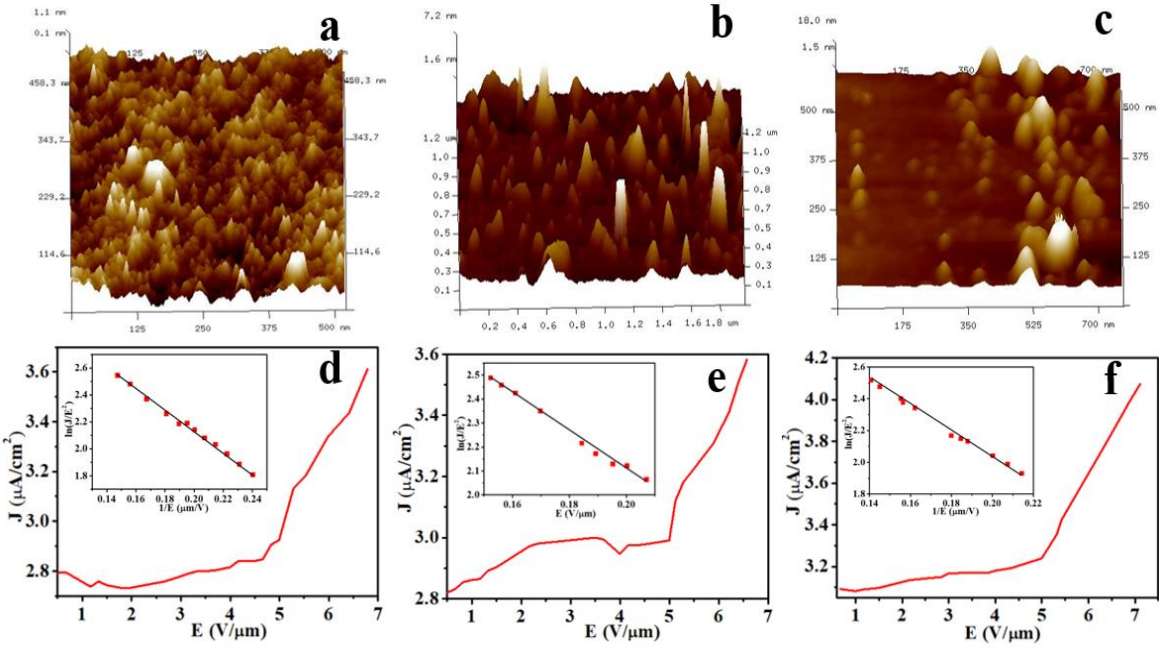

Figure 3.9. *AFM study of (a) S1. (b) S2. (c) S3. and J-E plot for (d) S1. (e) S2. (f) S3; inset figure is FN plot of corresponding J-E plot.*

Further, the field enhancement factor (β) can be calculated from F-N equation number 3.4, where B is constant, having a value of 6.83 X 10^3 VeV$^{-3/2,}$ and ϕ is equal to 1.5 eV. The obtained β value for S1, S2 and S3 are 1301, 1360 and 1490 respectively. The highest β for the nanorods in the present case may be due to the vertical alignment of GdB_6

nanorods; however, earlier, there are no reports for the field enhancement factor of GdB_6. All the field emission parameter has been included in Table 3.3.

Table 3.3. Various field emission parameters of samples S1, S2 and S3

Samples	Turn-on field [V/μm]	slope	β-factor	Max. FE current density [nA/cm^2] @ E_{Max}
S1	5.56	-9.61	1301	3582
S2	5.36	-9.19	1360	3612
S3	4.35	-8.39	1490	4075

Apart from the low turn-on field, the field emission current stability plays a very critical role in making practical use. The temporal stability of the sample has been assessed by calculating the fluctuation in current density using the following formula:

$$cf = \frac{|(x - \bar{x})|}{\bar{x}} \times 100 \qquad 3.5$$

where x represents the current density at each time interval and $\bar{x}$ is a mean electric current density. The stability of current at the potential 1800 V has been shown in Figure 3.10, which reveals only 2 % of electrical current fluctuation for a three and half-hour run.

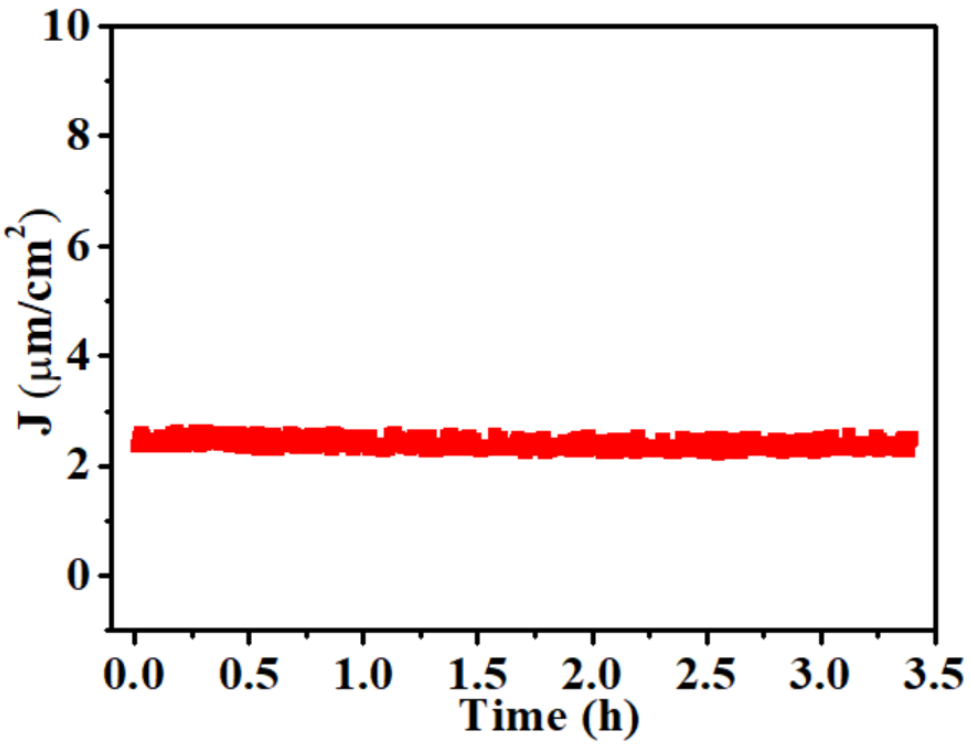

Figure 3.10. *Current density stability at 1800 V.*

Because of the above, here we have designed a simple methodology to obtained vertically aligned GdB_6 ultrafine nanorods for field emission application. This work will be helpful for the researcher who is working in the field of anisotropic boride synthesis.

3.3.1 Thermal stability of synthesised GdB_6 nanorods

It is a well-known fact that heating of hexaboride leads to the formation of surface oxide, which can reduce the field emission performance. In the present work, the rise in local temperature around the cathode occurs during the field emission study due to local heating. The high-temperature PXRD study at various temperature has been investigated in the atmospheric condition (in the air) at 10 ℃/h heating rate up to 800 ℃. It has been observed all the diffraction peaks matched well with JCPDS no. 03-065-1826 of cubic GdB_6 and high-intensity peaks around Bragg's angle 39.1 and 45.6 matched with platinum, which was utilized as a substrate for PXRD measurement (Figure 11a-b). Further, enhancement in temperature (600 ℃ and 800 ℃) leads to the oxidation of GdB_6 as there are arise of gadolinium borate peak (Figure 11 a-b). From the above observation, we can conclude that the GdB_6 can be used as efficient cathode material till 400 ℃.

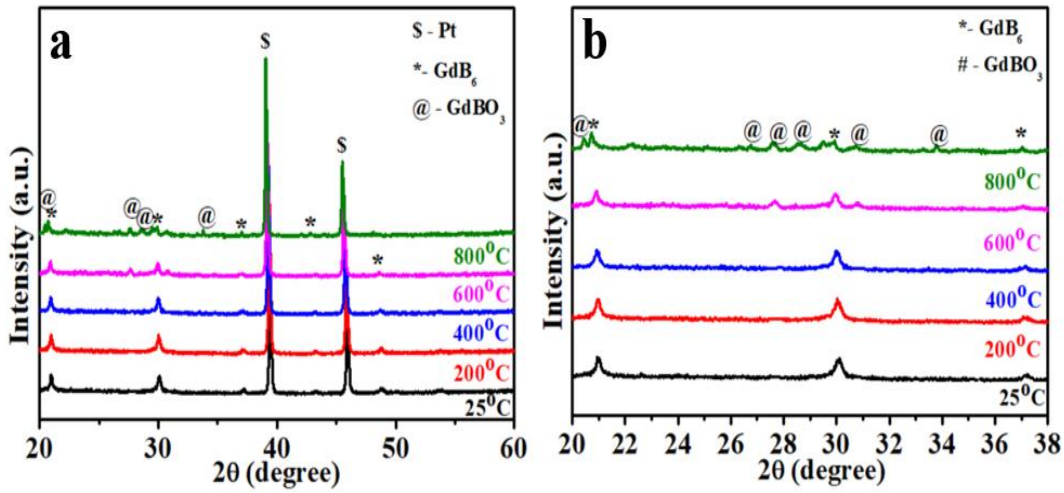

Figure 3.11. *(a) High-temperature XRD of GdB_6 nanorods. (b) Zoom view of HT-XRD.*

3.4 Conclusions

In the present work, low-temperature stabilization of GdB_6 nanorods has been carried out using ultrafine $Gd(OH)_3$ nanorods and $NaBH_4$ precursors. Ultrafine gadolinium hydroxide nanorods (width ~10 nm, length ~ 120 nm) were synthesised via hydrothermal route at 120 ℃. The as-obtained rods were annealed with $NaBH_4$ various ratio and various heating rates. It was observed that the slow heating rate (40 ℃/h) favours the formation of GdB_6 nanorods (40 nm X 150 nm); however, a higher heating rate leads to the formation of cubes (40-50 nm). Further, the synthesized GdB_6 have been dispersed in ethanol and

ethylene glycol mixture followed by spin coating over Si-substrate. The AFM study indicates the vertical alignment of GdB_6 nanorods over Si-substrate, which was utilized for field emission material. Field emission study of vertically oriented GdB_6 nanorods shows the low turn-on field (4.35 V/μm) for S3 and 5.36 and 5.56 V/μm for S1 and S2 respectively. The field enhancement factor (β) for S1, S2 and S3 are 1301, 1360 and 1490 respectively. The low turn-on field and high enhancement factor for sample S3 indicate the GdB_6 nanorods are an excellent cathode material for field emission. Further, HTXRD study indicates that the synthesised GdB_6 nanorods can be used up to 400 ℃ for temperature-dependent field emission study.

2.5 References

1 J. Nagamatsu, N. Nakagawa, T. Muranaka, Y. Zenitani and J. Akimitsu, *Nature*, 2001, **410**, 63–64.

2 K. K. Yadav, S. K. Guchhait, Sunaina, Ankush, C. M. Hussain, A. K. Ganguli and M. Jha, *J. Solid State Electrochem.*, 2019, **23**, 3243–3253.

3 J. Liu, Z. Zhang, Y. Zhao, X. Su, S. Liu and E. Wang, *Small*, 2005, **1**, 310–313.

4 L. Wang, L. Xu, Z. Ju and Y. Qian, *CrystEngComm*, 2010, **12**, 3923–3928.

5 K. R. Peschmann, J. T. Calow and K. G. Knauff, *J. Appl. Phys.*, 1973, **44**, 2252–2256.

6 G. G. Fritz, K. S. Wood, D. Van Vechten, A. L. Gyulamiryan, A. S. Kuzanyan, N. J. Giordano, T. M. Jacobs, H.-D. Wu, J. S. Horwitz and A. M. Gulian, eds. K. A. Flanagan and O. H. W. Siegmund, 2000, 459.

7 R. K. Selvan, I. Genish, I. Perelshtein, J. M. Calderon Moreno and A. Gedanken, *J. Phys. Chem. C*, 2008, **112**, 1795–1802.

8 S. Carenco, D. Portehault, C. Boissière, N. Mézailles and C. Sanchez, *Chem. Rev.*, 2013, 113, 7981–8065.

9 J. R. Brewer, R. M. Jacobberger, D. R. Diercks and C. Li Cheung, *Chem. Mater.*, 2011, **23**, 2606–2610.

10 A. A. Talin, K. A. Dean and J. E. Jaskie, *Solid. State. Electron.*, 2001, **45**, 963–976.

11 S. T. Nishanthi, A. Baruah, K. K. Yadav, D. Sarker, S. Ghosh, A. K. Ganguli and M. Jha, *Appl. Surf. Sci.*, 2019, **467**–**468**, 1148–1156.

12 Sunaina, M. Sreekanth, S. Ghosh, S. K. Mehta, A. K. Ganguli and M. Jha, *CrystEngComm*, 2017, **19**, 2264–2270.

13 J. Q. Xu, Y. M. Zhao, X. H. Ji, Q. Zhang and S. P. Lau, *J. Phys. D. Appl. Phys.*, 2009, **42**, 135403-6.

14 Q. Y. Zhang, J. Q. Xu, Y. M. Zhao, X. H. Ji and S. P. Lau, *Adv. Funct. Mater.*, 2009, **19**, 742–747.

15 R. Patra, S. Ghosh, E. Sheremet, M. Jha, R. D. Rodriguez, D. Lehmann, A. K. Ganguli, H. Schmidt, S. Schulze, M. Hietschold, D. R. T. Zahn and O. G. Schmidt, *J. Appl. Phys.*, 2014, **116**, 164309-6.

16 Menaka, R. Patra, S. Ghosh and A. Kumar Ganguli, *RSC Adv.*, 2012, **2**, 7875–7885.

17 C. Fu, J. Xu, Y. Chang, Q. Wang, Y. Wang, B. Yu, P. Guo, J. Xu, H. Sun, Y. Luo

and J. Liu, *J. Alloys Compd.*, 2017, **729**, 997–1003.

18 H. Zhang, Q. Zhang, G. Zhao, J. Tang, O. Zhou and L. Qin, *J. Am. Chem. Soc.*, 2005, **127**, 13120–13121.

19 M. Sreekanth, P. Srivastava and S. Ghosh, *Appl. Surf. Sci.*, 2020, **508**, 145215-9.

20 A. P. Dudka, O. N. Khrykina, N. B. Bolotina, N. Y. Shitsevalova, V. B. Filipov, M. A. Anisimov, S. Gabani, K. Flachbart and N. E. Sluchanko, *Phys. Rev. B*, 2019, **100**, 205103-7.

21 V. G. Pol, S. V. Pol and A. Gedanken, *Adv. Mater.*, 2011, **23**, 1179–1190.

22 G. Akopov, M. T. Yeung and R. B. Kaner, *Adv. Mater.*, 2017, **29**, 1604506-29.

23 H. Zhang, Q. Zhang, G. Zhao, J. Tang, O. Zhou and L. C. Qin, *J. Am. Chem. Soc.*, 2005, **127**, 13120–13121.

24 M. Hasan, H. Sugo and E. Kisi, *J. Alloys Compd.*, 2013, **578**, 176–182.

25 M. Zhang, Y. Jia, G. Xu, P. Wang, X. Wang, S. Xiong, X. Wang and Y. Qian, *Eur. J. Inorg. Chem.*, 2010, **2010**, 1289–1294.

26 J. T. Cahill and O. A. Graeve, *J. Mater. Res. Technol.*, 2019, 8, 6321–6335.

27 S. R. Suryawanshi, A. K. Singh, D. M. Phase, D. J. Late, S. Sinha and M. A. More, *Appl. Phys. A Mater. Sci. Process.*, 2016, **122**, 1–8.

28 Z. C. Zhong, P. A. Dowben and D. J. Sellmyer, *Mater. Lett.*, 1998, **37**, 320–324.

29 P. Peshev, *J. Solid State Chem.*, 1997, **133**, 237–242.

30 J. Xu, G. Hou, T. Mori, H. Li, Y. Wang, Y. Chang, Y. Luo, B. Yu, Y. Ma and T. Zhai, *Adv. Funct. Mater.*, 2013, **23**, 5038–5048.

31 L. Bao, X. Qi, Tana, L. Chao and O. Tegus, *CrystEngComm*, 2016, **18**, 1223–1229.

32 J. G. Kang, B. K. Min and Y. Sohn, *Ceram. Int.*, 2015, **41**, 1243–1248.

33 M. S. De Almeida, M. A. B. Dos Santos, R. De Fátima Gonçalves, M. R. De Cássia Santos, A. P. De Azevedo Marques, E. Longo, F. De Almeida La Porta, I. M. Pinatti, M. D. P. Silva and M. J. Godinho, *Mater. Res.*, 2016, **19**, 1155–1161.

34 V. M. Gaikwad, K. K. Yadav, Sunaina, S. Chakraverty, S. E. Lofland, K. V. Ramanujachary, S. T. Nishanthi, A. K. Ganguli and M. Jha, *J. Magn. Magn. Mater.*, 2019, **492**, 165652-7.

35 K. Momma and F. Izumi, *J. Appl. Crystallogr.*, 2008, **41**, 653–658.

36 W. Han, H. Zhang, J. Chen, Y. Zhao, Q. Fan, Q. Li, X. Liu and X. Lin, *Ceram. Int.*, 2016, **42**, 6236–6243.

37 N. Ogita, T. Hasegawa, M. Udagawa, F. Iga and S. Kunii, *J. Phys. Conf. Ser.*, 2009, **176**, 012032.

38 Y. F. Markov, V. N. Gurin and K. V. Ponkratov, *Phys. Solid State*, 2018, **60**, 719–722.

39 T. M. Mattox, S. Chockkalingam, I. Roh and J. J. Urban, *J. Phys. Chem. C*, 2016, **120**, 5188–5195.

40 H. C. Choi, Y. M. Jung and S. Bin Kim, *Vib. Spectrosc.*, 2005, **37**, 33–38.

41 M. Jha, R. Patra, S. Ghosh and A. K. Ganguli, *J. Mater. Chem.*, 2012, **22**, 6356–6366.

42 A. Datta, P. G. Chavan, F. J. Sheini, M. A. More, D. S. Joag and A. Patra, *Cryst. Growth Des.*, 2009, **9**, 4157–4162.

43 R. H. Fowler and L. Nordheim, *Proc. R. Soc. A Math. Phys. Eng. Sci.*, 1928, **119**, 173–181.

Chapter 4

Nanostructured lanthanum doped neodymium hexaborides and their field emission properties

4.1 Introduction

Nanostructured metal hexaboride has attracted lots of research interest because of their huge demand in field emission-based devices. Among many metal hexaborides, LaB_6 are well-known materials as an emitter for high-end electron microscopy. In the last two decades, researchers are very interested in exploring the field emission properties of rare earth hexaboride as these materials have low work function and high thermal stability.[1–3] Among various rare earth metal hexaborides, NdB_6 shows the lowest reported work function (1.6 eV). Earlier reports show that excellent field emission, field-induced ballistic emission and high thermionic emission occurs if the work function of any material will be less than 2 eV.[4] The lowest reported work function till now is a diamond film (work function of 0.3-0.9 eV); however, the synthesis of the diamond film is very challenging as it requires very high pressure with high temperature, which limits the large scale application of diamonds as an emitter source.[5,6] For a good field emitter, materials should have a good emission current with high stability, long life cycle, high brightness, low work function, chemically inertness, high melting point, and high mechanical strength.[7–9] The other possible application are high energy optical systems, sensors for photon detectors, electrical coatings for resistors, topological insulator, semi-conductivity, and superconductivity can be explored for rare-earth hexaboride.[10–12] The neodymium hexaboride crystallized in CsCl crystal structures with $Pm\bar{3}m$ space group, in which rare earth metal presents at Cs site and B at octahedron site of Cl^-. The covalent bonds between the B_6 (Octahedral cage) framework bring high thermal and chemical stability, which would be one of the necessary criteria for the material to be used in field emission devices (FED).[13] Despite several advantages of neodymium hexaboride as a field emitter, the practical application is limited due to the requirement of the adverse synthetic condition. Earlier, rare earth hexaboride including neodymium hexaboride has been synthesized using the floating zone method, solid-state reaction, borothermal reduction, carbo-thermal reduction, thermal evaporation, chemical vapour deposition (CVD), pulsed laser deposition (PLD), and selective area laser-induced deposition methods.[14–19] Earlier, Schmid *et. al.* suggests that effective work function can be reduced by doping of lanthanum in NdB_6 enhances the emission performances of field emission devices.[20] Very few studies have been done for the synthesis of lanthanum doped rare-earth hexaboride, which includes $La_xCe_{1-x}B_6$, $La_xBa_{1-x}B_6$, $La_xGd_{1-x}B_6$, $Nd_xGd_{1-x}B_6$, $La_{0.67}Nd_{0.33}B_6$.[1,21–25] In the present work, for the first time, we have attempted to synthesize $La_xNd_{1-x}B_6$ (x=0.1, 0.2, 0.3, 0.4 and 0.5) using lanthanum doped

neodymium hydroxide [$La_xNd_{1-x}(OH)_3$] precursor. In view of the above, in the present work, we have designed a new process for the stabilization of $La_xNd_{1-x}B_6$ (x=0.1, 0.2, 0.3, 0.4 and 0.5) using the $La_xNd_{1-x}(OH)_3$. The $La_xNd_{1-x}(OH)_3$ has been synthesized using the hydrothermal route. The as-obtained $La_xNd_{1-x}(OH)_3$ has been heated with $NaBH_4$ in the presence of Argon at 1000 ℃ to stabilize the $La_xNd_{1-x}B_6$. The as-synthesized $La_xNd_{1-x}B_6$ has been deposited on Si-substrate via spin coating by making of dispersion of $La_xNd_{1-x}B_6$ in a mixture of ethylene glycol and ethanol. Further, the field emission study has been performed and the result indicates that $La_{0.3}Nd_{0.7}B_6$ shows the lowest turn-on field (3.6 V/μm) with the highest field enhancement factor (β=2459).

4.2 Experimental

4.2.1 Materials

Neodymium chloride ($NdCl_3.xH_2O$, 99.99 %, CDH India), Lanthanum nitrate [$La(NO_3)_3.xH_2O$, 99.99 %, CDH India], Triton^{TM} X-100 (Sigma- Aldrich), acetone (C_3H_6O, Merck, 99 %), Hydrochloric Acid (HCl, 99 %, Merck) and Sodium borohydride ($NaBH_4$, 99.99 %, CDH India) were used for the synthesis of lanthanum doped neodymium hexaboride. All the chemicals were used as received without any further purification.

4.2.2 Synthesis of $La_xNd_{1-x}(OH)_3$ [x=0.1, 0.2, 0.3, 0.4 and 0.5]

For the synthesis of $La_{0.1}Nd_{0.9}(OH)_3$, 0.1 M aqueous lanthanum nitrate (7 ml) and 0.1 M aqueous $NdCl_3.xH_2O$ (63 ml) were mixed in the stoichiometric amount (Table 4.1) and stirred for 30 min.

Table 4.1: Amount of rare-earth salt concentration for the synthesis of $La_xNd_{1-x}(OH)_3$

0.1 M Lanthanum aqueous salt (ml)	0.1 M Neodymium aqueous salt (ml)	Rare earth hydroxide precursor	Rare earth hexaboride (Sample code)
7	63	$La_{0.1}Nd_{0.9}(OH)_3$	$La_{0.1}Nd_{0.9}B_6$ (S1)
14	56	$La_{0.2}Nd_{0.8}(OH)_3$	$La_{0.2}Nd_{0.8}B_6$ (S2)
21	49	$La_{0.3}Nd_{0.7}(OH)_3$	$La_{0.3}Nd_{0.7}B_6$ (S3)
28	42	$La_{0.4}Nd_{0.6}(OH)_3$	$La_{0.4}Nd_{0.6}B_6$ (S4)
35	35	$La_{0.5}Nd_{0.5}(OH)_3$	$La_{0.5}Nd_{0.5}B_6$ (S5)

In the above solution mixture, 5 % V/V TX-100 (3.5 ml) has been added and stirred for another 30 min. To this solution, 70 ml of 0.3 M NaOH containing 3.5 ml TX-100 was

further mixed, followed by stirring. The resultant solution mixture was stirred continuously for 1 h and then transferred into 200 ml Teflon lined stainless steel autoclave and heated at 120 ℃ for 24 h. The resultant solution after hydrothermal treatment was washed with methanol and dried in air at 80 ℃. Similarly, the other composition of lanthanum doped neodymium hydroxide [$La_xNd_{1-x}(OH)_3$] has been synthesised and the amount of lanthanum salt and neodymium salt has been mentioned in Table 4.1.

4.2.3 Synthesis of $La_xNd_{1-x}B_6$ [x=0.1, 0.2, 0.3, 0.4 and 0.5]

The as-obtained powder of $La_xNd_{1-x}(OH)_3$ has been used as a source of rare earth metal, and sodium borohydride has been used as a source of boron for the synthesis of lanthanum doped neodymium hexaboride [$La_xNd_{1-x}B_6$]. For the synthesis of $La_xNd_{1-x}B_6$, $La_xNd_{1-x}(OH)_3$ and $NaBH_4$ was grinded together in mortar and pestle to make a homogeneous mixture. The mole ratio of $La_xNd_{1-x}B_6$ to $NaBH_4$ fixed to 1: 30. The obtained homogeneous mixture was transferred to a recrystallized alumina boat and annealed at 1000 ℃ in an argon atmosphere for 6 h with a heating rate of 40 ℃/h. After completion of the reaction, the sample was allowed to cool to room temperature naturally and washed with dilute hydrochloric acid, water and acetone sequentially. The sample after washing was vacuum dried. **Table 4.1** gives details of the precursor's and their sample codes, which we will be used throughout the description of the present thesis.

4.2.4 Fabrication of $La_xNd_{1-x}B_6$ Film

For the preparation of rare earth hexaboride dispersion, 50 mg of as-synthesized powder (S1, S2, S3, S4 and S5) was mixed with 2 ml (1: 1) of ethanol and ethylene glycol mixture (V: V ratio) using ultrasonication. The resulting dispersion was spin-coated on the cleaned Si- substrate at a speed of 3000 rpm for 60 seconds. The process of the spin-coating was repeated four times to get the homogeneous and uniform film.

4.3 Results and discussion

In the present work, nanorods of lanthanum doped neodymium hexaboride ($La_xNd_{1-x}B_6$) have been stabilized at ambient pressure. The stabilization of ultrafine $La_xNd_{1-x}B_6$ nanorods has been involved in three steps. The first step deals with the synthesis of $La_xNd_{1-x}(OH)_3$ (x=0.1,0.2, 0.3, 0.4 and 0.5) nanorods using hydrothermal process. In the second step, $La_xNd_{1-x}(OH)_3$ nanorods were reduced with $NaBH_4$ followed by the annealing at 1000 ℃. Finally, as prepared nanostructures $La_xNd_{1-x}B_6$ has been deposited on Si- substrate via a spin coating process and their field emission properties study have been studied. The

powder X-ray diffraction pattern of the precipitates obtained after hydrothermal treatment, confirms the formation of hexagonal lanthanum doped neodymium hydroxide having space group P63/m, which is completely matched with the diffraction pattern of $Nd(OH)_3$ of JCPDS card no. 01-070-0214 (**Figure. 4.1a**).

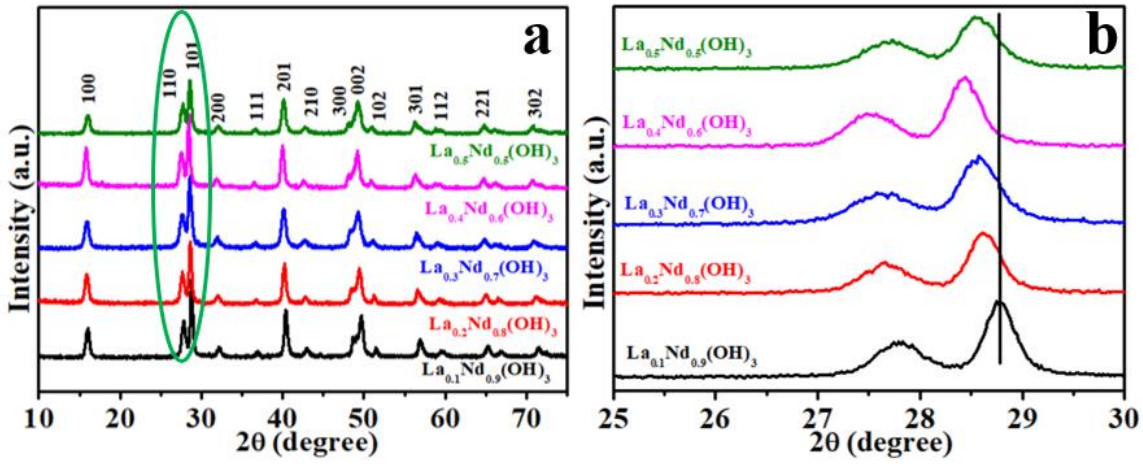

Figure 4.1. *(a) Powder X-ray diffraction of $La_xNd_{1-x}(OH)_3$ (where x=0.1, 0.2, 0.3, 0.4 and 0.5). (b) Zoom view of (110) and (101) peaks.*

The zoom view of (110) and (101) peaks has been shown in Figure 4.1b. It was observed that as the concentration of lanthanum ions in $La_xNd_{1-x}(OH)_3$ increases form x=0.1 to x=0.4, there is a shift in peak position towards the lower angle. This indicates the doping of lanthanum at the site of neodymium. It is a well-stabilized fact that as the larger radius cation being doped in the smaller radius atom, there will be a shift in peak position towards lower angle due to compressive stress.[22] TEM study has been carried out for the morphological study of prepared $La_xNd_{1-x}(OH)_3$. TEM micrograph of $La_xNd_{1-x}(OH)_3$ indicates the formation of nanorods of width 10-15 nm and length 105-130 nm (Figure 4.2a-e)**.** High-resolution transmission electron micrographs of $La_xNd_{1-x}(OH)_3$ have been shown in **Figure 4.2f-j.** Analysis of HRTEM micrograph shows the nanorods are oriented in (110) with interplanar d spacing of ~3.13 Å (Figure 4.2f-j). The selected area electron diffraction pattern shows the presence of 100, 110, 111 and 201 for $La_{0.2}Nd_{0.8}(OH)_3$ **(Figure 4.2k-o).** The SAED patterns of other sample show the presence of 100, 110, 201 and 002 planes **(Figure 4.2l-o)**. To confirms the loading of rare earth metals in synthesises $La_xNd_{1-x}(OH)_3$, inductive coupled plasma mass spectroscopy has been performed. The ICP-MS data has been included in Table 4.2 and reveals that the obtained composition of rare earth metals is in close agreements with the loaded composition.

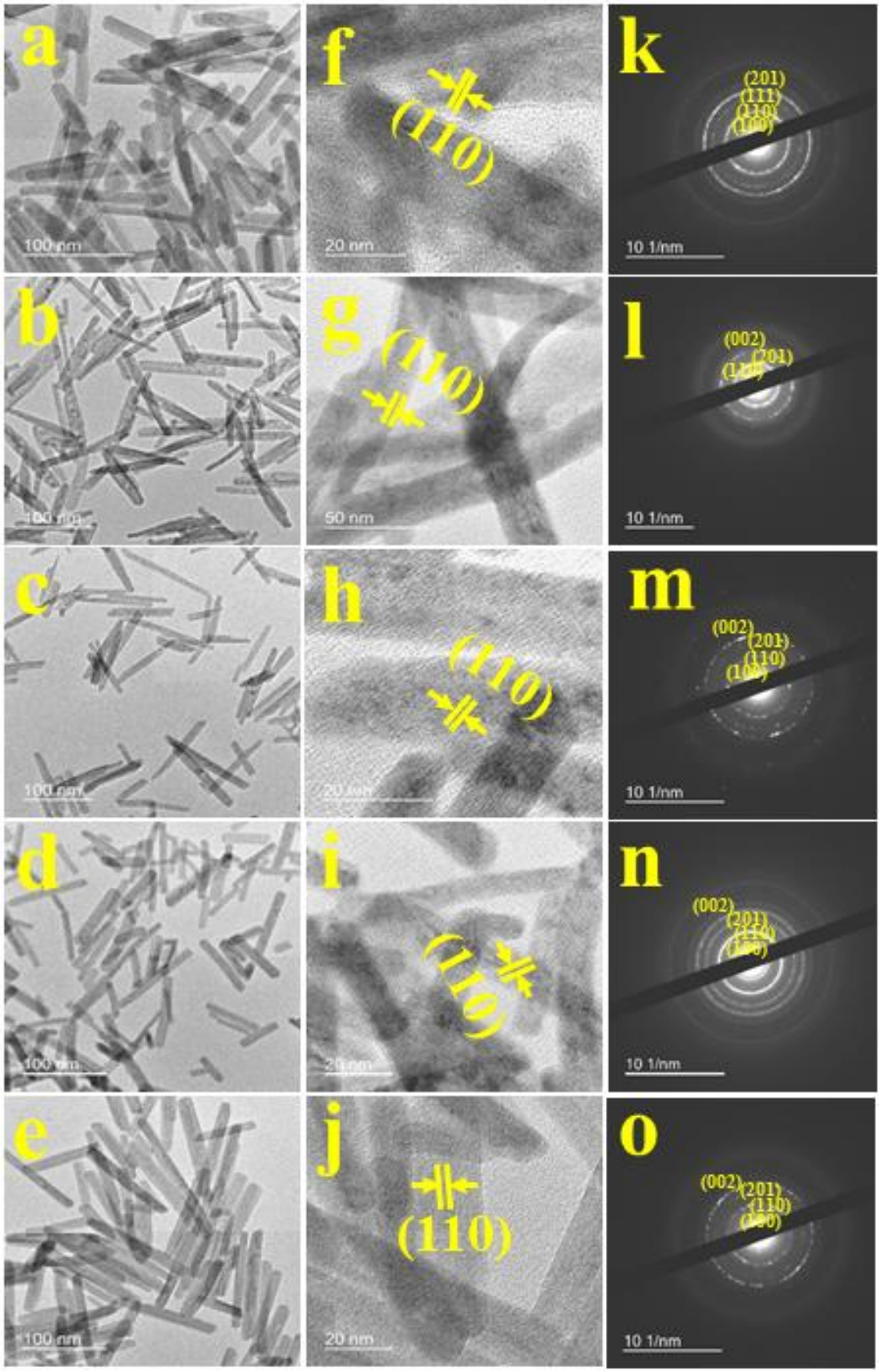

Figure 4.2. *TEM micrographs of $La_xNd_{1-x}(OH)_3$ where (a) x=0.1. (b) x=0.2. (c) x=0.3. (d) x=0.4. (e) x=0.5. (f-g) corresponding HRTEM. (k-o) corresponding selected area diffraction pattern.*

Table 4.2. The ratio of La: Nd in $La_xNd_{1-x}(OH)_3$ obtained from ICP-MS

Sample	Ratio of La: Nd
$La_{0.1}Nd_{0.9}(OH)_3$	1:8.97
$La_{0.2}Nd_{0.8}(OH)_3$	2:7.91
$La_{0.3}Nd_{0.7}(OH)_3$	3:6.99
$La_{0.4}Nd_{0.6}(OH)_3$	4:5.91
$La_{0.5}Nd_{0.5}(OH)_3$	5:4.95

Further, the as-synthesized $La_xNd_{1-x}(OH)_3$ was annealed with sodium borohydride in 1:30 mole ratio at 1000. The PXRD result of as-prepared samples has been shown in Figure 4.3. The PXRD pattern of all the sample has been matched with cubic NdB_6 having space group $Pm\bar{3}m$. The diffraction patterns of all the samples are matched with JCPDS card no 03-065-1828.

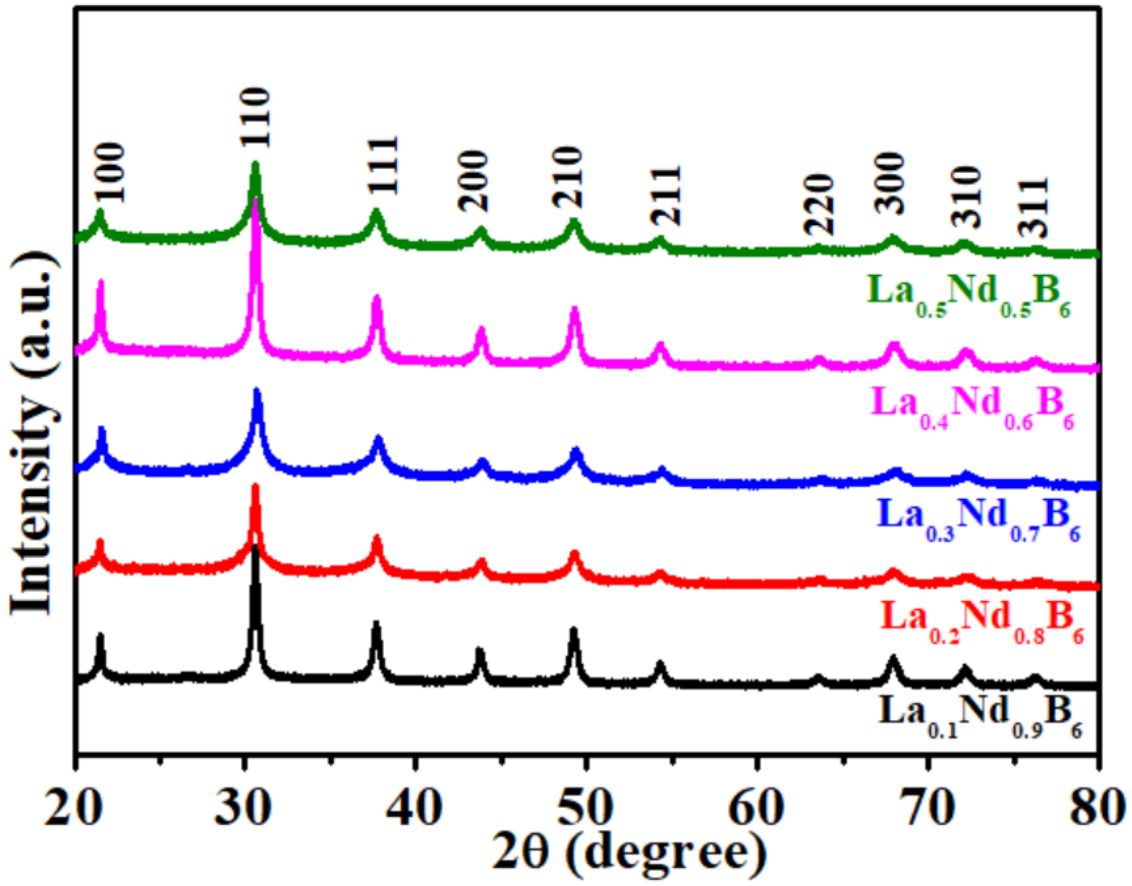

Figure 4.3. *Powder X-ray diffraction of $La_xNd_{1-x}B_6$ (x=0.1, 0.2, 0.3, 0.4 and 0.5).*

Rietveld refinement of all the samples has been carried out for the determination of structural parameter (Figure 4.4). The goodness of fit for S1, S2, S3, S4 and S5 are 1.71, 2.61, 2.20, 3.36 and 2.39, respectively. The observed cell parameter for S1, S2, S3, S4 and S5 are 4.143 (2), 4.136 (6), 4.142 (5), 4.139 (3) and 4.143 (2) Å respectively. All the

observed cell parameter value are in between the cell parameter value of NdB_6 (4.128 Å) and LaB_6 (4.155 Å), which complies well with Vegard's law. All the parameter obtained from Rietveld refinement has also been included in Table 4.3a-e.

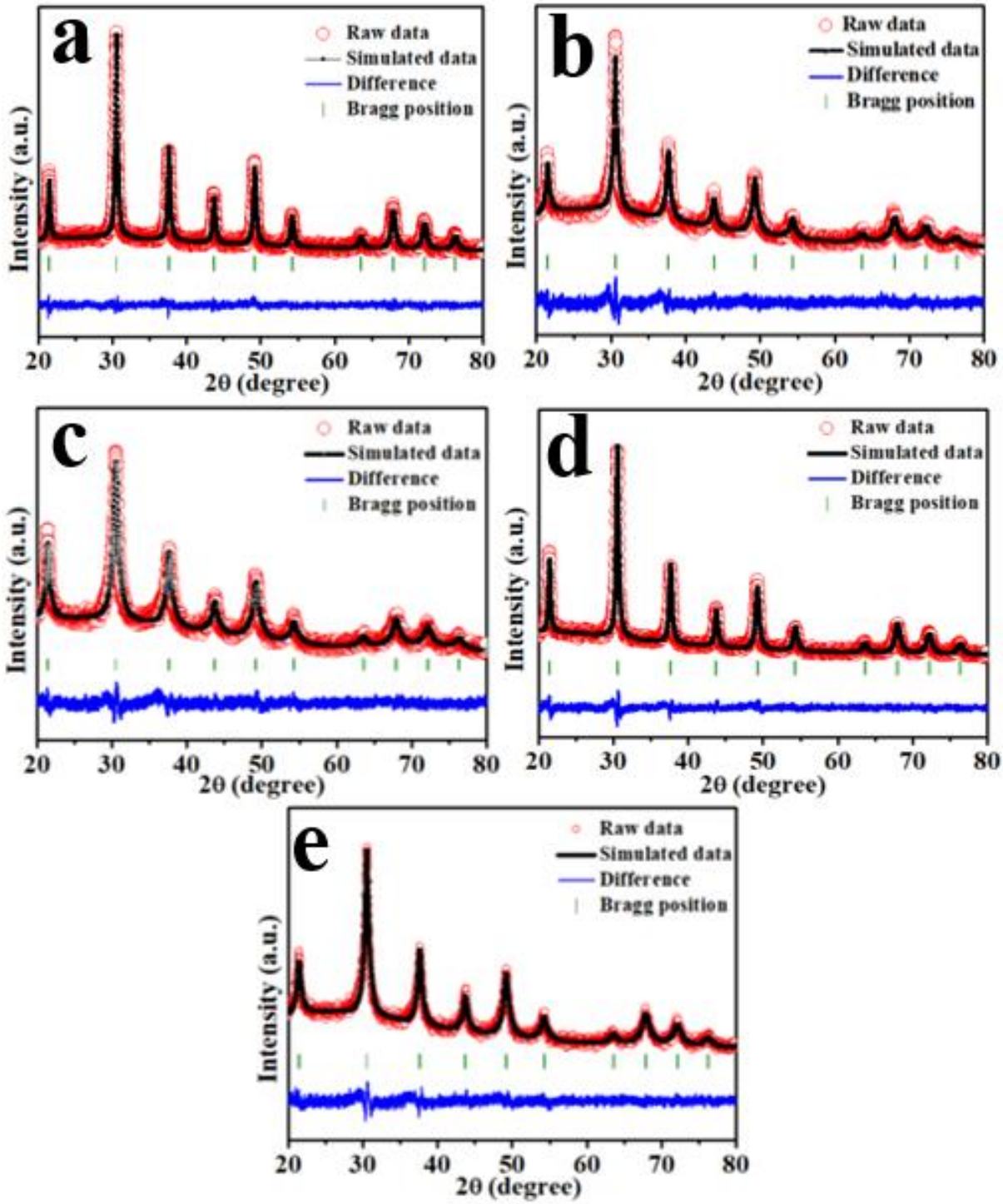

Figure 4.4. *Rietveld refined PXRD of (**a**) S1. (**b**) S2. (**c**) S3. (d) S4. (**e**) S5.*

Table 4.3. Rietveld Refined Parameter of lanthanum doped neodymium hexaboride

(a) Sample: S2, a: 4.143 (2) Å, R_{exp}:6.08, R_p:4.64, χ^2: 1.71					
Atoms	**Position**			**B_{iso} (Å^2)**	**Occupancy**
	X	**Y**	**Z**		
La	0	0	0	0.009 (12)	0.098
Nd	0	0	0	0.009 (12)	0.901
B	0.225 (3)	0.5	0.5	0.164 (7)	0.167
B	0.5	0.5	0.782 (5)	0.079 (9)	0.167
B	0.5	0.5	0.217 (5)	0.045 (6)	0.167
B	0.5	0.219 (2)	0.5	0.026 (5)	0.167
B	0.5	0.776 (4)	0.5	0.086 (5)	0.167
B	0.774 (5)	0.5	0.5	0.195 (12)	0.167

(b) Sample: S2, a: 4.136 (6) Å, R_{exp}:6.99, R_p:4.32, χ^2: 2.61					
Atoms	**Position**			**B_{iso} (Å^2)**	**Occupancy**
	X	**Y**	**Z**		
La	0	0	0	0.027 (3)	0.208
Nd	0	0	0	0.027 (8)	0.791
B	0.245 (5)	0.5	0.5	0.177 (7)	0.167
B	0.5	0.5	0.764 (5)	0.138 (4)	0.167
B	0.5	0.5	0.210 (6)	0.110 (9)	0.167
B	0.5	0.222 (3)	0.5	0.065 (11)	0.167
B	0.5	0.769 (5)	0.5	0.097 (16)	0.167
B	0.754 (6)	0.5	0.5	0.087 (3)	0.167

(c) Sample: S3, a: 4.142 (5) Å, R_{exp}:6.33, R_p:1.48, χ^2: 2.20					
Atoms	**Position**			**B_{iso} (Å^2)**	**Occupancy**
	X	**Y**	**Z**		
La	0	0	0	0.014 (16)	0.293
Nd	0	0	0	0.014 (16)	0.706
B	0.211 (16)	0.5	0.5	0.170 (4)	0.167
B	0.5	0.5	0.829 (5)	0.113 (2)	0.167
B	0.5	0.5	0.258 (2)	0.034 (3)	0.167
B	0.5	0.217 (9)	0.5	0.016 (16)	0.167
B	0.5	0.781 (6)	0.5	0.006 (19)	0.167
B	0.771 (11)	0.5	0.5	0.011 (11)	0.167

(d) Sample: S4, a: 4.139 (3) Å, R_{exp}:8.26, R_p:4.50, χ^2: 3.36					
Atoms	**Position**			**B_{iso} (Å^2)**	**Occupancy**
	X	**Y**	**Z**		
La	0	0	0	0.005 (11)	0.386
Nd	0	0	0	0.005 (11)	0.613
	0.213 (2)	0.5	0.5	0.199 (5)	0.164
	0.5	0.5	0.983 (9)	0.084 (2)	0.164
	0.5	0.5	0.172 (3)	0.053 (4)	0.164
	0.5	0.178 (4)	0.5	0.092(1)	0.164
	0.5	0.777 (4)	0.5	0.049 (11)	0.164
	0.903 (4)	0.5	0.5	0.062 (7)	0.164

(e) Sample: S5, a: 4.143 (2) Å, R_{exp}:7.09, R_p:4.58, χ^2: 2.39					
Atoms	**Position**			**B_{iso} (Å^2)**	**Occupancy**
	X	**Y**	**Z**		
La	0	0	0	0.005 (18)	0.505
Nd	0	0	0	0.005 (18)	0.495
B	0.178 (4)	0.5	0.5	0.209 (3)	0.165
B	0.5	0.5	0.829 (5)	0.092 (1)	0.165
B	0.5	0.5	0.213 (8)	0.141 (6)	0.165
B	0.5	0.199 (2)	0.5	0.132 (3)	0.165
B	0.5	0.811 (8)	0.5	0.31 (6)	0.165
B	0.837 (3)	0.5	0.5	0	0.165

The morphological study of synthesised samples has been done using TEM operated at 200 kV. It was observed that in all the cases, there is the formation of $La_xNd_{1-x}B_6$ nanorods. The width of sample S1 and S3 are ~25 nm with an average length of 100 nm. Whereas sample S2, S4 and S5 show the formation of nanorods of width ~30 nm and length 300 nm (Figure 4.5a-e). Further, the HRTEM of as-prepared samples (S1, S2, S3, S4 and S5) indicates the presence of (110) plane (Figure 4.5f-j). Further, TEM-EDX study of synthesised samples (S1, S2, S3, S4 and S5) shows the presence of lanthanum and neodymium elements (Figure 4.6) The Cu peak in EDX result arises due to the use of carbon-coated copper grids for the TEM-EDX study. To confirm the stoichiometry of samples, ICP-MS has been performed (Table 4.4). The observed composition of samples S1, S2, S3, S4 and S5 are matched with loaded composition. Further, the observed composition from ICP-MS has been also matched with the Rietveld refinement.

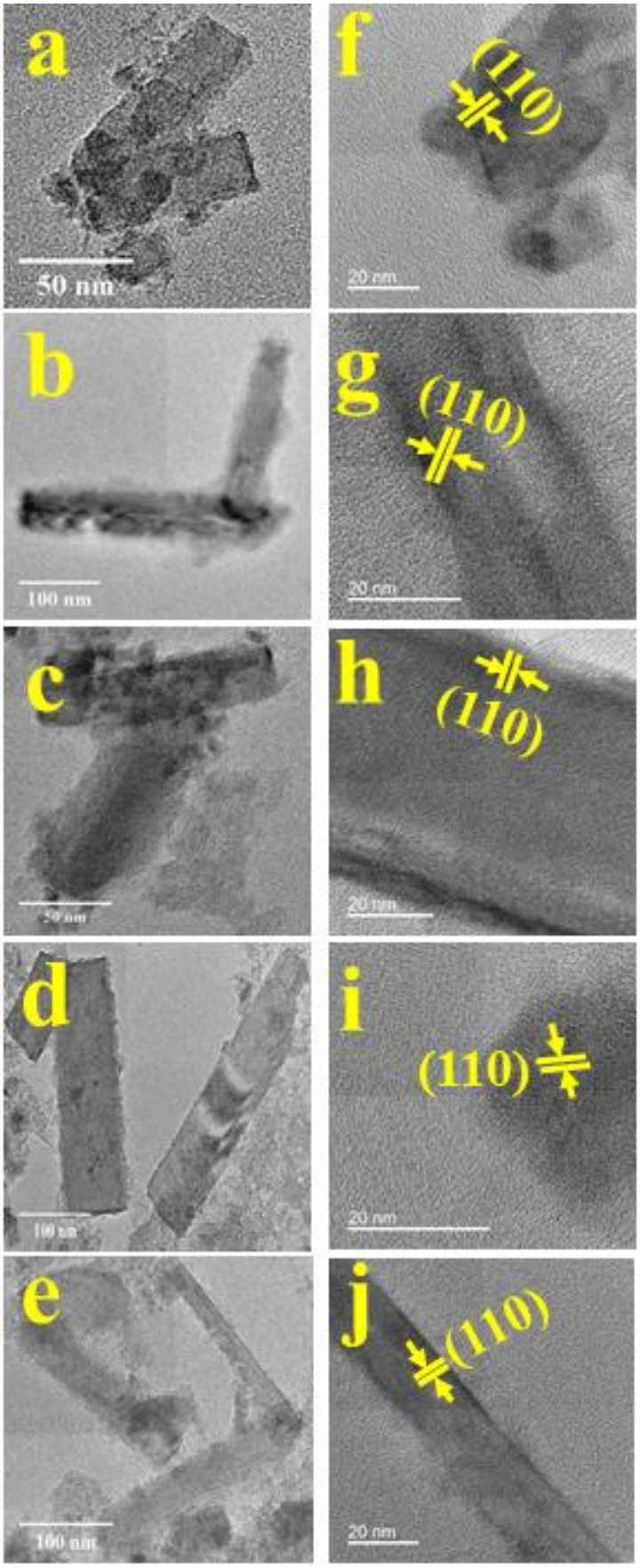

Figure. 4.5. *TEM micrographs of $La_xNd_{1-x}B_6$; (a) S1. (b) S2. (c) S3. (d) S4. (e) S5. (f-j) HRTEM of corresponding samples.*

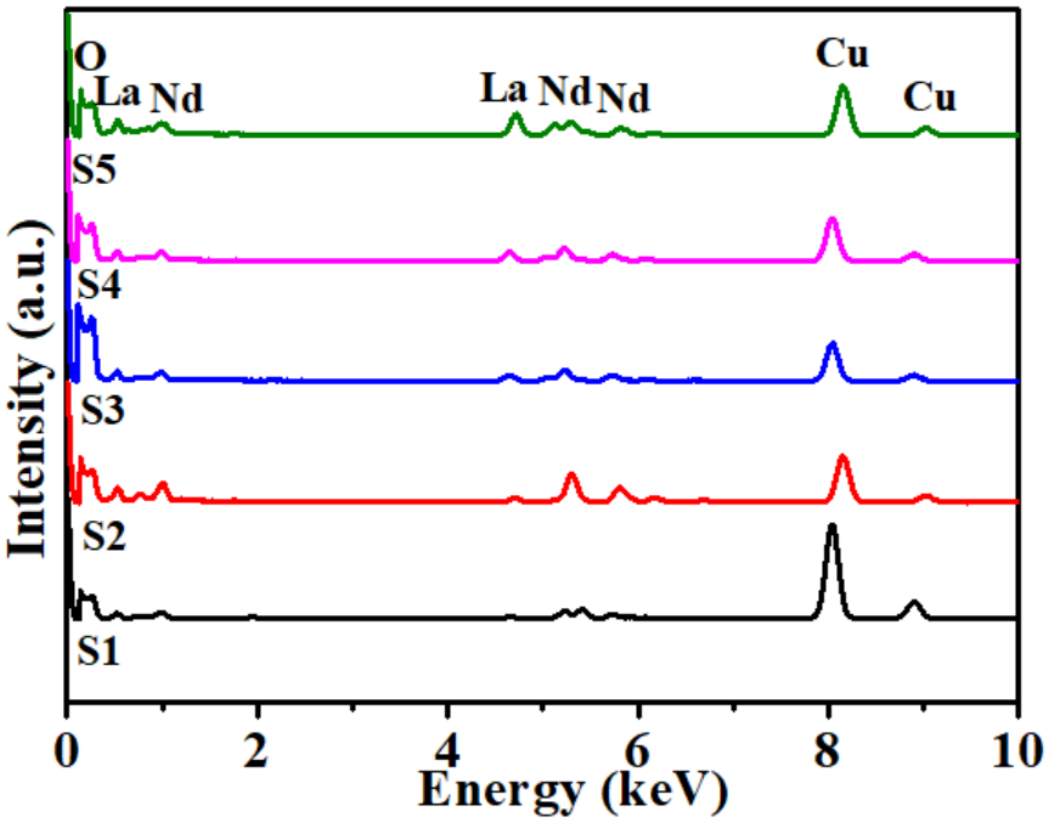

Figure 4.6. *EDX of $La_xNd_{1-x}B_6$ (x=0.1, 0.2, 0.3, 0.4 and 0.5).*

Table 4.4. Atomic percentage of lanthanum doped neodymium hexaboride

Sample	$La_{0.1}Nd_{0.9}B_6$	$La_{0.2}Nd_{0.8}B_6$	$La_{0.3}Nd_{0.7}B_6$	$La_{0.4}Nd_{0.6}B_6$	$La_{0.5}Nd_{0.5}B_6$
La:Nd ratio (EDX)	1:8.93	2:7.89	3:6.99	4:5.90	5:4.94
La:Nd ratio (ICP-MS)	1:8.95	2:7.92	3:6.97	4:5.94	5:4.96

4.3.1 Field emission study

For the field emission study, the synthesised samples (S1, S2, S3, S4 and S5) has been spin-coated on the silicon substrate. First, $La_xNd_{1-x}B_6$ dispersion has been made by ultrasonication of 50 mg of as synthesised powder in 2 ml mixture of ethanol and ethylene glycol. The as-prepared dispersion has been dropped on the silicon substrate and spin-coated. $La_xNd_{1-x}B_6$ coated samples were annealed in argon at 200 ℃ with 50 ℃/h heating rate. To the best of our knowledge, the *in-situ* synthesis of $La_xNd_{1-x}B_6$ nanorods has been done only by CVD route using BCl_3 as boron precursor.[22] However, in the present thesis, for the first time $La_xNd_{1-x}B_6$ film fabrication has been shown by the conventional spin-coating method. AFM micrograph of S1, S2, S3, S4 and S5 indicates that the nanorods are oriented vertically over the Si- substrate (Figure 4.7a-e).

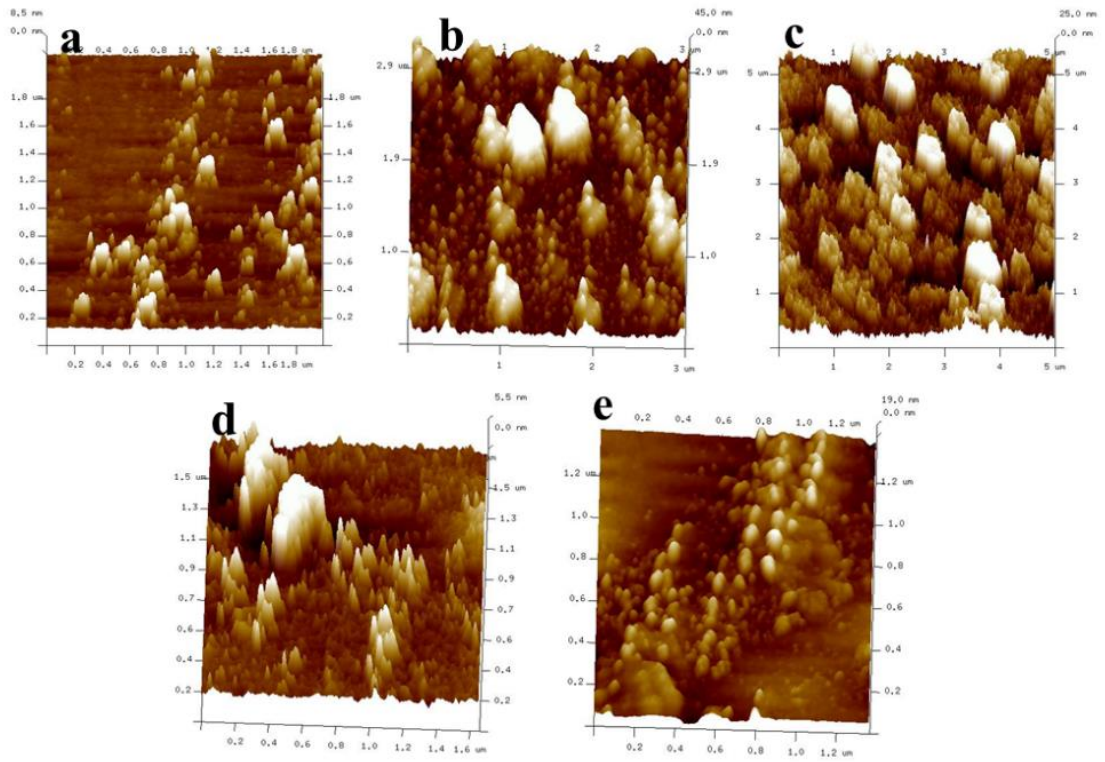

Figure 4.7. *Tapping mode atomic force microscopy of (a) S1. (b) S2. (c) S3. (d) S4. and (e) S5.*

The field emission study of S1, S2, S3, S4 and S5 sample have been performed using a field emission setup. The separation between the cathode (our samples) and anode (steel) was 300 μm with a high vacuum (~10^7 mbar). A diagram of device structures for the field emission has been shown in Figure 4.8. For the interpretation of field emission properties of $La_xNd_{1-x}B_6$ film, F-N equation has been used.[26] In the F-N equation, the current density (J) can be defined as:

$$J = \frac{A\beta^2 E^2}{\varphi} \exp\left(-\frac{B\varphi^{\frac{3}{2}}}{\beta E}\right) \quad 4.1$$

$$ln\frac{J}{E^2} = \ln\frac{A\beta^2}{\varphi} - \frac{B\varphi^{\frac{3}{2}}}{\beta E} \quad 4.2$$

Where A= 1.54 X 10^{-6} eVV^{-2}, B= 6.83 X 10^3 $VeV^{\frac{3}{2}}\mu m^{-1}$ J is current density, β is field enhancement factor, E is applied field and φ is the work function of emitting materials.

The J-E measurement of prepared cathode materials $La_xNd_{1-x}B_6$ (S1, S2, S3, S4 and S5) has been shown in Figure 4.8a. Figure 4.8a-e indicates that the current density vs applied electric field plot between the cathode and anode. The current density abruptly increases for sample S1, S2, S3, S4 and S5 after a certain field. The turn field in the present work is defined as the value of an applied field when the current density of $La_xNd_{1-x}B_6$ film reached

4 μA/cm^2. The observed turn-on field for S2, S3, S4 and S5 are 5.0, 3.6, 5.6 and 5.3 V/μm respectively (Figure 4.8b-e). It is worth to mention that there are only one reports for the field emission of $La_xNd_{1-x}B_6$.[22] The F-N plot (ln(J/E^2) vs 1/E) has been shown in the high electric field region, which gives a straight line with a negative slope, suggest that the emission current is due to the applied electric field (Figure 4.9).

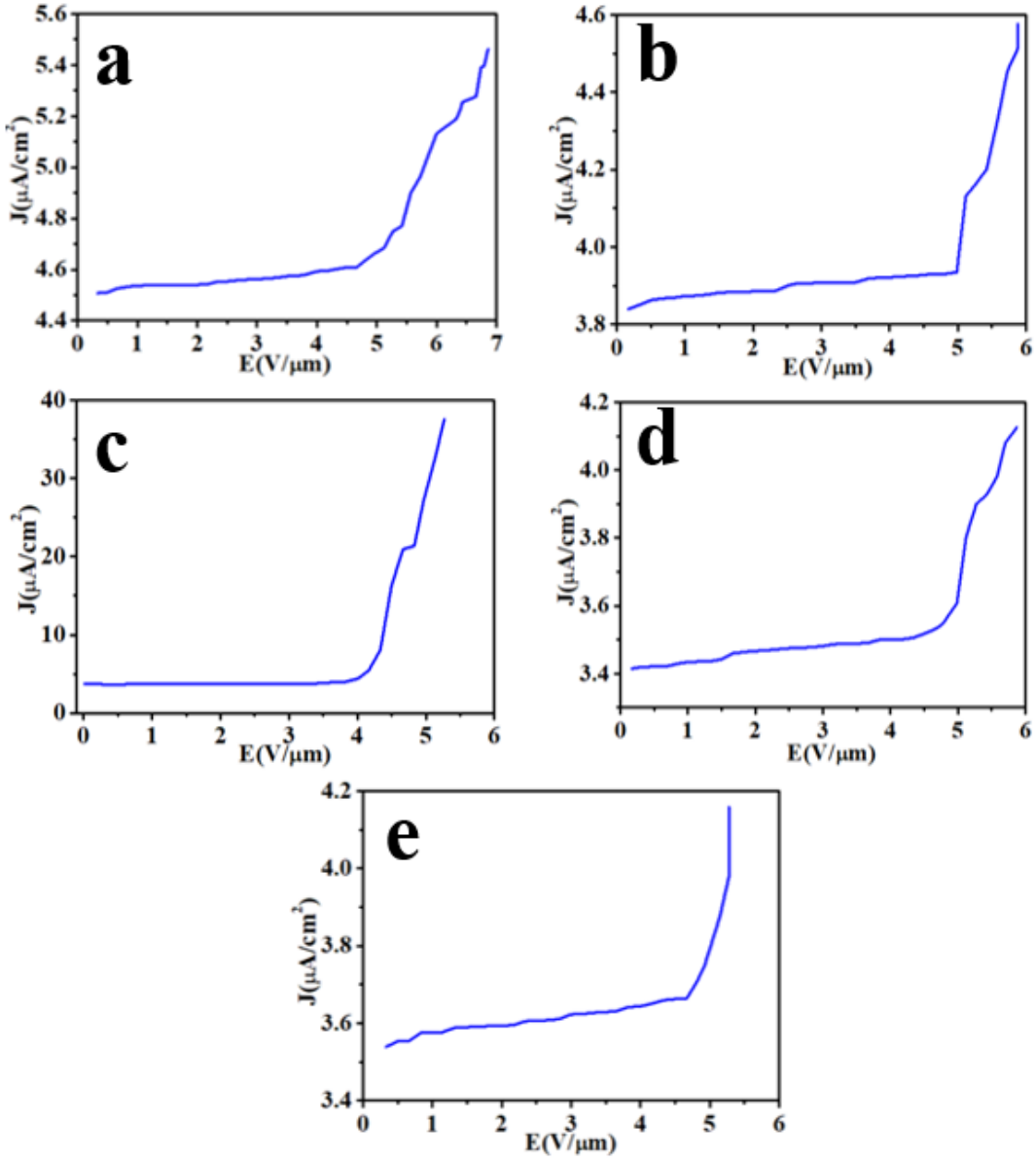

Figure 4.8. *Current density to applied potential (a) S1. (b) S2. (c) S3. (d) S4. and (e) S5.*

The linear behaviour in F-N plot shows the tunnelling mechanism of electric current from cathode to anode in the presence of an electric field. The FN-plot data for S1, S2, S3, S4 and S3 were fitted with a straight line, which gives the slope of -8.83, -7.36, -5.61, -7.12 and -7.92 respectively (Figure 4.9a-e).

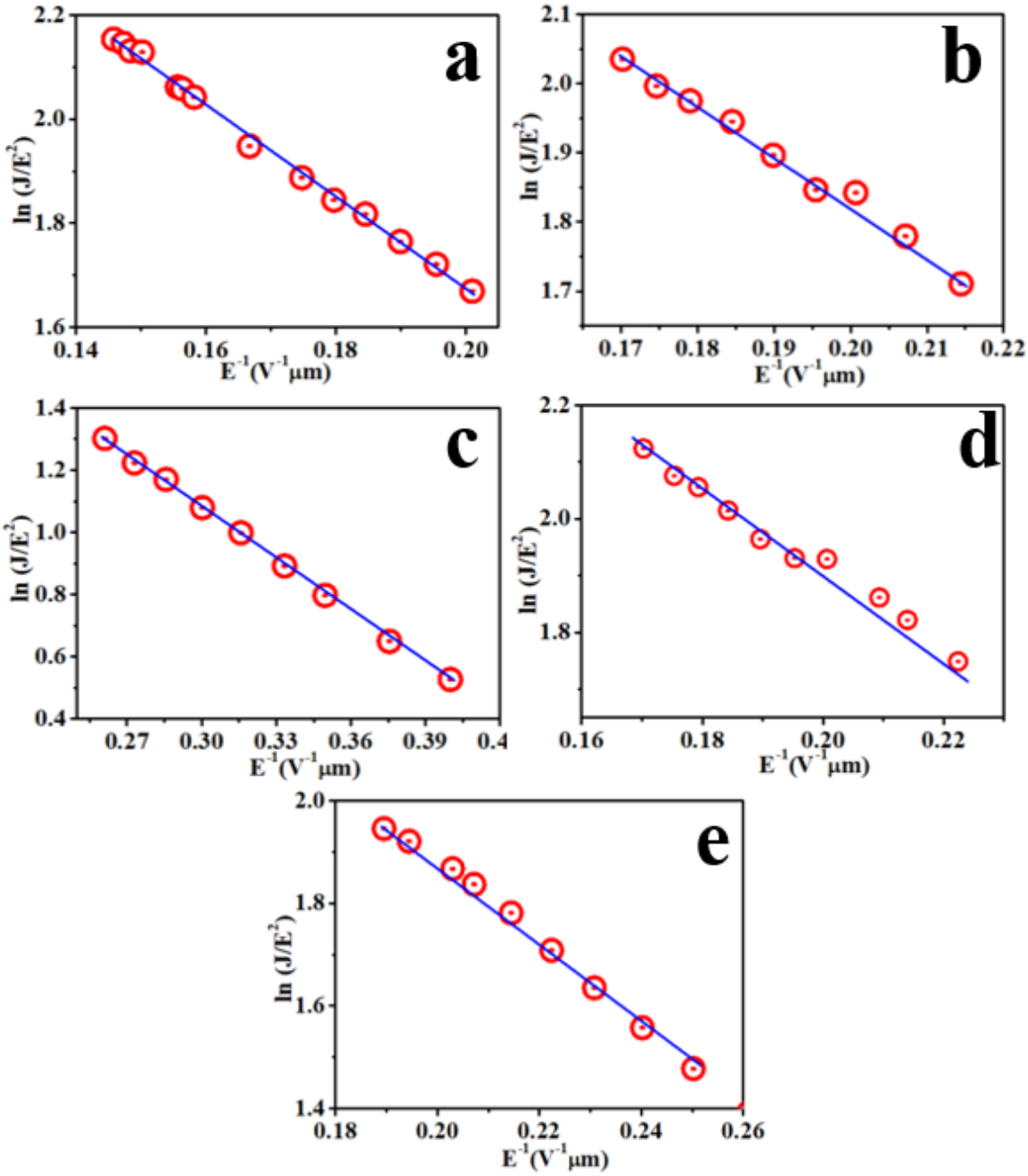

Figure 4.9. *F-N plot (a) S1. (b) S2. (c) S3. (d) S4. and (e) S5.*

Further, the field enhancement factor (β) can be calculated from F-N equation, by evaluating β as - $B\phi^{3/2}$/slope, where B is constant with values 6.83 X 10^3 $VeV^{-3/2,}$ and ϕ is the work function of cathode materials. The obtained β value for samples S1, S2, S3, S4 and S5 are 1556, 1878, 2459, 1937 and 1738 respectively. From the above results, it has been observed that S3 has the lowest turn-on field with the highest enhancement fact. Earlier, Xiaokun Yuan *et.al.* reported the less than 1 µm grain size of $La_{0.67}Nd_{0.33}B_6$ synthesised via the spark plasma sintering.[23] It may be noted that in the present thesis, the length of the synthesised nanorods is around 100-300 nm and diameter is around 25-30 nm.

The lower diameter of sample S3 is the possible reason for the higher enhancement factor. In the present work, anisotropic rare earth hexaboride ($La_xNd_{1-x}B_6$) has been synthesized and explored the next-generation field emitter properties.

4.3.2 Thermal stability of $La_{0.3}Nd_{0.57}B_6$ nanorods

The oxidation of $La_xNd_{1-x}B_6$ at higher temperature could lower the emission properties. Therefore, air oxidation of $La_xNd_{1-x}B_6$ has been done via a high-temperature X-ray diffraction study. The high-temperature PXRD study of $La_{0.3}Nd_{0.7}B_6$ nanorods has been done at 25 ℃, 200 ℃, 400 ℃, 600 ℃ and 800 ℃ at atmospheric condition (in the air) with the heating rate 10 ℃/h. It has been observed that all the diffraction peaks of samples up to temperature 400 ℃ matched with cubic NdB_6 of JCPDS no. 03-065-1828 (Figure 4.10a-b).

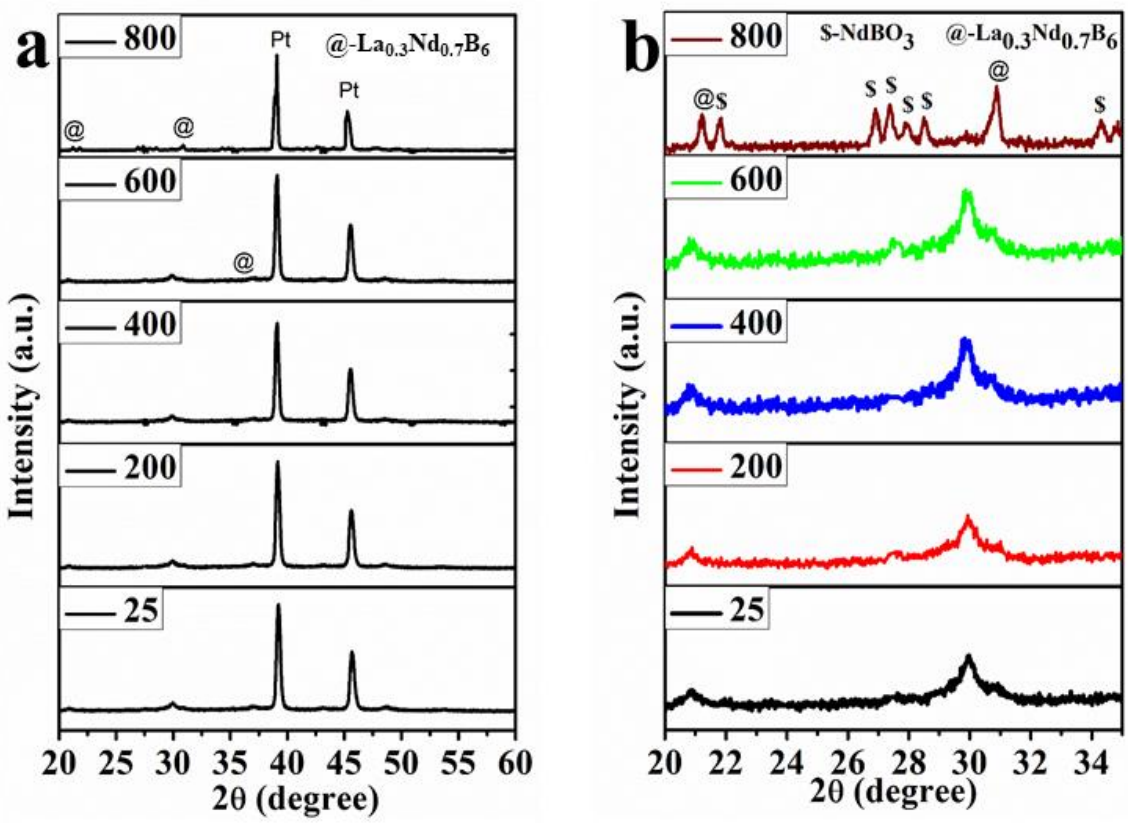

Figure 4.10. *(a) High-temperature XRD of GdB_6 nanorods. (b) Zoom view of HT-XRD.*

Further, increasing in the temperature results in some additional peaks which correspond to neodymium borate. The high-intensity diffraction peaks around the Bragg's position 39.09 and 45.62 are matched with platinum, which was utilized as a substrate for PXRD measurement (Figure 4.10a-b).

4.4 Conclusions

In the present work, synthesis of lanthanum doped neodymium hexaboride ($La_xNd_{1-x}B_6$) has been done for first-time via chemical route using $La_xNd_{1-x}(OH)_3$ precursor. $La_xNd_{1-x}(OH)_3$ [x=0.1,0.2, 0.3, 0.4 and 0.5] has been synthesised via a hydrothermal route at 120 ℃. The as-obtained $La_xNd_{1-x}(OH)_3$ mixed with $NaBH_4$ and annealed at the slow heating rate in the presence of an inert atmosphere to get the $La_xNd_{1-x}B_6$. Microstructural analysis of synthesised $La_xNd_{1-x}B_6$ has been done using TEM. The synthesised samples have been dropped on the copper grid for the TEM study. The TEM study reveals that the formation of nanorods of length ~100 nm and width ~25 nm for sample S1 and S3. Further, sample S2, S4 and S5 also show the formation of nanorods of 300 nm length and 30 nm. It has been observed that sample S3 ($La_{0.3}Nd_{0.7}B_6$) shows the highest enhancement factor (β=2459) with the lowest turn-on field (3.6 V/μm). The lowest turn-on field with the highest enhancement fact for S3 is due to the very thin width (25 nm -30 nm). Further, the air oxidation study via high-temperature X-ray shows that the $La_{0.3}Nd_{0.7}B_6$ nanorods will be stable up to 400 ℃ in the air. Further, this synthesis method can be extended to another family of complex rare earth hexaboride. The dual rare earth hexaboride can be used for field emitter as well as a photon detector.

4.5 References

1 M. M. Hasan, D. Cuskelly, H. Sugo and E. H. Kisi, *J. Alloys Compd.*, 2015, **636**, 67–72.

2 M. Jha, R. Patra, S. Ghosh and A. K. Ganguli, *Solid State Commun.*, 2013, **153**, 35–39.

3 M. Futamoto, M. Nakazawa and U. Kawabe, *Surf. Sci.*, 1980, **100**, 470–480.

4 V. T. Petrashov, R. S. Shaikhaidarov, I. A. Sosnin, P. Delsing, T. Claeson and A. Volkov, *Phys. Rev. B*, 1998, **58**, 15088–15093.

5 K. T. Narasimha, C. Ge, J. D. Fabbri, W. Clay, B. A. Tkachenko, A. A. Fokin, P. R. Schreiner, J. E. Dahl, R. M. K. Carlson, Z. X. Shen and N. A. Melosh, *Nat. Nanotechnol.*, 2016, **11**, 267–272.

6 S. Kim, M. Y. Lee, S. Lee and S. H. Jhi, *J. Phys. Condens. Matter*, 2017, **29**, 315702.

7 Q. Y. Zhang, J. Q. Xu, Y. M. Zhao, X. H. Ji and S. P. Lau, *Adv. Funct. Mater.*, 2009, **19**, 742–747.

8 J. Xu, G. Hou, T. Mori, H. Li, Y. Wang, Y. Chang, Y. Luo, B. Yu, Y. Ma and T. Zhai, *Adv. Funct. Mater.*, 2013, **23**, 5038–5048.

9 H. Zhang, Q. Zhang, G. Zhao, J. Tang, O. Zhou and L. C. Qin, *J. Am. Chem. Soc.*, 2005, **127**, 13120–13121.

10 M. A. Anisimov, A. V. Bogach, V. V. Glushkov, S. V. Demishev, N. A. Samarin, V. B. Filipov, N. Y. Shitsevalova, A. V. Levchenko, V. N. Gurin and N. E. Sluchanko, *Solid State Sci.*, 2012, **14**, 1601–1603.

11 V. G. Pol, S. V. Pol and A. Gedanken, *Adv. Mater.*, 2011, **23**, 1179–1190.

12 V. A. Petrosyan, *J. Contemp. Phys.*, 2011, **46**, 125–129.

13 G. Akopov, M. T. Yeung and R. B. Kaner, *Adv. Mater.*, 2017, **29**, 1604506-29.

14 C. H. Chen, T. Aizawa, N. Iyi, A. Sato and S. Otani, *J. Alloys Compd.*, 2004, **366**, 2003–2005.

15 R. K. Selvan, I. Genish, I. Perelshtein, J. M. Calderon Moreno and A. Gedanken, *J. Phys. Chem. C*, 2008, **112**, 1795–1802.

16 X. H. Ji, Q. Y. Zhang, J. Q. Xu and Y. M. Zhao, *Prog. Solid State Chem.*, 2011, **39**, 51–69.

17 H. Zhang, Q. Zhang, G. Zhao, J. Tang, O. Zhou and L. Qin, *J. Am. Chem. Soc.*, 2005, **127**, 13120–13121.

18 Z. C. Zhong, P. A. Dowben and D. J. Sellmyer, *Mater. Lett.*, 1998, **37**, 320–324.

19 M. Zhang, Y. Jia, G. Xu, P. Wang, X. Wang, S. Xiong, X. Wang and Y. Qian, *Eur. J. Inorg. Chem.*, 2010, **2010**, 1289–1294.

20 P. H. Schmidt and D. C. Joy, *J Vac Sci Technol*, 1978, **15**, 1809–1810.

21 Menaka, R. Patra, S. Ghosh and A. K. Ganguli, *J. Solid State Chem.*, 2012, **194**, 173–178.

22 Q. Li, H. Zhang, J. Chen, Y. Zhao, W. Han, Q. Fan, Z. Liang, X. Liu and Q. Kuang, *J. Mater. Chem. C*, 2015, **3**, 7476–7482.

23 X. Yuan, D. Zhang, S. Zhou, M. Yue, J. Zhang, J. Zhu, Q. Ma and Z. Wang, *CrystEngComm*, 2015, **17**, 4210–4217.

24 L.-H. Bao, J.-X. Zhang, N. Zhang, X.-N. Li and S.-L. Zhou, *Phys. Scr.*, 2012, **85**, 035710-6.

25 L. H. Bao, J. X. Zhang, S. L. Zhou and Tegus, *Chinese Phys. B*, 2011, **20**, 58101-7.

26 R. H. Fowler and L. Nordheim, *Proc. R. Soc. A Math. Phys. Eng. Sci.*, 1928, **119**, 173–181.

Chapter 5

Nanostructured lanthanum doped gadolinium hexaborides and their field emission properties

5.1 Introduction

Development of display devices and imaging tools in the scientific world requires the material having low work function, low bandgap, chemically and thermally stable, low cost as well as easy synthesis or production. Earlier, several materials such as reduced graphene oxide (rGO),[1] MoS_2,[2] MoO_2,[3], ZnO,[4] CuO,[5] Fe_2O_3,[6] boron-based materials,[7,8] investigated as a field emitter. The oxide-based emitter is quite good in terms of stability; however, due to large bang-gap, Joule heating (arises due to ohmic resistance) results in the poor practical application of the fabrication device. These shortcomings could be avoided by using rare-earth hexaboride as a field emitter. Earlier, LaB_6 is well-known cathode materials (field emitter) having work function 2.6 eV.[9,10] Apart from LaB_6, other rare-earth metal hexaborides such as CeB_6, NdB_6, GdB_6, PrB_6, and EuB_6 investigated for field emission study.[11–14] Theoretical study indicates materials having lower work function (<2 eV) could greatly enhanced field emission as well as thermionic emission.[15] The lowest reported work function in rare earth metal hexaborides is 1.5 eV for GdB_6. All the rare-earth hexaborides have CsCl type crystal structure. In this structure, the metal atoms presented at Cs site (centre of the cube) and boron at Cl site in octahedra fashion. In rare-earth hexaboride, 5 and 24 coordination number presented for boron and rare earth metal respectively.[16] The high conductivity in rare-earth hexaboride arises due to metallic bonding inside the rare-earth hexaboride; however, the covalent bond between B-B gives high stability such as high melting point, and high mechanical strength. The boron octahedra cage is electron deficient and thus electron move over low energy barrier from rare-earth hexaboride surface, which is terminated with rare-earth atoms. Apart from the field emission rare-earth hexaboride can also be used in modern application such as plasma/ion sources, optical coatings, thermionic converters, electron beam welders and free-electron lasers, sensors for photon detectors, electrical coatings for resistors, topological insulator, and used as an additive to improve the oxidation resistance of ZrB_2 based UHTCs.[17–20]

Rare earth hexaborides hold these interesting properties, which is strongly dependent on their morphology. However, their practical use is limited due to their complicated and costly synthesis technique. Earlier, rare earth hexaborides have been synthesised using floating zone method, solid-state reaction, autoclave, thermal evaporation, chemical vapour deposition (CVD), pulsed laser deposition (PLD), and selective area laser-induced deposition.[21–26] It is worth to mention that the rod-like structures can greatly enhance the field emission properties. In all the method, only the

CVD approach leads to the formation of anisotropic structure. However, the toxicity of the boron precursors used in the CVD process (BCl_3 or B_2H_6) is toxic as well costly, which make this method non-favourable for rare earth hexaboride synthesis. As mention above that low work function (>2 eV) can enhance the emission properties. It was reported that lanthanum doping could reduce the work function of rare-earth hexaboride.[27] Therefore, in the present study, lanthanum doped gadolinium hexaboride has been synthesized via solid-state borothermal reduction. Only a few studies have been done earlier for the lanthanum doped rare-earth hexaboride such as $La_xCe_{1-x}B_6$, $La_xBa_{1-x}B_6$, $Nd_xGd_{1-x}B_6$, $La_{0.67}Nd_{0.33}B_6$.[28–33] Earlier, there are only one reports for the synthesis of $La_xGd_{1-x}B_6$ via spark plasma sintering (SPS) technique at 1450 ℃, which was bulk in nature.[33] However, in the present study, first lanthanum doped gadolinium hydroxide [$La_xGd_{1-x}(OH)_3$] has been synthesised via hydrothermal route. The as-prepared $La_xGd_{1-x}(OH)_3$ mixed with $NaBH_4$ and annealed in an argon atmosphere to get the $La_xGd_{1-x}B_6$. Further, as obtained $La_xGd_{1-x}B_6$ fabricated over silicon substrate via spin coating method for the study of field emission.

5.2 Experimental

5.2.1 Materials

Gadolinium nitrate ($Gd(NO_3)_3.xH_2O$, 99.9 %, CDH India), Lanthanum nitrate [$La(NO_3)_3.xH_2O$, 99.99 %, CDH India], Triton™ X-100 (Sigma- Aldrich), acetone (C_3H_6O, Merck, 99 %), Hydrochloric Acid (HCl, 99 %, Merck) and Sodium borohydride ($NaBH_4$, 99.99 %, CDH India) were used for the synthesis of lanthanum doped gadolinium hexaboride. All the chemicals were used as received without any further purification.

5.2.2 Synthesis of $La_xGd_{1-x}(OH)_3$ (x= 0.1, 0.2, 0.3, 0.4 and 0.5)

For the synthesis of $La_xGd_{1-x}B_6$, $La_xGd_{1-x}(OH)_3$ (x= 0.1, 0.2, 0.3, 0.4 and 0.50 has been synthesis as precursors of La and Gd ions using the hydrothermal method. Here the procedure of synthesis of $La_{0.1}Gd_{0.9}(OH)_3$ has been described, and the other ratio can be synthesized using the same protocol using Table 5.1. In a typical synthesis, 0.1 M aqueous of $La(NO_3)_3.xH_2O$ (7 ml) mixed with and 0.1 M aqueous $Gd(NO_3)_3.xH_2O$ (63 ml) followed by stirring. To the above solution mixture, 3.5 ml TX-100 (5 % of total volume) was added. Further, 0.3 M of NaOH solution has been prepared in 70 ml DI water, which contains 3.5 ml TX-100 (5 % of total volume). The as-prepared 0.3 M NaOH solution has been added to the mixture of lanthanum and gadolinium and stirred for 1 h at room temperature. The as-prepared mixture transferred to 200 ml hydrothermal vessel and heated at 120 ℃ for 24

h and allowed to cool naturally. The as-obtained solution after hydrothermal treatment was washed and centrifuged with methanol, followed by drying at 70 ℃. The as-obtained sample is further used for the characterization. Further, the other composition of $La_xGd_{1-x}(OH)_3$ (x=0.2, 0.3, 0.4 and 0.5) could be synthesized in the same manner by utilizing the required amount of lanthanum and gadolinium salt solution (Table 5.1).

Table 5.1. Amount of rare-earth salt concentration for the synthesis of $La_xGd_{1-x}(OH)_3$

0.1 M Lanthanum Amount (ml)	0.1 M Gadolinium Amount (ml)	Rare earth metal hydroxide precursors	Metal hydroxide to $NaBH_4$ ratio	Hexaboride Name (sample code)
7	63	$La_{0.1}Gd_{0.9}(OH)_3$	1:30	$La_{0.1}Gd_{0.9}B_6$ (S1)
14	56	$La_{0.2}Gd_{0.8}(OH)_3$	1:30	$La_{0.2}Gd_{0.8}B_6$ (S2)
21	49	$La_{0.3}Gd_{0.7}(OH)_3$	1:30	$La_{0.3}Gd_{0.7}B_6$ (S3)
28	42	$La_{0.4}Gd_{0.6}(OH)_3$	1:30	$La_{0.4}Gd_{0.6}B_6$ (S4)
35	35	$La_{0.5}Gd_{0.5}(OH)_3$	1:30	$La_{0.5}Gd_{0.5}B_6$ (S5)

5.2.3 Synthesis of lanthanum doped gadolinium hexaboride

The as-synthesised $La_xGd_{1-x}(OH)_3$ hand grinded in a mortar and pestle with $NaBH_4$ in 1:30 weight ratio in presence of acetone to get a homogeneous distribution of precursors. The hand grinded precursors then placed in a recrystallized alumina boat and transferred into a horizontal tube furnace and annealed in an argon atmosphere at 1000 ℃ with 50 ℃/h heating rate. After completion of the reaction, the as-obtained samples have been washed with dilute HCl (1:1 V: V of HCl and H_2O) followed by washing with water and acetone and vacuum dried at 70 ℃. The synthesised sample used for the field emission application.

5.2.4 Silicon substrate cleaning method

The RCA cleaning procedure has been adopted for the cleaning of the Si- substrate, which has been used for the field emission study. The RCA procedure has been developed by Werner Kern. was used to prepare the film was cleaned by standard RCA (Radio Corporation of America) method, which was firstly developed by Werner Kern.

For cleaning Si-substrate, small pieces of substrates were immersed in acetone (heated at 50 ℃) and after 30 min, Si-substrate has been cleaned with water followed by isopropanol. During the acetone heating, around 10-20 % of acetone has been evaporated due to the low boiling point (56 ℃) of the acetone. In the second step, the substrate was treated with piranha solution for 10 min. Further, the cleaned substrates were cleaned with

5 % HF solution to remove native oxides followed by rinsing with water. The cleaned substrate again washed isopropyl alcohol followed by drying in a vacuum desiccator.

5.2.5 Fabrication of $La_xGd_{1-x}B_6$ Film

For the preparation of rare earth hexaboride dispersion, 50 mg of as-synthesized powder (S1, S2, S3, S4 and S5) was mixed with 2 ml (1: 1) of ethanol and ethylene glycol mixture (V: V ratio) using ultrasonication. The resulting dispersion was spin-coated on the cleaned Si- substrate at a speed of 3000 rpm for 60 seconds. The process of the spin-coating was repeated four times to get the homogeneous and uniform film. A typical view of spin coater (Figure 5.1).

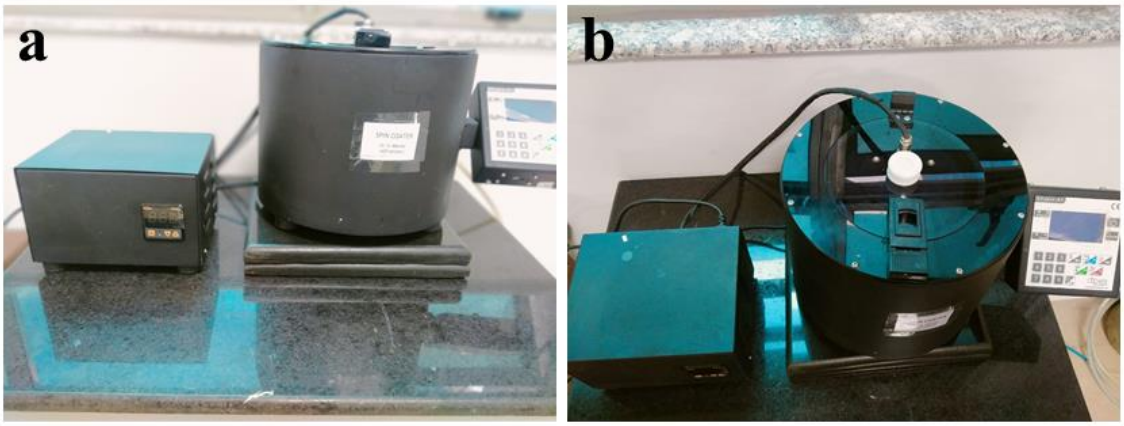

Figure 5.1. *(a) Font view of spin coating. (b) above view of a spin coater.*

5.3 Results and discussion

In the present study, first-time $La_xGd_{1-x}B_6$ has been synthesized using a solid-state borothermal reduction route in the presence of an argon atmosphere. The present work involves three-step. In the first step, $La_xGd_{1-x}(OH)_3$ has been synthesized using the hydrothermal route at 120 ℃. In the second step, synthesized $La_xGd_{1-x}(OH)_3$ annealed with $NaBH_4$ at a slow heating rate, which leads to the synthesis of $La_xGd_{1-x}B_6$. In the final step, the dispersion of synthesized $La_xGd_{1-x}B_6$ has been made in the solution of ethanol and ethylene glycol mixture, which was further deposited on a silicon substrate via spin coating followed by slow heating in argon for the preparation of $La_xGd_{1-x}B_6$ film.

The powder X-diffraction pattern of samples obtained after the hydrothermal route was matched with the JCPDS card number 01-083-2037 (Figure 5.2a). All the observed diffraction peaks matched with hexagonal crystal structure having P63/m (176) space group of $Gd(OH)_3$. A close observation of the highest intense diffraction peak reveals that there is a shift in the peak when the lanthanum concentration increases from x=0.1 to 0.5 (Figure

5.2b). It was observed that as the concentration of lanthanum ions increases forms x=0.1 to 0.3, there is a shift in peak position towards the lower angle, which suggests the doping of lanthanum at the site of gadolinium in $Gd(OH)_3$ in their hexagonal crystal structure. It is a well-stabilized fact that as the larger radius particles being doped in the smaller radius particles, there will be a shift in peak position towards lower angle due to compressive stress.[29]

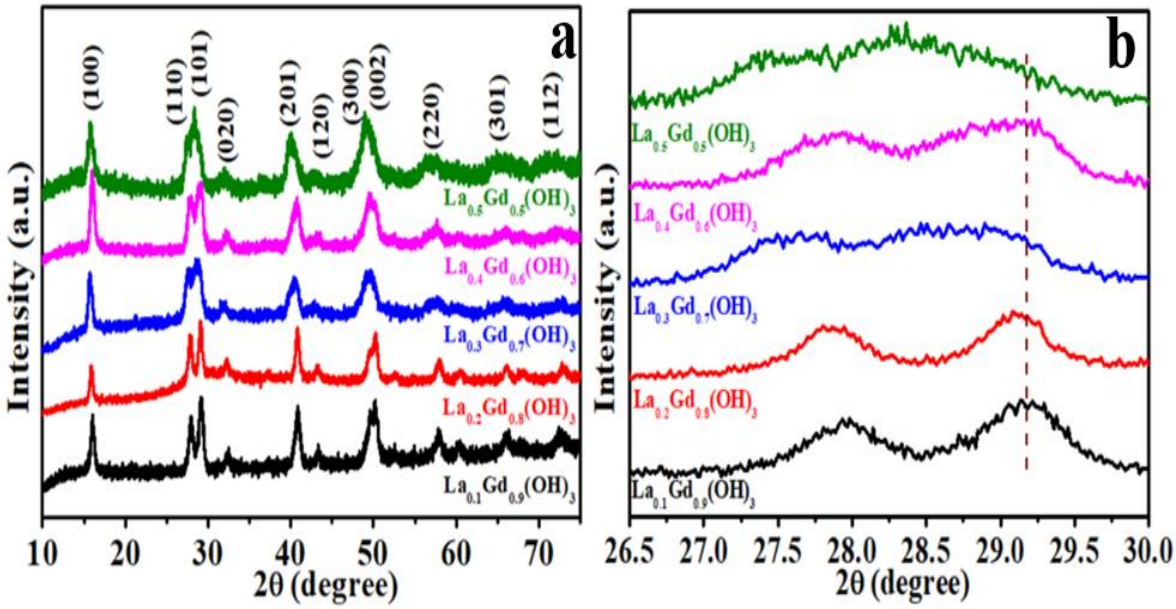

Figure 5.2. *(a) Powder X-ray diffraction of $La_xGd_{1-x}(OH)_3$, where x=0.1, 0.2, 0.3, 0.4 and 0.5. (b) Zoom view of (110) and (101) peaks.*

The microstructure analysis of synthesised samples has been carried out using TEM. It was observed that there is the formation of nanorods of average breadth around 10-13 nm with a length of 105-130 nm (Figure 5.3a-e). High-resolution transmission electron micrographs of $La_xGd_{1-x}(OH)_3$ corresponding to the orientation of (101) plane with an interplanar d spacing of ~3.04 Å (Figure 5.3f-j). The selected area electron diffraction pattern has been carried out, which confirms the polycrystalline nature of the synthesised $La_xGd_{1-x}(OH)_3$ samples (Figure 5.3k-o). Further, the doping concentration of lanthanum has been confirmed from the TEM-EDX study (Figure 5.4). The EDX spectra show the presence of only La, Gd and O peaks, which confirms the high purity of the synthesised sample (Figure 5.4).

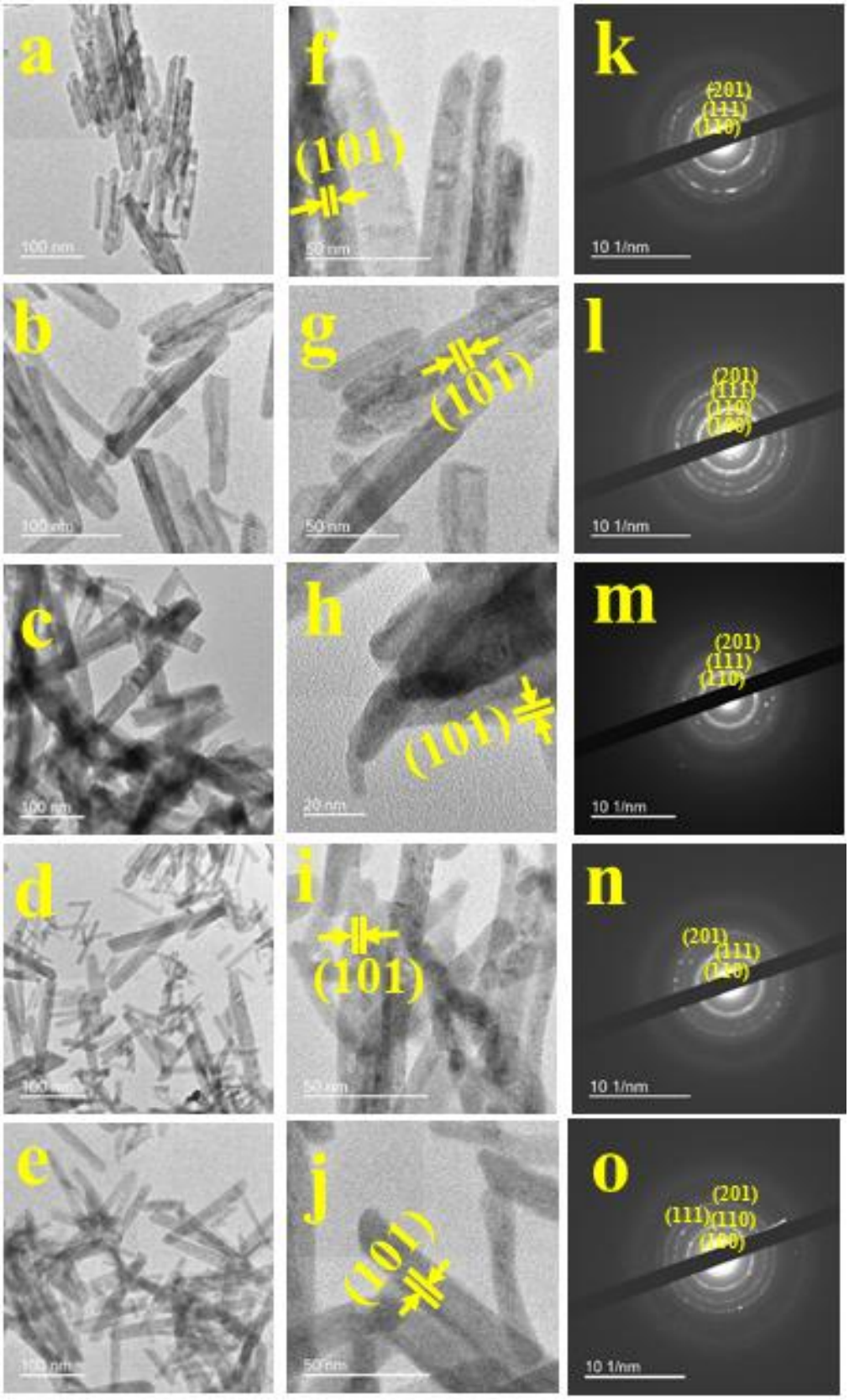

Figure 5.3. *TEM micrographs of, (a)$La_{0.1}Gd_{0.9}(OH)_3$. (b) $La_{0.2}Gd_{0.8}(OH)_3$. (c) $La_{0.3}Gd_{0.7}(OH)_3$. (d) $La_{0.4}Gd_{0.6}(OH)_3$. (e) $La_{0.5}Gd_{0.5}(OH)_3$. (f-g) corresponding HRTEM. (k-o) corresponding selected area diffraction pattern.*

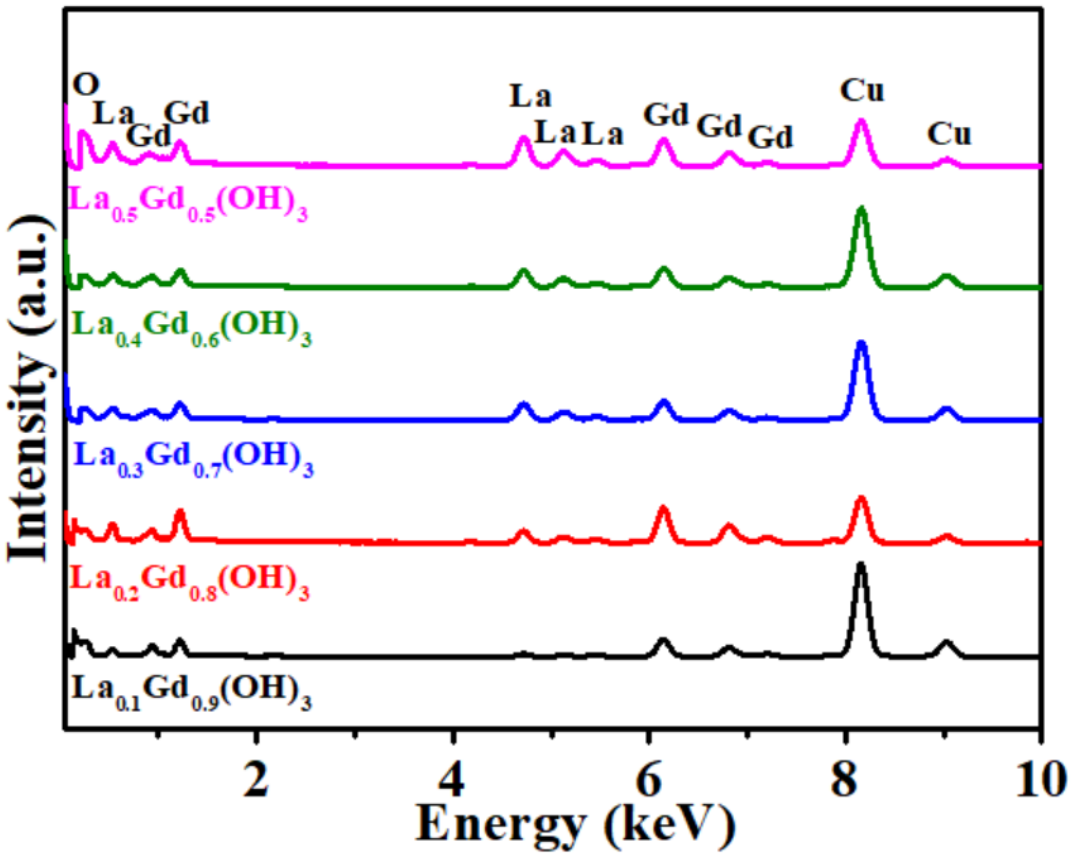

Figure 5.4. *TEM-EDX of various concentration of $La_xGd_{1-x}(OH)_3$ (X=0.1, 0.2, 0.3, 0.4 and 0.5).*

For the synthesis of $La_xGd_{1-x}B_6$, the synthesised $La_xGd_{1-x}(OH)_3$ was mixed with sodium borohydride and annealed (see details in the experimental section). The PXRD result of as-prepared samples of different doping concentration has been shown in Figure 5.5. The PXRD pattern of all the samples (S1, S2, S3, S4 and S5) has been matched with the JCPDS card no 03-065-1826 of cubic GdB_6 having space group $Pm\bar{3}m$, however; it was observed that there is peak shifting when lanthanum concentration exceeded than x=0.3 in $La_xGd_{1-x}B_6$ (Figure 5.5b). The microstructure of all the synthesised samples has been carried out using TEM. TEM study reveals that the formation of nanorods in all the composition of $La_xGd_{1-x}B_6$.

The width of the synthesised samples (S1, S2, S3, S4 and S5) are 30-40 nm. However, the length of samples S1, S3 and S4 have 130 nm and 300 nm for S2 and S5 respectively (Figure 5.6a-e). Further, the HRTEM of as-prepared samples suggest the d spacing of ~0.291 Å corresponds to (110) plane (Figure 5.6f-j). Further, the EDX study of synthesised samples has been performed and found that the final concentration of rare-earth metals has been in good agreement with the loaded amount and the ratio of La to Gd has

been given in **Table 5.2**. The atomic present ratio of La to Gd are 1:8.98, 2:7.94, 3:6.94, 4:5.92 and 5:4.97 for S1, S2, S3, S4 and S5, which is almost similar to the loaded composition.

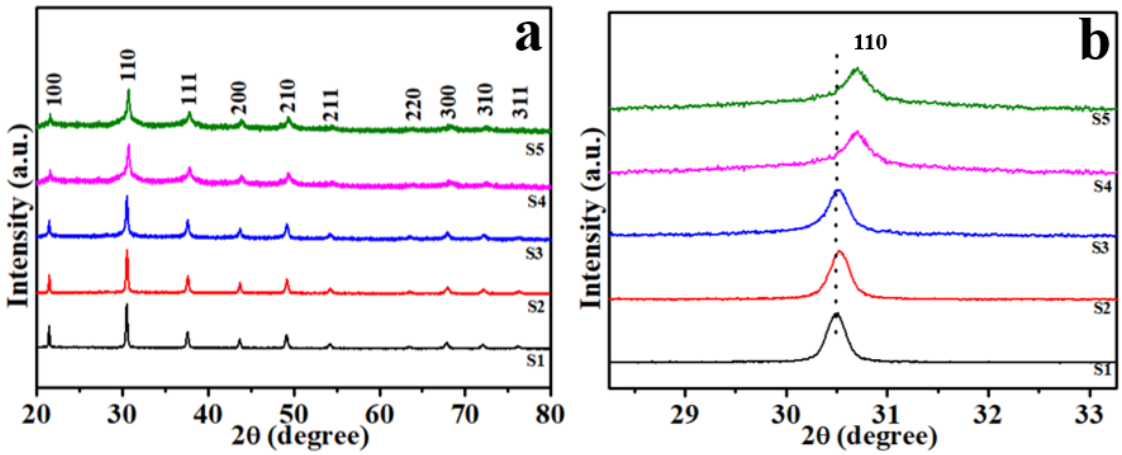

Figure 5.5. *(a) Powder X-ray diffraction of $La_xGd_{1-x}B_6$, where x=0.1, 0.2, 0.3, 0.4 and 0.5. (b) Zoom view of (110) plane.*

The surface properties of the fabricated film (S1, S2, S3, S4 and S5) were investigated using tapping mode AFM studies. The AFM study indicates that the particles are uniformly distributed over the substrate (Figure 5.7a-b). To the best of our knowledge, there are no reports available for vertically aligned nanorods for $La_xGd_{1-x}B_6$. It has been known that vertically oriented nanorods show better field emission properties compared to randomly oriented nanorods.

Table 5.2. Atomic percentage of lanthanum doped gadolinium hexaborides

Sample	Ratio of La:Gd
$La_{0.1}Gd_{0.9}B_6$	1:8.98
$La_{0.2}Gd_{0.8}B_6$	2:7.94
$La_{0.3}Gd_{0.7}B_6$	3:6.94
$La_{0.4}Gd_{0.6}B_6$	4:5.92
$La_{0.5}Gd_{0.5}B_6$	5:4.97

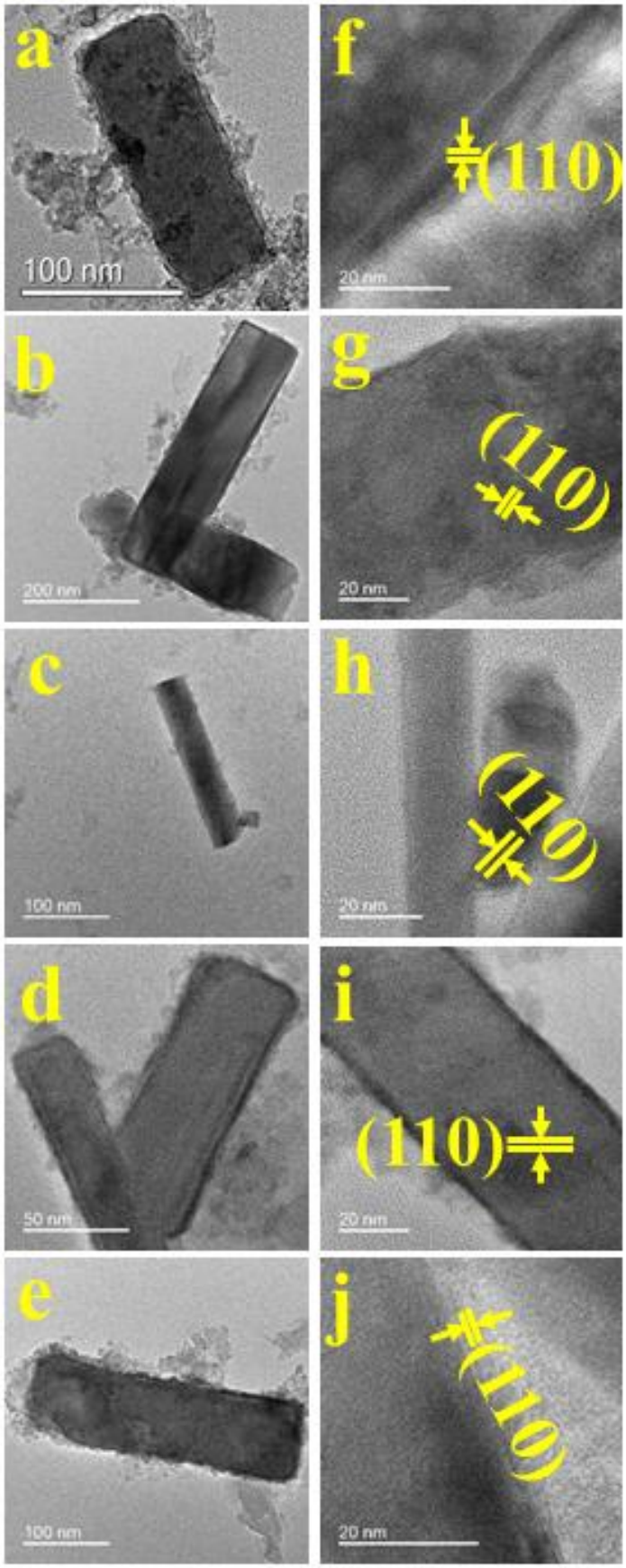

Figure 5.6. *TEM micrographs of $La_xGd_{1-x}B_6$, (a) S1. (b) S2. (c) S3. (d) S4. (e) S5. (f-j) HRTEM of corresponding samples.*

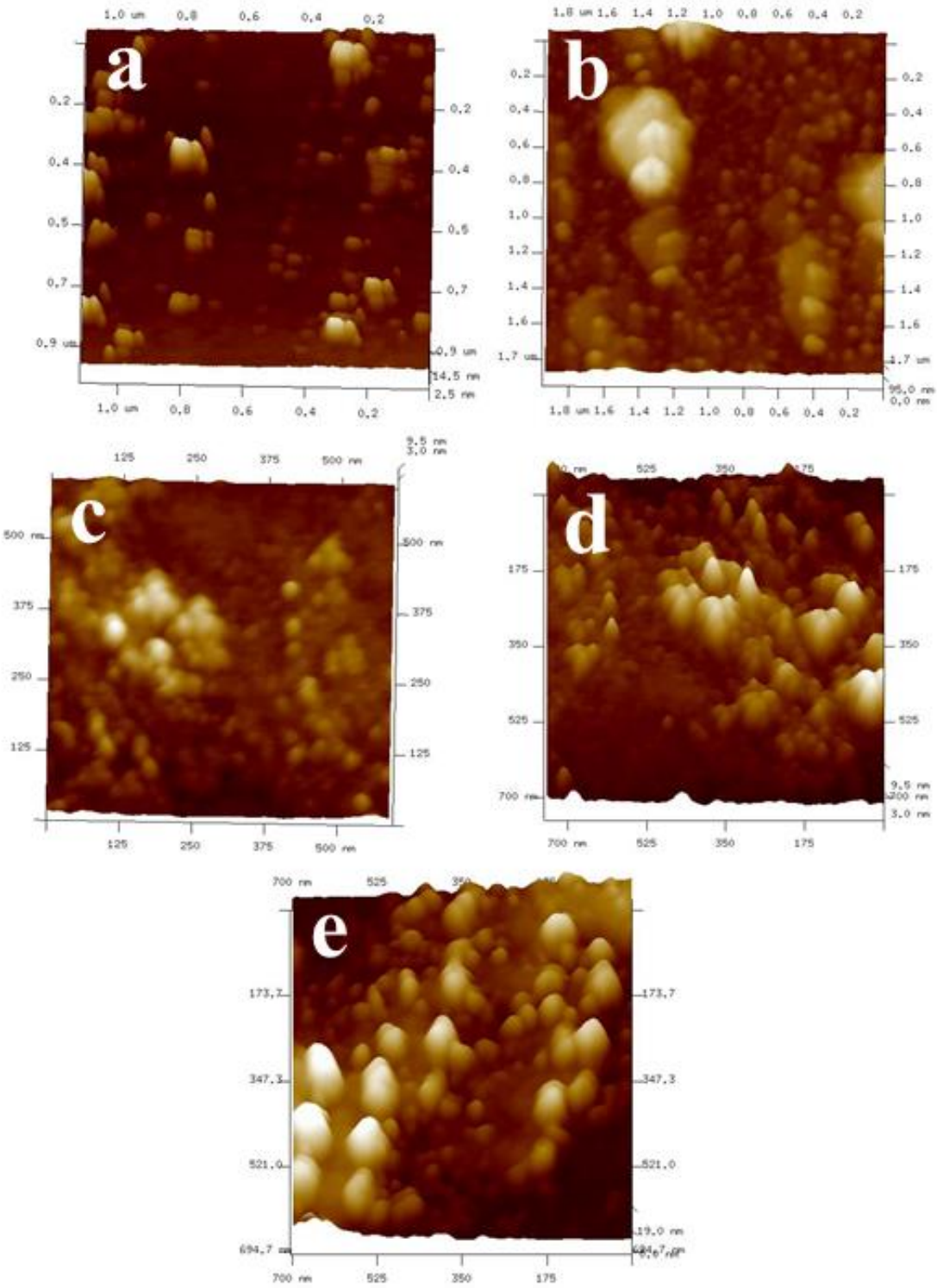

Figure 5.7. *AFM study of films of, (a) S1. (b) S2. (c) S3. (d) S4. (e) S5.*

5.3.1 Field emission study

For the field emission study, the synthesised samples (S1, S2, S3, S4 and S5) has been fabricated over silicon substrate via spin-coated followed by slow heating. $La_xGd_{1-x}B_6$ coated silicon substrate was annealed in argon at 200 ℃ with slow heating for the

evaporation of organic molecules. To the best of our knowledge, there is no report of the synthesis of anisotropic nanostructured $La_xGd_{1-x}B_6$. However, nanoparticles of $La_xGd_{1-x}B_6$ has been done using the spark plasma synthesis technique.[33] In field emission, ejection of electrons through quantum mechanical tunnelling from the metallic surface via applying a strong electric field. Fowler and Nordheim first time summarized the field emission phenomenon in the form of an equation, which is known as Fowler–Nordheim equation (F-N equation).[34] In the F-N equation, the current density (J) can be defined by following equations:

$$J = \frac{A\beta^2E^2}{\varphi}\exp\left(-\frac{B\varphi^{\frac{3}{2}}}{\beta E}\right) \quad 5.1$$

$$ln\frac{J}{E^2} = \ln\frac{A\beta^2}{\varphi} - \frac{B\varphi^{\frac{3}{2}}}{\beta E} \quad 5.2$$

Where A= 1.54 X $10^{-6}\, eVV^{-2}$, B= 6.83 X $10^3\, VeV^{\frac{3}{2}}\mu m^{-1}$

J is current density, β is field enhancement factor, E is applied field and φ is the work function of emitting materials. The J-E measurement of the fabricated cathode materials (S1, S2, S3, S4 and S5) on a silicon substrate has been shown in Figure 5.8. It has been observed that enhancement in the electric field leads to the enhancement in current density; however, at a certain field the current density increases rapidly (Figure 5.8a-e). The electric field where current density increases very rapidly defined as a turn-on field. The turn field for the sample S1, S2, S3, S4 and S5 are 5.02, 5.27, 4.51, 5.04 and 5.01 V/μm respectively (Figure 5.8a-e). The highest current density can be achieved for S5 sample, which is ~8.6 μA/cm^2. It is worth to mention that there are no reports for the field emission of $La_xGd_{1-x}B_6$.To confirm the emission is due to quantum mechanical tunnelling, the plot ln(J/E^2) against 1/E has been plotted (Figure 5.9). This plot is known as F-N plot and if the plot shows the negative slope with straight-line behaviour then the emission of electrons is due to field emission. The F-N plot for all the sample shows the straight-line behaviour confirming the tunnelling behaviour of electron emission (Figure 5.9).

The slop for S1, S2, S3, S4 and S3 are -8.10, -8.16, -8.23, -8.01 and -8.00 respectively (Figure 5.9a-e). Further, the electron enhancement factor (β) can be calculated from F-N equation, by evaluating β as - $B\phi^{3/2}$/slope, where B is constant with values 6.83 X 10^3 V $eV^{-3/2,}$ and ϕ is the work function of cathode materials (here $La_xGd_{1-x}B_6$ as cathode material). The obtained β value for samples S1, S2, S3, S4 and S5 are 1549, 1537, 1524, 1566 and 1568 respectively. It has been observed that sample S3 has the lowest turn-on field; however, at the same time shows the lowest enhancement fact (1524). The highest

current density for S5 sample might be due to the highest aspect ratio (~7-10) as compared to other samples. Earlier, reports indicates that 5-10 μm grain boundary of $La_xGd_{1-x}B_6$ (x = 0, 0.6, 0.8, 1).[33] In the present work, anisotropic rare earth hexaboride [$La_xGd_{1-x}B_6$, (x=0.1, 0.2, 0.3, 0.4, 0.5)] has been synthesized and explored the next-generation field emitter properties.

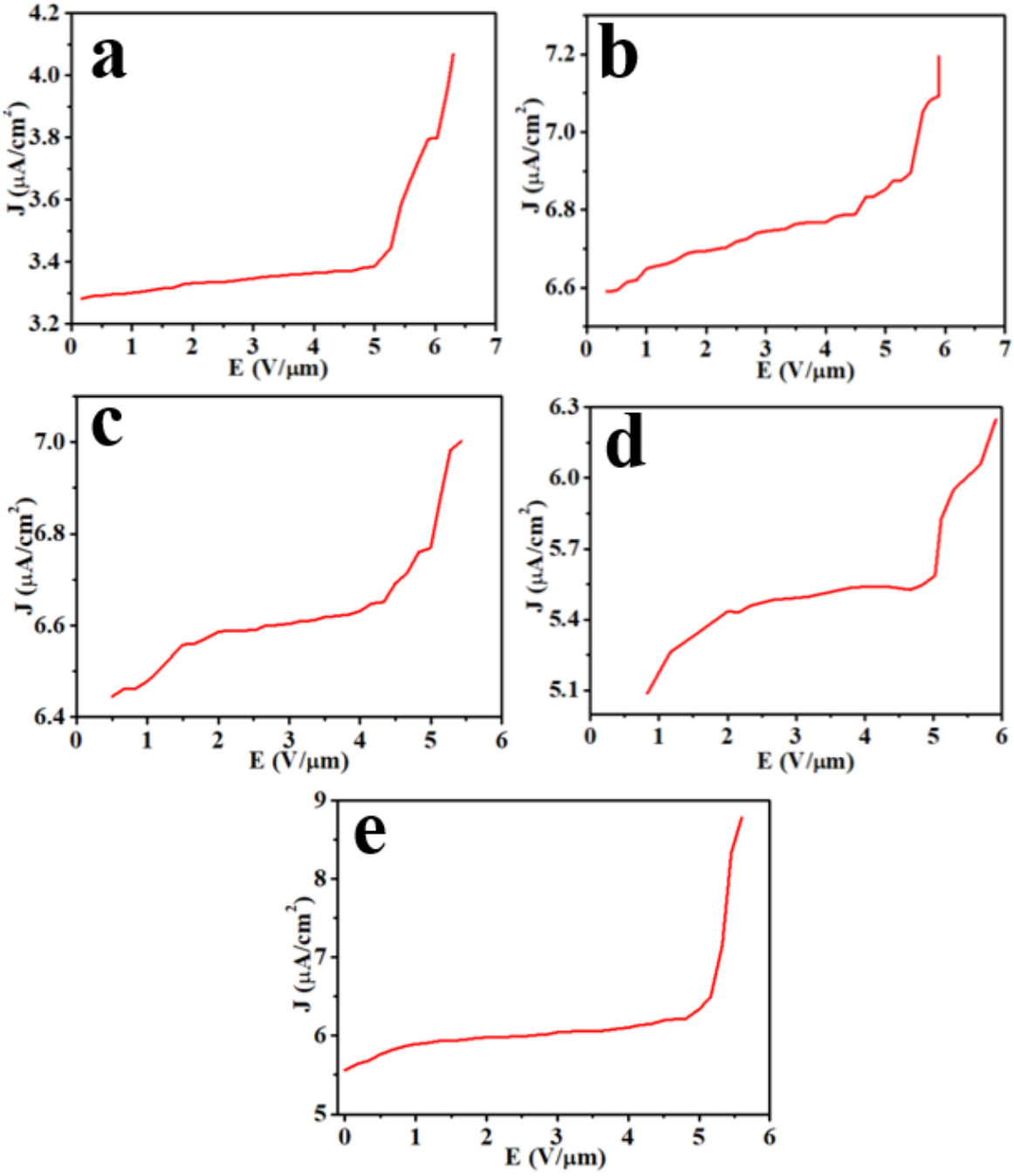

Figure 5.8. *Current density to applied potential (a) S1. (b) S2. (c) S3. (d) S4. and (e) S5.*

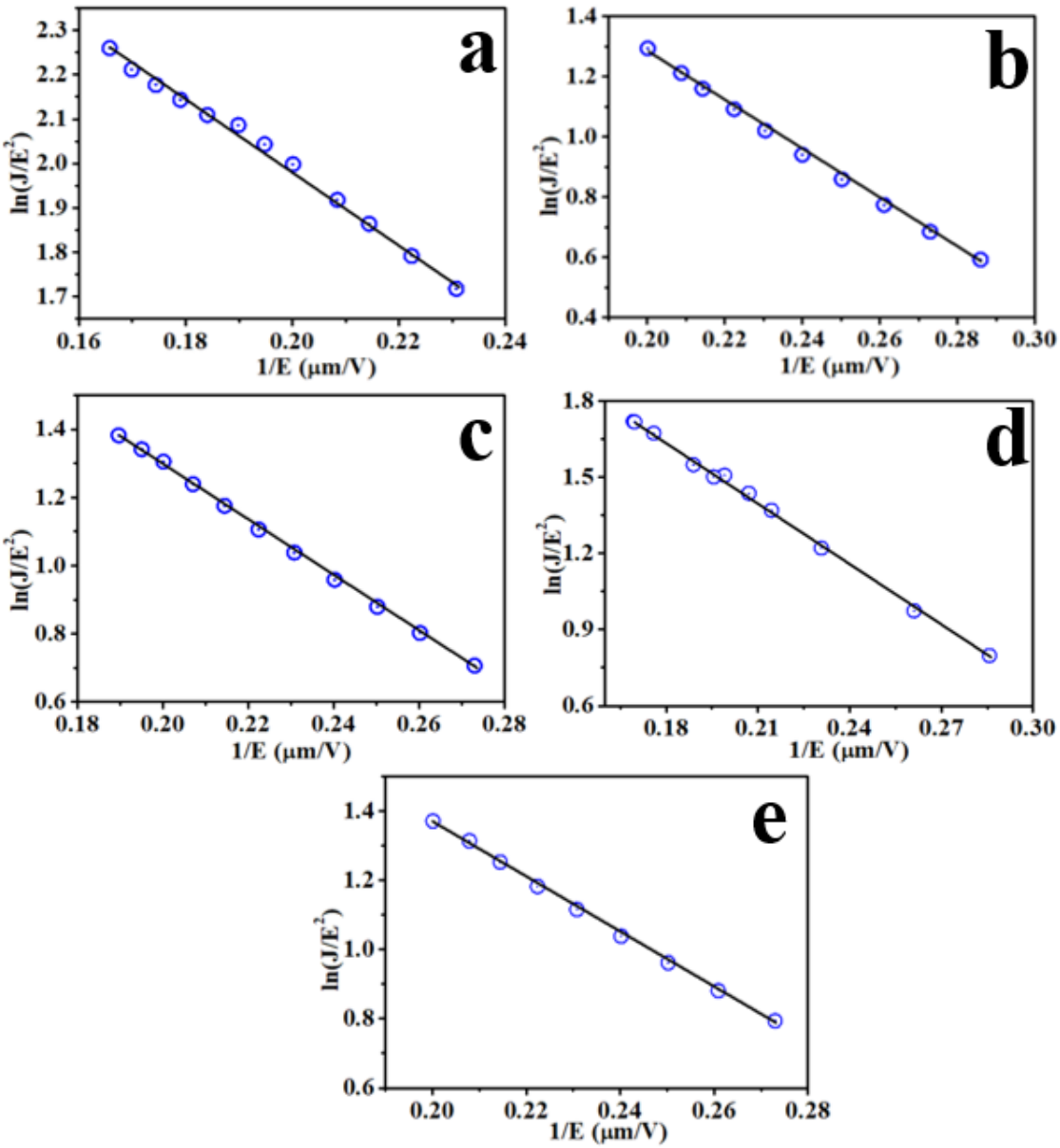

Figure 5.9. *F-N plot of (a) S1. (b) S2. (c) S3. (d) S4 and (e) S5.*

5.3.2 Thermal stability of synthesised $La_xGd_{1-x}B_6$ nanorods

It is well known that during the emission process, the local temperature increases, which may cause damage to the emitter due to the degradation of source materials. Therefore, the high-temperature PXRD study at various temperature (room temperature, 200 ℃, 400 ℃, 600 ℃, 800 ℃) used to investigate the effect of temperature in air. Oxidation study of sample S5 ($La_{0.5}Gd_{0.5}B_6$ nanorods) has been investigated up to 800 ℃. It has been observed all the diffraction peaks appears upto 400 ℃ matched well with cubic GdB_6 (JCPDS no. 03-065-1826) and high-intensity peaks around Bragg's angle 39.09 and 45.62 matched with platinum, which was used as a substrate while PXRD measurement

(Figure 5.10a-b). Further, enhancement in temperature (600 ℃ and 800 ℃) leads to the formation of the corresponding metal borate by oxidation of $La_{0.5}Gd_{0.5}B_6$ (Figure 5.10a-b).

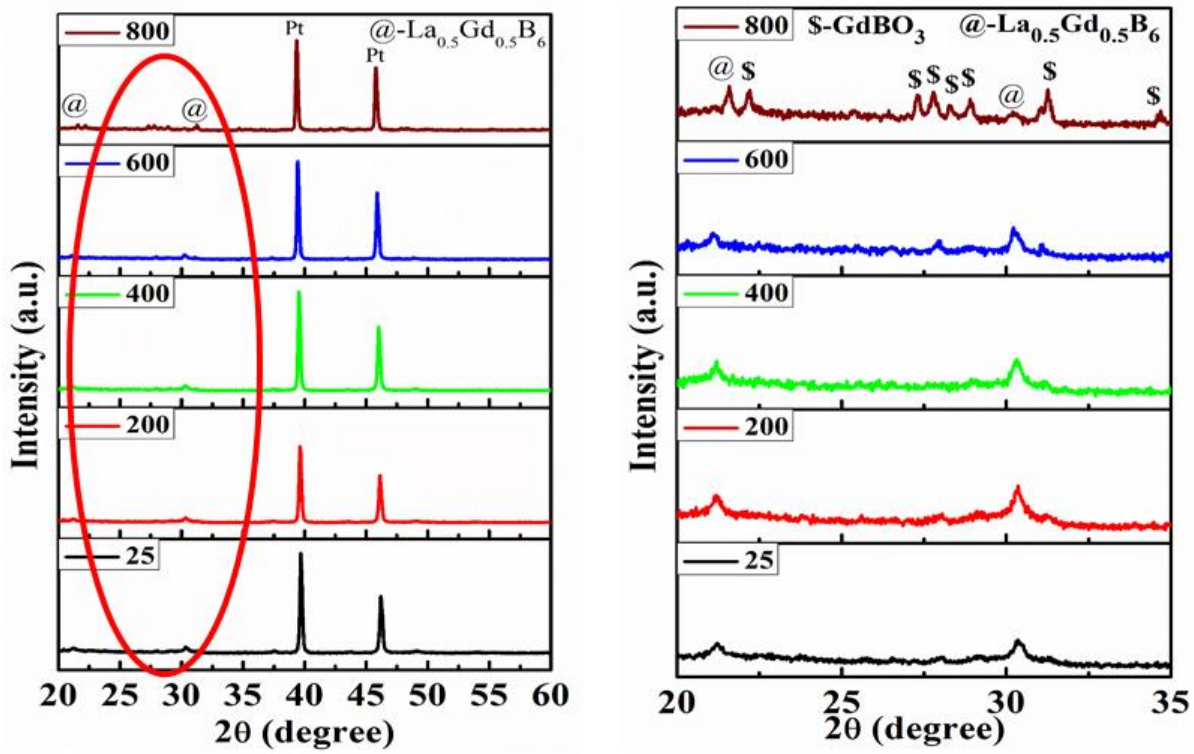

Figure 5.10. *HT-XRD of $La_{0.5}Gd_{0.5}B_6$ (sample S5). (a) S5. (b) zoom view of angle 20-35.*

5.4 Conclusions

In the present chapter, the synthesis of lanthanum doped gadolinium hexaboride has been done for the first-time via solid-state route. Initially, nanorods of $La_xGd_{1-x}(OH)_3$ [x=0.1, 0.2, 0.3, 0.4 and 0.5] has been synthesised via a hydrothermal route at 120 ℃. The microstructure analysis of synthesised $La_xGd_{1-x}(OH)_3$ shows the anisotropic structures of average width 10-13 nm with an average length of 105-130 nm. Further, the as-obtained $La_xGd_{1-x}(OH)_3$ anisotropic nanostructures mixed with $NaBH_4$ and annealed with the slow heating rate in the presence of inert atmosphere to get the $La_xGd_{1-x}B_6$. The powder X-ray diffraction study reveals the formation of $La_xGd_{1-x}B_6$. Further, TEM study shows the formation of nanorods of $La_xGd_{1-x}B_6$ (x=0.1, 0.2, 0.3, 0.4 and 0.5). The width of samples (S1, S2, S3, S4 and S5) are 30-40 nm. However, the length of samples S1, S3 and S4 have 130 nm and 300 nm for S2 and S5 respectively. The synthesised sample has been drop casted over the silicon substrate and used for field emission study. Field emission study reveals that $La_{0.3}Gd_{0.7}B_6$ shows the lowest turn-on filed (4.51 V/μm). The high-temperature XRD shows that $La_{0.5}Gd_{0.5}B_6$ nanorods are stable up to 400 ℃ in the air.

5.5 References

1 H. Yamaguchi, K. Murakami, G. Eda, T. Fujita, P. Guan, W. Wang, C. Gong, J. Boisse, S. Miller, M. Acik, K. Cho, Y. J. Chabal, M. Chen, F. Wakaya, M. Takai and M. Chhowalla, *ACS Nano*, 2011, **5**, 4945–4952.

2 R. V. Kashid, D. J. Late, S. S. Chou, Y.-K. Huang, M. De, D. S. Joag, M. A. More and V. P. Dravid, *Small*, 2013, **9**, 2730–2734.

3 S. T. Nishanthi, A. Baruah, K. K. Yadav, D. Sarker, S. Ghosh, A. K. Ganguli and M. Jha, *Appl. Surf. Sci.*, 2019, **467**–**468**, 1148–1156.

4 Sunaina, M. Sreekanth, S. Ghosh, S. K. Mehta, A. K. Ganguli and M. Jha, *CrystEngComm*, 2017, **19**, 2264–2270.

5 L. Feng, H. Yan, H. Li, R. Zhang, Z. Li, R. Chi, S. Yang, Y. Ma, B. Fu and J. Liu, *AIP Adv.*, 2018, 8, 045109-8.

6 Wv Junqing, Deng Shaozhi, Xu Ningsheng and Chen Jun, *Nanotechnology*, 2018, **29**, 1–13.

7 J. Tian, C. Hui, L. Bao, C. Li, Y. Tian, H. Ding, C. Shen and H. J. Gao, *Appl. Phys. Lett.*, 2009, **94**, 083101-4.

8 R. Patra, S. Ghosh, E. Sheremet, M. Jha, R. D. Rodriguez, D. Lehmann, A. K. Ganguli, H. Schmidt, S. Schulze, M. Hietschold, D. R. T. Zahn and O. G. Schmidt, *J. Appl. Phys.*, 2014, **116**, 164309-7.

9 H. Zhang, J. Tang, Q. Zhang, G. Zhao, G. Yang, J. Zhang, O. Zhou and L. C. Qin, *Adv. Mater.*, 2006, **18**, 87–91.

10 J. T. Cahill and O. A. Graeve, *J. Mater. Res. Technol.*, 2019, **8**, 6321–6335.

11 J. Xu, G. Hou, T. Mori, H. Li, Y. Wang, Y. Chang, Y. Luo, B. Yu, Y. Ma and T. Zhai, *Adv. Funct. Mater.*, 2013, **23**, 5038–5048.

12 H. Zhang, Q. Zhang, G. Zhao, J. Tang, O. Zhou and L. C. Qin, *J. Am. Chem. Soc.*, 2005, **127**, 13120–13121.

13 Q. Y. Zhang, J. Q. Xu, Y. M. Zhao, X. H. Ji and S. P. Lau, *Adv. Funct. Mater.*, 2009, **19**, 742–747.

14 J. Xu, X. Chen, Y. Zhao, C. Zou, Q. Ding and J. Jian, *J. Cryst. Growth*, 2007, **303**, 466–471.

15 V. T. Petrashov, R. S. Shaikhaidarov, I. A. Sosnin, P. Delsing, T. Claeson and A. Volkov, *Phys. Rev. B*, 1998, **58**, 15088–15093.

16 J. M. Lafferty, *J. Appl. Phys.*, 1951, **22**, 299–309.

17 F. Monteverde, D. Alfano and R. Savino, *Corros. Sci.*, 2013, **75**, 443–453.

18 D. M. Goebel and R. M. Watkins, *Rev. Sci. Instrum.*, 2010, **81**, 083504-7.

19 K. Leung, *Vacuum*, 1986, **36**, 865–867.

20 V. G. Pol, S. V. Pol and A. Gedanken, *Adv. Mater.*, 2011, **23**, 1179–1190.

21 C. H. Chen, T. Aizawa, N. Iyi, A. Sato and S. Otani, *J. Alloys Compd.*, 2004, **366**, 2003–2005.

22 R. K. Selvan, I. Genish, I. Perelshtein, J. M. Calderon Moreno and A. Gedanken, *J. Phys. Chem. C*, 2008, **112**, 1795–1802.

23 X. H. Ji, Q. Y. Zhang, J. Q. Xu and Y. M. Zhao, *Prog. Solid State Chem.*, 2011, **39**, 51–69.

24 H. Zhang, Q. Zhang, G. Zhao, J. Tang, O. Zhou and L. Qin, *J. Am. Chem. Soc.*, 2005, **127**, 13120–13121.

25 Z. C. Zhong, P. A. Dowben and D. J. Sellmyer, *Mater. Lett.*, 1998, **37**, 320–324.

26 M. Zhang, Y. Jia, G. Xu, P. Wang, X. Wang, S. Xiong, X. Wang and Y. Qian, *Eur. J. Inorg. Chem.*, 2010, **2010**, 1289–1294.

27 P. H. Schmidt and D. C. Joy, *J Vac Sci Technol*, 1978, **15**, 1809–1810.

28 Menaka, R. Patra, S. Ghosh and A. K. Ganguli, *J. Solid State Chem.*, 2012, **194**, 173–178.

29 Q. Li, H. Zhang, J. Chen, Y. Zhao, W. Han, Q. Fan, Z. Liang, X. Liu and Q. Kuang, *J. Mater. Chem. C*, 2015, **3**, 7476–7482.

30 L. H. Bao, J. X. Zhang, S. L. Zhou and Tegus, *Chinese Phys. B*, 2011, **20**, 58101-6.

31 X. Yuan, D. Zhang, S. Zhou, M. Yue, J. Zhang, J. Zhu, Q. Ma and Z. Wang, *CrystEngComm*, 2015, **17**, 4210–4217.

32 M. M. Hasan, D. Cuskelly, H. Sugo and E. H. Kisi, *J. Alloys Compd.*, 2015, **636**, 67–72.

33 L.-H. Bao, J.-X. Zhang, N. Zhang, X.-N. Li and S.-L. Zhou, *Phys. Scr.*, 2012, **85**, 035710-6.

34 R. H. Fowler and L. Nordheim, *Proc. R. Soc. A Math. Phys. Eng. Sci.*, 1928, **119**, 173–181.

Chapter 6

Nanostructured zirconium diboride and their corrosion resistance properties

6.1 Introduction

Metal boride gains much attention from the scientific community due to its interesting properties such as high chemical, mechanical, and thermal stability, high melting point, ultra-incompressible, broad neutron capture cross-section,[1] good oxidation resistance,[1] high strength-to-weight ratio,[2] excellent thermal shock resistance,[2] and nonbrittle fracture behaviour[2] superconductivity,[3] high catalytic performance[4] optical, electronic and refractory properties.[5] These properties make metal borides to find application in high-efficient catalysis, thermal neutron detectors, flat plane display, made of corrosion-resistant materials, cutting tools, the nose cone of aerospace and electron emission nanodevices. In the present work, ZrB_2 has been synthesised, which have similar properties to other metal diborides. Further, an electrochemical anticorrosion study of ZrB_2 coated stainless steel (SS) has been done. It is believed that SS is anticorrosive in several media; however, there is a scope to improve the anticorrosive nature of SS. The metal coating such as Zn, Mo, Sn, Cu on stainless steel has been widely used to prevent air oxidation of stainless steel.[6] Whereas, for preventing the corrosion of stainless steel in acidic and basic media use of transition metal borides, metal carbides and metal nitrides have been previously reported.[7–12] The transition metal borides which can sustain harsh media longer time will be the right choice for anticorrosive material such as CrB_2, ZrB_2 and HfB_2.[13,14] Chromium boride is one of the very well studied anticorrosive material, however; due to its carcinogenic nature, chromium-free materials are in great demand.[8,13] To explore the possibility of making anticorrosive stainless steel anti-corrosive nature of ZrB_2 deposited on stainless have been studied. Earlier, the corrosion behaviour of D.C. Magnetron sputtered zirconium boride (ZrB_2) and zirconium boron nitride (Zr-B-N) on carbon steel have been investigated by M.Urgen *et. al.* in neutral and acidic media.[15] C. Monticellia *et. al.* also reported anticorrosive properties of ZrB_2 sintered with Si_3N_4 and ZrB_2/SiC composite in different aqueous solution.[16] In this context, from our best knowledge, scalable ZrB_2 film formation on 304 stainless steel and their corrosion behaviour study in the different aggressive medium has not been reported yet. Zirconium boride has properties such as high chemical inertness against molten metals,[15,17] high melting point,[18] low density,[2] high electrical and thermal conductivity,[19] and excellent thermal shock resistance.[19] These properties make them a good candidate for anticorrosive coating material in acidic and alkaline as well as in neutral media.[15,20–23] These excellent properties arise from its robust crystal structure (hexagonal AlB_2 type), where boron atoms

form honeycomb layers and zirconium ion located at the centre of the hexagonal ring formed by B sheets (Figure 6.1).[24,25]

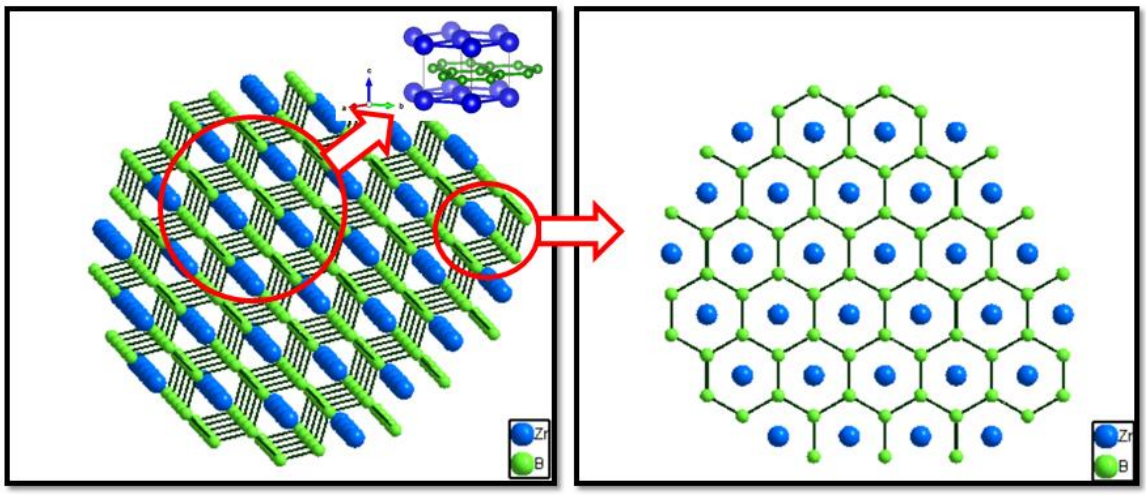

Figure 6.1. *Crystal structure of ZrB_2.*

The strong interatomic bonding of B-B and Zr-B atoms of the B-B rings and the covalent bond between zirconium with boron, gives very high hardness, high strength, chemical inertness and high-temperature stability.[26] These properties meet the requirement for making components of space vehicles such as sharp wing leading edges (in space shuttle), nose cones and propulsion components in future thermal protection systems of the hypersonic vehicles.[27] Despite the good anticorrosive nature, the synthesis of ZrB_2 is very challenging, as it requires high temperature, pressure and inertness condition. Conventionally, ZrB_2 is synthesised at high temperature under vacuum (~1400 °C). Earlier, synthesis of ZrB_2 has been carried out by chemical routes,[28–30] reduction processes,[31,32] hot pressing,[33,34] spark plasma sintering,[35] pressureless sintering,[36] chemical vapour deposition,[37] self-propagating high-temperature synthesis,[38] magnesiothermic reduction,[39] and borothermal reduction.[40] The synthesis method other than the chemical route and reduction process requires expensive equipment and a complicated synthetic process. Typically, the solid-state borothermal reduction process has been widely used due to in-expensiveness, and a one-step process; however, this process requires high temperature (~ 1500 °C) as well as pressure. In the present study, nanostructured ZrO_2 and amorphous boron were used as starting materials for the synthesis of ZrB_2 at ambient pressure and relatively lower temperature (1200 °C).

Further, the ZrB_2 have been coated onto stainless steel via doctor blade technique. There are several coating techniques have been used to fabricate ZrB_2 film previously. The commonly used coating process are pack-cementation,[41] hydrothermal electrophoretic

deposition,[42] electrodeposition,[2] chemical vapour deposition,[43] magnetron sputtering,[15] reactive multilayer technic,[44] and e-beam co-evaporation.[45] Thick films are one of the primary criteria for the anticorrosive nature of the film, and the above-listed process often provides the film in thickness range ≤ 1 μm.[13] Qian et at reported that high-temperature electrodeposition of ZrB_2 by the molten mixture of NaCl-KCl-K_2ZrF_6-KBF_4 at ~1100 K.[46] In the electrodeposition technique, the thickness can be tuned as a function of temperature and applied potential, which is an energy-intensive process. In the present work, we have used a doctor blade technique, which is economical, and film of controlled thickness can be easily made. The phase, microstructure, and electrochemical impedance spectroscopy (EIS) of the coated ZrB_2/304SS were investigated in the different corrosive medium (pH 1, pH 7 and pH 13). ZrB_2 coated stainless steel shows 73-98 % protective efficiency as compared to the bare stainless steel in the different corrosive medium.

6.2 Experimental

6.2.1 Materials

Stainless steel 304 grade (Alfa Aesar; 70 weight % iron, 19 weight % chromium and 11 weight % nickel). Zirconyl oxychloride octahydrate ($ZrOCl_2.8H_2O$, Sigma-Aldrich, 98 %), sodium hydroxide (NaOH, Merck, 97 %), triton^{TM} X-100 (Sigma- Aldrich), acetone (C_3H_6O, Merck, 99 %), methanol (CH_3OH, Merck, 99 %), boron (Loba Chem, 99 %) were used. All the chemicals have been used as received.

6.2.2 Methods

For the preparation of nanostructured ZrO_2, 30 ml of 0.1 M $ZrOCl_2.8H_2O$ containing 10 % TX-100 mixed with 30 ml of 0.3 M NaOH containing 10 % TX-100 and stirred for 1 h. The resulting solution was transferred to Teflon lined stainless steel autoclave and heated at 120 °C for 24 h. After completion of the reaction, it was allowed to cool down naturally to room temperature, the resultant solution was centrifuged, and precipitates were washed with methanol and water. ZrB_2 was synthesised by solid-state borothermal reduction method by using ZrO_2 as the precursor. The as-obtained ZrO_2 powder was mixed with amorphous boron in 1:10, 1:20 and 1:27 molar ratio into mortar pestle. The resultant mixture was placed in a recrystallised alumina boat and annealed at 1200 °C for 24 h in an argon atmosphere.

6.2.3 Preparation of working electrode and electrolyte

Stainless steel substrates were cut in a size of 1 cm^2 area and cleaned using detergent, water and ethanol. For the preparation of ZrB_2 paste, 50 mg of ZrB_2 was mixed with 100 µl ethylene glycol and 10 µL Nafion. The prepared paste was coated on one side of 304SS, and the other side was covered by epoxy to avoid any interference from the bare side. The electrochemical studies were conducted in three different electrolytes having pH 1, pH 7 and pH 13. For the preparation of pH=7 electrolyte, 3.55 g of sodium sulfate (Na_2SO_4) (0.5 N) was dissolved in 50 ml distilled water. For the preparation of pH=1 electrolyte, 25 ml of 0.5 N Na_2SO_4 was mixed with 25 ml of 0.5 N H_2SO_4. Similarly, pH 13 electrolyte was prepared by mixing 25 ml of 0.5 N Na_2SO_4 with 25 ml of 0.5 N NaOH.

6.2.4 Corrosion behaviour of ZrB_2 coated stainless steel

The electrochemical behaviour of ZrB_2/304SS was evaluated by linear sweep voltammetry (LSV) and electrochemical impedance spectroscopy (EIS) measurements. The standard three-electrode system was used to study the corrosion properties of the ZrB_2/304SS and bare 304 stainless steel within a fixed volume of electrolyte. The ZrB_2/304SS act as a working electrode and Ag/AgCl (3M) electrode used as a reference electrode with platinum as an auxiliary electrode. Polarization experiments were carried out after 30 min, 2 days and 14 days immersion in different electrolytes with scan rate 10 mV/s in potential window -1 V to +1 V. Apart from the corrosion potential and corrosion current, the protective efficiency $PE_{(j)}$ of the coated material was also calculated by using the following equation 6.1.

$$PE_{(j)} = \left(1 - \frac{j_{\mathrm{corr}}}{j^0_{\mathrm{corr}}}\right) \times 100\% \qquad 6.1$$

Where j_{corr} is the current density of coated stainless steel and j^0_{corr} corresponds to the uncoated stainless steel. The EIS was measured in a frequency ranging from 0.001 Hz up to 100 kHz. The impedance spectra were analysed with Nova 1.1 software and the best curve fitting was obtained by reducing the goodness value $<10^{-3}$.

6.3 Results and discussion

The present investigation deals with the synthesis of nanostructured ZrB_2 and the fabrication of ZrB_2 film on stainless steel to make it anticorrosive. To explore the objective, the work has been carried out in three steps. The first step deals with the synthesis and stabilisation of ZrB_2 at 1200 °C under ambient pressure using ZrO_2 precursor. In the second step, the fabrication of ZrB_2 film on a stainless-steel substrate via the doctor blade process.

Finally, the study of the corrosion behaviour of ZrB_2/304SS in aggressive media has been carried out.

Powder X-ray diffraction (PXRD) pattern of the product obtained from hydrothermal treatment of $ZrOCl_2$ shows the formation of ZrO_2 (Figure 6.2). All the

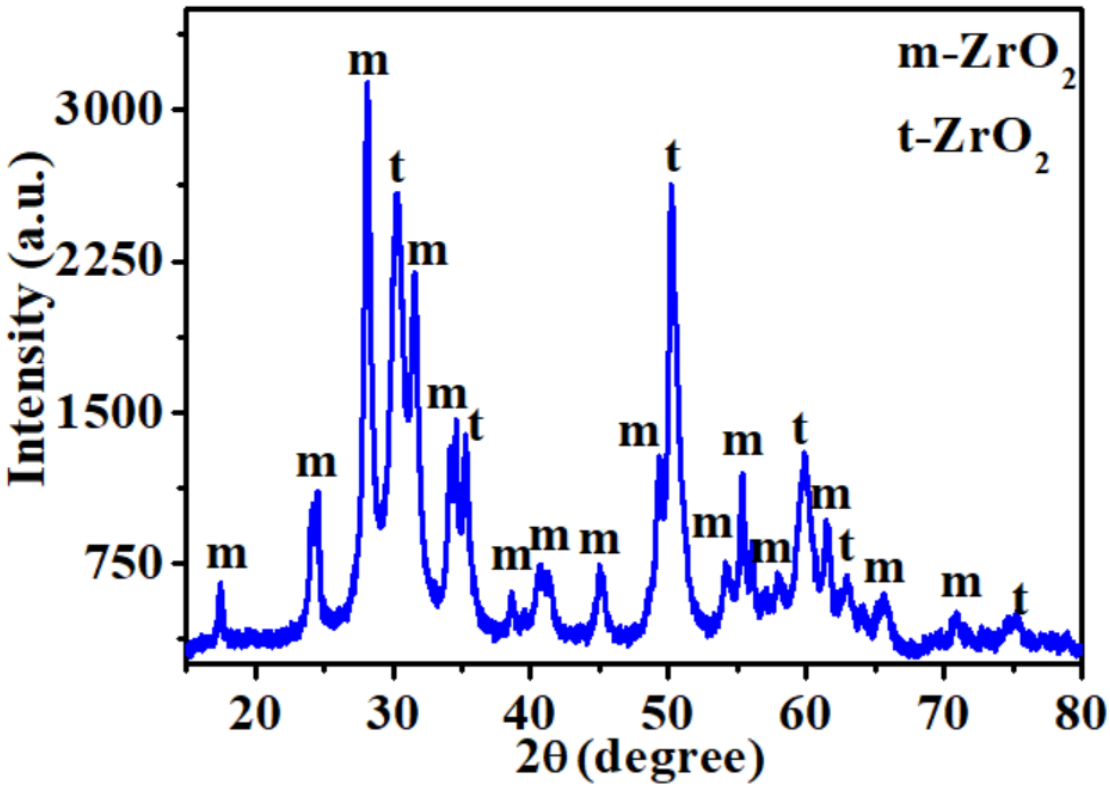

Figure 6.2. *Powder X-ray diffraction pattern of hydrothermally synthesised zirconia.*

reflection planes are well-matched with a mixture of tetragonal (JCPDS card no. 00-003-0640) and monoclinic-ZrO_2 (JCPDS card no. 00-037-1484). TEM micrograph shows the formation of cubic ZrO_2 particles of the average size of 10 nm (Figure 6.3a). EDX spectra further confirm the purity of ZrO_2 (Figure 6.3b). In Figure 6.3c, high-resolution transmission electron microscopy (HRTEM) shows the presence of monoclinic (003), (-212) and tetragonal (012) plane corresponds to *d*-spacing 1.68, 1.68 and 2.10 Å respectively. The selected area diffraction pattern (SAED) illustrated in Figure 6.3d also confirmed the presence of monoclinic as well as tetragonal phase of ZrO_2.

For the synthesis of ZrB_2, boron and ZrO_2 were mixed in 1:10 and 1:20 molar ratio and annealed at 1200 ℃ in the presence of an argon atmosphere. The PXRD pattern of the synthesised sample shows the formation of the mixed-phase of ZrB_2 (JCPDS card no. 00-034-0423) and m-ZrO_2 (JCPDS card no. 00=037-1484) (Figure 6.4a-b). It has been

observed that with the increase of boron content 1:10 to 1:20 (ZrO_2: B molar ratio), the ZrB_2 phase percentage increased in the final product (Figure 6.4a-b). Further, as the molar ratio of both precursors reached 1:27 and annealed at 1200 ℃ in an argon atmosphere for 24 h pure phase of ZrB_2 was obtained, which is well-matched with JCPDS card no. 00-034-0423 (Figure 6.4c).

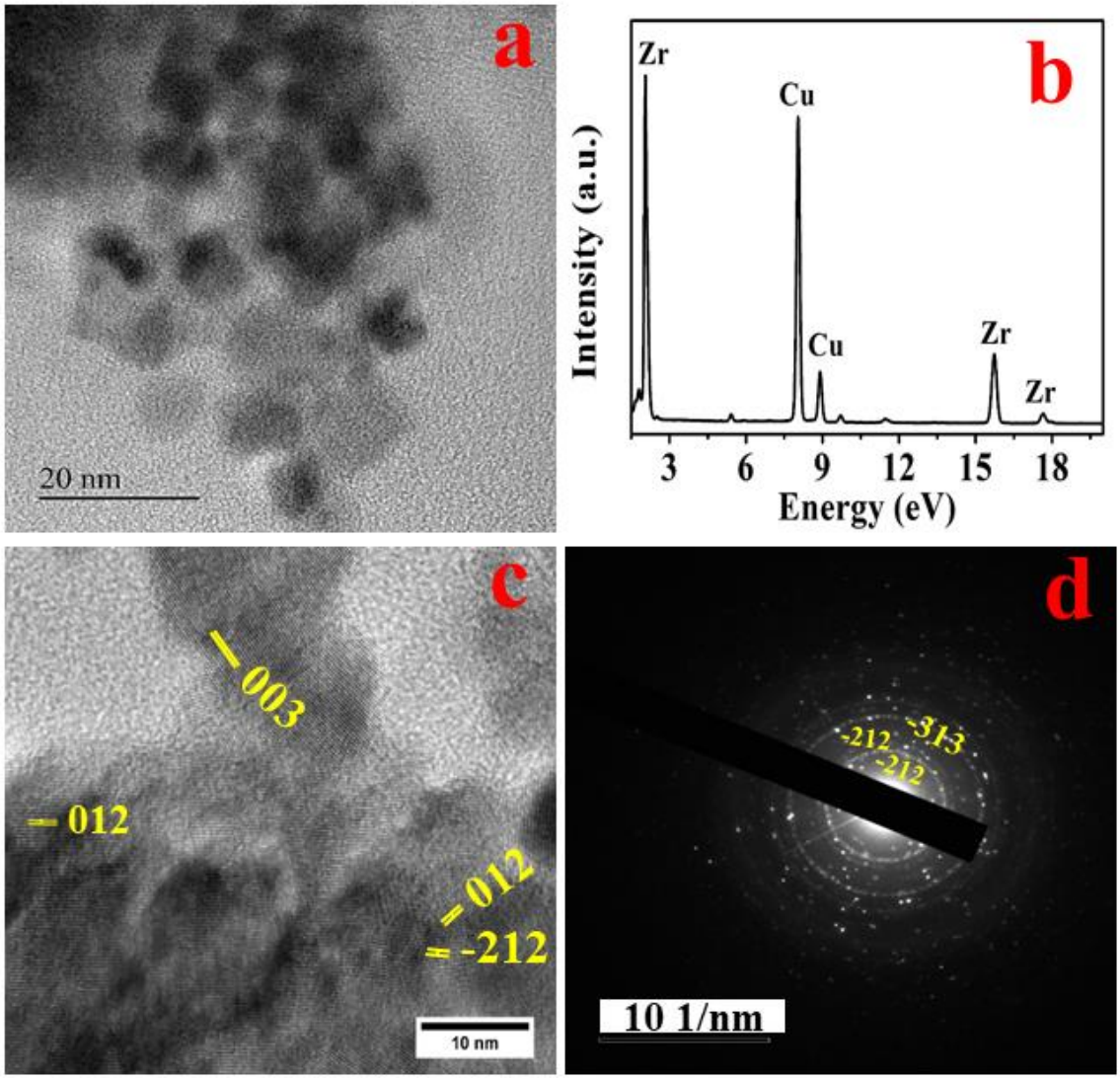

Figure 6.3. *(a) Transverse electron micrograph of zirconia powder. (b) elemental analysis of synthesised zirconia. (c) high-resolution transverse electron micrograph of zirconia indicating d space. (d) selected area electron diffraction pattern of zirconia.*

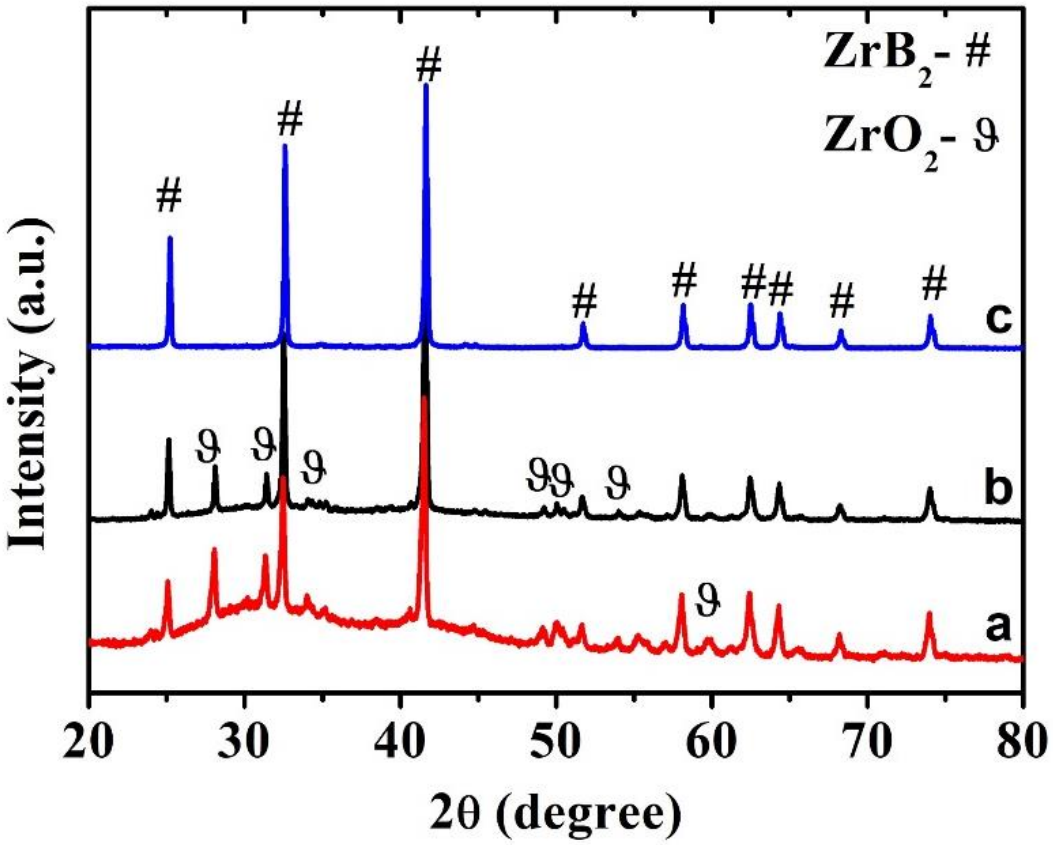

Figure 6.4. *Powder x-ray diffraction of synthesised ZrB_2 at (a) synthesis temperature 1000 ºC. (b) synthesis temperature 1100 ºC. and (c) synthesis temperature 1200 ºC.*

We have also attempted to stabilise ZrB_2 pure phase with 1:27 molar ratio of ZrO_2 to B at a lower temperature (1100 ℃, and 1000 ℃). PXRD patterns of the product obtained at 1000 ℃ and 1100 ℃ shows the formation of a mixture of ZrO_2 (JCPDS card no. 00=037-1484) and ZrB_2 (JCPDS card no. 00-034-0423) (Figure 6.5). The Full prof software has been used for Rietveld refinement of ZrB_2. The lattice parameter $a=b=$ 3.170(5) Å and c=3.531(8) Å have been generated after Rietveld refinement. The Rietveld refined X-ray diffraction pattern of ZrB_2 has been shown in Figure 6.6. The refined lattice parameter has been used to create the crystal structure of ZrB_2 (Figure 6.1). The parameters after refinement have been included in Table 6.1. To investigate the morphology of ZrB_2, transmission electron microscopic (TEM) studies have been carried out, which shows the ZrB_2 particles having an average size of 150 nm (Figure 6.7a). Further, TEM-EDX study shows the presences of zirconium peak with small spectra of oxygen (Figure 6.7b).

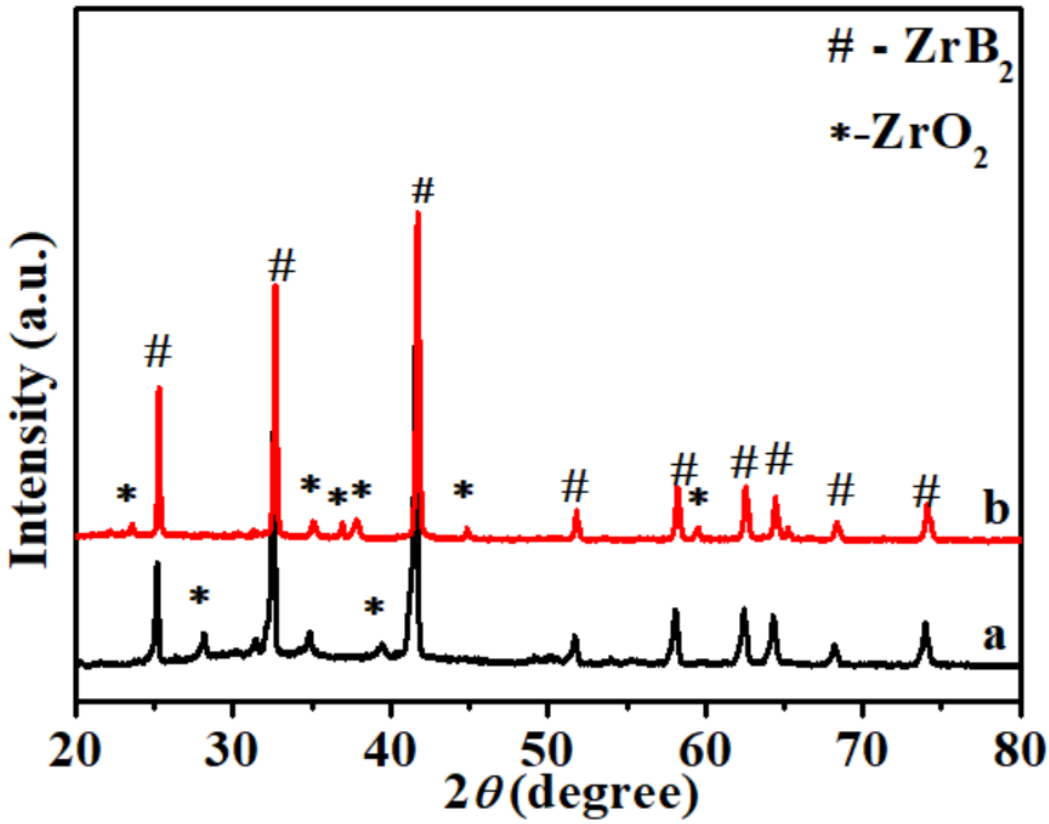

Figure 6.5. *Powder X-ray diffraction pattern of ZrB_2 powder annealed at, (a) at 1100 °C. (b) at 1000 °C.*

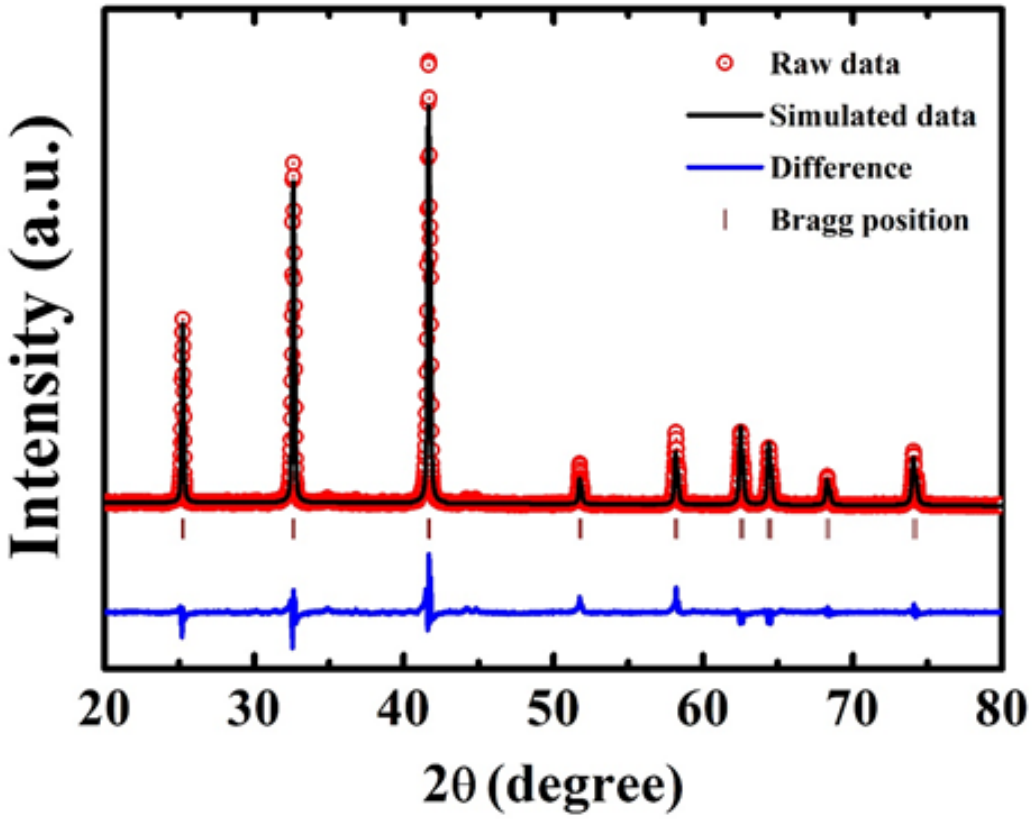

Figure 6.6. *Rietveld refined powder X-ray diffraction pattern of synthesised ZrB_2.*

Table 6.1. Parameter obtained from the refinement

Factors	Values
2θ	20-80
Step Size	0.016
Wavelength (Å)	1.54018
Space Group	P6/mmm
a (Å)	3.170 (5)
c (Å)	3.531 (8)
Unit cell Volume ($Å^3$)	30.734 (5)
R_{wp}	16.7
R_{exp}	8.69
R_p	19.4
χ^2 (GOF)	3.67

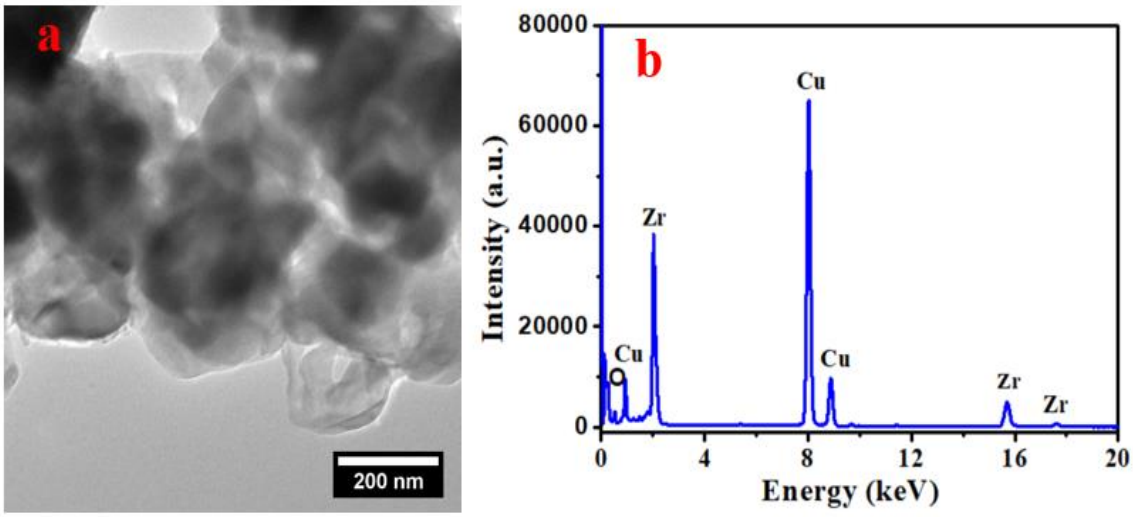

Figure 6.7. *Transmission electron microscopy (TEM) of as synthesised ZrB_2 powder; (a) ZrB_2 powder. (b) Elemental analysis of ZrB_2.*

6.3.1 Anticorrosion study

For an anticorrosion study of synthesised ZrB_2, a scalable doctor blade technique has been used for the fabrication of ZrB_2 film on the steel substrate. The optical image of the fabricated ZrB_2 film on SS before and after corrosion study has been shown in Figure 6.8. A surface profilometer study reveals that an average 19 μm film was formed on stainless steel. Further, the PXRD pattern before and after the corrosion study of ZrB_2/304SS have been shown in Figure 6.9 and Figure 6.10, which is matched with ZrB_2 having JCPDS no 00-034-0423. The absence of 304SS diffraction peaks in PXRD indicates uniform and the non-transparent coating was achieved, which is intact even after corrosion study after. SEM and line EDX study have been carried out to investigate the film, as shown in Figure 6.11. Figure 6.11a shows the SEM of coated ZrB_2 on 304SS before the EIS study,

which is smooth and uniform. The corresponding line EDX of ZrB_2/304SS before the study has been presented in Figure 6.11e. The line EDX

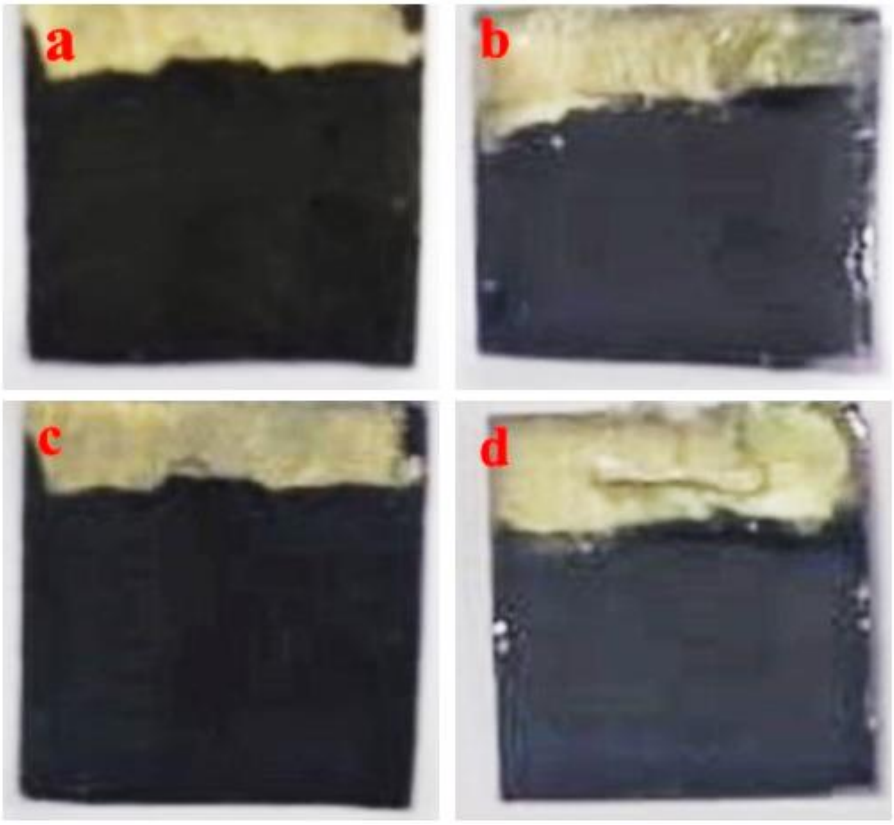

Figure 6.8. *Optical images of coated steel, (a) before EIS study. (b) For pH 1 electrolyte. (c) For pH 7 electrolyte. (d) For pH 13 electrolyte.*

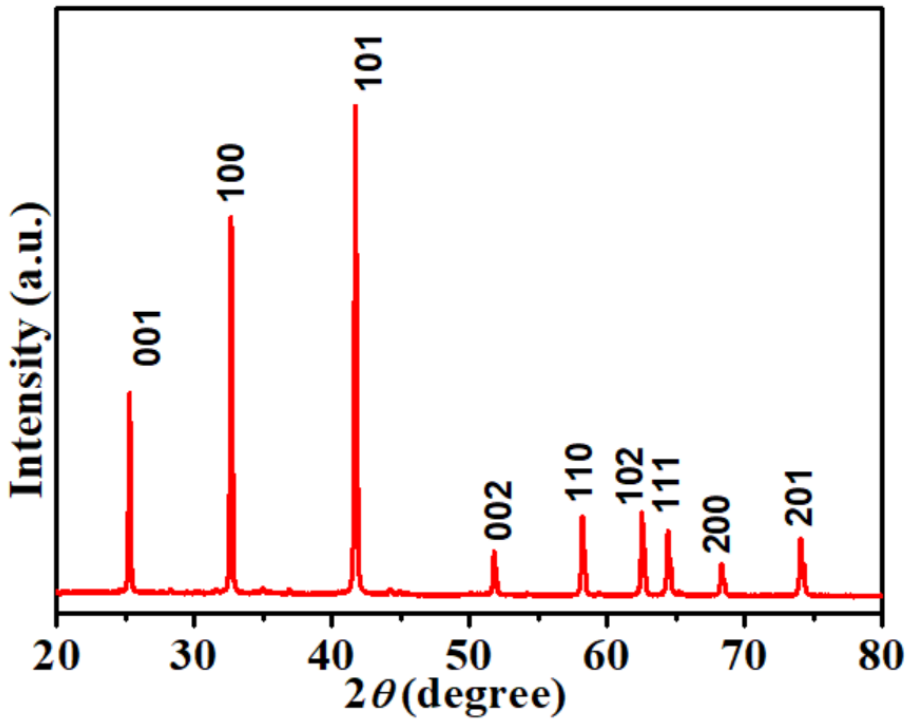

Figure 6.9. *Powder X-ray diffraction pattern of ZrB_2 coated stainless steel before the EIS study.*

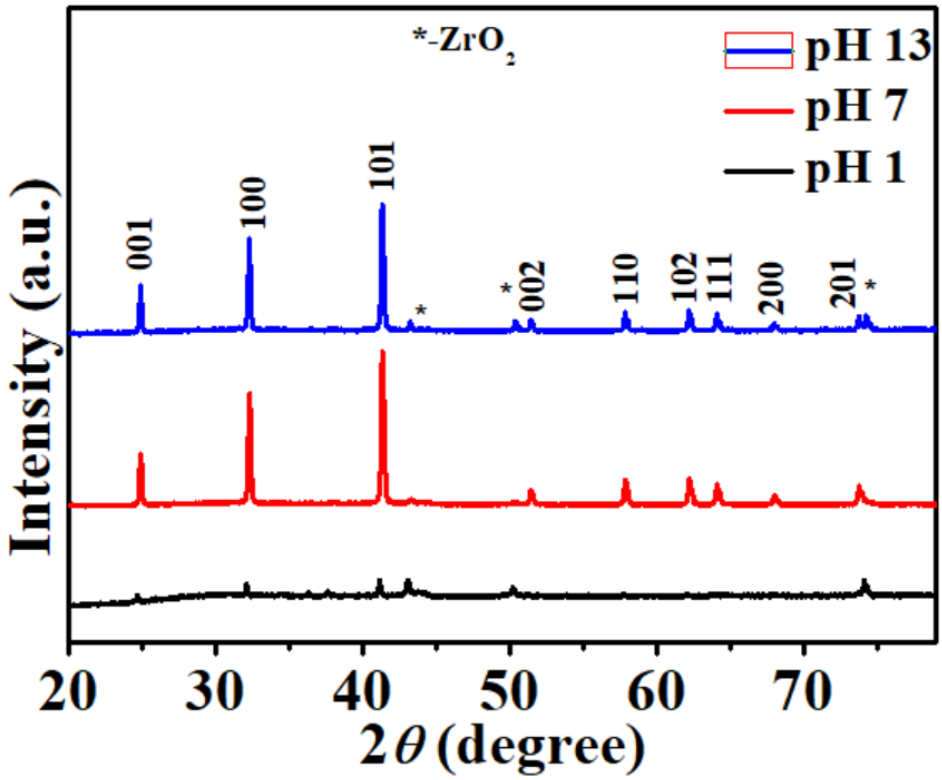

Figure 6.10. *Powder X-ray diffraction pattern coated on stainless steel after EIS study, (a) pH 1. (b) pH 7. (c) pH 13.*

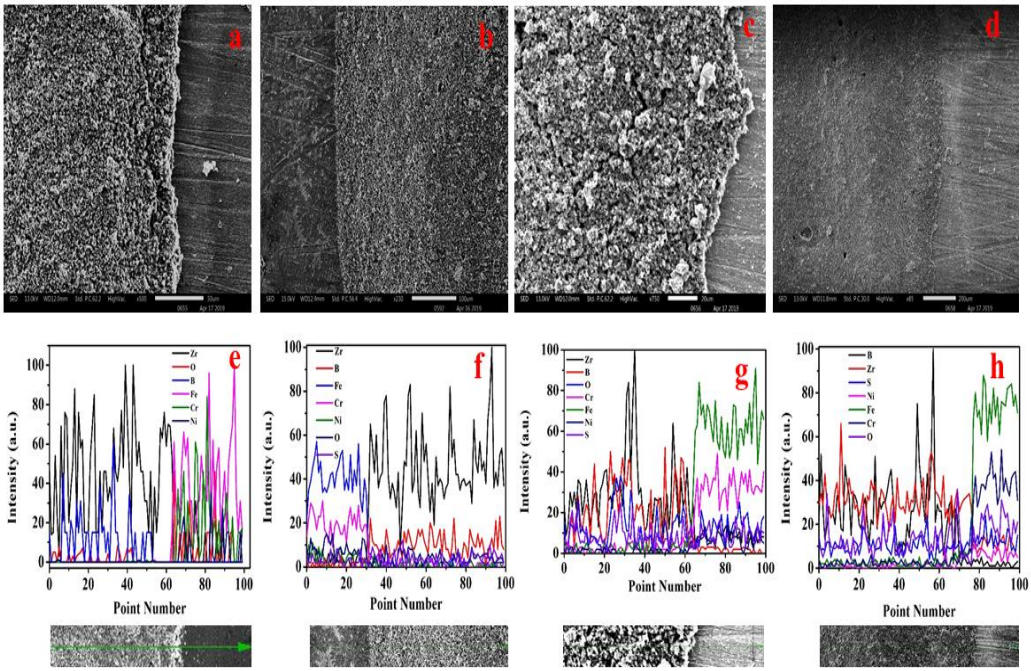

Figure 6.11. *SEM and line EDX of ZrB_2/304SS before and after EIS study, (a) before EIS study. (b) For pH 7 electrolyte. (c) For pH 1 electrolyte. (d) For pH 13 electrolyte. (e) line EDX of ZrB_2/304SS before study. (f) line EDX after study in pH 7. (g) line EDX after study in pH 1. (h) line EDX after study in pH 13.*

shows that the presence of Zr and very little intensity of O spectrum on the coated surface and Fe, Ni and Cr have been observed (where the coating is not present). SEM of ZrB_2/304SS after EIS measurement in different pH have been displayed in Figure 6.11b-d. The SEM study suggests that the film is still uniform even after the electrochemical corrosion test. Further, the line EDX, after the electrochemical corrosion study confirms no direct exposer of 304SS to the electrolyte. The line SEM-EDX in different pH shows no peak corresponding to components of 304SS (Fe, Ni and Cr) in the coated region after exposing to the aggressive media which shows the robustness of the ZrB_2 films (Figure 6.11f-g). The sulphur peak that appears in the coated region after the electrochemical corrosion study is due to the presence of sulphur in the electrolyte. Figure 6.12a-c shows the polarization curves of ZrB_2/304SS and bare stainless steel after 30 minutes, 2 days and 14 days immersion in different electrolyte having different pH as discussed in the experimental section. Figure 6.12a the polarization curves of ZrB_2/304SS with bare stainless steel at different immersion time in a neutral medium (pH 7). It is observed that corrosion current density (j_{corr}) of bare 304SS after 30 minutes immersion in the neutral medium is 2681.9 nA/cm^2. The effect of ZrB_2 coating on 304SS can be observed after 30 minutes immersion of ZrB_2/304SS material (j_{corr}= 80.84 nA/cm^2) as its corrosion current density is decreased by 40 times than bare stainless steel (Figure 6.13d). It is also found that after 2 days and 14 days immersion of ZrB_2/304SS in the neutral medium the change of corrosion current density is negligible ($j_{corr\ (after\ 2days)}$ = 64.08 nA/cm^2, $j_{corr\ (after\ 14\ days)}$ = 211.89 nA/cm^2) as compared to bare stainless steel immersed for same immersion time. The negligible enhancement of corrosion current density was may be due to a decrease in local pH around the surface of ZrB_2 and electrolyte. However, the corrosion potential (E_{corr}), ZrB_2/304SS shows comparable effectiveness than bare stainless steel after different immersion time (Figure 6.13a). The present study shows only 2-fold current density enhancement, while in previous reports 4 fold enhancement has been observed in neutral media.[47,48] The less current density enhancement suggests that the good anticorrosive nature of ZrB_2/304SS. The effect of pH on the electrochemical behaviour of ZrB_2/304SS has also been studied. In acidic sulphate solution (at pH 1), the corrosion current density of ZrB_2/304SS is 162.67 nA/cm^2, which is almost 50 times lower than bare stainless steel (j_{corr}=8401.1 nA/cm^2) after 30-minute immersion (Figure 6.13e). However, the bare stainless steel shows passivity upto 0.8 V in acidic electrolyte after 30 min immersion (Figure 6.12b). Like neutral media with increasing immersion time, ZrB_2 coating shows an excellent corrosion resistance in strongly acidic media as compared to bare stainless steel

as illustrated in Figure 6.12b & Figure 6.13b. For instance, ZrB_2 coating shows nearly five times lower corrosion current density (j_{corr} = 1792.82 nA/cm^2) after 14 days immersion than bare stainless steel immersed for 30 minutes. A little enhancement of corrosion current density is observed for ZrB_2 coating as immersion time increase. The following way can explain the enhancement of corrosion current density; In acidic media, ZrB_2 might form insoluble ZrO_2 (equation 6.2), which is readily attacked by SO_4^{2-} ions in strong acidic media to form a soluble $[ZrO(SO_4)_2]^{2-}$ as the immersion time increased.[16,49,50] As a result, the protectiveness of ZrB_2 is reduced with increasing immersion time in sulphuric acid media. On the other hand, ZrB_2 coating behaves significantly in alkaline media (at pH 13) as compared to acidic media. Figure 6.12c shows comparative polarization curves of ZrB_2/304SS and bare stainless in a strongly alkaline solution.

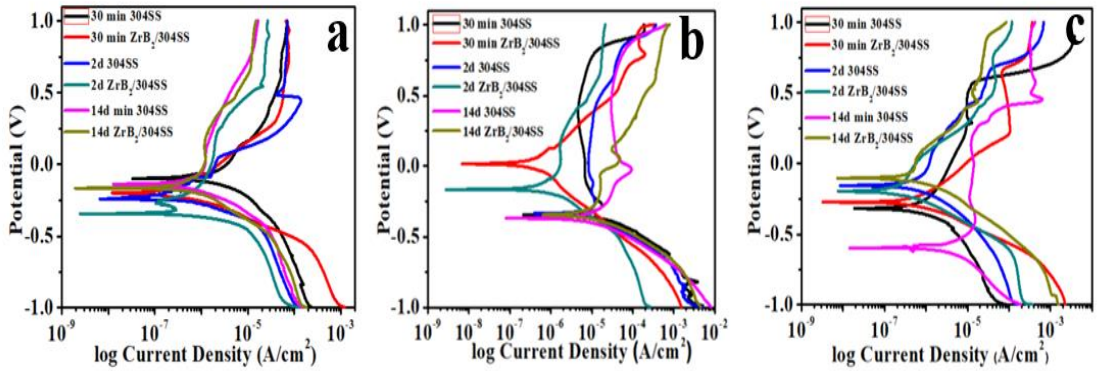

Figure 6.12. *Potentiodynamic curve of ZrB_2/304SS after 30 min, 2 days, 14 days immersion in; (a) pH 7. (b) pH 1. (c) pH 13.*

In alkaline media (at pH 13) ZrB_2 coating shows ($j_{corr\ after\ 14\ days}$ = 152.37 nA/cm^2) excellent, which is nearly eight times superior corrosion resistant properties than bare stainless steel ($j_{corr\ after\ 14\ days}$ =1135.9 nA/cm^2). It has also been observed that with increasing immersion time corrosion potential of ZrB_2 coated stainless steel shifted towards the anodic region, which suggested the enhancement of materials effectiveness towards anticorrosive nature (Figure 6.13c). The enhancement of the corrosion-resistant properties of ZrB_2 in alkaline media can be explained by the formation of stable ZrO_2 on stainless steel in alkaline media according to the reaction equation 6.3.[49] Pourbaix diagram also supports that in alkaline media ZrO_2 is more stable than acidic or neutral media.[51] Simultaneously, ZrO_2 does not soluble quickly in the solution due to the presence of OH^- ion which restricts the formation of soluble $[ZrO(SO_4)_2]^{2-}$.

$$ZrB_2 + 8H_2O \rightarrow ZrO_2 + 2H_3BO_3 + 10H^+ + 10e^- \quad 6.2$$

$$ZrB_2 + 10OH^- \rightarrow ZrO_2 + B_2O_3 + 5H_2O + 10e^- \quad 6.3$$

Electrochemical Impedance Spectroscopy (EIS) study was carried out for understanding the electrochemical behaviour at the electrolyte-coating-metal interface.[52] It is a well-stabilized fact that charge transfer resistance (R_t) and impedance log (Z/Ω) increases with decreasing double-layer capacitance value (Q_{dl}) value if a protective film is formed on the surface of the metal. The overall process is defined by an equivalent AC circuit and can be described by the Bode and Nyquist plots. The EIS spectra of bare 304SS and ZrB_2/304SS after 30 min, 2 days, and 14 days immersion time in different electrolyte after fitting with the equivalent model circuit shown in Figure 6.14 and the electrochemical impedance data is tabulated in Table 6.2. Figure 6.15a corresponds to the uncoated circuit for 304SS, and Figure 6.15b corresponds to ZrB_2/304SS. In Figure 6.15b, there are two sub-electrochemical interfaces: electrolyte/ ZrB_2 coating and ZrB_2/304SS interface.

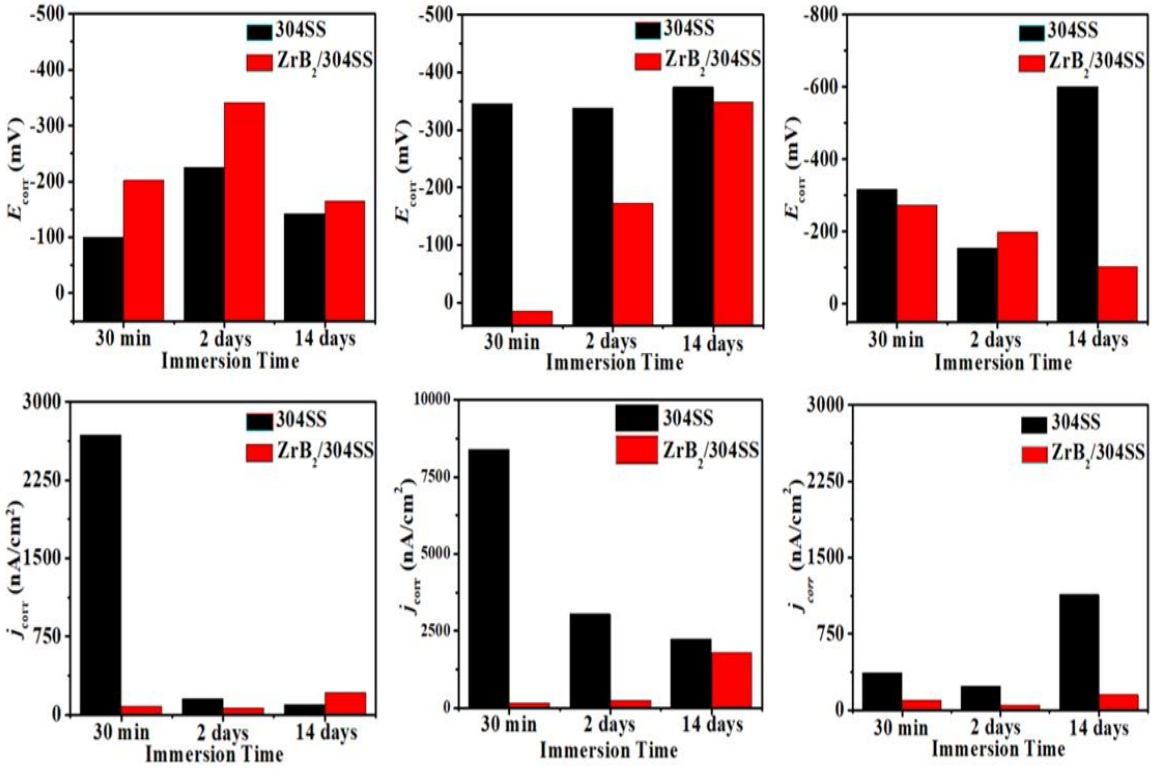

Figure 6.13. *Comparison of corrosion potential of (a) pH 7. (b) pH 1. (c) pH 13. and corrosion current density (d) pH 7. (e) pH 1. (f) pH 13.*

R_s, *CPE-1*, *CPE-2*, R_{pore}, and R_{ct} represents the solution resistance, the constant phase element of ZrB_2 film, the constant phase element of double layer, pore resistance of the coated film and charge transfer resistance due to the formation of double-layer capacitance. Mathematically, CPE impedance expressed by equation 6.4.

$$Z_{CPE} = \frac{1}{Y_0(j\omega)^n} \qquad 6.4$$

Where *j* is the imaginary function, *ω* is the angular frequency, Y_0 is *CPE* constant, *n* is an exponent of *CPE* ranging from 0 to 1. A high *n* value is typically for the smoother surface with coating and has a strong capacitive nature. A higher charge transfer resistance implies greater corrosion resistance of the material in that environment. The capacitances themselves used to identify the corrosion, coating, and diffusion processes with different time constants. Thus, the results obtained from polarization curves revealed that the ZrB_2-coated stainless steel shows good corrosion resistance in both strongly alkaline (high pH) as well as in neutral pH and its corrosion current had significantly influenced by pH of the electrolyte. Figure 6.16 shows the protection efficiency of ZrB_2/coated 304 stainless steel after 14 days of immersion compared with bare stainless steel.

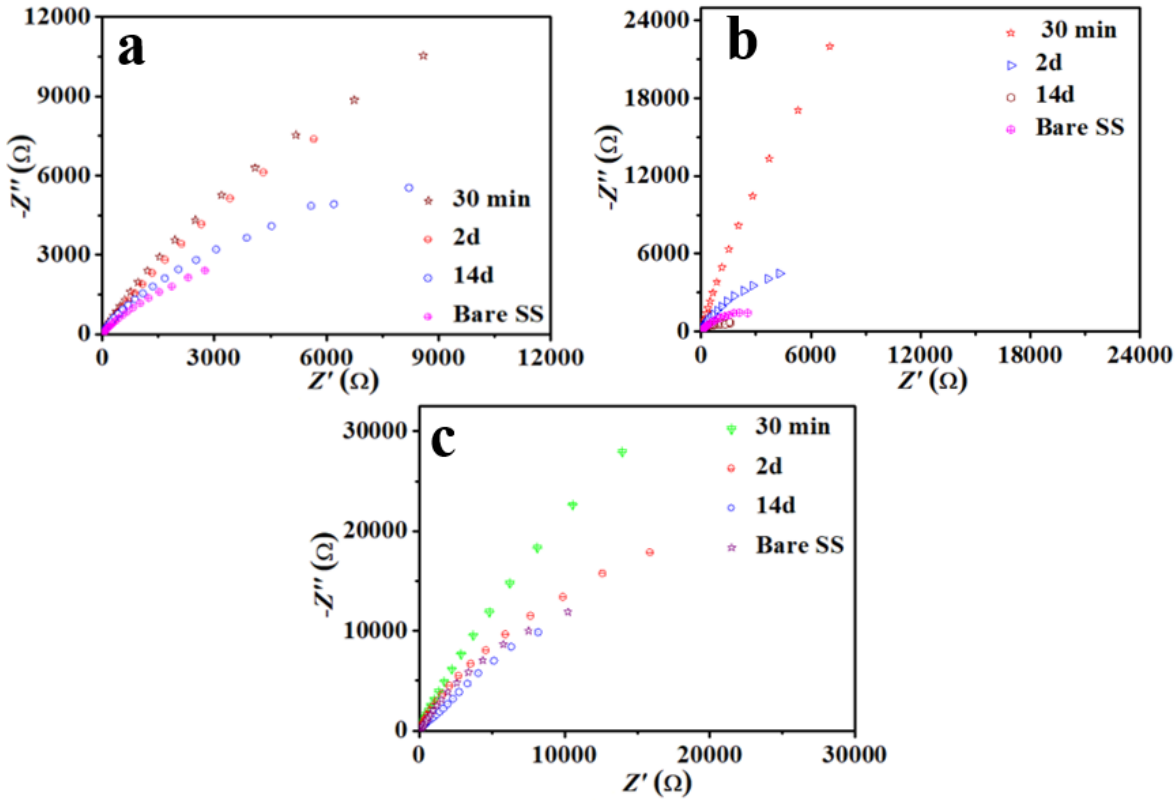

Figure 6.14. *Nyquist Plot of ZrB_2/304SS after 30 min, 2 days, 14 days immersion time and compare with bare 304SS, (a) pH 7. (b) pH 1. and (c) pH 13.*

Table 6.2. Electrochemical Impedance Data for the different samples

Electrolyte	Immersion time	R_s (Ω)	R_{po} film (Ω)	CPE-1		R_{ct} (KΩ)	CPE-2	
				Y_{film} (µ mho)	n film		Y (µ Mho)	n interface
Na_2SO_4+ H_2SO_4 pH=1	Bare SS	24.7	-	255	0.735	3.8	-	-
	30 min	10.8	30.2	2.35	0.665	70	64.9	0.901
	2 days	12.4	10.3	3.24	0.897	15	168	0.753
	14 days	22.2	5.13	4.65	0.761	2.2	234	0.706
Na_2SO_4 pH=7	Bare SS	16.6	-	282	0.732	6.7	-	-
	30 min	3.43	20	3.92	0.687	35	81.1	0.781
	2 days	2.1	12.4	4.38	0.693	32	134.1	0.771
	14 days	15.7	2.5	26	0.691	15	154.2	0.719
Na_2SO_4 + NaOH pH=13	Bare SS	33.8	-	91.9	0.747	50.2	-	-
	30 min	24.1	373	24.5	0.102	108	42	0.849
	2 days	17.2	3.86	148	0.932	66.1	64	0.792
	14 days	23.4	13.2	1.2	0.8	22.4	565	0.646

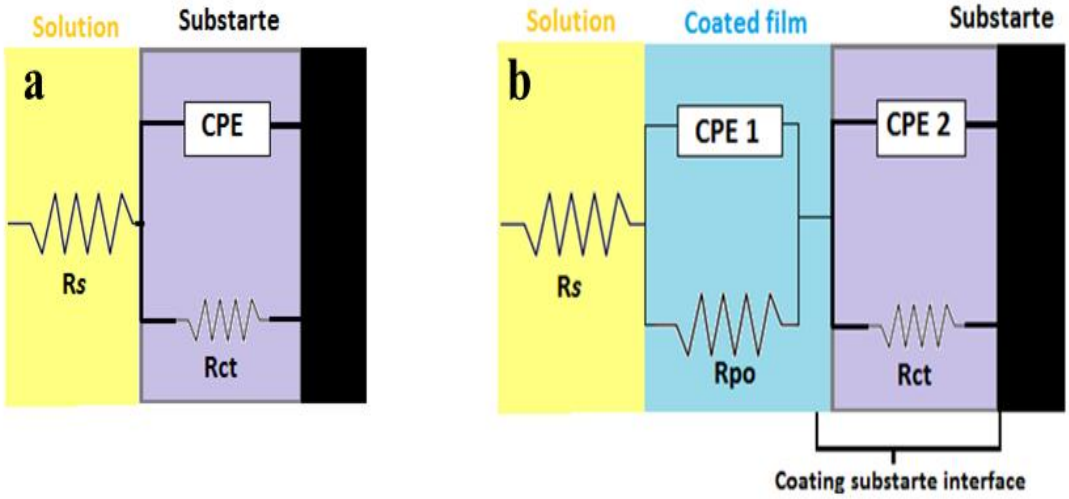

Figure 6.15. *Equivalent model for fitting EIS data (a) Bare stainless steel. (b) coated stainless steel.*

The protection efficiency (PE %) of ZrB_2 coating is calculated from the polarization data and is found to be 98 %, 96 % and 73 % after 30 min of immersion of ZrB_2/304SS in pH 1, pH 7 and pH 13 solution (Figure 6.16a). It is noted that with increasing immersion time in acidic solution (pH 1), the protective efficiency decreases from 98 % (PE after 30 min of immersion) to 20 % (after 14 days of immersion) whereas in aggressive alkaline solution, the protective efficiency of ZrB_2 increases from 73 % to 86 % with increasing immersion time from 30 min to 14 days of immersion (Figure 6.16b).

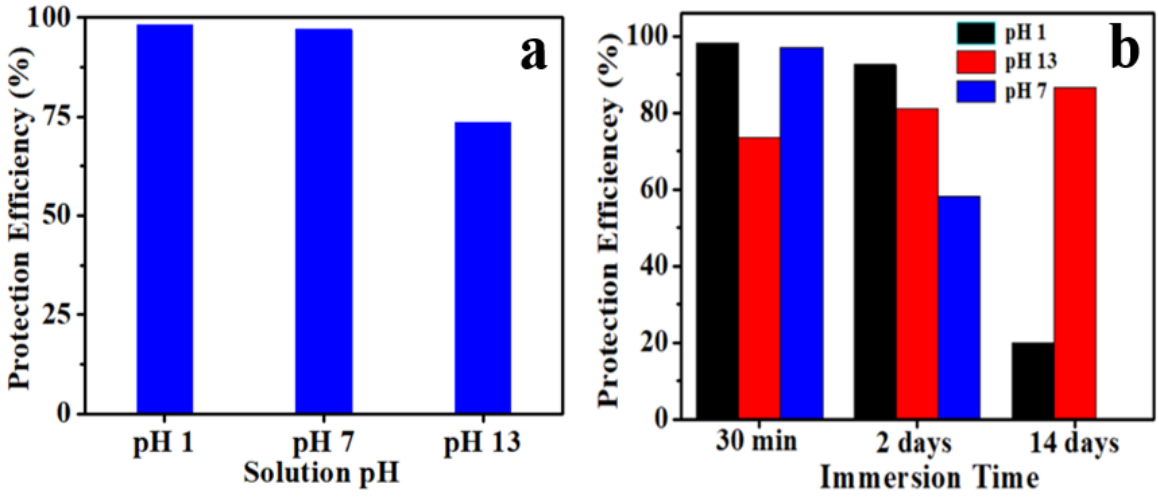

Figure 6.16. *Protection efficiency of ZrB_2, (a) after 30 min immersion time in different pH. (b) with different pH and immersion time.*

The impedance response verifies the polarization study. From the Bode phase plot (Figure 6.17d), 30 min immersed ZrB_2/304SS has the highest phase angle (~ -52°) compare to bare SS (~ -42°). Higher phase angle at low frequency implies the enhancement in the corrosion resistance.

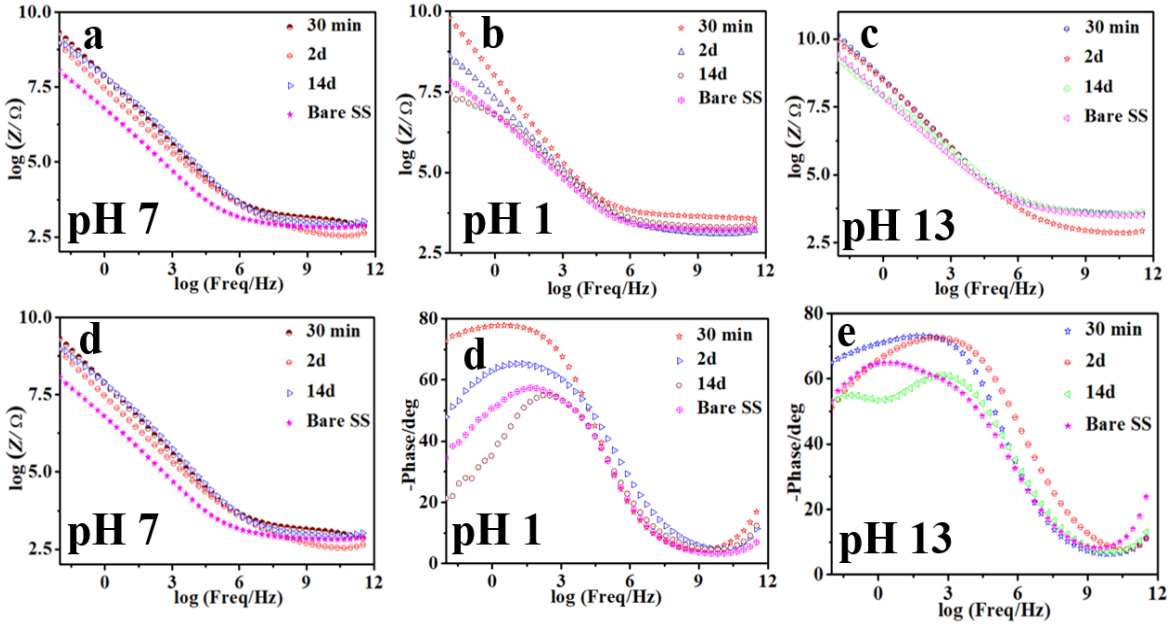

Figure 6.17. *Bode phase and magnitude plot of ZrB_2/304SS after 30 min, 2 days, 14 days immersion time and relate with bare 304SS, (a-c) Bode magnitude plot. (d-f) Bode phase plot in different pH.*

As the immersion time increased from 30 min to 2 days, phase angle slightly decreased due to the deterioration of coating by the electrolyte. As a result, the protectiveness of the coating is decreased. However, when the material immersed for 14 days, its phase angle

and impedance value further increased. Figure 6.14a is showing the Nyquist plot of the same electrochemical system. It is seen that the radius of the semicircle decreased with an increase in immersion time. In other words, with increasing, immersion time charge transfer resistance (R_{ct}) of the ZrB_2/SS is decreased but still higher than the bare SS. Bode magnitude plot in pH 1 at lower frequency region after 30 min and 2 days immersed ZrB_2/304SS shows highest impedance value (Figure 6.17b). Therefore, with increasing immersion time the corrosion of ZrB_2/304SS in acidic solution is more as compared to the neutral solution. It is observed that with increasing immersion time of ZrB_2/304SS the phase angle at lower frequency shifts towards positive value. 30 min immersed ZrB_2/304SS showing highest phase angle (~ -78°) compare to bare SS (~ - 58°) whereas phase angle of 2 days and 14 days immersed ZrB_2/304SS shifted to less negative value ~ -65° and ~ -55° respectively (Figure 6.17e). As a result, enhancement of corrosion current density (j_{corr} = 1791.8 nA/cm^2) took place as compare to 30 min immersed ZrB_2 coated SS (j_{corr} =162.67 nA/cm^2). It is observed that with increasing the immersion time the radius of the semicircle decreases, which supports the observed results (Figure 6.14b). In alkaline solution, there is a negligible shift of phase angle (~ -73°) is observed at lower frequency region for ZrB_2/304SS when immersion time increased to 2 days from 30 min (Figure 6.17f). However, when compared with 30 min immersed bare stainless steel the phase angle shifted to (~-65°) at the lower frequency region. Moreover, from the Nyquist plot, the radius of the semicircle is getting decrease with the increase of immersion time (Figure 6.14c).

6.4 Conclusions

In the present study, ZrB_2 have successfully synthesised by solid-state borothermal reduction route at relatively low temperature (1200 ℃) and ambient pressure. The TEM study of synthesised ZrB_2 powder shows the formation of particles having 150 nm size. The doctor blade technique (economical and scalable) has been employed to fabricate ZrB_2 film on a stainless-steel substrate. The corrosion-resistant properties of ZrB_2/SS have been successfully investigated in a different electrolyte by potentiodynamic polarization and EIS study. The electrochemical studies show that ZrB_2 films would be an excellent anticorrosive coating material in strong acid, strong alkaline as well as neutral media. It was observed that ZrB_2/304SS have more resistance in neutral solution than acidic and alkaline solutions containing sulfate ion up to 2 days immersion. The corrosion current density (j_{corr}) of ZrB_2 coated stainless steel is less than bare stainless steel in acidic as well as the alkaline medium. Initially, ZrB_2 coating offered maximum corrosion resistance

properties as measured by polarization curve and EIS study which indicates ZrB_2 shows highest charge transfer resistance (R_{ct}). This study will contribute a worth full knowledge for those who are working in the field of material science, solid-state chemistry, and protection of materials from corrosion.

6.5 References

1 J. Zhang, J. Liu, H. Liao, M. Zeng and S. Ma, *J. Mater. Res. Technol.*, 2019, **8**, 6308–6320.

2 L. Li, H. Li, Y. Li, X. Yin, Q. Shen, Q. F.-A. S. Science and U. 2015, *Appl. Surf. Sci.*, 2015, 465–471.

3 J. Nagamatsu, N. Nakagawa, T. Muranaka, Y. Zenitani and J. Akimitsu, *Nature*, 2001, **410**, 63–64.

4 X. Wang, G. Tai, Z. Wu, T. Hu and R. Wang, *J. Mater. Chem. A*, 2017, **5**, 23471–23475.

5 G. Akopov, M. T. Yeung and R. B. Kaner, *Adv. Mater.*, 2017, **29**, 1604506-29.

6 E. Budman and D. Stevens, *Anti-Corrosion Methods Mater.*, 1998, **45**, 327–332.

7 M. Audronis, P. J. Kelly, R. D. Arnell, A. Leyland and A. Matthews, *Surf. Coatings Technol.*, 2005, **200**, 1616–1623.

8 J. Tedim, S. K. Poznyak, A. Kuznetsova, D. Raps, T. Hack, M. L. Zheludkevich and M. G. S. Ferreira, *ACS Appl. Mater. Interfaces*, 2010, **2**, 1528–1535.

9 S. Sutthiruangwong and G. Mori, *Int. J. Refract. Met. Hard Mater.*, 2003, **21**, 135–145.

10 P. C. R. Nunes and L. V. Ramanathan, *Corrosion*, 1995, **51**, 610–617.

11 C.-T. Kao, S.-J. Ding, Y.-C. Chen and T.-H. Huang, *J. Biomed. Mater. Res.*, 2002, **63**, 786–792.

12 F. Mahvash, S. Eissa, T. Bordjiba, A. C. Tavares, T. Szkopek and M. Siaj, *Sci. Rep.*, 2017, **7**, 42139-5.

13 J. Dennis and T. Such, in *Nickel and Chromium Plating* , Woodhead Publishing Limited, 3rd edn., 1993.

14 G. F. Sun, Y. K. Zhang, M. K. Zhang, R. Zhou, K. Wang, C. S. Liu and K. Y. Luo, *Appl. Surf. Sci.*, 2014, **295**, 94–107.

15 M. Ürgen, A. F. Çakir, O. L. Eryilmaz and C. Mitterer, *Surf. Coatings Technol.*, 1995, **71**, 60–66.

16 C. Monticelli, A. Bellosi and M. Dal Colle, *J. Electrochem. Soc.*, 2004, **151**, B331-B339.

17 I. A.-A.-R. P. on M. Engineering and U. 2008, *Recent Patents Mech. Eng.*, 2008, **1**, 1–7.

18 M. Brach, V. Medri and A. Bellosi, *J. Eur. Ceram. Soc.*, 2007, **27**, 1357–1360.

19 J. W. Zimmermann, G. E. Hilmas, W. G. Fahrenholtz, R. B. Dinwiddie, W. D.

Porter and H. Wang, *J. Am. Ceram. Soc.*, 2008, **91**, 1405–1411.

20 H. P. Feng, C. H. Hsu, J. K. Lu and Y. H. Shy, *Mater. Sci. Eng. A*, 2003, **349**, 73–79.

21 S. S. El-Egamy and W. A. Badaway, *J. Appl. Electrochem.*, 2004, **34**, 1153–1158.

22 R. T. Loto, *Int. J. Phys. Sci.*, 2012, **7**, 1677–1688.

23 Y. Ohko, S. Saitoh, T. Tatsuma and A. Fujishima, *J. Electrochem. Soc.*, 2001, **148**, B24.

24 I. Loa, K. Kunc, K. Syassen and P. Bouvier, *Phys. Rev. B*, 2002, **66**, 1–8.

25 H. Kinoshita, S. Otani, S. Kamiyama, H. Amano, I. Akasaki, J. Suda and H. Matsunami, *Japanese J. Appl. Physics, Part 2 Lett.*, 2001, **40**, 10–13.

26 R. Telle, L. S. Sigl and K. Takagi, in *Handbook of Ceramic Hard Materials*, Wiley-VCH Verlag GmbH, 2000, pp. 802–945.

27 Y. Xin, H. Qizhong, S. Zhean, C. Xin, X. Liang, Z. Ping and L. Jun, *Corros. Sci.*, 2016, **107**, 9–20.

28 Y. Zhang, R. Li, Y. Jiang, B. Zhao, H. Duan, J. Li and Z. Feng, *J. Solid State Chem.*, 2011, **184**, 2047–2052.

29 S. K. Mishra, S. Das and L. C. Pathak, *Mater. Sci. Eng. A*, 2004, **364**, 249–255.

30 L. Chen, Y. Gu, Z. Yang, L. Shi, J. Ma and Y. Qian, *Scr. Mater.*, 2004, **50**, 959–961.

31 H. Zhao, Y. He and Z. Jin, *J. Am. Ceram. Soc.*, 1995, **78**, 2534–2536.

32 R. Li, H. Lou, S. Yin, Y. Zhang, Y. Jiang, B. Zhao, J. Li, Z. Feng and T. Sato, *J. Alloys Compd.*, 2011, **509**, 8581–8583.

33 C. Tian, D. Gao, Y. Zhang, C. Xu, Y. Song and X. Shi, *Corros. Sci.*, 2011, **53**, 3742–3746.

34 A. L. Chamberlain, W. G. Fahrenholtz and G. E. Hilmas, 2004, **1172**, 1170–1172.

35 J. K. Sonber and A. K. Suri, *Adv. Appl. Ceram.*, 2011, **110**, 321–334.

36 S. C. Zhang, G. E. Hilmas and W. G. Fahrenholtz, *J. Am. Ceram. Soc.*, 2006, **89**, 1544–1550.

37 P. Wang, Y. Qi, S. Zhou, P. Hu, G. Chen, X. Zhang and W. Han, *Phys. Status Solidi*, 2016, **253**, 1590–1595a.

38 V. G. Pol, S. V. Pol and A. Gedanken, *Adv. Mater.*, 2011, **23**, 1179–1190.

39 S. Zhang, M. Khangkhamano, H. Zhang and H. A. Yeprem, *J. Am. Ceram. Soc.*, 2014, **97**, 1686–1688.

40 S. Ran, O. Van Der Biest and J. Vleugels, *J. Am. Ceram. Soc.*, 2010, **93**, 1586–

1590.

41 X. Zou, Q. Fu, L. Liu, H. Li, Y. Wang, X. Yao and Z. He, *Surf. Coatings Technol.*, 2013, **226**, 17–21.

42 O. Haibo, L. Cuiyan, H. Jianfeng, C. Liyun, F. Jie, L. Jing and X. Zhanwei, *Corros. Sci.*, 2016, **110**, 265–272.

43 S. Motojima, K. Funahashi and K. Kurosawa, *Thin Solid Films*, 1990, **189**, 73–79.

44 D. Lee, G. D. Sim, K. Xiao and J. J. Vlassak, *J. Phys. Chem. C*, 2014, **118**, 21192–21198.

45 D. M. Stewart, R. W. Meulenberg and R. J. Lad, *Thin Solid Films*, 2015, **596**, 155–159.

46 Q. Wang, Y. L. Wang, H. J. Liu and C. L. Zeng, *J. Electrochem. Soc.*, 2016, **163**, D636–D644.

47 R. Di Maggio, L. Fedrizzi, S. Rossi and P. Scardi, *Thin Solid Films*, 1996, **286**, 127–135.

48 M. Abdallah, *Mater. Chem. Phys.*, 2003, **82**, 786–792.

49 Z. Wang, Q. Zhao, L. Jing, Z. Wu and X. Sun, *Ceram. Int.*, 2016, **42**, 2926–2932.

50 C. Monticelli, F. Zucchi, A. Pagnoni and M. Dal Colle, *Electrochim. Acta*, 2005, **50**, 3461–3469.

51 R. W. Revie, *Uhlig's corrosion handbook*, Wiley, 3rd edn., 2011.

52 M. E. Orazem and B. Tribollet, *Electrochemical Impedance Spectroscopy*, John Wiley & Sons, 2011.

Chapter 7

Conclusion and future prospect

Metal borides are compounds of boron with less electronegative elements. Metal borides have a high melting point, low work function, low vapour pressure, high mechanical and chemical strength, broad neutron capture cross-section, good oxidation resistance, high strength-to-weight ratio, excellent thermal shock resistance and nonbrittle fracture behaviour, superconductivity, high catalytic performance, optical, electronic and refractory properties. These properties make metal borides find applications in the field of ultrahigh incompressible, materials, field emitters, anticorrosive coatings, nose cones in rockets, IR sensor and so on. Despite interesting properties, metal borides require challenging synthesis condition. There are very few reports on the synthesis of metal borides of controlled shape and size via chemical routes. Here, in the present work, we aim to synthesise the metal borides of the desire shape and size at low temperature using the chemical route. For the synthesis of metal borides, first, the metal hydroxide or metal oxide of the desired shape has been synthesised. Further, as-synthesised metal oxide or metal hydroxide precursors has been decorated with boron source (boron or $NaBH_4$) followed by annealing in an argon atmosphere to form the metal borides. The film of synthesised metal borides has been fabricated over the desired substrate via spin coating or doctor blade coating. The as-synthesised metal boride film has been used for the field emission and anticorrosive properties study. The entire thesis has been divided into seven chapters.

Chapter 1st deals with the introduction of metal boride including synthesis, its properties and application.

In chapter 2, neodymium hexaboride has been synthesised at low temperature using the chemical route. For the synthesis of NdB_6, first anisotropic $Nd(OH)_3$ nanostructured of size 10 nm X 120 nm has been synthesised via hydrothermal route. The synthesised sample has been annealed with boron precursors ($NaBH_4$) to get the NdB_6. It has been shown that the precursor ratio as well as the heating rate affect the final morphology of the synthesised sample. TEM study reveals that the formation of ultrafine nanocube of size 15-20 nm at a heating rate (250 °C/h), while at the slow heating rate (40 °C/h) leads to the formation of ultra-fine nanorods (10 nm X 100 nm). The synthesised powder has been dispersed in a mixture of ethanol and ethylene glycol and the prepared final mixture has been coated over Si- substrate via the spin coating followed by a slow heating rate at 200 °C/h, 12 h in Argon atmosphere. NdB_6 coated silicon substrate has been used for the field emission study. The study of the film of NdB_6 shows that ultrafine nanorods provide the highest current density at the lowest turn-on field. The highest achieved current density was 2.3 $\mu A/cm^2$ for nanorods. Apart from the lowest turn-on field, the highest enhancement factor (β=2263)

was also achieved from ultrafine nanorods. Further, the oxidation study of NdB_6 nanorods shows that the retention of NdB_6 phase up to 400 ℃ in the air.

In continuation of previous work, in 3rd chapter, I have attempted to synthesised GdB_6 using a chemical route using gadolinium hydroxide [$Gd(OH)_3$] anisotropic structures (dia ~10 nm, length ~ 120 nm), which has been synthesised via hydrothermal route at 120 ℃. The synthesised $Gd(OH)_3$ was annealed with boron precursors ($NaBH_4$) in an inert atmosphere at the various heating rate to obtain GdB_6. It was observed that the slow heating rate (40 ℃/h) favours the formation of GdB_6 nanorods (40 nm X 150 nm); however, a higher heating rate leads to the formation of nanocubes of size 40-50 nm. Further, the synthesized GdB_6 have been dispersed in ethanol and ethylene glycol mixture and spin coating over Si- substrate followed by slow heating at 200 ℃ and utilized for field emission material. Field emission study of vertically oriented GdB_6 nanorods shows the low turn-on field (4.35 V/μm) for GdB_6 nanorods. The observed field enhancement factor (β) of GdB_6 nanorods was 1490. The low turn-on field and high enhancement factor indicate the GdB_6 nanorods are an excellent cathode material for field emission study. Further, the HTXRD study indicates that the synthesised GdB_6 is stable up to 400 ℃.

It has been demonstrated by scientist that doping of La at A site in AB_6 metal hexaboride could reduce the work function. Therefore, in the 4th chapter, the various concentration of Lanthanum has been doped in NdB_6 at Nd site for the synthesis of lanthanum doped neodymium hexaboride ($La_xNd_{1-x}B_6$). For the stabilization of $La_xNd_{1-x}B_6$, first $La_xNd_{1-x}(OH)_3$ has been synthesised. The lanthanum doped neodymium hydroxide has been synthesised via the hydrothermal method. Microstructure analysis shows the anisotropic structures of $La_xNd_{1-x}(OH)_3$ [x=0.1,0.2, 0.3, 0.4 and 0.5]. The as-obtained $La_xNd_{1-x}(OH)_3$ mixed with $NaBH_4$ and annealed with the slow heating rate at the presence of an inert atmosphere to get the $La_xNd_{1-x}B_6$. The TEM study of $La_xNd_{1-x}B_6$ (x=0.1 and 0.3) reveals that the formation of nanorods of length ~100 nm and width ~25 nm. Further, the samples $La_xNd_{1-x}B_6$ (x=0.2, 0.4 and 0.5) also show the formation of nanorods of 300 nm length and 30 nm. It has been observed that the $La_{0.3}Nd_{0.7}B_6$ sample shows the highest enhancement factor (β=2459) with the lowest turn-on field (3.6 V/μm). The lowest turn-on field with the highest enhancement fact for $La_{0.3}Nd_{0.7}B_6$ might be due to the uniform distribution of $La_{0.3}Nd_{0.7}B_6$ nanorods over the silicon substrate. Further, the oxidation study of $La_{0.3}Nd_{0.7}B_6$ nanorods shows that the materials will be stable up to 400 ℃ in the air.

We have also attempted to stabilize lanthanum doped gadolinium hexaboride ($La_xNd_{1-x}B_6$) in 5th chapter via chemical route using $La_xGd_{1-x}(OH)_3$ precursor. First, $La_xGd_{1-x}(OH)_3$ [x=0.1,0.2, 0.3, 0.4 and 0.5] has been synthesised via a hydrothermal route at 120 ℃. The microstructure analysis of synthesised $La_xGd_{1-x}(OH)_3$ shows the anisotropic structures of average width 10-13 nm with an average length of 105-130 nm. Further, the as-obtained $La_xGd_{1-x}(OH)_3$ anisotropic nanostructures mixed with $NaBH_4$ and annealed at the slow heating rate in the presence of inert atmosphere to obtain $La_xGd_{1-x}B_6$. The powder X-ray diffraction study reveals the formation of lanthanum doped gadolinium hexaboride. Further, TEM study shows the formation of nanorods of $La_xGd_{1-x}B_6$ [x=0.1,0.2, 0.3, 0.4 and 0.5]. The width of samples $La_xGd_{1-x}B_6$ [x=0.1,0.2, 0.3, 0.4 and 0.5] are 30-40 nm. The length of samples $La_xGd_{1-x}B_6$ [x=0.1, 0.3, and 0.4] have 130 nm and 300 nm $La_xGd_{1-x}B_6$ [x=0.2, and 0.5] respectively. Field emission study reveals that $La_{0.3}Gd_{0.7}B_6$ has the lowest turn-on filed (4.51 V/μm); however, the maximum current density has been observed for the $La_{0.5}Gd_{0.5}B_6$. Further, high-temperature XRD of $La_{0.5}Gd_{0.5}B_6$ nanorods has been done, which reveals the $La_{0.5}Gd_{0.5}B_6$ is stable upto 400 ℃ in the air.

Table 7.1. *Field emission parameter of metal hexaborides*

Materials	**Field Emission Characteristic**
NdB_6	Turn-on field < 4.5 V/μm; β = 2263
GdB_6	Turn-on field = 4.35 V/μm; β = 1490
Lanthanum doped gadolinium hexaboride ($La_xNd_{1-x}B_6$)	x=0.2; Turn-on field = 5 V/μm; β = 1878
	x=0.2; Turn-on field = 3.6 V/μm; β = 2459
	x= 0.4; Turn-on field = 5.6 V/μm; β = 1937
	x=0.5; Turn-on field = 5.3 V/μm; β = 1738
Lanthanum doped gadolinium hexaboride ($La_xGd_{1-x}B_6$)	x=0.1; Turn-on field = 5.02 V/μm; β = 1549
	x=0.2; Turn-on field = 5.27 V/μm; β = 1537
	x=0.3; Turn-on field = 4.51 V/μm; β = 1524
	x=0.4; Turn-on field = 5.04 V/μm; β = 1566
	x=0.5; Turn-on field = 5.01 V/μm; β = 1568

It is well known that the work function of LaB_6, NdB_6 and GdB_6 are 2.6 eV, 1.6 eV and 1.5 eV respectively. The as-synthesised NdB_6 and GdB_6 have been deposited over a silicon substrate and field emission study were performed. The observed enhancement factor (β) of NdB_6 and GdB_6 nanorods were 2263 and 1490 respectively. Further, the doping of

lanthanum at the metal site in MB_6 (where M=Nd and Gd) was attempted. The field emission study of all the samples ($La_xM_{1-x}B_6$; M=Nd/Gd, x=0.1, 0.2, 0.3, 0.4 and 0.5) indicates that the sample having composition x = 0.3 shows better results (low turn-on field and high enhancement factor) as compared to other composition of $La_xM_{1-x}B_6$. The enhanced field emission properties of $La_xM_{1-x}B_6$ with x = 0.3 is due to the exposer of the 110 plane, which contains more metal terminated region. The presence of metal termination facilitates the emission of electrons from the surface of the cathode in the presence of the applied electric field.

In contrast to boron rich boride such as NdB_6, GdB_6, $La_xNd_{1-x}B_6$, $La_xGd_{1-x}B_6$, I have also synthesised the boron deficient metal boride *i.e.* zirconium diboride (ZrB_2). First, nanostructured zirconium oxide (ZrO_2) of size 10-15 nm has been synthesised using the hydrothermal route at 120 ℃. The synthesised ZrO_2 has been annealed with elemental boron at 1200 ℃ in an inert atmosphere for the synthesis of ZrB_2. The TEM study of synthesised ZrB_2 powder shows the formation of particles having a size of 150 nm. The doctor blade technique (economical and scalable) has been employed to fabricate ZrB_2 film on a stainless-steel substrate. The corrosion-resistant properties of ZrB_2/SS have been investigated in a different electrolyte by potentiodynamic polarization and EIS study. The electrochemical studies show that ZrB_2 films would be an excellent anticorrosive coating material in strong acid, strong alkaline as well as neutral media. It was observed that ZrB_2/304SS have high resistance in neutral solution than acidic and alkaline solutions containing sulfate ion upto several days immersion. The corrosion current density (j_{corr}) of ZrB_2 coated stainless steel is less than bare stainless steel in acidic as well as alkaline medium. Initially, ZrB_2 coating offered maximum corrosion resistance properties as measured by polarization curve and EIS study which indicates ZrB_2 shows the highest charge transfer resistance (R_{ct}) value.

The synthesis method developed here can be further used for another metal boride. The low-temperature synthesis of metal diboride can further utilized for the other ultra-high-temperature metal diboride such as HfB_2, TiB_2, CrB_2. Here, the process for the development of metal hexaboride nanorods can be extended to many other complex metal borides, metal oxide and metal chalcogenides which are known for their optical and electrical properties. The present thesis will contribute a worth full knowledge for the synthesis of metal boride powder and their film fabrication of metal borides. The obtained

metal borides show excellent field emission as well as anticorrosion properties using metal hexaboride and zirconium diboride respectively.

Annexure

Chapter A1

New low temperature environmental friendly process for the synthesis of tetragonal MoO_2 and Its field emission properties

A1. Introduction

Molybdenum-containing materials play an important role in the technology sectors of today's growing industries due to their exotic electronic and physical properties.[1,2] They are widely used in the fabrication of electronic circuits,[3,4] catalysts,[5] lubricants,[6] field emitters,[7] sensing,[8] electrochromic displays,[8] and energy storage applications.[9] Among these, molybdenum oxides are technologically important materials because of its applications in tvarious electronic product due to their structural & electronic properties.[10,11] It is well known that MoO_2 could be crystallized in monoclinic, tetragonal and hexagonal.[12] Among these polymorphs, nanostructured monoclinic MoO_2 has been used as field emitters.[13,14] Although monoclinic MoO_2 shows field emission characteristics;[15–17] however, requires a higher temperature ~1370 °C for stabilization under ambient conditions, thus, making its usage in devices is unfeasible. Earlier, synthesis of the monoclinic phase of MoO_2 has been carried out by reduction of starting materials,[8,18–20] hydrothermal route,[20] electrodeposition,[21] thermal vapour deposition, chemical vapour deposition and electrospinning.[8] Though many efforts have been made by the researchers for the synthesis of monoclinic MoO_2, the tetragonal MoO_2 has only been synthesized by thermal decomposition of molybdenum methoxide complexes at 500 °C under N_2 atmosphere.[22] Thermal decomposition of methoxide complexes is a tedious and complex process and scaling up would be a challenging task. Moreover, the expensive processing of the starting materials makes a thin film fabrication process uneconomical. So, it is important to develop a green synthetic route, which would be scalable too. Besides that, there are no reports on the fabrication of tetragonal MoO_2 films via a spin coating process. The motivation of the present study is to develop an economical, low temperature and environmental-friendly process for the synthesis of tetragonal MoO_2. To achieve this goal, here we have attempted to synthesise highly stable tetragonal MoO_2 using hot injection method at 200 °C in refined oil (as solvent). In the above process, the utilization of refined oil makes the process economical, scalable as well as environmental-friendly. Earlier, synthesis of MoO_2 has been carried out via electrodeposition, thermal vapour deposition, chemical vapour deposition, hydrothermal, electrospinning and high-temperature thermal decomposition of molybdenum methoxide complexes.[19,20,23–26] To the best of our knowledge, there is no report on the synthesis of tetragonal MoO_2 at ambient pressure and low temperature in biocompatible solvents. Earlier, production of various nanostructured material (silver, biodiesels as well as polymers) in the presence of vegetable oils have been done because of its inherent biodegradability, low toxicity and abundant in nature.[27–31]

Here, we have shown low-temperature synthesis of t-MoO_2 and their thin-film fabrication via a spin coating process. Finally, we have studied their field emission property and the hydrogen evolution reaction (HER). To the best of our knowledge, only monoclinic MoO_2 has been investigated for field emission properties.

A1.2 Experimental details

A1.2.1 Materials

Ammonium molybdate tetrahydrate (Alfa Aesar, 99%), thiourea (Alfa Aesar, 99%) and oleic acid (Alfa Aesar, 99%) was used as a starting material. Refined oil [composition: Linoleic acid (polyunsaturated omega-6) 59%; Oleic acid (monounsaturated omega-9) 30%; Stearic acid (saturated) 6%; Palmitic acid (saturated) 5%] was purchased from the local market for the synthesis. All the reagents have been used as received.

A1.2.2 Synthesis of molybdenum (IV) oxide

Hence in the present study, for the synthesis of MoO_2, 0.6 gm of ammonium molybdate dispersed in 15 ml of refined oil and 1 ml of oleic acid as Mo-precursor. The mixture was stirred continuously in a three-necked round bottom flask onto the hot plate at 500 rpm in a nitrogen atmosphere. The reaction temperature was increased from room temperature to 100 °C for 30 min followed by then further increased in temperature to 200 °C for 1 h. After 1 h, the reaction temperature was reduced to 100 °C, 0.7 gm of thiourea was dispersed in 5 ml of distilled water as S- precursor. The S-precursor was slowly injected into Mo-precursor solution and maintained the reaction temperature at 100 °C for 1 h under continuous stirring and N2 atmosphere. The obtained black colour homogeneous dispersion was separated by centrifugation followed by washing with acetone and then dried in air. Finally, a black colour shiny fine powder was obtained and was used for further analysis. The schematic representation of MoO_2 synthesized using hot injection route is given in Figure A1. 1.

A1.2.3 Silicon substrate cleaning

Silicon wafer oriented in (1 0 0) direction has been taken and cut into 1 X 1 cm^2 piece. These pieces were first cleaned by ultra-sonication in Isopropyl alcohol for 15 minutes and then rinsed with double distilled water followed by piranha washing (3:1; H_2SO_4: H_2O_2) for 10 min to remove the organic residues present on the surface. Finally, it was dried in a vacuum desiccator for further use.

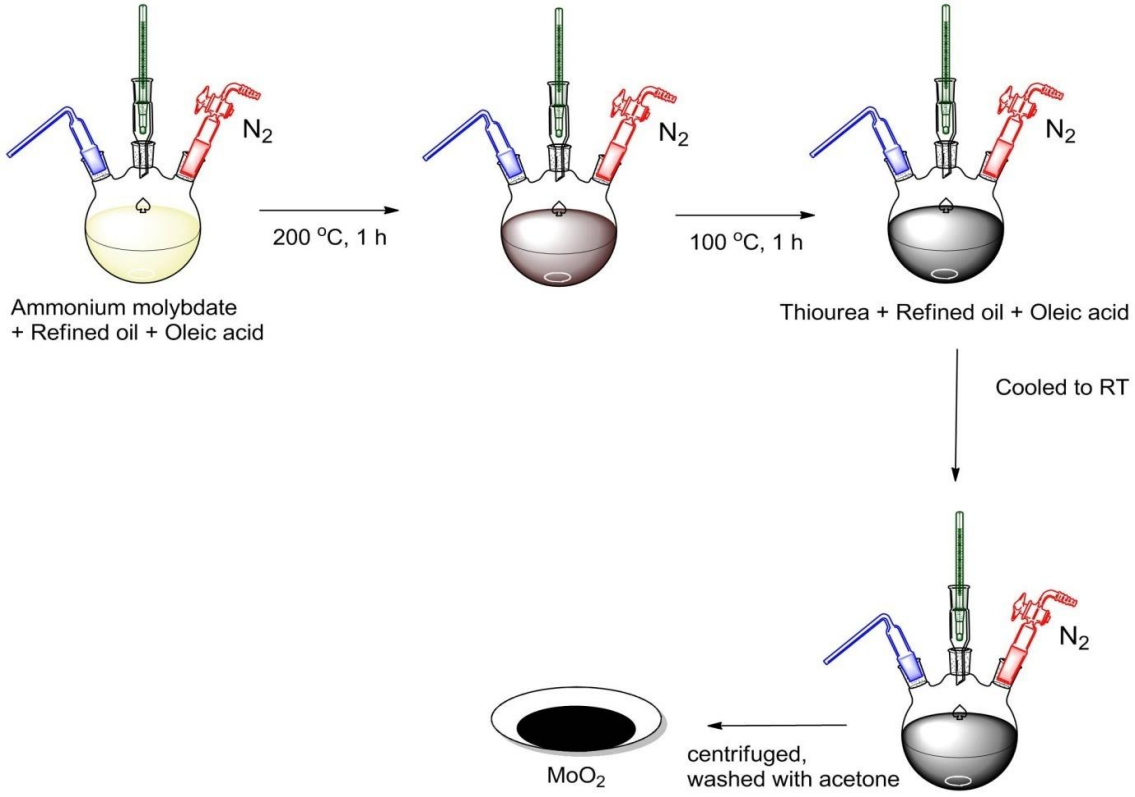

Figure A1.1. *Schematic representation of the synthesis of MoO_2.*

A1.2.4 Fabrication of molybdenum (IV) oxide film

50 mg of synthesized molybdenum dioxide powder was dispersed in 2 ml of a mixture of ethanol and ethylene glycol (1:1 volume ratio), sonicated for 30 min to get uniform dispersion. 200 µl of resulting dispersion was subjected to spin coating onto cleaned Si substrate at 1000 rpm for 1 min. The process of spin coating MoO_2 was repeated twice. The film was further dried in an argon atmosphere at 200 °C for 12 h with slow heating rate and cooling rate of 20 °C/min.

A1.2.5 Field emission measurements

Field emission can be defined as the emission of electrons from conducting/semiconducting materials via quantum mechanical tunnelling process, wherein the electrons tunnel through the surface potential barrier by the application of a very strong electrostatic field of the order of 10^6–10^7 V/cm. Nowadays, 2D materials like graphene and MoS_2 nanosheets based materials have much been explored in field emission studies due to their excellent electrical conductivity, ease of synthesis, thermal and mechanical stability.[32–35] Field emission (FE) measurements were performed in ultra-high vacuum set-up using diode geometry, with a base pressure of ~1.5×10^{-6} Torr at room temperature. An APLAB high voltage DC power supply (0.5–5 kV; 20 mA) and a Keithley electrometer

was used to measure the FE characteristics. The applied electric field was estimated by dividing the applied voltage by the inter-electrode gap (typically, 250 μm). The measured emission area of MoO_2 thin film was 1×1 cm^2. In the present measurement, the turn on-field and threshold field were measured at the current density of 1 μA/cm^2 and 10 μA/cm^2 respectively.

A1.2.6 Electrochemical measurements

The electrochemical performance of tetragonal MoO_2 nanosheets has been carried out in a standard three-electrode system with MoO_2 coated on carbon cloth act as working electrode, Platinum strip as counter electrode and Ag/AgCl served as a reference electrode. The working electrode was prepared with a slurry containing 80 wt % of active material (MoO_2), 10 wt% of conducting carbon (acetylene black) and 10 wt% of PVDF as a binder. Then the slurry was coated on the fresh carbon cloth (0.5×0.5 cm^2) on both sides and dried at 80 °C for 12 h. For hydrogen evolution reaction (HER) activity of tetragonal MoO_2, linear sweep voltammetry (LSV) measurement was carried out in a 0.5M H_2SO_4 as an electrolyte (pH~1). The LSV was measured in the voltage range of 0 to -1.0 V at a scan rate of 5 mV/s. The reference electrode potential was calibrated to the standard hydrogen electrode (SHE) using the equation, $E_{SHE}=E_{Ag/AgCl}+0.059\ pH+E^0_{Ag/AgCl}$.

A1.3 Results and discussion

In the present study, we have attempted to develop a low-temperature, environmentally friendly process for stabilization of tetragonal MoO_2 nanostructures and their thin films and have studied their application as field emitters. To achieve this goal, the process involves three steps. The first step deals with the design of green synthesis process for stabilization of nanostructured tetragonal MoO_2 at low temperature. The synthesis of tetragonal MoO_2 has been carried out using ammonium molybdate and refined oil by a low-temperature process (200 °C) as compared to earlier reports (minimum reported temperature is 550 °C).[22] In the second step, a low-cost spin coating process has been employed to fabricate MoO_2 films on a silicon substrate. Further, the field emission properties of MoO_2 film have been studied. The powder X-ray diffraction pattern of the product obtained by reaction of ammonium molybdate and thiourea in presence of refined oil at 200 °C shows the formation of highly crystalline tetragonal MoO_2 with sharp diffraction peaks (Figure A1.2). All the diffraction peaks were indexed based on the standard X-ray diffraction data of tetragonal MoO_2 (JCPDS: 01-074-4517) with a space

group of P42/mnm. The refined tetragonal lattice parameters are a=4.821 (4) Å and c=2.871 (7) Å. The morphology of the synthesised sample has been first investigated via Field emission scanning electron microscopy (FESEM). The FRSEM micrograph shows the formation of porous agglomerated nanosheets of MoO_2 (Figure A1.3). The FESEM-EDX shows the presence of Mo and O elements (Figure A1.3b). The absence of sulphur (from the thiourea source) was confirmed by EDX mapping (Figure A1.3c-d).

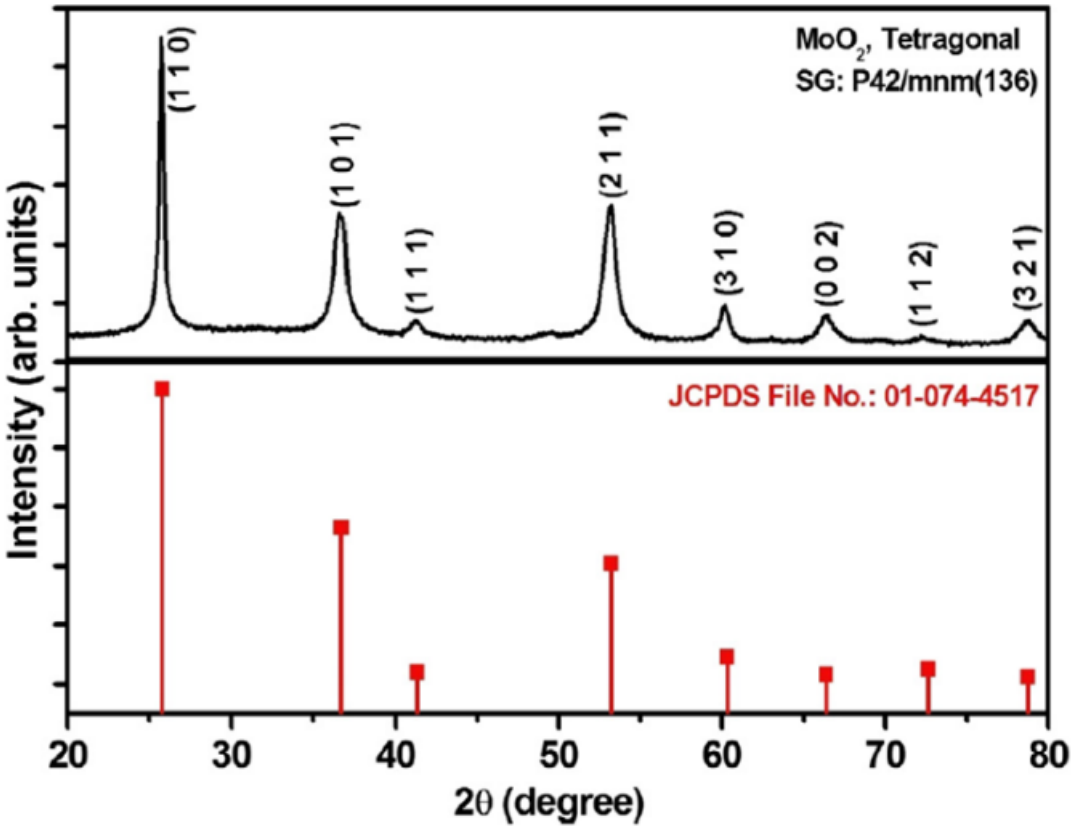

Figure A1.2. *Powder X-ray diffraction pattern of powder MoO_2.*

Further, transmission electron microscopy (TEM) study also confirms the formation of thin nanosheets. A close observation suggests the pores like a thin sheet of the synthesised sample (Figure A1.4a). High-resolution TEM micrograph (Figure A1.4b) shows the lattice fringes with a spacing of 3.47 Å correspond to (1 1 0) plane. TEM-EDX also confirms the presence of only Mo and O (Figure A1.4c).

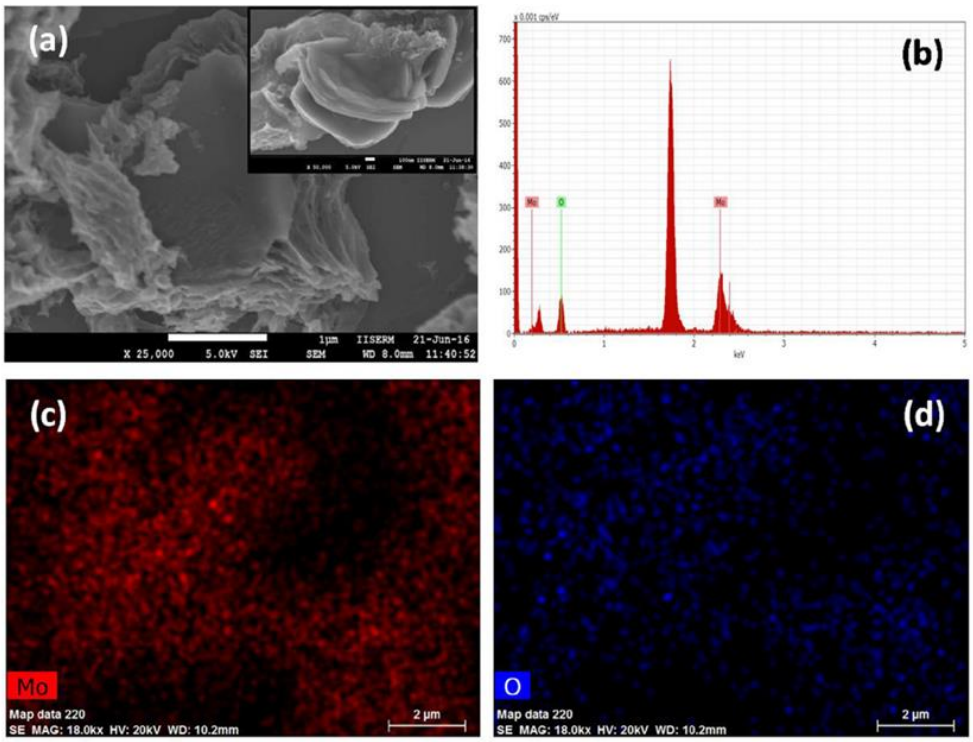

Figure A1.3. *FESEM micrographs of (a) powder MoO_2. (b) EDX spectrum. (c & d) EDX mapping showing Mo and O.*

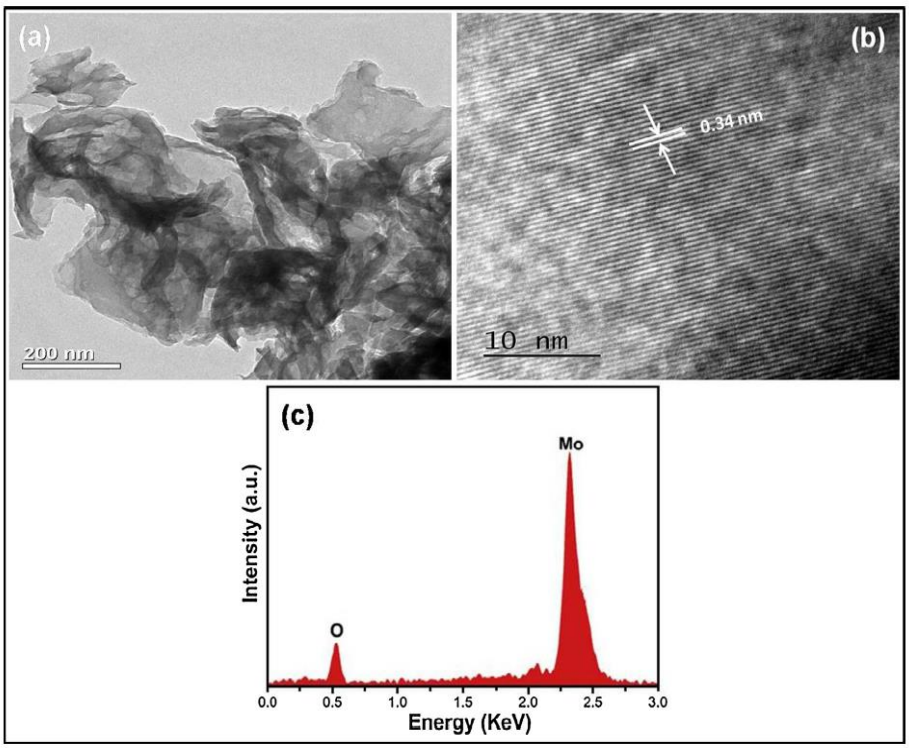

Figure A1.4. *(a) TEM micrograph. (b) HRTEM micrograph. and (c) EDX of powder MoO_2.*

The chemical composition and the electronic state of MoO_2 have analysed from XPS studies.

A typical survey scan of MoO_2 displayed in Figure A1.5a having four distinct peaks at 230.7 (Mo 3d), 399.5 (Mo $3p_{3/2}$), 416.2 (Mo $3p_{1/2}$) and 530.9 eV (O 1s) of molybdenum dioxide. High-resolution spectra of Mo 3d is deconvoluted into two peaks at 230.6 eV and 232.9 eV of Mo (IV)3d5/2 and Mo (IV)$3d_{3/2}$ corresponding to Mo (IV) oxidation state of MoO_2 (Figure A1.5b). Interestingly, the characteristic peak at 236.4 eV belongs to Mo (VI)$3d_{3/2}$ of MoO_3 is not observed in our studies. The O 1 s spectrum (Figure A1.5c) indicates that the peak at 530.9 eV belongs to Mo-O bond.[36–39] The XPS valence band (VB) spectrum of MoO_2 shown in Figure A1.5d gives a VB maximum of MoO_2 as 1.98 eV below the Fermi level which is calculated from the intercepts between the tangent of the spectra and baseline from the lower binding energy region.

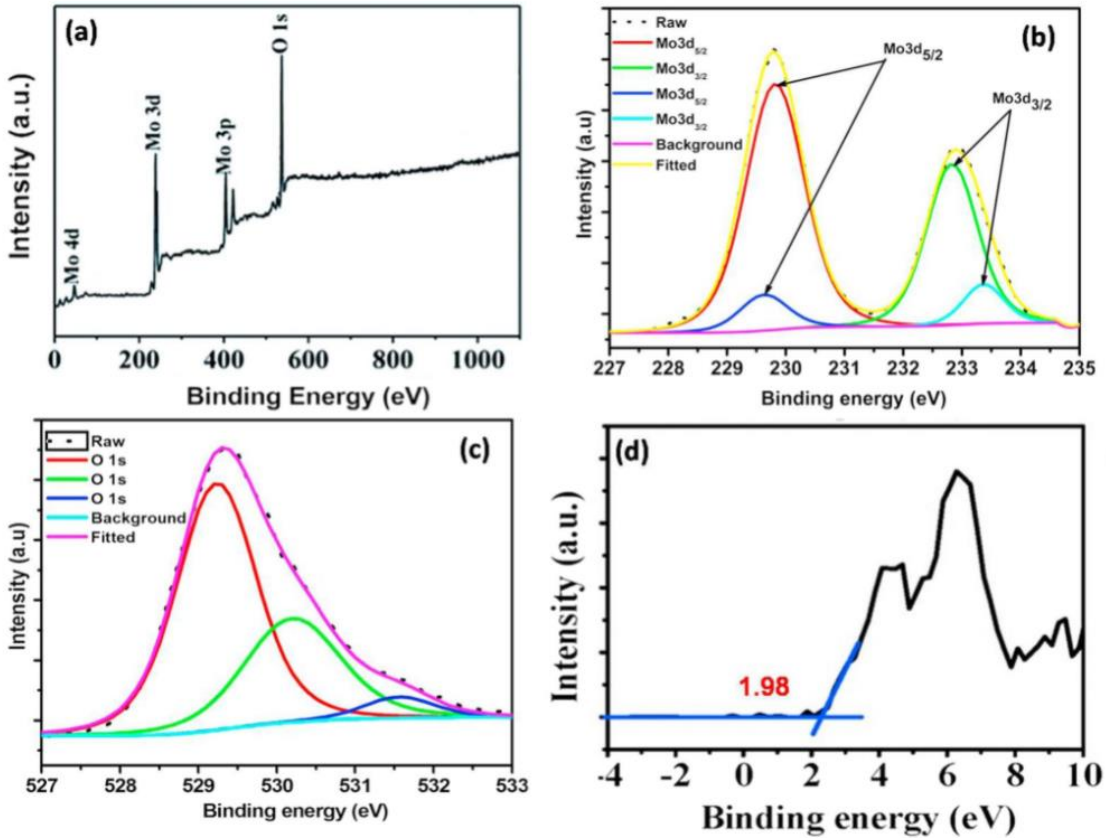

Figure A1.5. *(a) XPS survey spectrum of MoO_2. (b) Deconvoluted spectra of Mo 3d. (c) O 1s and (d) valence band XPS spectrum of MoO_2.*

The nitrogen adsorption-desorption isotherm plot of the synthesised sample shows a type IV isotherm having H3 type hysteresis loop, which indicates the presence of a porous structure (Figure A1.6). In the present work, the surface area of tetragonal MoO_2 exhibits ~92 m^2/g calculated using the Brunauer-Emmett-Teller (BET) method, which is nearly 6 times higher than the earlier report of monoclinic MoO_2 [40]. The pore volume was estimated from the amount adsorbed at a relative pressure of 0.4–0.6 and the value is found to be

~7.03 cc/g. The pore size distribution is estimated using the Barette-Joyner-Halenda (BJH) method from the desorption branch of the isotherm and it is found to be ~6.3 nm. To the best of our knowledge, there is no earlier report on a surface area of tetragonal MoO_2.

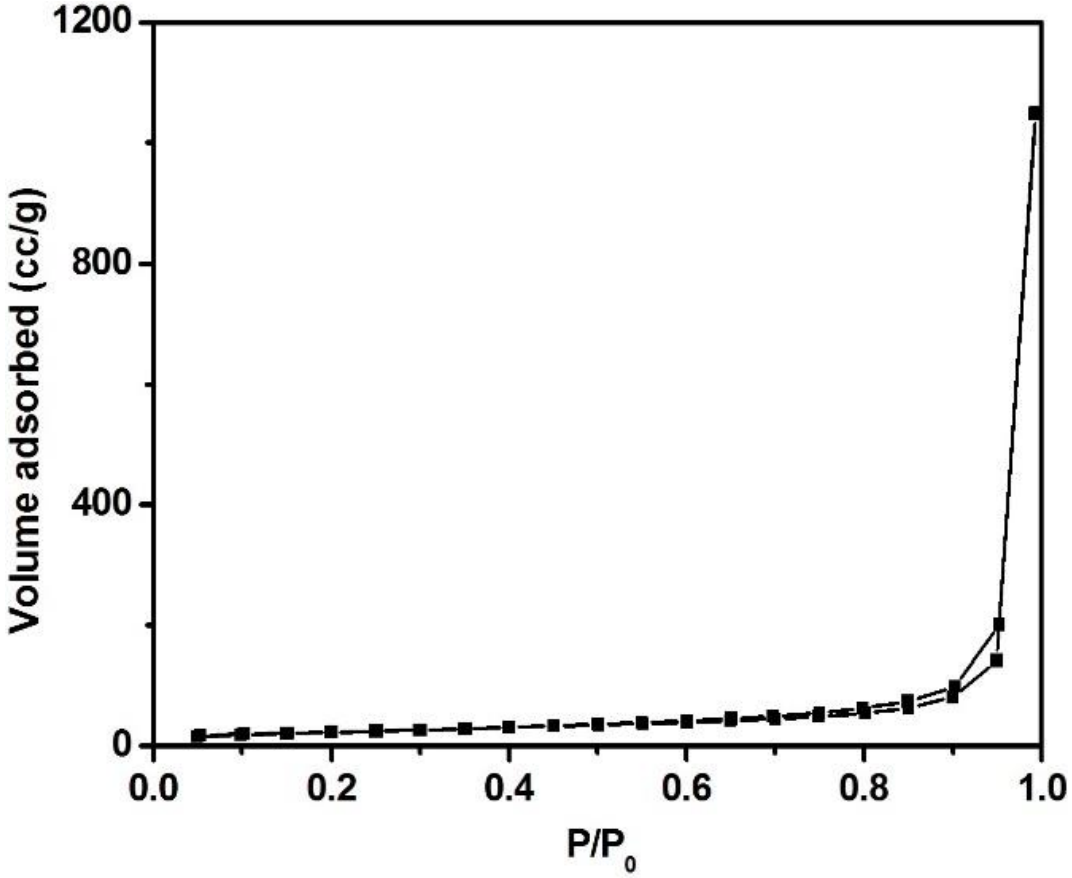

Figure A1.6. *Nitrogen adsorption-desorption isotherm curve of powder MoO_2.*

FTIR spectrum shows the (Figure A1.7a) absorption peaks at 743 and 957 cm^{-1} are ascribed to the vibrational mode of Mo-O-Mo bond, which is in close agreement with the earlier report of the thin film[41] and crystalline bulk sample.[42] The weaker absorption peaks at 2923 and 3423 cm^{-1} were characterized to -OH vibrations of adsorbed moisture. The peak at 1626 cm^{-1} can be assigned to the C=C stretching mode for oleic acid as well as the remaining hydroxyl groups on the MoO_2 surface.[43,44] The optical absorption spectrum of MoO_2 was measured in the wavelength range of 200–800 nm at room temperature (Inset of Figure A1.7b). The absorption maximum is at 436 nm, which lies in the visible region, and its absorption edge was at around 535 nm. The absorption coefficient (α) is calculated using equation $(\alpha h\upsilon)^2=B^2(h\upsilon-E_g)$, where hυ is photon energy and B is a constant related to the material. The optical band gap (E_g) of MoO_2 is calculated by extrapolating the linear portion of the plot of $[F(R)h\upsilon]^2$ vs photon energy (hυ) and is found to be 2.39 eV (Figure

A1.7b). Liu *et al*. reported the bandgap of monoclinic MoO_2 micro-sheets is 4.22 eV[45] and Mohamed *et al.* reported the bandgap of monoclinic molybdenum oxide thin films varies from 2.64-2.69 eV[46] and increased slightly with the increasing oxygen partial pressure. The earlier reports explain that the variation in the optical band gap of molybdenum oxides depend on the stoichiometry and structure of the oxide. The bandgap of tetragonal MoO_2 in the visible region compared to the monoclinic MoO_2 phase.

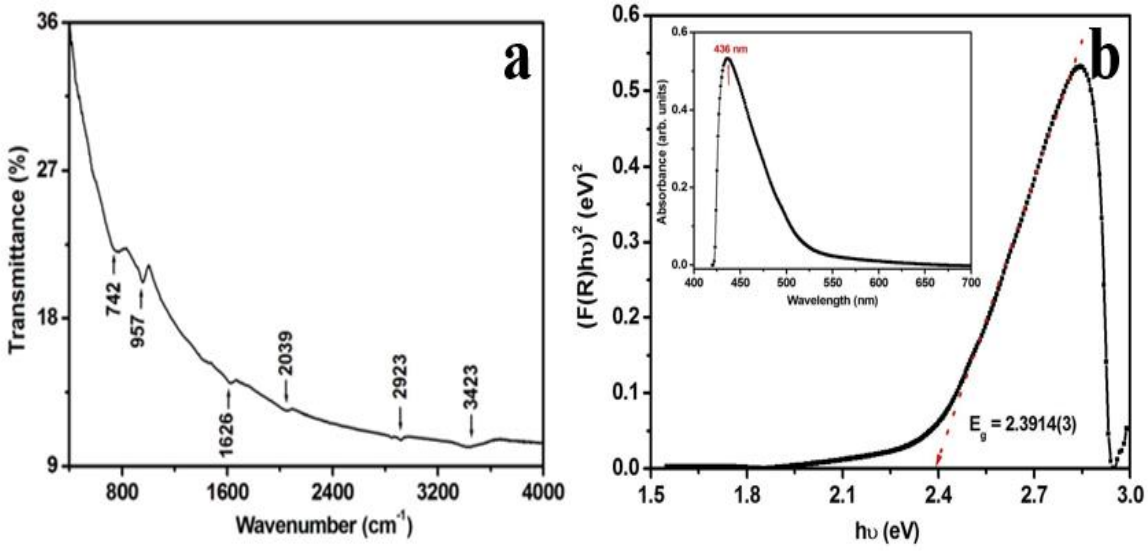

Figure A1.7. *(a) FTIR spectrum. (b) Diffuse reflectance spectra of powder MoO_2 nanosheets (Inset: absorption spectrum).*

A1.3.1 Field emission study

The field emission characteristics of MoO_2 film were measured by the method described in the experimental section. The field emission properties of tetragonal MoO_2 are not reported yet. From the morphological studies, the prepared MoO_2 thin film shows the sheet-like structure with edges and a large proportion of nano-protrusions resulting in higher field emission strength. Figure A1.8a shows the characteristics of field emission current density as a function of an applied electric field for several bias voltage sweeps. The emission current increases rapidly with the increase in applied voltage. The obtained current vs electric field (J-E) plot indicates the turn-on field (defined as the field required to produce an emission current density of 0.1 μA/cm^2) is found to be 0.325 V/μm, while the threshold field (defined as to draw emission current density of~50 μA/cm^2) is ~5.5 V/μm respectively.

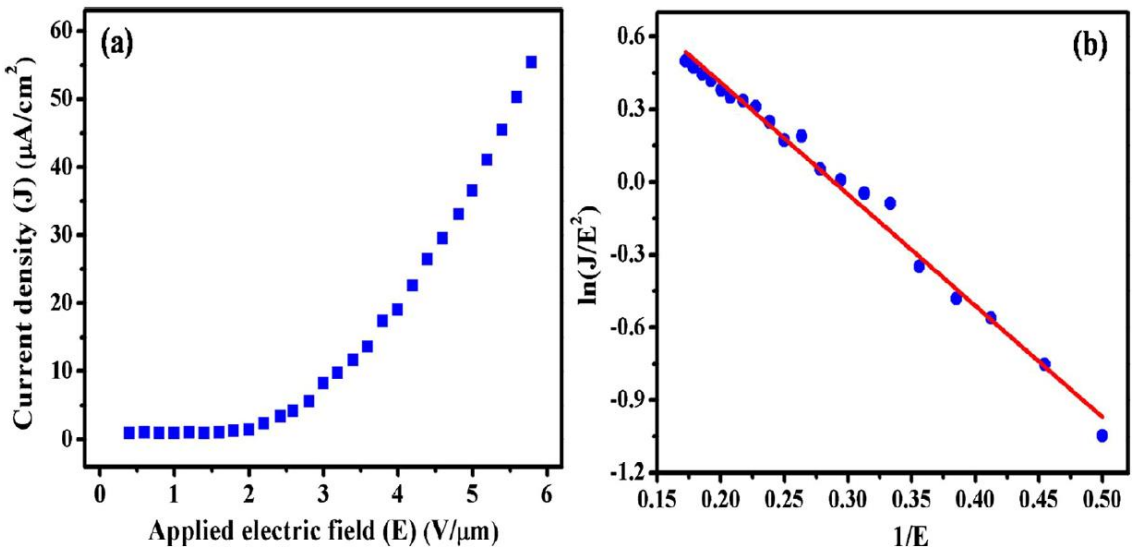

Figure A1.8. *Field emission studies of tetragonal MoO_2. (a) applied electric field vs field emission current density. (b) F-N plot showing linear behaviour.*

The field emission current density can be expressed by a simplified Fowler-Nordheim (F-N) equation,[47–49] $\ln(J/E^2)=(1/E)\,(-B\varphi^{3/2}/\beta) + \ln(A\beta^2/\varphi)$, where β is the field enhancement factor, φ is the work function of an emitter (5.7 eV for molybdenum oxides), J is the emitter current density, E is the applied electric field. A and B are constants with the values of 1.56×10^{-10} A V^{-2} eV and 6.83×103 $eV^{-3/2}$ V μm^{-1} respectively. According to FN theory, the plot of ln (J/E^2) versus 1/E gives a straight line, which indicates that the emitting electrons have mainly originated from quantum mechanical tunnelling of electrons. For a metallic emitter, the FN plot exhibits linear behaviour whereas non-linear nature indicates the semiconducting behaviour of the field emitters. In the present study, the FN plot is found to be nearly linear and this observation is in close agreement with reports on metallic nanomaterials (Figure A1.8b).[50] The field enhancement factor (β) is calculated from the work function of the emitter and the slope of FN plot using the relation: $\beta=[Bd\varphi^{3/2}]/S$, where d is the anode-cathode separation and S is the slope of the FN plot. The calculated FN enhancement factor (β) of MoO_2 sheets is found to be ~21,460. It is shown that field emission properties might be dependent on the morphology of emitter material. Khademi *et al.* obtained the enhancement factor for MoO_2 nanowires with nano-protrusions and nanostars were found to be 13,784 and 5257.[51] The present result shows that higher enhancement factor and lower turn-on field for MoO_2 as compared with the reported MoO_2. The synthesized tetragonal MoO_2 nanosheets show better field emission than other well-known metal oxide nanomaterials including ZnO, WO_x and molybdenum oxides.[7,49,52–59] The FE efficiency is dependent on the electronic structure near the valence

band and the narrow bandgap of this MoO_2 is probably monitoring the current density.[60] Also, the porosity of MoO_2 sheet plays a role in controlling the conductivity and hence the FE current density of this planar emitter. Thus, the above observations point toward that the synthesized tetragonal MoO_2 nanosheets are good candidates for the application of cold cathode emitters due to their relatively low turn-on field and high enhancement factor.

A1.3.2 Hydrogen evolution reaction

Finally, the prepared tetragonal MoO_2 nanosheets were used as an electrode material for the study of electrocatalytic hydrogen evolution reaction. Figure A1.9a shows the LSV curves of bare carbon cloth (CC) and modified by MoO_2 electrode at a scan rate of 5 mV/s. It is seen that bare CC does not exhibit any HER activity.

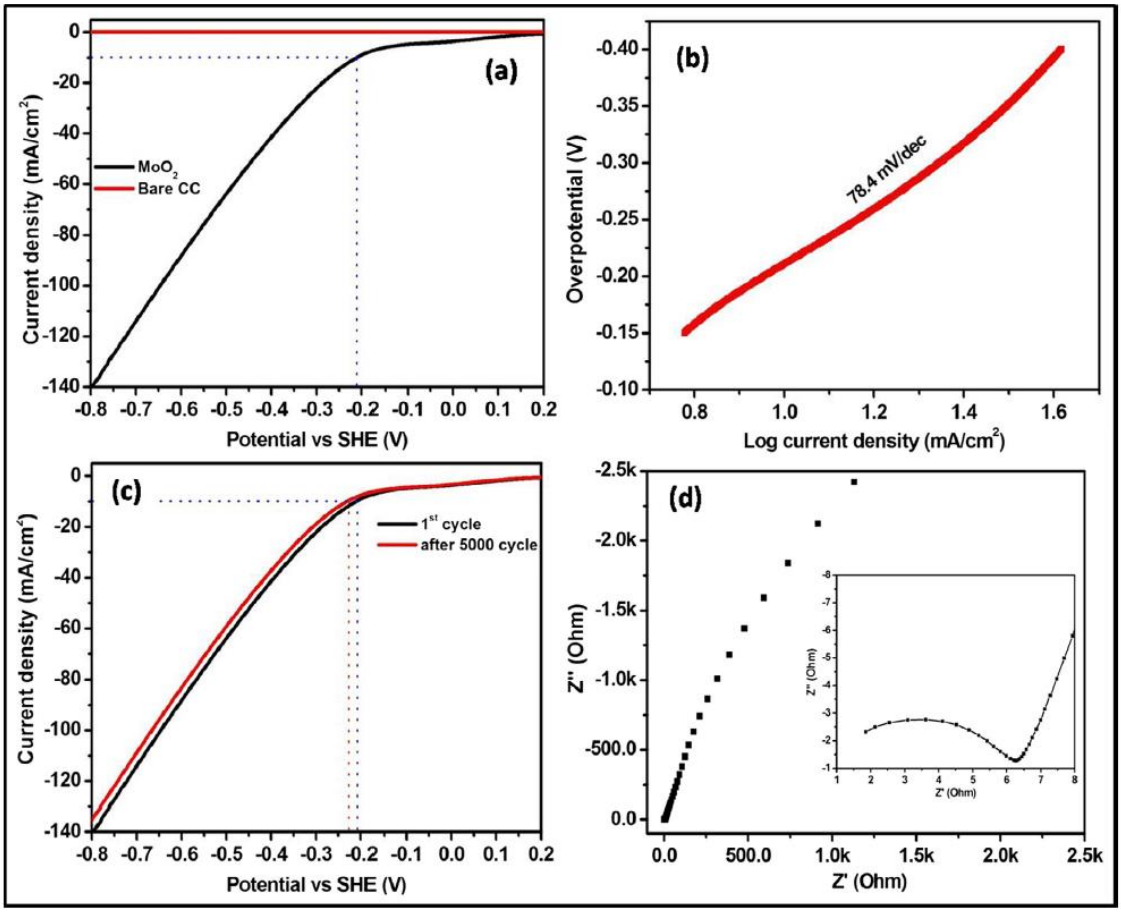

Figure A1.9. *(a) LSV polarization curves for HER activity in 0.5M H_2SO_4 at a scan rate of 5 mV/s. (b) Tafel plot. (c) HER polarization curves for MoO_2 before and after 5000 cycles of potential sweeps at 50 mV/s. (d) EIS spectra of MoO_2.*

In contrast, MoO_2 electrode shows excellent HER activity and it requires the overpotential of -210 mV vs SHE to achieve a current density of 10 mA/cm^2. The HER kinetics of the tetragonal MoO_2 is evaluated from Tafel slope using the equation, $\eta = b \log j + a$, where b is the Tafel slope and j is the exchange current density. The tetragonal MoO_2

catalyst shows the Tafel slope of 78.4 mV/dec (Figure A1.9b). The stability of the electrocatalyst is a crucial factor in HER activity, hence the MoO_2 electrode tested for 5000 cycles at 50 mV/s (Figure A1.9c). It is observed that MoO_2 electrode shows good stability even after 5000 cycles in an acidic medium. This result emphasizes the good stability and strong interaction of the electrode material and electrode. The electrode kinetics has been studied from electrochemical impedance spectra (EIS) given in Figure A1.9d. As can be seen in the inset of Figure A1.9d, the curve has a semicircle at high-frequency and a vertical line at low-frequency regions. The diameter of the semicircle is attributed to the contact and charge-transfer impedance of the electrode.[59] The tetragonal MoO_2 exhibits a lower charge-transfer resistance of ~5.2 Ω which suggests a highly efficient electron transport and favourable HER kinetics at the electrode/electrolyte interface.

A1.4 Conclusions

We have developed a simple and efficient approach to synthesize pure phase porous tetragonal MoO_2 nanosheets at low temperature in the presence of refined oil. The synthesised MoO_2 powder has been spin-coated over silicon substrate via spin coating. The field emission studies of the fabricated film show a low turn-on field (0.325 V/μm) and can obtain a maximum current density of ~55 μA/cm^2 at an applied field of 5.8 V/μm. This work may open the way for the potential use of tetragonal MoO_2 related to flexible field-emission displays and electronic devices because of their exotic field emission properties. Also, electrochemical studies of tetragonal MoO_2 showed HER activity with a reasonable overpotential of -210 mV in an acidic medium.

A1.5 References

1 D. Y. Park, Y. K. Sun and S. T. Myung, *J. Power Sources*, 2015, **280**, 1–4.

2 Y.-K. Liu, C.-G. Liang, Z.-L. Wang, Y.-Z. He, X.-L. Lang and M.-H. Zhou, *Jpn. J. Appl. Phys.*, 2000, **39**, 3915–3918.

3 V. S. Saji and C.-W. Lee, *ChemSusChem*, 2012, **5**, 1146–1161.

4 Y. F. Lin and W. B. Jian, *Nano Lett.*, 2008, **8**, 3146–3150.

5 Y. Okamoto, N. Oshima, Y. Kobayashi, O. Terasaki, T. Kodaira and T. Kubota, *Phys. Chem. Chem. Phys.*, 2002, **4**, 2852–2862.

6 M. Zalaznik, S. Novak, M. Huskić and M. Kalin, *Lubr. Sci.*, 2016, **28**, 27–42.

7 J. Zhou, S. Z. Deng, N. S. Xu, J. Chen and J. C. She, *Appl. Phys. Lett.*, 2003, **83**, 2653–2655.

8 Y. Shi, B. Guo, S. A. Corr, Q. Shi, Y. S. Hu, K. R. Heier, L. Chen, R. Seshadri and G. D. Stucky, *Nano Lett.*, 2009, **9**, 4215–4220.

9 L. Q. Mai, B. Hu, W. Chen, Y. Y. Qi, C. S. Lao, R. S. Yang, Y. Dai and Z. L. Wang, *Adv. Mater.*, 2007, **19**, 3712–3716.

10 S.-L. Zhang and F. M. d'Heurle, *Appl. Phys. Lett.*, 2000, **76**, 1831-4.

11 W. H. Lai, M. H. Hon, L. G. Teoh, Y. H. Su, J. Shieh and C. K. Chen, *J. Electron. Mater.*, 2008, **37**, 1082–1087.

12 K. T. Jacob, V. S. Saji, J. Gopalakrishnan and Y. Waseda, *J. Chem. Thermodyn.*, 2007, **39**, 1539–1545.

13 L. Kumari, Y. R. Ma, C. C. Tsai, Y. W. Lin, S. Y. Wu, K. W. Cheng and Y. Liou, *Nanotechnology*, 2007, **18**, 115717-8.

14 W. Dong, H. Huang, Y. Zhu, X. Li, X. Wang, C. Li, B. Chen, G. Wang and Z. Shi, *Nanotechnology*, 2012, **23**, 425602.

15 F. Wang and B. Lu, *Phys. B Condens. Matter*, 2009, **404**, 1901–1904.

16 J. Liu, Z. Zhang, C. Pan, Y. Zhao, X. Su, Y. Zhou and D. Yu, *Mater. Lett.*, 2004, **58**, 3812–3815.

17 A. Khademi, R. Azimirad, A. A. Zavarian and A. Z. Moshfegh, *J. Phys. Chem. C*, 2009, **113**, 19298–19304.

18 L. C. Yang, Q. S. Gao, Y. Tang, Y. P. Wu and R. Holze, *J. Power Sources*, 2008, **179**, 357–360.

19 Y. Zhao, Y. Zhang, Z. Yang, Y. Yan and K. Sun, *Sci. Technol. Adv. Mater.*, 2013, **14**, 043501–043514.

20 C. Guo, G. Zhang, Z. Shen, P. Sun, Z. Yuan, Q. Jin, B. Li, D. Ding and T. Chen,

Chinese J. Chem. Phys., 2006, **19**, 543–548.

21 M. P. Zach, K. Inazu, K. H. Ng, A. J. C. Hemminger and R. M. Penner, *Chem. Mater.*, 2002, **14**, 3206–3216.

22 G. A. Seisenbaeva, M. Sundberg, M. Nygren, L. Dubrovinsky and V. G. Kessler, *Mater. Chem. Phys.*, 2004, **87**, 142–148.

23 U. Č. Lačnjevac, *J. Serbian Chem. Soc.*, 2013, **78**, 549–554.

24 L. Zeng, X. Huang, X. Chen, C. Zheng, R. Liu, G. Chen, Q. Qian, Q. Chen and M. Wei, *RSC Adv.*, 2016, **6**, 105558–105564.

25 L. Zhou, H. Bin Wu, Z. Wang and X. W. D. Lou, *ACS Appl. Mater. Interfaces*, 2011, **3**, 4853–7.

26 W. Luo, X. Hu, Y. Sun and Y. Huang, *Phys. Chem. Chem. Phys.*, 2011, **13**, 16735–16740.

27 M. Robaiah, M. Rusop, S. Abdullah, Z. Khusaimi, H. Azhan and N. A. Asli, *AIP Conf. Proc.*, 2017, **1877**, 030008-8.

28 M. Gobin, P. Loulergue, J. L. Audic and L. Lemiègre, *Ind. Crops Prod.*, 2015, **70**, 213–220.

29 Y. Xia and R. C. Larock, *Green Chem.*, 2010, **12**, 1893–1909.

30 A. Kshirsagar, T. Khanna, V. Dhanwe, K. H. Kate and P. K. Khanna, *J. Nanosci. Nanotechnol.*, 2018, **18**, 386–393.

31 M. J. Garcia-Campo, L. Quiles-Carrillo, J. Masia, M. J. Reig-Pérez, N. Montanes and R. Balart, *Materials (Basel).*, 2017, **10**, 1339–1358.

32 M.-J. Lee, S. Han, S. H. Jeon, B. H. Park, B. S. Kang, S.-E. Ahn, K. H. Kim, C. B. Lee, C. J. Kim, I.-K. Yoo, D. H. Seo, X.-S. Li, J.-B. Park, J.-H. Lee and Y. Park, *Nano Lett.*, 2009, **9**, 1476–1481.

33 M. Chhowalla, H. S. Shin, G. Eda, L.-J. Li, K. P. Loh and H. Zhang, *Nat. Chem.*, 2013, **5**, 263–275.

34 K. K. Naik, R. T. Khare, M. A. More, D. J. Late and C. S. Rout, *RSC Adv.*, 2016, **6**, 29734–29740.

35 K. K. Naik, R. T. Khare, R. V. Gelamo, M. A. More, R. Thapa, D. J. Late and C. S. Rout, *Mater. Res. Express*, 2015, **2**, 095011-7.

36 H. Zhang, L. Zeng, X. Wu, L. Lian and M. Wei, *J. Alloys Compd.*, 2013, **580**, 358–362.

37 J. F. Moulder, W. F. Stickle, P. E. ' Sobol, K. D. Bomben and J. Chastain, *Handbook of X-ray Photoelectron Spectroscopy AReference Book of Standard Spectra for*

Identification and Interpretation of XPS Data, .

38 J. Ni, Y. Zhao, L. Li and L. Mai, *Nano Energy*, 2015, **11**, 129–135.

39 X. Chen, Z. Zhang, X. Li, C. Shi and X. Li, *Chem. Phys. Lett.*, 2006, **418**, 105–108.

40 X. Wang, Y. Xiao, J. Wang, L. Sun and M. Cao, *J. Power Sources*, 2015, **274**, 142–148.

41 R. Mercier, O. Bohnke, C. Bohnke, G. Robert, B. Carquille and M.-F. Mercier, *Mater. Res. Bull.*, 1983, **18**, 1–7.

42 K. Eda, *J. Solid State Chem.*, 1991, **95**, 64–73.

43 M. Jafarpour, M. Ghahramaninezhad and A. Rezaeifard, *New J. Chem.*, 2014, **38**, 2917.

44 C. Avendaño, A. Briceño, F. J. Méndez, J. L. Brito, G. González, E. Cañizales, R. Atencio and P. Dieudonné, *Dalt. Trans.*, 2013, **42**, 2822–2830.

45 X. Liu, Y. He, S. Wang and Q. Zhang, *J. Alloys Compd.*, 2011, **509**, S408–S411.

46 S. . Mohamed, O. Kappertz, J. . Ngaruiya, T. . Leervad Pedersen, R. Drese and M. Wuttig, *Thin Solid Films*, 2003, **429**, 135–143.

47 G. . Fursey, *Appl. Surf. Sci.*, 2003, **215**, 113–134.

48 R. H. Fowler and L. Nordheim, *Proc. R. Soc. A Math. Phys. Eng. Sci.*, 1928, **119**, 173–181.

49 Sunaina, M. Sreekanth, S. Ghosh, S. K. Mehta, A. K. Ganguli and M. Jha, *CrystEngComm*, 2017, **19**, 2264–2270.

50 R. T. Khare, R. V. Gelamo, M. A. More, D. J. Late and C. S. Rout, *Appl. Phys. Lett.*, 2015, **107**, 123503-5.

51 A. Khademi, R. Azimirad, Y.-T. Nien and A. Z. Moshfegh, *J. Nanoparticle Res.*, 2011, **13**, 115–125.

52 I.-C. Yao, P. Lin and T.-Y. Tseng, *Nanotechnology*, 2009, **20**, 125202-6.

53 C. J. Lee, T. J. Lee, S. C. Lyu, Y. Zhang, H. Ruh and H. J. Lee, *Appl. Phys. Lett.*, 2002, **81**, 3648–3650.

54 K. Huang, Q. Pan, F. Yang, S. Ni and D. He, *Mater. Res. Bull.*, 2008, **43**, 919–925.

55 Y. B. And and K. Yong, *J. Phys. Chem. C*, 2007, **111**, 1213–1218.

56 J. Liu, Z. Zhang, Y. Zhao, X. Su, S. Liu and E. Wang, *Small*, 2005, **1**, 310–313.

57 G. Wei, W. Qin, D. Zhang, G. Wang, R. Kim, K. Zheng and L. Wang, *J. Alloys Compd.*, 2009, **481**, 417–421.

58 Y. B. Li, Y. Bando, D. Golberg and K. Kurashima, *Appl. Phys. Lett.*, 2002, **81**, 5048–5050.

59 Y.-J. Tang, M.-R. Gao, C.-H. Liu, S.-L. Li, H.-L. Jiang, Y.-Q. Lan, M. Han and S.-H. Yu, *Angew. Chemie Int. Ed.*, 2015, **54**, 12928–12932.

60 D. Sarker, S. Bhattacharya, R. D. Rodriguez, E. Sheremet, D. Kabiraj, D. K. Avasthi, D. R. T. Zahn, H. Schmidt, P. Srivastava and S. Ghosh, *ACS Appl. Mater. Interfaces*, 2016, **8**, 4994–5001.

Chapter A2

New sustainable and environmental friendly process of synthesis of highly porous Mo_2S_3 nanoflowers in cooking oil and their electrochemical properties

A2.1 Introduction

Nowadays, the synthesis of nanostructured metal chalcogenide using environmentally friendly process have attracted lots of researcher's interest because of their wide variety of application in batteries, fuel cells and supercapacitor.[1,2] Electrochemical capacitors such as ultracapacitors or supercapacitors have rapid charge/discharge cycle, higher power density, longer cycle life and relatively low cost than secondary batteries.[3–6] Recently, nanostructured metal chalcogenides have been widely used as efficient and promising materials in high-performance supercapacitors because of their large in-plane conductivity arise due to layer type structure.[7–9] Metal sulfides have attracted the attention of researchers because of their unique optical and electronic properties.[10–13] Among the metal sulfides, molybdenum disulfide (MoS_2) is one of the most suitable candidates for application of supercapacitors due to its conductivity and layered structure.[14–16] In Mo-S phase diagram, MoS_2 and Mo_2S_3 are two intermediate stable phases, which possesses layered structure. Earlier, MoS_2 nanostructures have been prepared by various methods such as chemical vapour deposition,[17] hydrothermal route,[18] template method, and sulfurization of MoO_2.[19] It may be noted that Mo_2S_3 is stable above 630 °C and below this temperature; Mo_2S_3 decomposes to MoS_2 and Mo. The MoS_2 nanoparticles find applications in catalysis,[20,21] and as a solid lubricant,[22] while the Mo_2S_3 has been widely used as a cathode material in lithium-ion based batteries because of its metallic conductivity.[23,24] The existence of Mo_2S_3 as the sulphide phase in equilibrium, at the temperature of 850-1200 °C established first by McCabe [25] and later by Stubbles and Richardson.[26] It has been found that Mo_2S_3 possessed the lowest sulfur content in the Mo-S system at 1400 °C and that on heating to 1600 °C, Mo_2S_3 dissociates to give molybdenum and sulfur. Based on the bulk Mo-S phase diagram, MoS_2 is thermodynamically more stable and exists up to ~2000 K, while the formation of Mo_2S_3 is possible in the range from 937 to 2000 K.[27] Due to instability in its phase, trivalent molybdenum sulfide nanostructure is difficult to synthesize at low temperature. Che *et al.* have shown that the Mo_2S_3 nanorods can be synthesized via solid-gas reaction at 870 °C in the presence of H_2S/Ar.[28] Zhong *et al.* synthesized Mo_2S_3 nanostructures through chemical vapour deposition method at 810 °C,[29] while Tiwari *et al.* studied the surface reconstruction of MoS_2 to Mo_2S_3 using ultra-high vacuum scanning tunnelling microscopy.[30] However, controlled synthesis of uniform Mo_2S_3 nanostructures at low temperature (< 600 °C) and ambient atmosphere is still a challenge. The present work shows an environmental friendly economical process of the synthesis of pure monoclinic Mo_2S_3 stabilized at low temperature (150 °C) using

hydrothermal route. The lower temperature synthesis helped us to retain the lower dimension of the particle (nanoflowers with a diameter of ~0.5 to 2.0 μm and thickness of ~10 nm). These Mo_2S_3 nanoflowers have shown the super-capacitance properties with high specific capacitance (248 F/g) and energy density (98.7 $Whkg^{-1}$) till the stability of 3000 cycles.

A2.2 Experimental

A2.2.1 Materials

Ammonium molybdate tetrahydrate (Alfa Aesar, 99 %), thiourea (Alfa Aesar, 99 %) and oleic acid (Alfa Aesar, 99 %) was used as a starting material. Refined oil [composition: Palmitic acid (saturated); 5% Stearic acid (saturated); 6% Oleic acid (monounsaturated omega-9); 30% Linoleic acid (polyunsaturated omega-6): 59%] was purchased from local market for the synthesis. All the reagents have been used as received.

A2.2.2 Synthesis of molybdenum (III) sulphide

In a typical synthesis, 0.6 gm of ammonium molybdate and 0.9 gm of thiourea were dispersed in 15 ml of refined oil and followed by 1 ml of oleic acid added as a capping agent, stirred for 15 min at room temperature. The mixture was transferred to a 50 ml Teflon lined stainless steel autoclave, tightly sealed and maintained at 150 °C in an air oven for 24 h. After cooling to room temperature naturally, the resulting black products were separated by centrifugation followed by washing with acetone several times and dried in air.

A2.2.3 Preparation of electrodes and electrochemical measurements

Electrochemical studies of nanostructured Mo_2S_3 were performed in the three-electrode system (CHI 660E, Sinsil International Instrument, Inc.). Mo_2S_3 sample was deposited on a glassy electrode and used as a working electrode. Ag/AgCl and platinum were used as the reference electrode and the counter electrode respectively. For deposition of sample on glassy carbon electrode (GCE) of 3 mm diameter, the electrode was first polished with fine emery paper and 0.3 μm Al_2O_3 powder. Then cleaned it in an ultrasonic bath and dried in a vacuum. In a typical process for the sample deposition, the 1 mg of Mo_2S_3 was dispersed through ultra-sonication in an ethanol-water mixture (1:1) with 5 μL of Nafion solution to get a homogenous solution and drop cast on GCE and dried in vacuum. Electrochemical experiments carried out in 1 M aqueous Na_2SO_4 solution as the electrolyte and the potential window for cycling was confined between −0.4 and +0.6 V. Before doing the electrochemical measurement, we purged inert gas in the electrolyte to

remove the oxygen present in the solution. A galvanostatic charge-discharge (GCD) test was conducted at different current densities (1, 2, 3, 4, 5 and 10 mA/g) for the as-prepared electrodes. Electrochemical impedance spectroscopy (EIS) measurements were studied by applying an AC voltage with 5 mV amplitude in the frequency range from 0.01 Hz to 100 kHz.

A2.3 Results and discussion

Metal chalcogenides, especially molybdenum sulphide is scientifically and industrially very important materials due to their exotic physics and a wide range of applications. The only drawback associated with this is its complex synthetic conditions and toxic starting material, which prevents its large-scale production. In the present study, we have developed a new process for the synthesis of nanostructured Mo_2S_3 using cooking oil as a solvent and studied their electrochemical properties. The powder X-ray diffraction pattern of the product obtained at 150 ℃ is indicating polycrystalline in nature of the sample (Figure A2.1). All the diffraction peaks refined with cell software and indexed to monoclinic Mo_2S_3 with lattice parameters a = 6.084(3) Å, b = 3.218(7) Å, c = 8.623(5) Å and β = 102º which are consistent with the standard data (JCPDS File No. 01-078-1332) [34]. No other secondary phases and impurities were detected, which shows high purity of the synthesised sample.

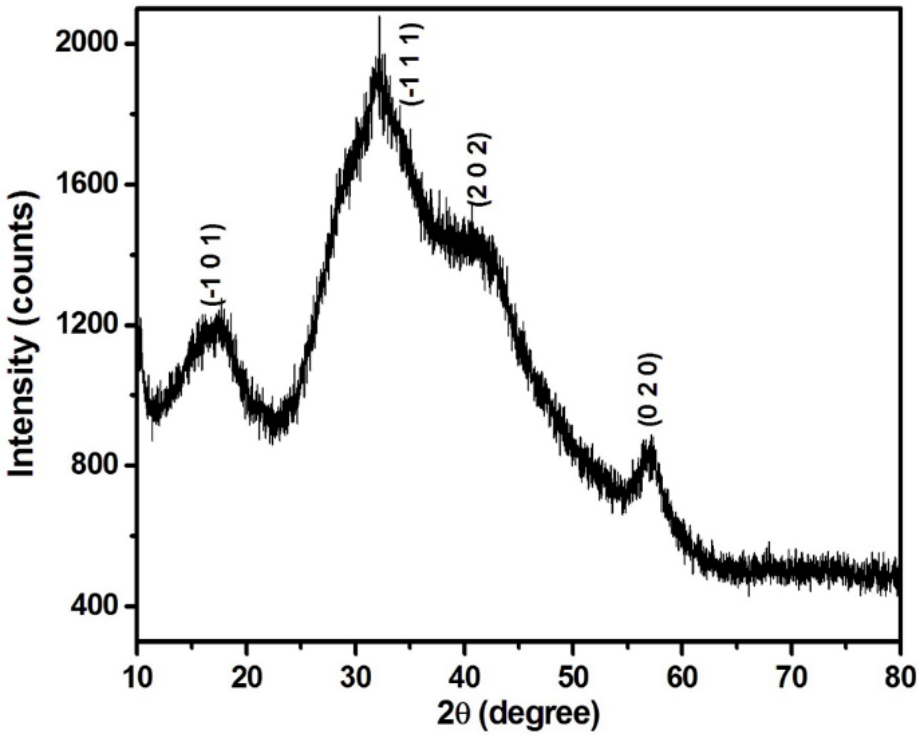

Figure A2.1. *Powder X-ray diffraction pattern synthesised sample.*

The thermogravimetric studies show that the first step of weight loss before 200 ℃ is due to removal of moisture. The second step of mass loss between 200 to 300 ℃ is due to the removal of organic residues from the sample surface (Figure A2.2).

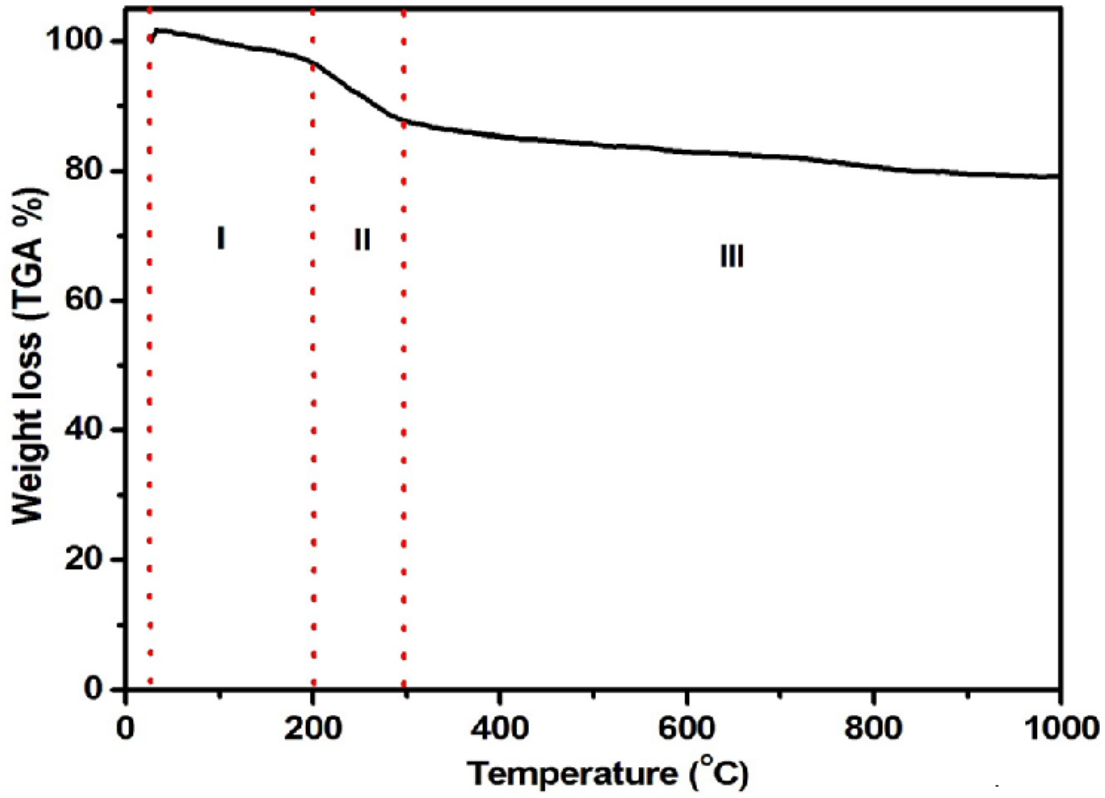

Figure A2.2. *Thermogravimetric studies of Mo_2S_3 in a Nitrogen atmosphere.*

The insignificant weight loss above 300 °C reveals the complete decomposition of organic moiety resulting in the formation of Mo_2S_3. The particle size and morphology of Mo_2S_3 nanostructures have been characterized by FESEM analysis, which indicates the particles are dense and shows three-dimensional flower-like morphology (Figure A2.3). The diameter of the nanoflowers in the range of 0.5 µm to 2.0 µm. Each flower consists of nano pedals having a smooth surface with sharp edges and slightly curved in nature. The sharp edges of the nanopetals have a thickness of around 10 nm, which are quite dense and closely packed. As shown in FigureA2.3, few layers of Mo_2S_3 layered type structures are held tightly together by interparticle interaction arises due to van der Waal's forces. These Van der Waals forces help thin sheets to curl up and self-assembled into Mo_2S_3 microspheres (flower-like morphology). Earlier, Mo_2S_3 nanoflowers morphology was reported by Zhong *et al*., synthesized by chemical vapour deposition process at the higher temperature of 810 °C,[29] while in the present study we have achieved the Mo_2S_3 (nanoflowers with a diameter of ~0.5 to 2.0 µm and thickness of ~10 nm) phase at a low temperature of 150 °C, by a

simple hydrothermal route using refined oil as a solvent. The simplicity of the proposed method allows one to prepare in large scale Mo_2S_3 nanoflowers for potential applications. The presence of Mo and S elements are further confirmed from the EDX analysis and the EDX-Elemental mapping which shows that Mo and S distributed uniformly throughout the entire sample (Figure A2.3b-e).

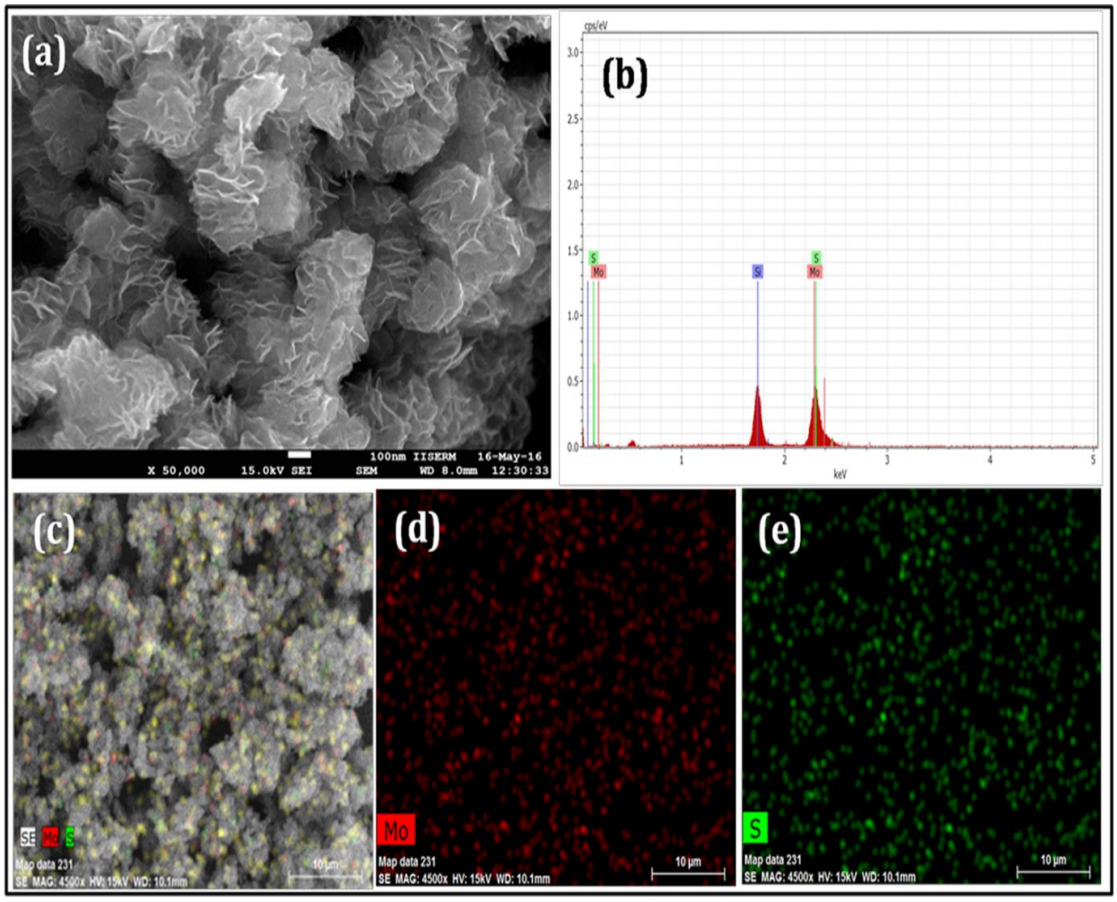

Figure A2.3. *(a) FESEM image. (b) EDX spectrum. (c-e) Elemental mapping of synthesized Mo_2S_3.*

TEM image further confirmed the well-defined nanoflowers-like structure, which is consistent with the FESEM analysis. As presented in Figure A2.4a, Mo_2S_3 nanoflowers having the diameters of 200 nm composed of sheet-like subunits in random orientation with a thickness of around 10 nm. The existence of the Mo_2S_3 phase has been analyzed from the SAED pattern with clear ring diffraction patterns, which are indexed to a monoclinic P21/m (11) space group (Figure A2.4b).

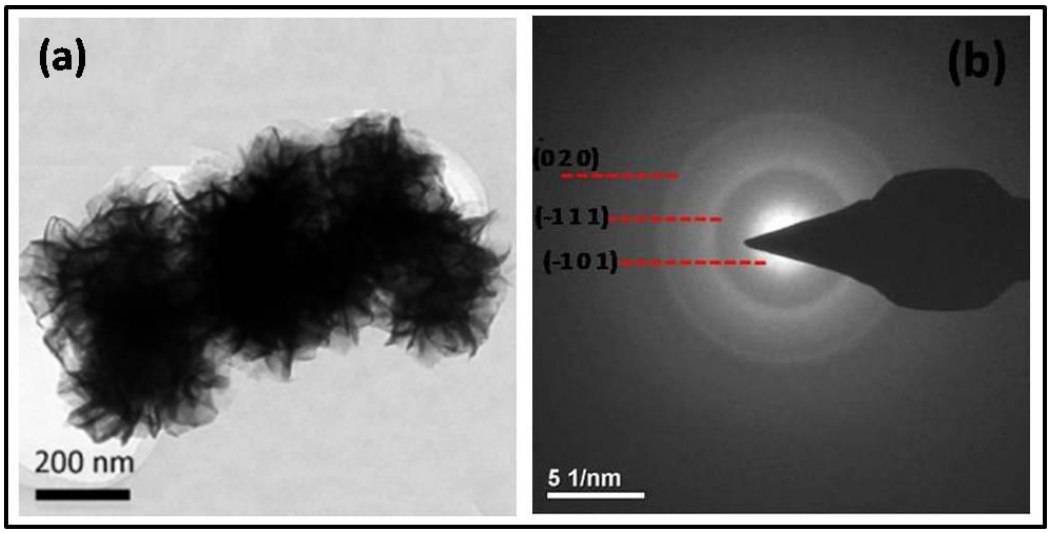

Figure A2.4. *(a) TEM image. (b) SAED pattern of Mo_2S_3 nanoflowers.*

To investigate the chemical composition and oxidation state of Mo_2S_3, XPS has carried out and provided in Fig. S2. The survey XPS spectrum of Mo_2S_3 indicates the coexistence of O 1s, Mo 3d and S 2p, indicating the formation of Mo_2S_3 (Figure A2.5a). The high-resolution XPS spectra of Mo 3d and S 2p are shown in Figure A2.5b-c respectively. The peaks at 232.7 and 229.1 eV are related to the Mo $3d_{3/2}$ and Mo $3d_{5/2}$ binding energies, respectively, corresponding to the Mo^{4+} oxidation state in Mo_2S_3, while the peak centred at 226.5 eV can be ascribed to the S 2s binding energy of Mo_2S_3. Notably, there is a peak at 235.7 eV indexed to Mo^{6+} $3d_{5/2}$ of MoO_3, which is mainly caused by the atmospheric oxygen. The XPS peaks at 161.4 eV and 163.6 eV are attributed to the binding energy for S $2p_{3/2}$ and S $2p_{1/2}$ respectively, which are mainly characteristic of S^{2-} of Mo_2S_3 (Figure A2.5c).

Surface area of prepared sample has been done using BET measurement. Figure A2.6a shows Mo_2S_3 exhibits type IV isotherm having H1 hysteresis loop that is characteristics of mesoporous. The BET surface area of the product obtained at 150 ℃ is found to be ~170 m^2/g. The pore size distribution of Mo_2S_3 nanoflowers shows the bimodal pore size distribution estimated using BJH desorption method (Figure A2.6b). The Mo_2S_3 nanoflowers are in the mesoporous range with a peak centred at 8-11 nm and the macroporous range at 30-32 nm. To the best of our knowledge, there is no report on the surface area of Mo_2S_3 hence the results of the surface area of the Mo_2S_3 is compared with the recent reports of the similar layered-type structure of MoS_2. MoS_2 nanostructures were reported by hydrothermal route with the surface area of ~105 m^2/g.[31] The surface area of ~16 m^2/g was observed in carbon dot assisted synthesis of MoS_2 nanoflowers by

hydrothermal method. N-doped MoS_2 flower-like structure with the surface area of ~114 m^2/g.[32] From the above-reported studies, the Mo_2S_3 synthesized by our method shows the highest surface area of ~170 m^2/g which may be due to lower synthesis temperature in the presence of cooking oil. The nanostructured Mo_2S_3 has the large number of pores of ~10 nm with high pore volume which facilities the fast ion transport within the electrode surface. These larger surface area and mesoporous structure provides an efficient transport pathway for ions with the help of pore channels and enhanced the electrode-electrolyte interfacial area. This process is quite beneficial for the enhancement of electrochemical performance of the Mo_2S_3 which we will discuss later.

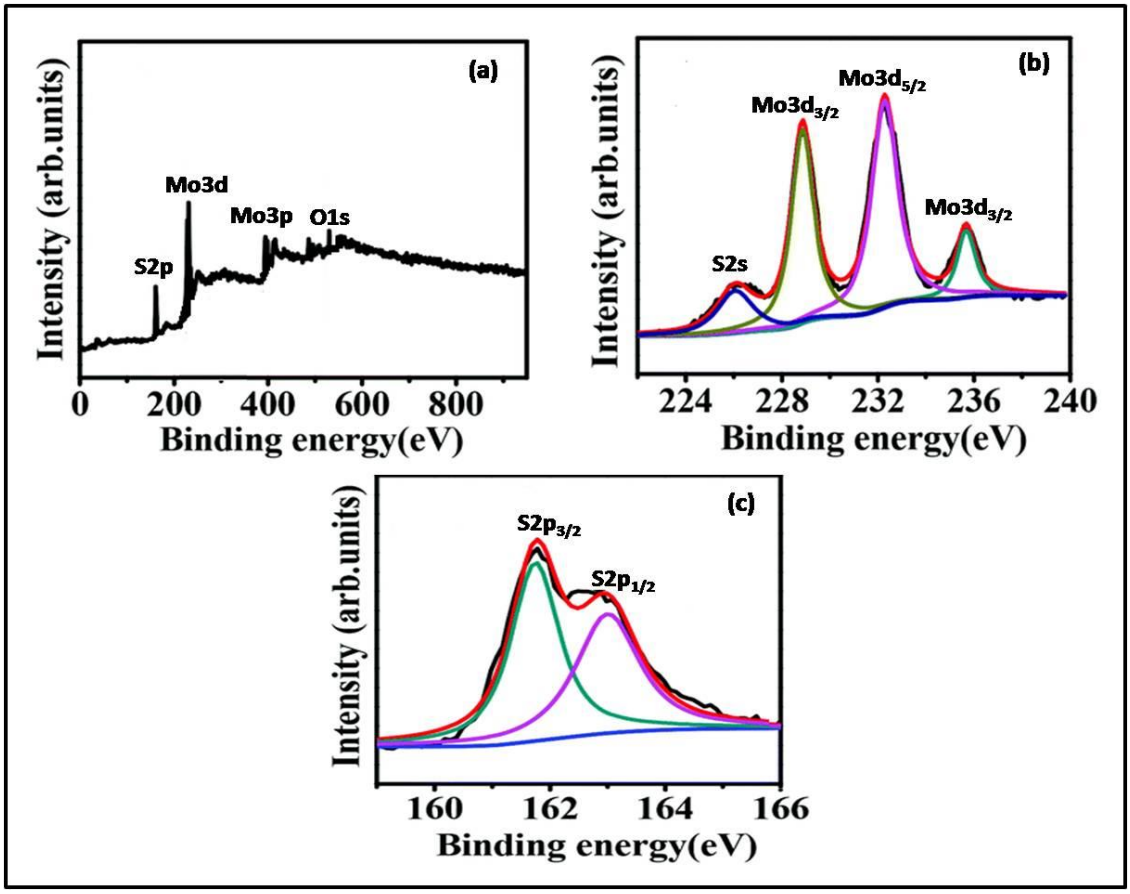

FigureA2.5. *(a) XPS survey spectra. High resolution deconvoluted spectra of (b) Mo3d. (c) S2p.*

Zeta potential is one of the important factors for characterizing the stability of the nanoparticles. The stability of the nanoparticles is the result of the two opposing forces and the particles with zeta potentials values of > +30 mV or > -30 mV have considered as good stability due to interparticle electrostatic repulsion.[33] For the Mo_2S_3, the measured Zeta potential is found to be -38 mV. Higher zeta potential results show the Mo_2S_3 are relatively stable in nature. Based on the above observations, it appears that the mechanism behind the

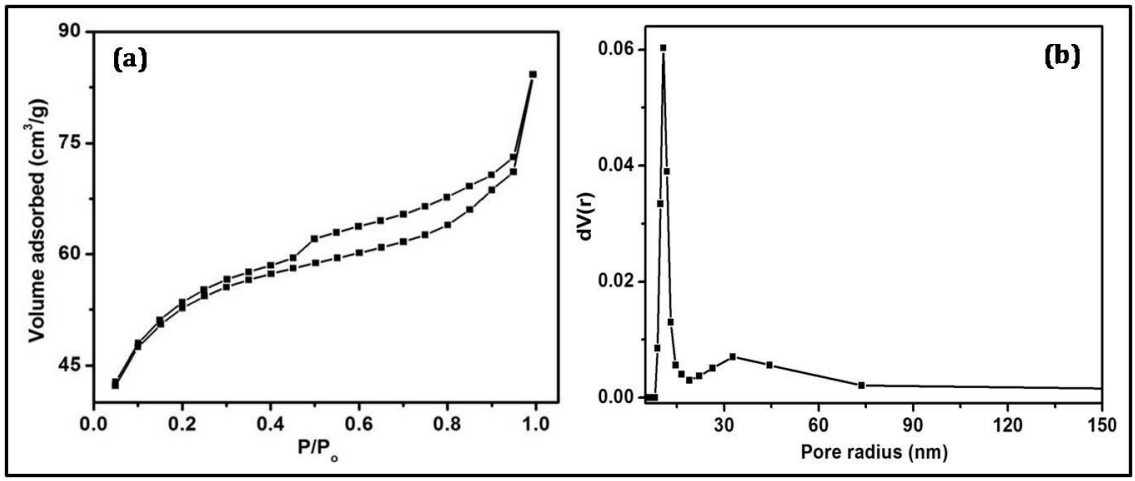

Figure A2.6. (a) Nitrogen isotherm curve. (b) Pore size distribution curve of Mo_2S_3.

formation of three-dimensional flower-like morphology is due to Mo_2S_3 nanosheets having layered structures are assembled to form microspheres having a wrinkled surface (assembled by ultrathin sheets) then finally flower-like structures undergo a series of clusters process. During this process initially, Mo and S precursors react at 150 °C and formed Mo_2S_3 nanoparticles, in the presence of oleic acid leads to forms microsphere. Similar morphology was observed by Parveen *et al.* and studied the growth mechanism of $Ni(OH)_2$ nanoflowers concerning reaction time.[34] The size of the 3D structures increased with reaction time and a flower-like morphology with a network of sheets on their surfaces was realized. These morphological changes from sheets to 3D architectures is due to nucleation/ growth, self-assembly processes aggregation and Ostwald ripening. In the present study, during the reaction at 150 °C, growth of Mo_2S_3 occurred in two directions, which result in the formation of nanosheets like structures. The layered type nanosheets were interacts among themselves by Van-der Waals interaction and finally self-assembled to form Mo_2S_3 microspheres with flower-like morphology (Figure A2.7). Moreover, with narrow pore size distribution and larger surface area, the Mo_2S_3 nanoflowers are expected to show better electrochemical properties. The nanostructures morphology greatly reduces the diffusion length over the ions and electrons must transfer during the charge-discharge process.[35,36]

To study the supercapacitor applications of Mo_2S_3, we have performed cyclic voltammetry (CV) measurements using 1 M Na_2SO_4 electrolyte. Figure A2.8a shows the characteristic CV curves with Mo_2S_3 electrode as a working electrode at various scan rates. From the cyclic voltammetric studies at various scan rate, we observe that the Mo_2S_3 electrodes show pseudo capacitance because the shape of the CV curve is quasi-rectangular

and symmetric, which is in close agreement with previous studies.[37–39] The peak current density increases with increasing scan rate, which indicates the diffusion-controlled reaction kinetics of the process. In general, the cyclic voltammetry curve of supercapacitors should have low contact resistance and a rectangular shape.

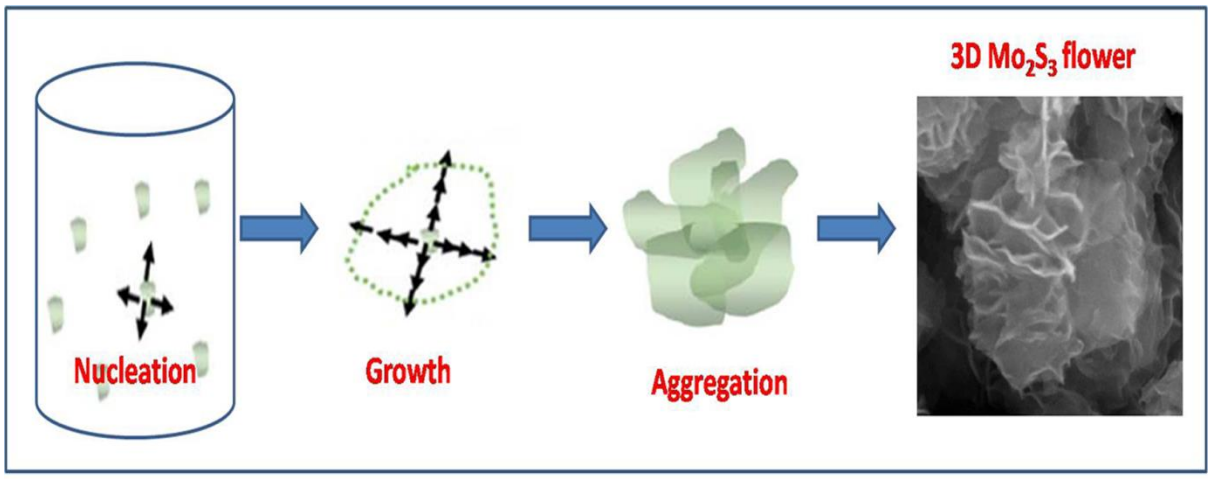

Figure A2.7. *Schematic representation of the mechanism of growth of three-dimensional layered type Mo_2S_3 nanoflowers.*

In the present study, cyclic voltagramm shows rectangle-shaped CV loops acquired at various scan rates, indicating good capacitance behaviour and high charge transfer capability of Mo_2S_3 nanoflowers. High specific capacitance (~243 F/g) is observed for Mo_2S_3 electrodes at a low scan rate of 10 mV/s (Figure A2.8b). It is also noticed that the specific capacitance of the Mo_2S_3 electrode decreases with increasing scan rate, which is due to the lower duration for the electrochemical reaction at the electrode surface. The electrochemical performances of Mo_2S_3 electrode were further studied by Galvanostatic charge-discharge measurements at different current densities. The charge-discharge plot is nearly triangular and symmetric in nature (Figure A2.8c). The studies indicate that Mo_2S_3 nanoflowers have good capacitative behaviour, high electrochemical reversible redox reaction and fast kinetics. The specific capacitance is calculated using the equation $C_{sp} = (I.\ \Delta t)/(\Delta V.m)$,[40] where C_{sp}, ΔV, I, Δt and m are specific capacitance (F/g), potential difference window (V), discharge current (A), discharge time (s), and weight of the active material (g) respectively. Figure A2.8d shows the variation of specific capacitance to discharge current for the Mo_2S_3 electrode. As seen in Figure A2.8d, the specific capacitance decreases with increasing discharge current because of the increase in potential drop and inadequate Faradaic redox reaction at higher discharge currents. The fabricated Mo_2S_3 electrode exhibited specific capacitance of 240.5, 236.1, 234.3, 231.6, 228.4 and 221.6 F/g

at the current density of 1, 2, 3, 4, 5 and 10 mA/g respectively. The highest specific capacitance of the Mo_2S_3 electrode is ~240 F/g for a discharge current density of 1 mA/g. The better electrochemical capacitance of 3D architecture Mo_2S_3 facilitates the rapid electron-transport in electrode reactions because of the higher surface area and active sites.

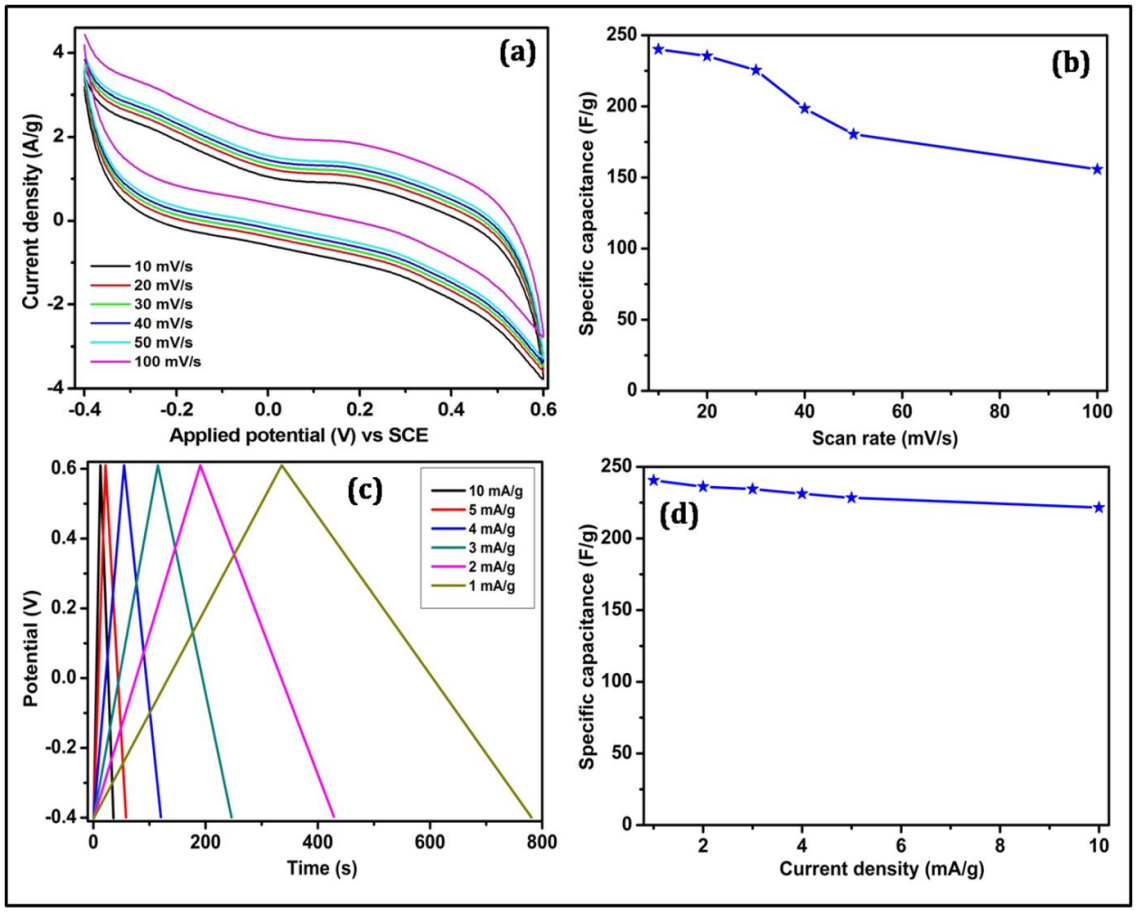

Figure A2.8. *(a) CV curve of different scan rate. (b) Specific capacitance vs scan rate curve. (c) Galvanostatic charging-discharging curve with different current densities. (d) Specific capacitance vs current density of Mo_2S_3 in 1.0 M Na_2SO_4 electrolyte.*

The energy density and power density for the Mo_2S_3 nanoflowers electrodes are calculated using the equation;[41] $E = (C_{sp} \times \Delta V^2)/2 \times 3.6$; $P = (E \times 3600)/\Delta t$: ΔV is the potential difference (V) and Δt is the discharge time (s). Here, our results show that the current density increases from 1 to 10 mA/g at the same time when specific energy density (E) decreases 98.7 to 82.5 $Whkg^{-1}$ and the power density increased from 0.6 to 15.98 $kWkg^{-1}$. The long-term cycling stability of the Mo_2S_3 electrode was studied for 3000 cycles (Figure A2.9a) and there is no change in CV curve up to 3000 cycles. It is observed that the specific capacitance remains constant at approximately 238 F/g in 1 M Na_2SO_4 upto 3000 cycles, which demonstrates the stability of the Mo_2S_3 electrode. The reported specific capacitance values and its capacitive retention of MoS_2 based nanocomposites are

compared with the present work (Table A2.1). It is noted that all the reported values of specific capacitance are exhibited from the MoS_2 nanocomposite.[42–50] However, in our case we have shown the higher specific capacitance of 240 F/g for pristine Mo_2S_3, without any modification of conducting materials.

Table A2.1. Comparison of specific capacitance of different metal chalcogenides materials

Electrode	**Electrolyte**	**Specific capacitance (F/g)**	**Capacitive retention (%) for 1000 cycles**	**Ref**
MoS_2	1 M KCl	168 at 1 A/g	96	47
MoS_2/graphene	1 M Na_2SO_4	243 at 1 A/g	92.3	48
MoS_2/C nanofibers	6 M KOH	355.6	93	49
MoS_2 nanosheets	1 M Na_2SO_4	129.2 at 1 A/g	85.1 (after 500 cycles)	50
MoS_2 nanospheres	1 M KCl	142 at 0.59 A/g	92	51
MoS_2 nanoflakes	1 M Na_2SO_4	183		52
Cu doped MoS_2	1 M Na_2SO_4	502 at 1 A/g	95	53
MoS_2/Mo	1 M Na_2SO_4	192.7 at 1 mA/cm^2	98	54
MoS_2/3D graphene	1 M Na_2SO_4	410 at 1 A/g	80.3	55
Mo_2S_3	1 M Na_2SO_4	248 at 1 mA/g	-	Present work

Further, an Electrochemical impedance study has been carried out to understand the electrochemical behaviour of material of interest in bulk and at the interface between the electrode and the electrolyte. Figure A2.9b shows the Nyquist plot of the Electrochemical impedance study (EIS) data acquired for the Mo_2S_3 electrode after 1^{st} and 3000^{th} cycles (see details in experimental section). It is noted that both the curve are similar in shape which consists of a semicircle in the high-frequency region and a straight line inclined at nearly 45° at low-frequency region which is related to the interfacial charge transfer resistance at the electrode-electrolyte interface and ideal capacitive behaviour respectively.[50–52] The corresponding equivalent circuit of EIS data are fitted by ZView software and presented in the inset of Figure A2.9b. Where the contribution from the electrolyte resistance is R_e, charge-transfer resistance between the electrode and passive film is denoted by R_{ct} and CPE is associated with constant phase element; Z_w represents the Warburg impedance.[5,53] It may be noted that the Nyquist plots (before and after 3000 cycles) showed classic features of rough and porous electrodes having 45° Warburg region at high frequencies, while nearly vertical line have been seen at low frequencies. The length of the 45° Warburg region at high frequencies region is related to the ion diffusion/

transport process occurs due to the penetration of electrolyte into the porous structure. The charge transfer resistance measured after 3000th cycles show the nearly 7-fold enhancement of resistance from 4.5 to 28.6 Ω. The probable reason for such enhancement is a loss of adhesion of some active materials in the long term charging-discharging process.[54,55] Furthermore, the longer Warburg segment after 3000 cycles indicates an enhanced Warburg resistance encountered by ions present in an electrolyte during their transport through the surface into the porous region.

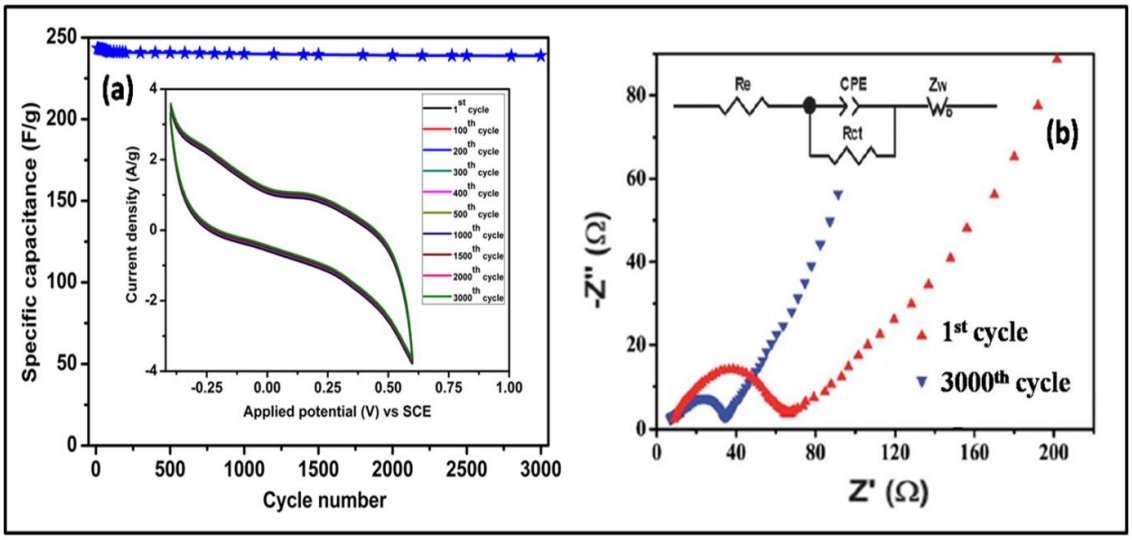

Figure A2.9. *(a) Variation of specific capacitance vs number of cycles for Mo_2S_3 electrode (Inset: CV curves of the Mo_2S_3 electrode at different cycles). (b) Nyquist plot of Mo_2S_3electrode before and after 3000 cycles (Inset: Corresponding equivalent circuit).*

The Mo_2S_3 electrode stability has also studied after the cycling studies using XRD and FESEM analysis (Figure A2.10). It is interesting to note that, there is no identification of structural changes in Mo_2S_3. Compared to as-prepared Mo_2S_3, there is a decrease in XRD peak intensity and crystallinity of used Mo_2S_3 (Figure A2.10a). The FESEM analysis, it is showing that retaining the flower-like microsphere morphology without any major changes. Smaller size crystals are seen on the surface of the spheres (marked in the red circle, Figure A2.10b), which is due to some sodium crystals may be deposited from the electrolyte. In the present study, we have attempted to establish the simple hydrothermal process for stabilization of Mo_2S_3 in refined oil for the first time. Here we have shown the process for substitution of complex and expensive organic solvent use for metal chalcogenides with an environmental friendly solvent like cooking oil.

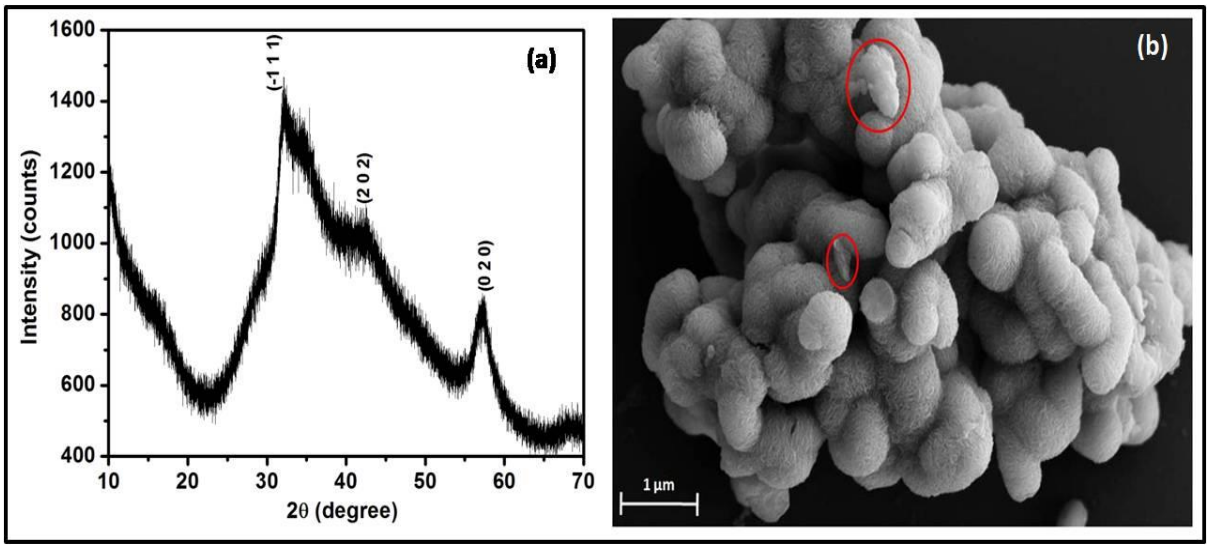

Figure A2.10. *(a) XRD pattern. (b) FESEM image of Mo_2S_3 after cycling studies.*

A2.4 Conclusions

Metal chalcogenides are one of the industrially promising materials because of their utilization in the fabrication of high-performance supercapacitors electrodes. The synthesis of metal chalcogenides requires expensive chemicals and sophisticated equipment. In the present study, we have developed a new synthetic process for the synthesis of Mo_2S_3 (Metal chalcogenides) in cooking oil instead of another complex organic solvent. The Mo_2S_3 electrode showed high specific capacitance (~243 F/g at a scan rate of 10 mV/s) and high energy density (~82 $Whkg^{-1}$) with long duration stability. The surface area was measured by BET method and show a higher surface area of 170 m^2/g for the first time. These promising results suggest that Mo_2S_3 electrodes would be a promising candidate as electrode materials for energy storage applications. This eco-friendly process will be easy to scale up for industry without any pollution, as the solvent, refined oil, is environmentally friendly and this sustainable chemical process can be extended for the synthesis of other important metal chalcogenides.

A2.5 References

1 H. C. Chien, W. Y. Cheng, Y. H. Wang and S. Y. Lu, *Adv. Funct. Mater.*, 2012, **22**, 5038–5043.

2 D. P. Kumar, M. I. Song, S. Hong, E. H. Kim, M. Gopannagari, D. A. Reddy and T. K. Kim, *ACS Sustain. Chem. Eng.*, 2017, **5**, 7651–7658.

3 M. F. El-Kady, V. Strong, S. Dubin and R. B. Kaner, *Science*, 2012, **335**, 1326–30.

4 L. Hao, X. Li and L. Zhi, *Adv. Mater.*, 2013, **25**, 3899–3904.

5 G. Wang, L. Zhang and J. Zhang, *Chem. Soc. Rev.*, 2012, **41**, 797–828.

6 Y. Zhu, S. Murali, M. D. Stoller, K. J. Ganesh, W. Cai, P. J. Ferreira, A. Pirkle, R. M. Wallace, K. A. Cychosz, M. Thommes, D. Su, E. A. Stach and R. S. Ruoff, *Science (80-.).*, 2011, **332**, 1537–1541.

7 M.-R. Gao, J. Jiang and S.-H. Yu, *Small*, 2012, **8**, 13–27.

8 C.-H. Lai, M.-Y. Lu and L.-J. Chen, *J. Mater. Chem.*, 2012, **22**, 19–30.

9 P. D. Antunez, J. J. Buckley and R. L. Brutchey, *Nanoscale*, 2011, **3**, 2399- 2411.

10 C.-M. Lee, Y.-H. Choi, J.-H. Ha and W.-S. Woo, *Int. J. Precis. Eng. Manuf. Technol.*, 2017, **4**, 457–468.

11 S. Shen and Q. Wang, *Chem. Mater.*, 2013, **25**, 1166–1178.

12 W.-S. Song and H. Yang, *Chem. Mater.*, 2012, **24**, 1961–1967.

13 Y. Wang, C. Li, Y. Zhang, M. Yang, B. Li, L. Dong and J. Wang, *Int. J. Precis. Eng. Manuf. Technol.*, 2018, **5**, 327–339.

14 S. Das, M. Kim, J. Lee and W. Choi, *Crit. Rev. Solid State Mater. Sci.*, 2014, **39**, 231–252.

15 N. Choudhary, M. Patel, Y. H. Ho, N. B. Dahotre, W. Lee, J. Y. Hwang and W. Choi, *J. Mater. Chem. A*, 2015, **3**, 24049–24054.

16 Z. Wu, B. Li, Y. Xue, J. Li, Y. Zhang and F. Gao, *J. Mater. Chem. A*, 2015, **3**, 19445–19454.

17 W. Lee, T. Besmann, M. W. Stott, J. Mater. Res., 1994, 9, 1474-1483.

18 Y. Tian, Y. He and Y. Zhu, *Mater. Chem. Phys.*, 2004, **87**, 87–90.

19 Y. B. Li, Y. Bando and D. Golberg, *Appl. Phys. Lett.*, 2003, **82**, 1962–1964.

20 M. A. Lukowski, A. S. Daniel, F. Meng, A. Forticaux, L. Li and S. Jin, *J. Am. Chem. Soc.*, 2013, **135**, 10274–10277.

21 S. K. Srivastava and B. N. Avasthi, *J. Mater. Sci.*, 1993, **28**, 5032–5035.

22 W. K. Hsu, Y. Q. Zhu, H. W. Kroto, D. R. M. Walton, R. Kamalakaran and M.

Terrones, *Appl. Phys. Lett.*, 2000, **77**, 4130.

23 E. Shembel, R. Apostolova, I. Kirsanova and V. Tysyachny, *J. Solid State Electrochem.*, 2008, **12**, 1151–1157.

24 Fagerquist and Kirby, *Phys. Rev. B. Condens. Matter*, 1988, **38**, 3973–3985.

25 C. L. McCabe, *J. Met.*, 1955, **7**, 61–63.

26 J. R. Stubbles and F. D. Richardson, *Trans. Faraday Soc.*, 1960, **56**, 1460-7.

27 W. B. Johnson, W. S. Hong and D. W. Readey, *Scr. Metall.*, 1983, **17**, 919–922.

28 R. C. Che, N. Bai and L.-M. Peng, *Appl. Phys. Lett.*, 2003, **83**, 3561–3563.

29 Y. Zhong, Y. Zhang, G. Zhang, R. Li and X. Sun, *Appl. Surf. Sci.*, 2012, **263**, 410–415.

30 R. K. Tiwari, J. Yang, M. Saeys and C. Joachim, *Surf. Sci.*, 2008, **602**, 2628–2633.

31 J. Wu, J. Dai, Y. Shao, M. Cao and X. Wu, *RSC Adv.*, 2016, **6**, 77999–78007.

32 P. Liu, Y. Liu, W. Ye, J. Ma and D. Gao, *Nanotechnology*, 2016, **27**, 225403.

33 A. Ghadimi, R. Saidur and H. S. C. Metselaar, *Int. J. Heat Mass Transf.*, 2011, **54**, 4051–4068.

34 I. Popa, G. Gillies, G. Papastavrou and M. Borkovec, *J. Phys. Chem. B*, 2010, **114**, 3170–3177.

35 N. Parveen and M. H. Cho, *Sci. Rep.*, 2016, **6**, 27318-10.

36 S. Chen, J. Zhu, X. Wu, Q. Han and X. Wang, *ACS Nano*, 2010, **4**, 2822–2830.

37 Y. Chen, B. Qu, L. Hu, Z. Xu, Q. Li and T. Wang, *Nanoscale*, 2013, **5**, 9812-9820.

38 J. M. Soon and K. P. Loh, *Electrochem. Solid-State Lett.*, 2007, **10**, A250-6.

39 C. Altavilla, M. Sarno and P. Ciambelli, *Chem. Mater.*, 2011, **23**, 3879–3885.

40 J. Xie, H. Zhang, S. Li, R. Wang, X. Sun, M. Zhou, J. Zhou, X. W. D. Lou and Y. Xie, *Adv. Mater.*, 2013, **25**, 5807–5813.

41 P. Ragupathy, H. N. Vasan and N. Munichandraiah, *J. Electrochem. Soc.*, 2008, **155**, A34-A40.

42 X. Wang, J. Ding, S. Yao, X. Wu, Q. Feng, Z. Wang and B. Geng, *J. Mater. Chem. A*, 2014, **2**, 15958–15963.

43 K. J. Huang, L. L. L. Wang, Y. J. Y. M. Liu, Y. J. Y. M. Liu, H. B. Wang, T. Gan and L. L. L. Wang, *Int. J. Hydrogen Energy*, 2013, **38**, 14027–14034.

44 R. Kumuthini, R. Ramachandran, H. A. Therese and F. Wang, *J. Alloys Compd.*, 2017, **705**, 624–630.

45 K. J. Huang, J. Z. Zhang, G. W. Shi and Y. M. Liu, *Electrochim. Acta*, 2014, **132**, 397–403.

46 L. Wang, Y. Ma, M. Yang and Y. Qi, *Electrochim. Acta*, 2015, **186**, 391–396.

47 T. N. Y. Khawula, K. Raju, P. J. Franklyn, I. Sigalas and K. I. Ozoemena, *J. Electrochem. Soc.*, 2016, **163**, A1927–A1935.

48 B. D. Falola, L. Fan, T. Wiltowski and I. I. Suni, *J. Electrochem. Soc.*, 2017, **164**, D674–D679.

49 K. Krishnamoorthy, G. K. Veerasubramani, P. Pazhamalai and S. J. Kim, *Electrochim. Acta*, 2016, **190**, 305–312.

50 T. Sun, Z. Li, X. Liu, L. Ma, J. Wang and S. Yang, *J. Power Sources*, 2016, **331**, 180–188.

51 S. Chaudhari, D. Bhattacharjya and J.-S. Yu, *RSC Adv.*, 2013, **3**, 25120.

52 B.-Y. C. And and S.-M. Park, *Anal. Chem.*, 2005, **78**, 1052–1060.

53 D.-L. Fang, Z.-D. Chen, X. Liu, Z.-F. Wu and C.-H. Zheng, *Electrochim. Acta*, 2012, **81**, 321–329.

54 J. Yan, Z. Fan, T. Wei, W. Qian, M. Zhang and F. Wei, *Carbon N. Y.*, 2010, **48**, 3825–3833.

55 P. Guo, H. Song and X. Chen, *Electrochem. commun.*, 2009, **11**, 1320–1324.

Chapter A3

Utilization of coir fibre for the synthesis template free porous graphene oxide for energy storage application

A3.1 Introduction

Energy is one of the utmost requirements to us for making our lifestyle easy. The requirement of energy has been fulfilled by fossil fuel such as coal, petroleum reserves or another hydrocarbon by burning and using their heat as an energy source.[1] However, the depletion of fossil fuel has limited the possibility of its sustainable availability. Also, the combustion of fossil fuel creates a secondary problem of global warming product, which is hazardous for the environment because it increases global warming issues.[2] Several methods have been introduced to generate energy without polluting environments such as fuel cell, solar cell, batteries, supercapacitor, and electrochemical water splitting.[3,4] Among these methods, a supercapacitor is very promising as it is economical and store a huge amount of energy, which can be quickly delivered on requirements. Several materials have been introduced for the supercapacitor application such as metal chalcogenide,[5] transition metal oxides (Mn_3O_4, MnO_2, Co_3O_4, RuO_2 so on),[6–8] transition metal hydroxide,[9] conductive polymers,[10] and 2D materials (graphene oxide, MoS_2, WS_2).[11,12] Use of renewable energy source synthesised using biowaste will reduce environmental pollution and produce energy at a low cost. Earlier, several attempts have been carried out to derive carbon-based materials.[13–15] Apart from the low specific surface area and low conductivity in biocarbon, the graphene-like structure has a hexatomic ring, which leads to high conductivity and high specific surface area.[16–18] Interestingly, it has been reported that the graphene-like structure can be derived from biocarbon (large amount of bio-waste).[19] Biocarbons residues such as wood, water plants, and plant waste fibres (banana, sisal, jute, hemp, coconut fibres, pineapple leaf fibre and flax etc) can be converted into highly conducting graphene-like structure.[19,20] Natural fibres such as coconut husk fibre (coir) will be a good candidate to convert in graphene-like structure because of their high abundance, low cost and eco-friendly nature.[14] It has been known that coir is the highest durable materials among all the other natural fibre due to the presence of a high amount of lignin and silica.[14,21] Coconut fibre (coir) can be obtained from the pericarp of coconut and ~35 % by w/w coconut was made up of coir fibres.[15] Almost every part of a coir plant can be used for diverse purposes such as building materials, decoration, food packaging, broomsticks, coconut water and coir husk can be used as fuel and coir fibres are used as ropes.[19,22] Besides the above facts, significant research has been carried out to get the desired morphology of graphene oxide such as porous graphene oxide through templates assist method, three-dimensional graphene oxide, graphene quantum dots, graphene oxide assembled foam, paper of graphene oxide, graphene oxide fibre, and graphene oxide based

hydrogel via different methods for advanced applications.[23] The properties of these materials significantly improved by the modification in structure and become an excellent electrode material for supercapacitor applications. However, the performance of these materials still lower than metal-doped graphene oxide due to less conductivity. The conductivity can be significantly enhanced by doping heteroatoms such as nitrogen (N), phosphorus (P), boron (B), and sulphur (S).[24,25] It is known that graphene oxide or graphene inevitably contains oxygen groups, and doping leads to replacing of some oxygen groups and some carbon atoms by these heteroatoms.[26] These heteroatoms are responsible for creating defects, which cause changes in the property of graphene oxide.[27] For capacitor applications doping of heteroatom (N, B, S, and P) in graphene are preferable due to large surface area, high conductivity, low cost, good chemical and electrochemical stability.[28–30]

In view of the above facts, here we have used the natural structure of coir fibre as a template and carbon source for the synthesis of porous graphene oxide. To design the process for coir fibre conversion in graphene oxide, first, the investigation of the elemental distribution of coir fibre has been done. SEM-EDS mapping result indicates that silica spheres were distributed homogeneously throughout the coir fibre. The homogeneous distribution of silica was used to make porous graphene oxide. Further, doping of Nitrogen and Sulphur has been done to increase the energy storage capacity. The supercapacitor properties have been investigated by cyclic voltammetry (CV) and galvanic charge-discharge (GCD) study in 1 M sodium sulphate solution.

A3.2 Experimental

A3.2.1 Materials and Methods

Coir (coconut fibre) used in the study was purchased from local shops in Mohali, India. Potassium hydroxide (KOH, 99%, Merck), Hydrochloric acid (HCL, 99%, Merck), Nitric Acid (HNO_3, 99%, Merck), Urea (NH_2CONH_2, 99.9%, Merck), and Sulphur (S, 99.9%, Merck) were used without any further purification.

A3.2.2 Preparation of porous Graphene from waste coir fibres

Coir fibres were first scratched from the coconut. The scratched coir fibre was washed with distilled water then dried to reduce moisture content. The dried coir fibre is cut into pieces of about 1 cm. Small pieces of coir fibres were again washed by DI water and dried at 100 ℃ overnight. A solution of 1:10 w/V ratio of KOH and DI water being prepared and coir fibre having a similar weight to KOH has been added in the above mixture and stirred for 2 h. Further, the mixture was heated at 100 ℃ to get a solid mass.

The as-obtained KOH treated coir fibres were annealed in a tube furnace in an inert atmosphere. The annealing was carried out in two steps. In the first step, the sample was heated for 1 h at 300 ℃ and then the temperature of the reaction was increased to 750 ℃ for 3 h in an argon atmosphere. After natural cooling, the obtained sample was dispersed in HCl for 12 hours. The as-obtained product was washed five times with DI water followed by drying at 70 ℃ overnight. The as-obtained dried samples were further dispersed in HNO_3 for 12 h and then washed with water followed by drying at 70 ℃. The as-obtained black powder is used for further study and denoted as CG throughout this manuscript. . The schematic diagram for the synthesis has been given in Figure A3.1.

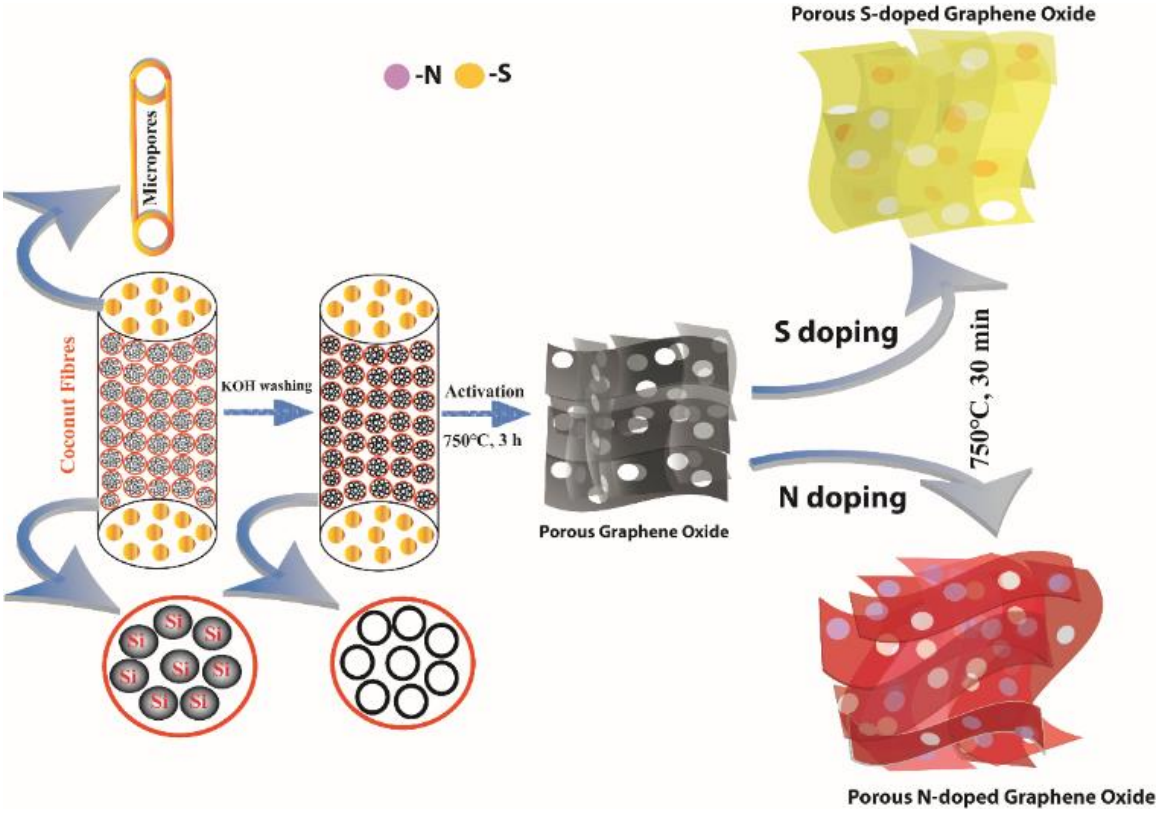

Figure A3.1. *Synthesis scheme of porous graphene oxide.*

A3.2.3 Synthesis of N-doped and S-doped graphene oxide

Urea and Sulphur being used as the source of nitrogen and sulphur for doping in graphene oxide respectively. An equal amount of CG and Urea/Sulphur were mixed in a minimum amount of DI water at vigorous stirring for 1 h. The as-obtained mixture was dried at 110 ℃. The as-obtained powder was annealed in the horizontal tube furnace at 450℃ in an argon atmosphere for 40 min. Further, the temperature was increased up to 750 ℃ in the presence of hydrogen for 30 min. Finally, the sample was allowed to cool naturally. The entire heat treatment was done at the rate of 200 ℃/h. The as-obtained black

powder after annealing was washed by hot distilled water to remove the residual followed drying at 80 ℃. It may be noted that for the synthesis of N-doped graphene (UG), urea was used as starting materials along with graphene oxide (CG) while for the synthesis of S-doped graphene (SG), sulphur powder was used as starting materials. The schematic diagram for the synthesis has been given in Figure A3.1.

A3.3 Results and discussion

The present work has been aimed to design a process for the synthesis of porous graphene oxide from waste coir fibre (*Cocos nucifera L.*). The different part of coir being disintegrated as shown in Figure A3.2. The digital picture indicates that coir is made up of three-part: coconut, coconut shell and coconut fibre (coir).

Figure A3.2. *Disintegration of coir fibres.*

Among these, coir is normally thrown away as waste. The composition analysis of coir was carried out using PXRD, SEM, EDX and CHNS. The PXRD of fibres shows the diffraction peaks at position 16.7 and 22.9º correspond to the fibre cellulose having monoclinic units, which is in good agreement with the earlier report by Priscila *et al.* [20] (Figure A3.3a). SEM-EDX analysis of fibre indicates the presence of C, O, Na and Si (Figure A3.3b). The thermogravimetric analysis (TGA) of the fibre indicates a continuous loss in weight up to 254 ℃ is due to loss of water molecules. Further, there are two steep reductions in weight, which can be correlated with the removal of fibre cellulose (Figure A3.3c).

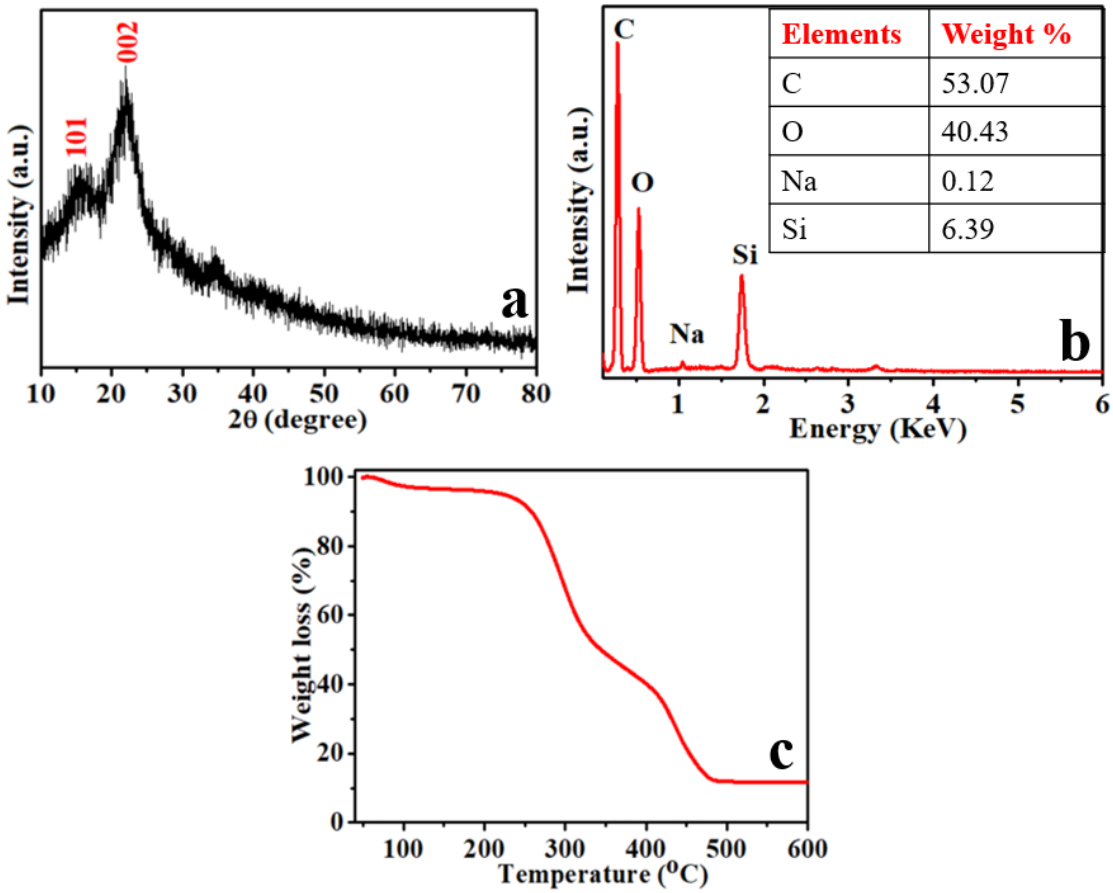

Figure A3.3. *(a) PXRD of as obtained Fibres of coconut. (b) Elemental analysis of fibres (inset is the elemental percentage). (c) TGA of as received fibre.*

Surface morphology of fibre was studied using SEM, which confirms that the fibre was embedded by spheres with an average inner diameter 22 μm (Figure A3.4a-b). To investigate the composition of spheres embedded in fibre matrix, elemental mapping of fibre has been carried out. SEM-EDX mapping results indicate that the spheres were made up of silicon and oxygen. From the elemental distribution, it seems that silica was present only at the rings and C, O and Na distributed throughout the fibres (Figure A3.4c-g). Earlier reports on the composition of coir fibre indicate that coir consists of cellulose (32-43%), lignin (40-45 %), pectin (3-4%) and rest are Si, Ca and K elements composition.[14] It has been reported that Si was present in the form of SiO_2 to increase the mechanical properties of coir fibre. Here, our aim is to remove the silica to enhance the porosity of the materials. For this purpose, first coir fibre has been mixed with KOH and heated in inert atmosphere followed by washing with a series of solvents to remove the potassium silicates and forms porous biocarbon.

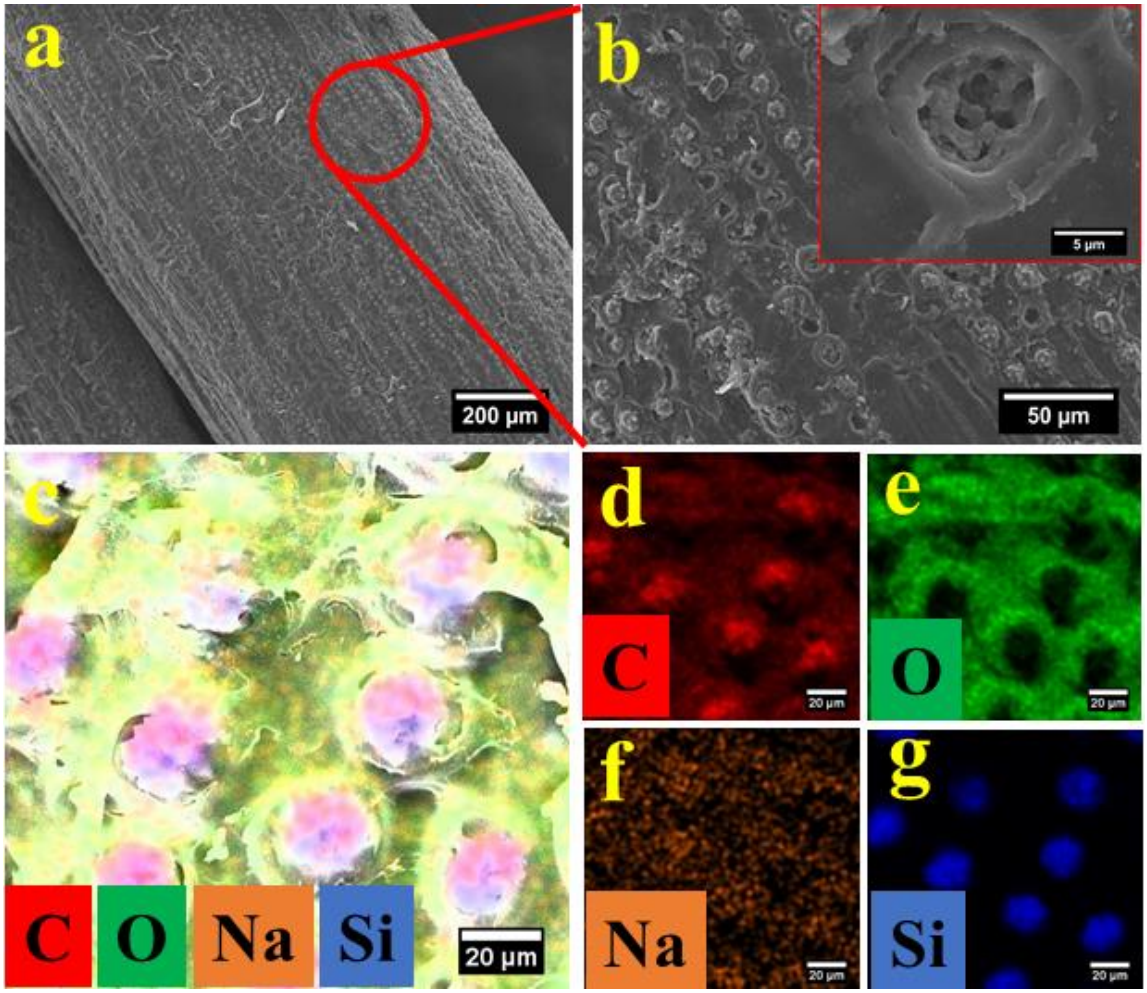

Figure A3.4. *(a-b) Scanning electron microscopy of coir fibre. (c-g) elemental mapping of fibre.*

The as-synthesised samples have been investigated through various technique. Among them, Raman spectroscopic technique has been widely used for the characterization of carbon-based samples. Figure A3.5a represents the Raman spectra of CG, SG and UG. The D band position was at ~1340.18, 1344.1 and 1344.2 cm^{-1} for sample CG, SG and UG respectively. The G band Raman shift 1583.1, 1584.2, 1584.9 cm^{-1} for CG, SG and UG respectively. There was a blue shift observed when sulphur and nitrogen being doped in graphene (CG). The observed value of D and G band is in good agreements with earlier reports.[27] The I_D/I_G ratio is 0.98, 1.07 and 1.18 for CG, SG and UG respectively, which is in agreement with the earlier reported I_D/I_G ratio.[31] It is known that higher I_D/I_G ratio favours the better electron transport because of the presence of defect sites. Apart from these bands, the presence of a weak band ~2680 cm^{-1} this band can be used to calculate the number of graphene layer in these samples. It was observed that CG is more graphitic than the SG and UG because of the less intensity of the 2D band. The thickness of the prepared

film was calculated using atomic force microscopy (AFM). The AFM study suggests that the thickness of graphene oxide for CG, SG and UG are 4.19, 1.76 and 0.91 nm (Figure A3.6). Figure A3.5b presents the PXRD patterns of CG, UG and SG. It was observed that peaks at 2θ position 24.4 and 42.3º, matched with JCPDS no. 00-046-0944, which confirms the formation of graphene oxide. However, the 2θ value 24.4 is lower than bulk graphite and confirms the formation of good quality graphene oxide.[32,33]

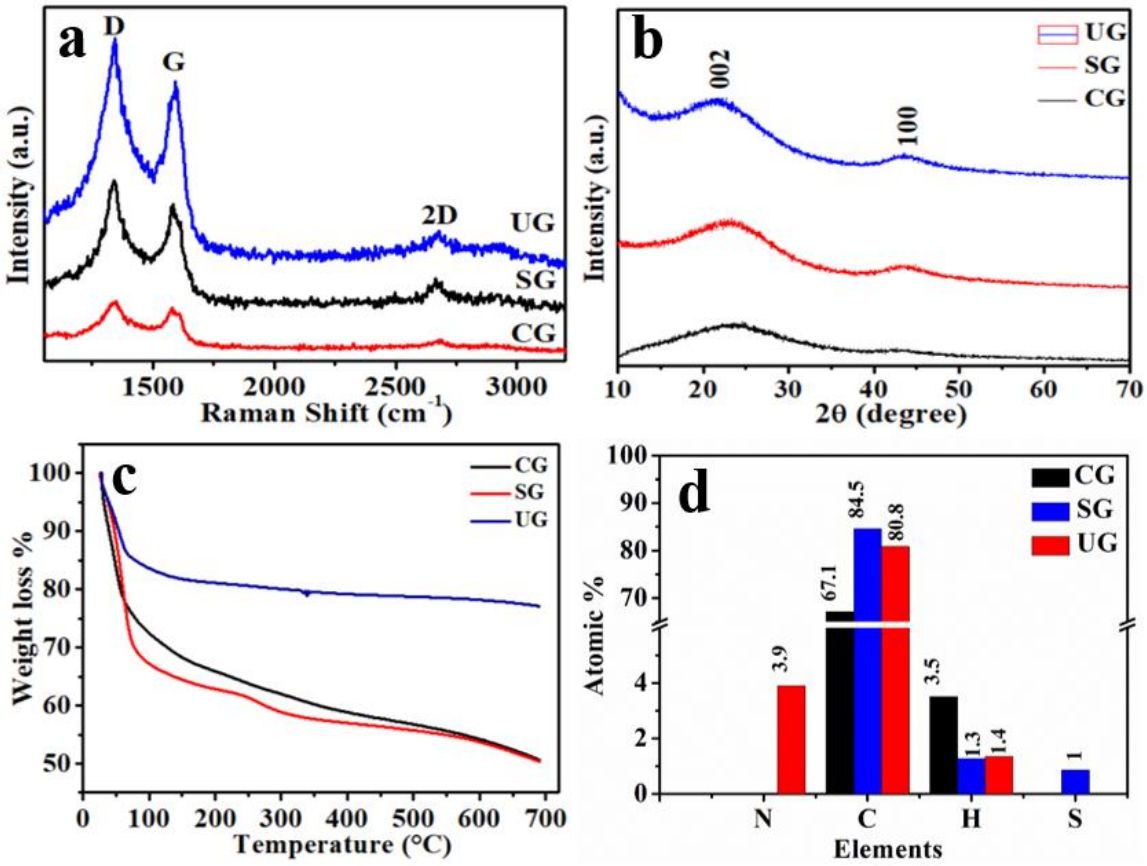

Figure A3.5. *Characterization of CG, SG and UG (a) Raman studies. (b) PXRD of as synthesised samples. (c) TGA studies. (d) CHNS analysis.*

Further, sulphur and nitrogen being doped individually in synthesised graphene oxide. Sulphur and Nitrogen doping leads to 2θ shift towards lower diffraction angle (higher d value). The thermal degradation behaviour of synthesised samples was performed using TGA measurement in the presence of argon atmospheres at a heating rate of 10 ℃/min (Figure A3.5c). There is around 22 % weight loss observed in CG; however, in the case of SG and UG ~30 % and ~14 % weight loss at temperature ranges up to 150 ℃ observed, respectively. The reduction in mass loss is due to the removal of adsorbed moisture, loss of several oxygen functional groups as well as residues during the rapid expansion of the GO.[34] There is no sharp change observed in UG and total ~23 % weight reduced upto 700

°C (Figure A3.5c). However, there is total ~49 % weight loss observed in SG and CG up to 700 °C. This result is in good agreement with earlier reports.[35,36] It was observed that as the different atoms being doped in CG, the I_D/I_G ratio enhanced from 0.98 to 1.07, which depends upon the amount of dopant. Therefore, CHNS analysis has been carried out for identification of the exact doped amount. The elemental percentage of C, N, H and S has been represented in Figure A3.5d. It was observed that nitrogen was doped up to 3.9 weight % in UG while there is only 0.9 weight % sulphur being doped in SG. The higher loading density leads to more defects in UG, which is clearly reflected in Raman spectra. The reason behind the low loading of S in CG is the high-temperature heating process (750 °C) in which sulphur might evaporate.

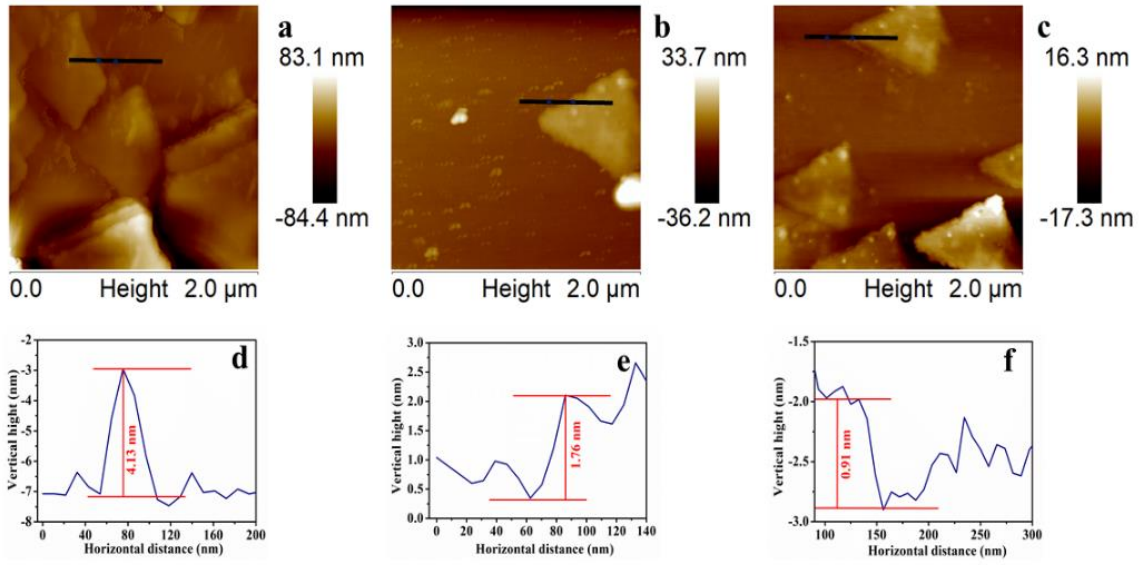

Figure A3.6. *AFM topographical image of (a) CG. (b) SG. (c) UG. and (d) height profile for CG. (e) height profile for SG. (f) height profile for UG.*

To investigate the morphology of synthesised samples, SEM has been carried out. It was observed that synthesised samples CG, SG and UG have highly uniform porous structure (Figure A3.7a-c). In CG samples, pores were distributed throughout the sample surface (Figure A3.7a). The elemental mapping indicates that there are no particles or flakes present on the surface of the pores (Figure A3.8). Doping of sulphur and nitrogen leads to distortion in the pores (Figure A3.7b-c). Further, the distribution of sulphur and nitrogen in SG and UG can be observed from the elemental mapping (Figure A3.9 & Figure A3.10).

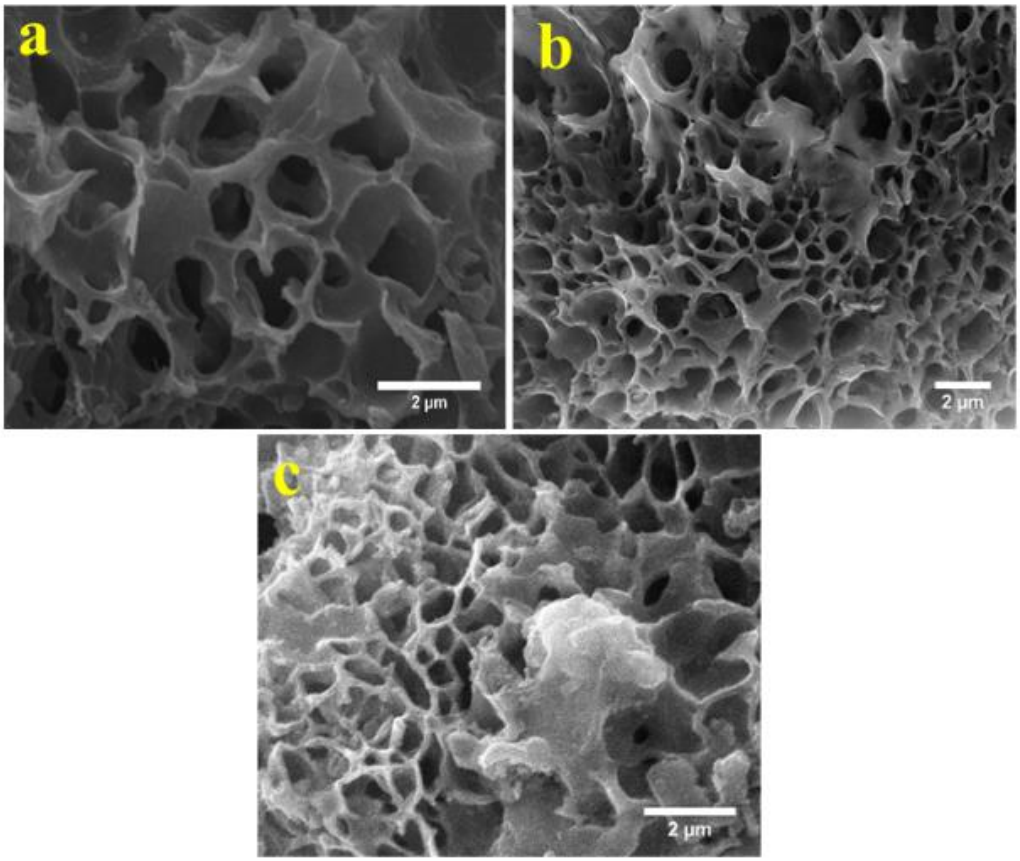

Figure A3.7. *Scanning electron micrograph of (a) CG. (b) SG. and (c) UG.*

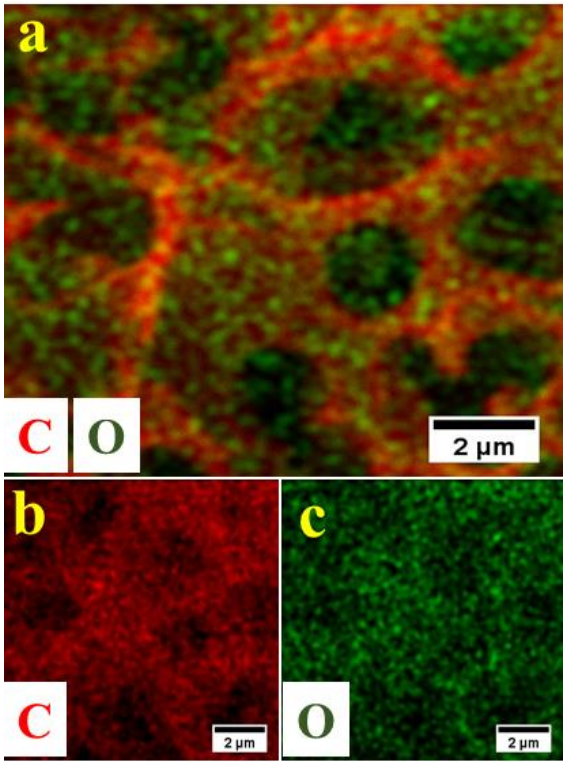

Figure A3.8. *(a-c) EDX elemental mapping of CG.*

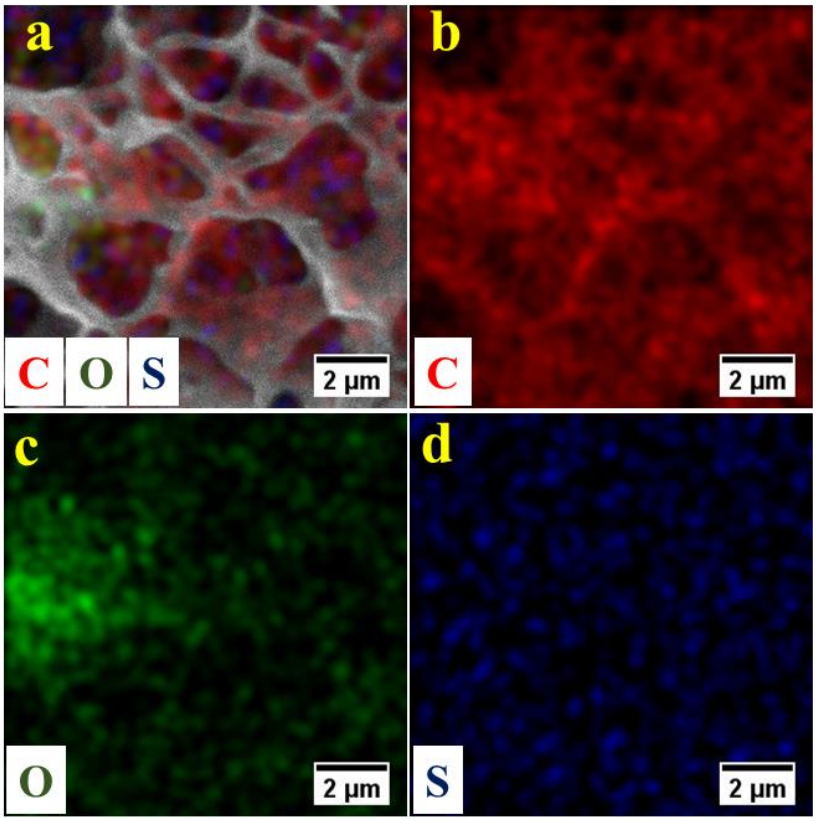

Figure A3.9. *(a-d) EDX elemental mapping of SG.*

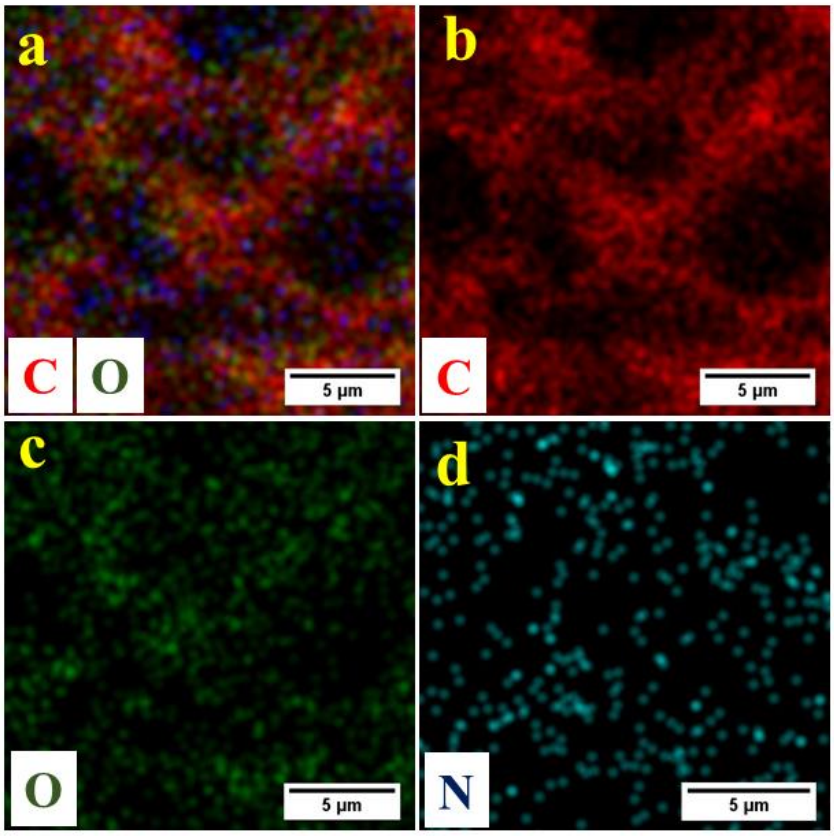

Figure A3.10. *EDX elemental mapping of UG.*

The wide scan of X-ray photo spectroscopy (XPS) study of CG, SG and UG has been shown in Figure A3.11a, Figure A3.11d and Figure A3.11h. It has been observed that the amount of carbon is lower in CG as compared to SG and UG. The higher concentration of oxygen efficiently removed by doping of Sulphur and Nitrogen.[37] The high-resolution XPS of C 1s have been deconvoluting in 284.3 eV, 284.92 eV in CG, 284.1 eV, 284.5 eV, 288.1 eV in SG and 284.34 eV, 284.81 eV and 288.07 eV in UG respectively (Figure A3.11b,e,i). Further, high-resolution XPS of S2p has been deconvoluting in 163.3, 164.3, and 164.9 eV for SG sample (Figure A3.11g) and N 1s have been deconvoluted in 397.04, 398.1, 400.01 and 402.9 eV for UG sample (Figure A3.11k). In SG, peak position 163.3 eV is due to S $2p_{1/2}$ and 164.3, and 164.9 eV peaks arise due to S $2p_{3/2}$.[38] The obtained peak position of sulphur is lower than the α-S suggest that the strong reduction of graphene oxide to reduced graphene oxide.[39] The raise of 163.3 and 164.3 eV peaks of sulphur can be also marked as C-S_n-C and C=S.[40] In UG sample, peaks 397.04, 398.1, and 400.01 eV defined as pyridinic N, pyrrolic N and graphitic N. The peak at 402.9 eV corresponds to N-oxide.[41] The graphitic N arises due to the N doping from urea. It is believed that graphitic N enhanced electrocatalytic activity of UG.[41] Apart from this pseudocapacitive behaviour will be observed for UG due to dominant N-pyrrolic peak.[40] The high-resolution XPS spectra of CG, SG and UG have been well-matched with the earlier reports of bare and doped graphene oxide.[37,42]

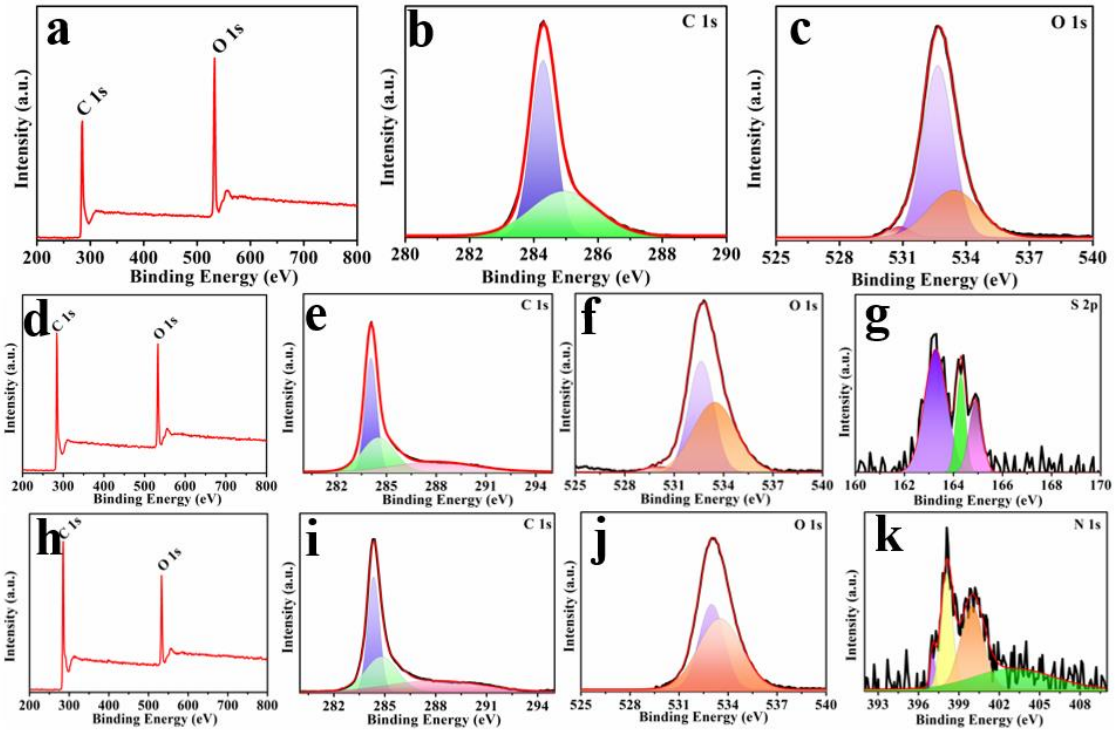

Figure A3.11. *XPS study of (a-c) CG. (d-g) SG. (h-k) UG.*

For the catalytic activity, surface area and pore size have been measured. It is known that the higher the surface area, the better will be the electrocatalytic properties.[43] However, as the pore size increase, the conductivity of the final product reduced. This will not be beneficial for high energy storage supercapacitor.[44] To overcome less conductivity, in the present work S/N has been doped to enhance the conductivity of the final product. The N_2 adsorption-desorption isotherm of all the samples shows the type IV isotherm (Figure A3.12a-c).

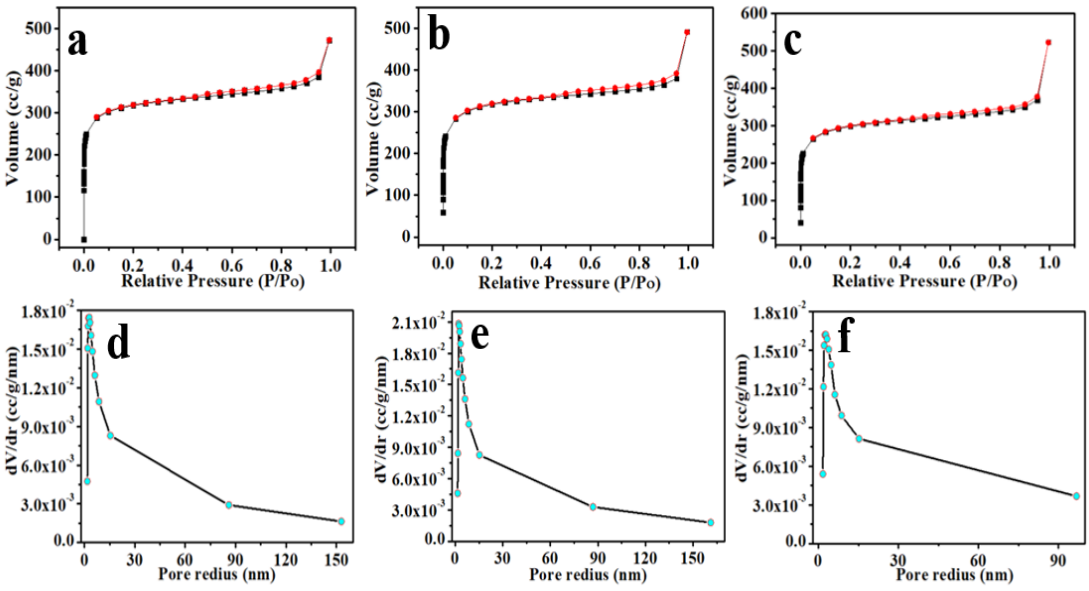

Figure A3.12. *BET surface area of (a) CG. (b) SG. (c) UG. and the pore size distribution of (d) CG. (e) SG. (f) UG.*

The steep uptake in N_2 isotherm confirms a large number of microspores present in the prepared samples (CG, SG and UG).[13] However, the hysteresis behaviour suggests that mesoporous nature also presents in the samples as split in hysteresis starts from low relative pressure (~0.4) to high relative pressure (~0.9). A close view of isotherm confirms that there are few macropores presents as there is a noteworthy enhancement in volume adsorb at relatively high pressure (0.9 to 1).[45] Further, the mesoporous nature can also be verified from the pore size distribution of each sample, which was represented at the inset of the corresponding isotherm. A sharp peak nearly 1.9-2.8 nm pore radius confirm the probability of pores in micro as well as mesoporous. Pore size distribution was computed using the desorption branch of the isotherm by the BJH, showing an average pore size of 1.80 nm, 1.85 nm and 1.90 nm for CG, UG and SG respectively (Figure A3.12d-f). Microporous and mesoporous substances with an enhanced surface area are ideal for high

capacitance and power density in aqueous electrolyte because of high conductivity. The specific BET surface area for CG, SG and UG are 1113, 1083 and 1114 m^2/g respectively. The high surface area and high pore volume will be beneficial during the charge-discharge process as it produced additional active site.

The electrochemical performance towards supercapacitor of as synthesised graphene and doped graphene has been evaluated via three-electrode cell. The glassy carbon electrode on which prepared ink was drop casted was used as a working electrode with 3 M Ag/AgCl and Pt as a reference and counter electrode, respectively. All the electrochemical measurement was performed in 1 M Na_2SO_4 aqueous solution in the potential window 1 V (-0.2 to 0.8 vs Ag/AgCl). The cyclic voltammetry has been carried out to evaluate the formation of electric double layer formation at 20 mVs^{-1} for CG, SG and UG (Figure A3.13a).

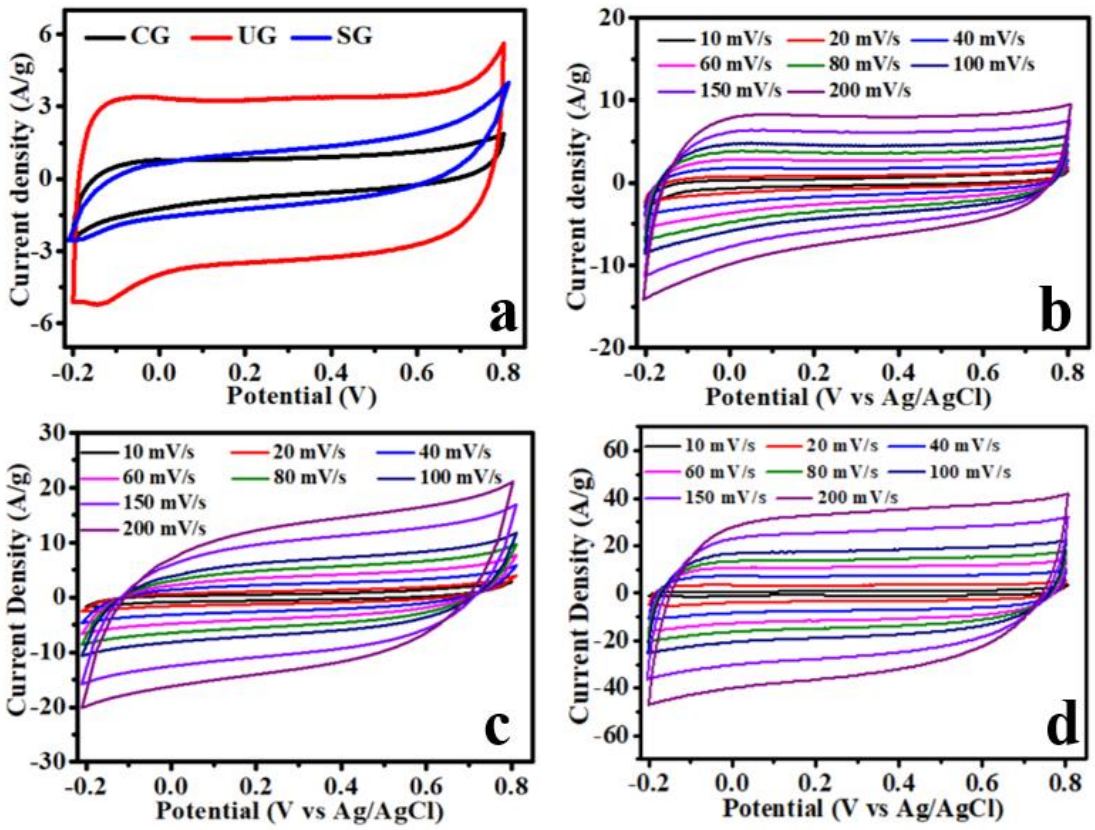

Figure A3.13. *(a) CV profile of CG, SG and UG at 20 mV/s. (b) CV profile of CG at different scan rate. (c) CV profile of SG at different scan rate. (d) CV profile of UG at a different scan rate.*

Figure A3.13a indicates that the quasi-rectangular curve of UG electrode makes it high efficient electrode for storage of charge as compared to CG and SG electrode. The cyclic

voltammetry plot of CG and UG shows the quasi rectangular but the less symmetric as well as the reduced area under the curve as compared to UG. It may be noted that at slow scan, there is a bump in case of UG indicates a little contribution of redox species to the electrochemical capacitance. Further, the CV of CG, SG and UG electrodes being done at various scan rate (10, 20, 40, 60, 80, 100, 150, 200 mV/s) as represented in Figure A3.13b-d. The shape of CV at 200 mV/s in CG, SG and UG remain almost like 10 mV/s. However, it can be observed that as the scan rate increase the electric double area enhanced more rapidly in UG as compared to CG and SG. The area of the electrochemical double layer can be found in CG < SG < UG. The higher electrochemical properties of doped graphene are due to presence of S/N as dopant which creates electronic active sites. It is known that the defect in graphene oxide with less number of stacked graphene layers influenced the electronic properties.[46] In the present case, Raman study indicates that UG has less number of graphene layers than CG and SG, which leads to the generation of the high electrochemical double layers capacitance. The galvanostatic charge-discharge (GCD) study has been carried out at different current (1, 3, 5, 7 to 10 A/g). A comparative GCD plot at 1 A/g being represented in Figure A3.14a. All the charge-discharge plots are quasi-triangular and nearly symmetrical, which is beneficial for fast and efficient charge transfer and superior electrical conductivity. It has been observed in Figure A3.14a, the triangular shape little distorted in discharging time, which is maybe due to the oxygen reduction reaction at the surface.[27] The specific capacitance of CG, SG and UG was 161.1, 199.2, and 278.6 F/g at 1 A/g respectively. Calculated specific capacitance is in close agreement with the earlier reports.[19,47–50] The doping leads to the enhancement in specific capacitance due to the synergetic effect. The specific capacitance of SG and UG electrode material is in good agreement among previously reported biomass-derived graphene oxide.[37,40,51–53] The specific capacitance retention with increasing current density (rate capability) is another important key factor for practical application and is plotted in Figure A3.14b-d. The specific capacitance for CG is 165.2, 132, 83, 81.2 and 82 F/g at current density 1, 3, 5, 7 and 10 A/g respectively (Figure A3.14b). Sulphur doping in CG leads to an increase in capacitance and reached to 199.2, 166.9, 162.8, 159.8, 154.8 F/g at 1, 3, 5, 7 and 10 A/g respectively (Figure A3.14c). The increase in capacitance is due to an increase in electrochemical active size. Further, the specific capacitance of UG was 278.6, 261.8, 256.8, 254.1, and 252.6 at 1, 3, 5, 7 and 10 A/g current density (Figure A3.14d). The highest specific capacitance of UG may be attributed to the highest loaded nitrogen that can improve the wettability of nitrogen-doped graphene in aqueous electrolyte even at high

current densities.[54] It can be observed that even at a high current density up to 10 A/g, the shape of the GCD curve is still intact in a quasi-triangular shape. The quasi-triangular and quasi-symmetrical shape of GCD curves even at higher current density, suggesting fast charge-discharge reversibility, high electrical conductivity and poses typical electrical double layer capacitive behaviour.[49]

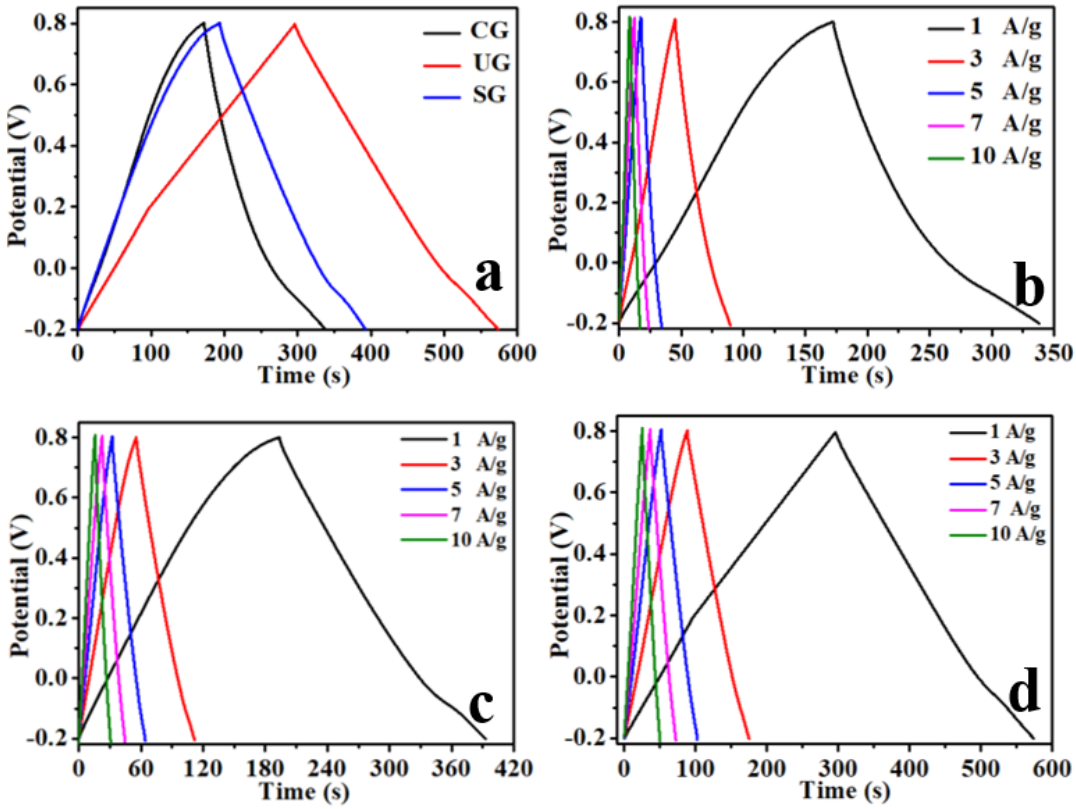

Figure A3.14. *(a) GCD profile of CG, SG and UG at 1 A/g. (b) GCD profile of CG at different current density. (c) GCD profile of SG at different current density. (d) GCD profile of UG at a different current density.*

The wettability and hydrophilic or hydrophobic behaviour of as-prepared samples have been conducted using contact angle (CA) measurements. Based on CA any surface can be classified as super hydrophilic (CA < 5°), hydrophilic (CA < 90°), hydrophobic (CA > 90°), or superhydrophobic (CA > 150°).[55] The contact angle was measured using 3 µL of 1 M aqueous solution of Na_2SO_4 on CG, SG, UG and Silicon substrate. The contact angles of CG, SG, UG and Silicon substrate are approximately 75.5, 63.1, 51.8 and 104.7, respectively (Figure A3.15a-d). Nitrogen-doped graphene oxide (UG) shows the lowest contact angles among all the samples implying the highest hydrophilicity of prepared samples. The improved wettability of the UG confirms that there will be higher diffusion occurs through the catalyst, which leads to improvement in supercapacitive behaviour.[56]

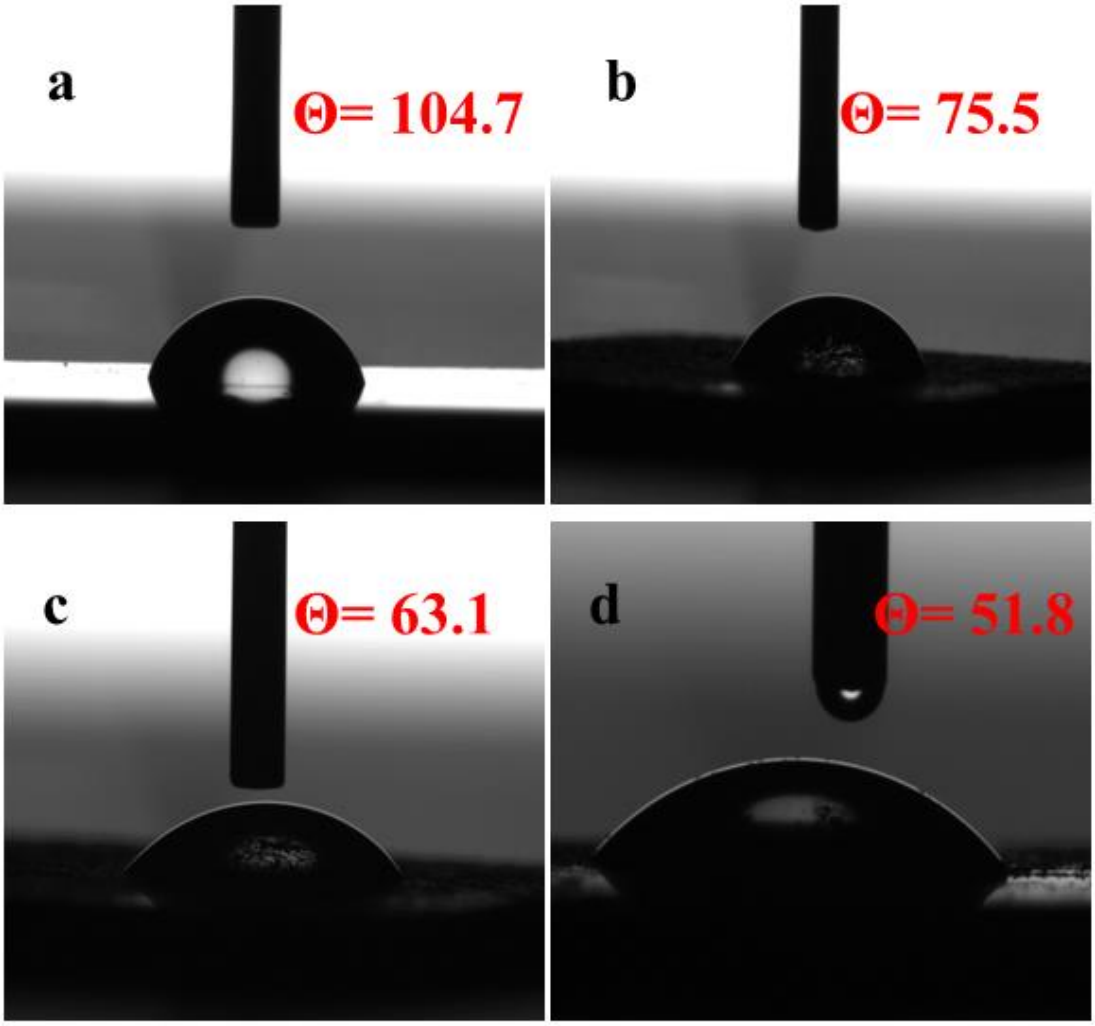

Figure A3.15. *Contact angle of (a) silicon substrate. (b) CG. (c)SG. (d) UG.*

It is exciting to note that the capacitance decreases with increased current density due to the slow diffusion of ions in the electrolyte and can also be ascribed that active material is not fully utilized at higher current.[57] However, at the same time UG has the highest retention of capacitance, which is 90.6 % even at 10 A/g current density as compared to 49.6 % and 77.35 % of CG and SG respectively (Figure A3.16a). This result further confirms the superiority of Nitrogen-doped graphene oxide over the sulphur doped graphene oxide (SG) and without doped graphene oxide (CG). Galvonic charge discharged (GCD) stability of all the prepared electrode was carried out in 1 M Na_2SO_4 at 3 A/g current density. There is a little enhancement in specific capacitance of CG sample up to 200 cycles and then decreases. However, it may be noted that there is a continuous reduction of specific capacitance in CG (Figure A3.16b). There are 89.8 % and 82.2 % capacitance

retain for SG and UG samples respectively even after 2000 cycles, which is good enough at this current density (Figure A3.16c-d).

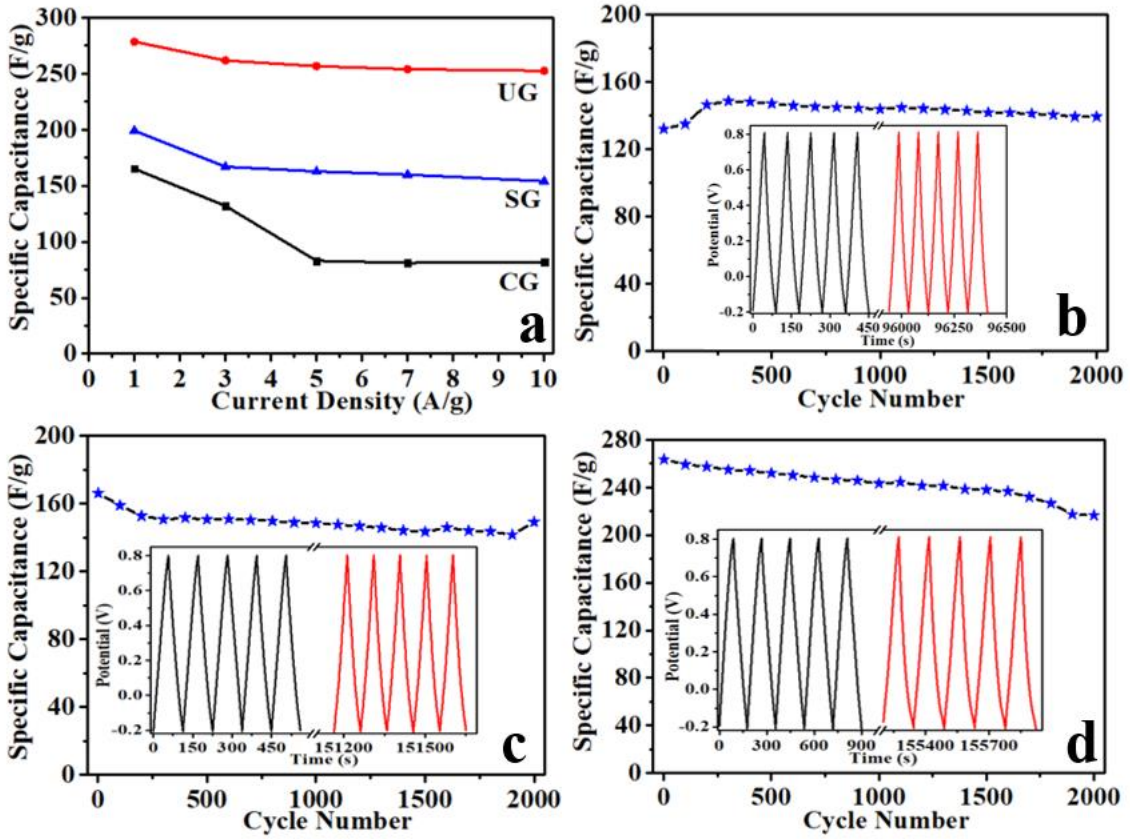

Figure A3.16. *(a) Capacitance retention of CG, SG and UG at different current density. (b) Capacitance retention of CG after 2000 cycle GCD. (c) Capacitance retention of SG after 2000 cycle GCD. (d) Capacitance retention of UG after 2000 cycle GCD (inset of b-d represent the first and last 5 GCD cycle).*

For the practical application of advanced supercapacitor, energy density should be high without sacrificing the power density. High CSP with increased operating potential window is preferable for enhanced energy density of the supercapacitor material. From the Ragone plot (Figure A3.17a), it can be observed that UG shows the highest energy density of 38.53 W h Kg^{-1} against a reasonably good power density of 499 W Kg−1 in the potential window of 1 V (−0.2 V0.8 V). However, at the same time CG and SG show 22.54 and 27.64 W h Kg^{-1} energy density with 490 and 499 W Kg^{-1} power density respectively (Figure A3.17a). The electrical impedance spectroscopy (EIS) study being used for the frequency response of the synthesised electrode material (Figure A3.17b). The obtained EIS data were fitted with Nova 1.1. The fitted solution resistance (Rs) for CG, SG, and UG are 50.1, 16.2 and 17.3 Ω, respectively. The Warburg-type line (the slope of the 45º region of the plots) in CG, SG and UG implying that the short ion diffusion pathways, which is in close

agreements with the previous work for supercapacitor nature.[58] These results are attributed to the presence of the nitrogen and sulphur atoms, which are consistent with the earlier finding that doping creates defect, which will simultaneously enhance the electrical conductivity and electrochemical activity of graphene oxide.

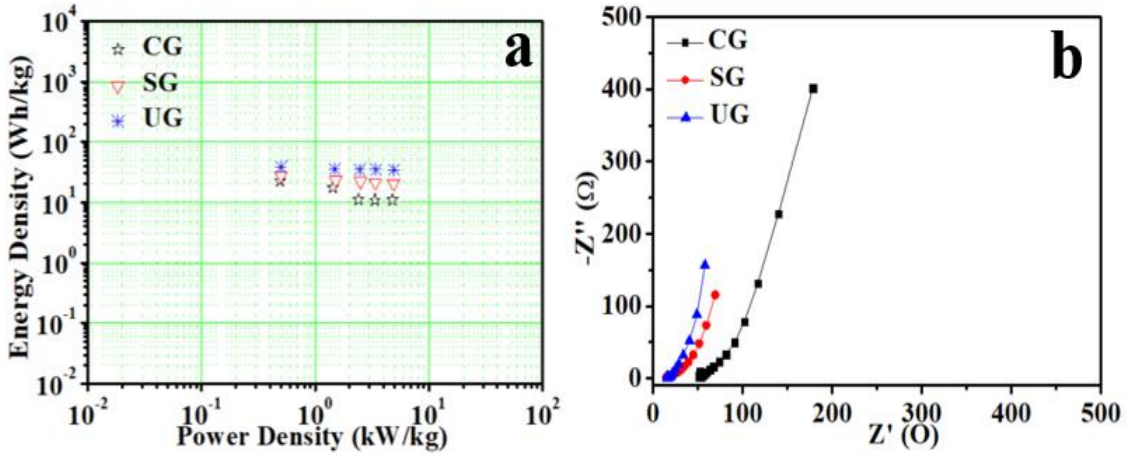

Figure A3.17. *(a) comparative Ragone plot of CG, SG and UG. (b) EIS study of the prepared electrocatalyst.*

Carrier density available in the synthesised catalyst has been calculated using the Mott-Schottky (MS) study at frequency 1 kHz. The MS plots of all the catalyst have been represented in Figure A3.18a-c. The carrier density has been calculated using the following equation.[59]

$$\frac{1}{C^2} = \left[\frac{2}{\epsilon\epsilon_0\, eN}\right]\left[E - E_{fb} - \frac{kT}{E}\right] \qquad \text{A3.1}$$

Where E and E_{fb} are the applied potential and the flat-band potential respectively, C is the charge capacitance, ε is the semiconductor dielectric constant (~35000 at 1 kHz in the present manuscript),[60] ε_0 is the permittivity of the vacuum, k is the Boltzmann constant, e is the electron charge (1.602 x 10^{-19} C), and T is temperature and the value of $\frac{kT}{E}$ is negligible at room temperature. The negative slope of Mott-Schottky (MS) plots indicates that all the catalyst are p-type semiconductors. The flat band potential (E_{fb}) potential was evaluated using extrapolating $1/C^2 = 0$. The obtained slope for extrapolating $1/C^2 = 0$ was used to calculate the carrier density. The observed slope value for CG, SG and UG are 7.8 x10^{13}, 3.8 x10^{13}, and 4.2 x10^{12} $F^{-2}V$, respectively. By using equation 1 and slope value, charge carrier density has been calculated for CG, SG and UG, which are 5.1 x10^{13}, 1.1 x10^{14} and 9.7 x10^{14} cm^{-3} respectively (Figure A3.18d). The highest specific capacitance was observed for UG sample, which is due to the highest charge carrier density. We believed that the

present study would be helpful for the reduction of bio-waste to valuable materials for energy-related application.

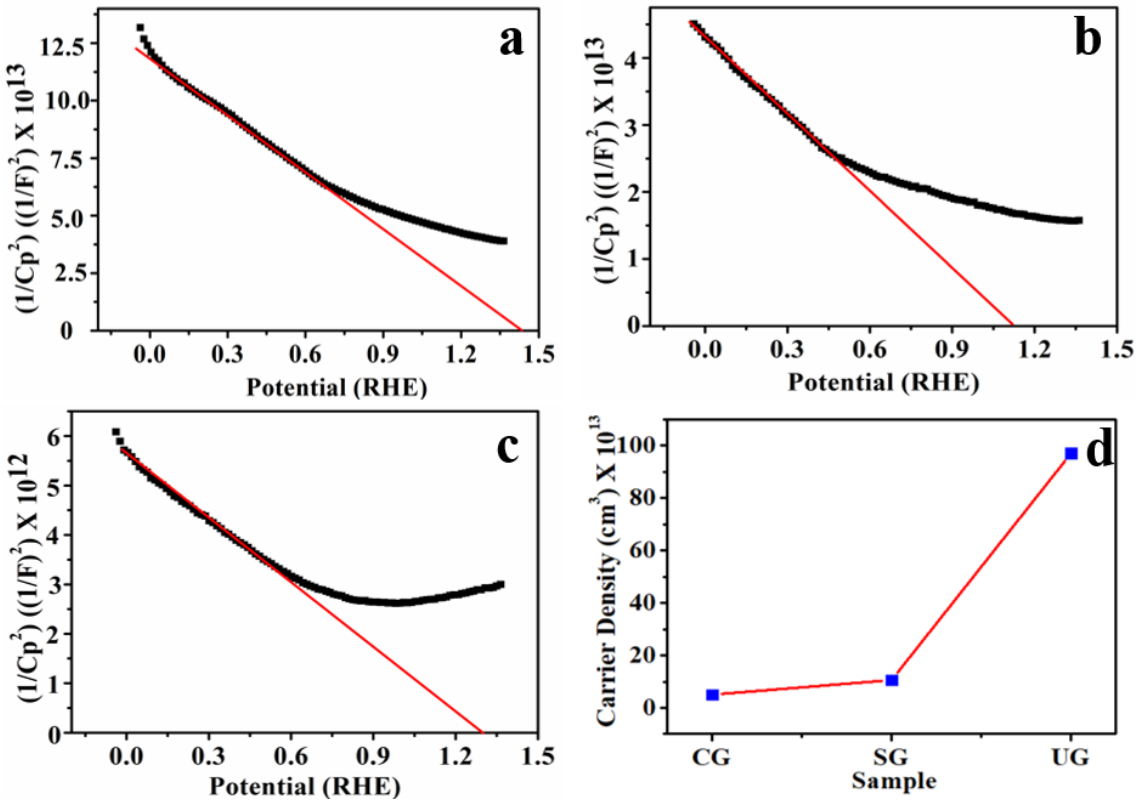

Figure A3.18. *Mott-Schottky plot of (a) CG. (b) SG. (c) UG. (d) Charge carrier concentration density in CG, SG and UG.*

A3.4 Conclusions

The present work deals with the synthesis of template free porous graphene oxide derived from coir. Here, coir was activated using alkaline metal hydroxide and then exfoliated via a chemical process. Further, to increase the conductivity of the synthesized sample, sulphur and nitrogen being doped individually. The thickness of graphene layers has been calculated using Raman and AFM study. These studies confirm the nitrogen-doped graphene has only 2-3 layers. SEM study reveals that the synthesised graphene oxide has a porous structure. The as-obtained graphene and N/S doped graphene has been further utilized for the supercapacitor application. The nitrogen-doped graphene oxide shows the highest specific capacitance (278.6 F/g @ 1 A/g) as compared to sulphur doped graphene oxide (199.2 F/g) and bare graphene oxide (161.1 F/g) at 1 A/g current density respectively. The observed high specific capacitance of nitrogen-doped graphene is due to the high charge carrier density in the catalyst, which was calculated using the Mott-Schottky (MS) study. The nitrogen-doped graphene 90.6 % capacitance retention even at 10 A/g as compared to sulphur-doped graphene and bare graphene, which were 49.6 % and 77.35 %

respectively. The GCD repeatability behaviour of UG shows 82.2 % capacitance even after 2000 GCD cycle at 3 A/g.

A3.5 References

1 B. Zhang, H. Wang, Z. Zuo, H. Wang and J. Zhang, *J. Mater. Chem. A*, 2018, **6**, 15728–15737.

2 J. H. Montoya, L. C. Seitz, P. Chakthranont, A. Vojvodic, T. F. Jaramillo and J. K. Nørskov, *Nat. Mater.*, 2016, **16**, 70–81.

3 Y. Dou, T. Liao, Z. Ma, D. Tian, Q. Liu, F. Xiao, Z. Sun, J. Ho Kim and S. Xue Dou, *Nano Energy*, 2016, **30**, 267–275.

4 K. K. Yadav, A. Gupta, M. Sharma, N. Dabas, A. K. Ganguli and M. Jha, *Mater. Res. Express*, 2017, **4**, 105044-23.

5 S. T. Nishanthi, K. K. Yadav, A. Baruah, A. K. Ganguli and M. Jha, *Electrochim. Acta*, 2019, **300**, 177–185.

6 T. Xiong, W. S. V. Lee, X. Huang and J. M. Xue, *J. Mater. Chem. A*, 2017, **5**, 12762–12768.

7 Y. R. Ahn, C. R. Park, S. M. Jo and D. Y. Kim, *Appl. Phys. Lett.*, 2007, **90**, 122106-3.

8 Q. Liao and C. Wang, *CrystEngComm*, 2019, **21**, 662–672.

9 F. Shi, L. Li, X. L. Wang, C. D. Gu and J. P. Tu, *RSC Adv.*, 2014, 4, 41910–41921.

10 Q. Meng, K. Cai, Y. Chen and L. Chen, *Nano Energy*, 2017, 36, 268–285.

11 Y. Han, Y. Ge, Y. Chao, C. Wang and G. G. Wallace, *J. Energy Chem.*, 2018, 27, 57–72.

12 Y. Liu and X. Peng, *Appl. Mater. Today*, 2017, **8**, 104–115.

13 J. Xia, N. Zhang, S. Chong, D. Li, Y. Chen and C. Sun, *Green Chem.*, 2018, **20**, 694–700.

14 M. Mittal and R. Chaudhary, 2018, **13**, 12237–12243.

15 G. A. Adewumi, N. Revaprasadu, A. C. Eloka-Eboka, F. L. Inambao and C. Gervas, *Lect. Notes Eng. Comput. Sci.*, 2017, **2**, 577–582.

16 Y. Wang, Y. Shao, D. W. Matson, J. Li and Y. Lin, *ACS Nano*, 2010, **4**, 1790–1798.

17 Y. Li, Z. Li and P. K. Shen, *Adv. Mater.*, 2013, **25**, 2474–2480.

18 M. A. Worsley, P. J. Pauzauskie, T. Y. Olson, J. Biener, J. H. Satcher and T. F. Baumann, *J. Am. Chem. Soc.*, 2010, **132**, 14067–14069.

19 E. Taer, R. Taslim, A. W. Putri, A. Apriwandi and A. Agustino, *Int. J. Electrochem. Sci.*, 2018, **13**, 12072–12084.

20 P. F. de Oliveira and M. de F. V Marques, *J. Reinf. Plast. Compos.*, 2014, **33**, 430–

439.

21 M. F. Anuar, Y. W. Fen, M. H. M. Zaid, K. A. Matori and R. E. M. Khaidir, *Results Phys.*, 2018, **11**, 1–4.

22 D. A., S. A. B. A. Manaf, Y. S., C. K., K. N. and G. Hegde, *J. Energy Chem.*, 2016, **25**, 880–887.

23 L. Wang, X. Li, J. Ma, Q. Wu and X. Duan, *Sustain. Energy*, 2014, **2**, 39–43.

24 F. Dong, Y. Cai, C. Liu, J. Liu and J. Qiao, *Int. J. Hydrogen Energy*, 2018, **43**, 12661–12670.

25 M. Wu, J. Qiao, K. Li, X. Zhou, Y. Liu and J. Zhang, *Green Chem.*, 2016, **18**, 2699–2709.

26 S. Yang, L. Zhi, K. Tang, X. Feng, J. Maier and K. Müllen, *Adv. Funct. Mater.*, 2012, **22**, 3634–3640.

27 N. Parveen, M. O. Ansari, S. A. Ansari and M. H. Cho, *J. Mater. Chem. A*, 2016, **4**, 233–240.

28 Y. Zhao, C. Hu, Y. Hu, H. Cheng, G. Shi and L. Qu, *Angew. Chemie Int. Ed.*, 2012, **51**, 11371–11375.

29 H. M. Jeong, J. W. Lee, W. H. Shin, Y. J. Choi, H. J. Shin, J. K. Kang and J. W. Choi, *Nano Lett.*, 2011, **11**, 2472–2477.

30 X. Wang, X. Li, L. Zhang, Y. Yoon, P. K. Weber, H. Wang, J. Guo and H. Dai, *Science*, 2009, **324**, 768–771.

31 Mark Wall, *The Raman Spectroscopy of Graphene and the Determination of Layer Thickness*, Madison, 2011.

32 Thomas N. Blanton and Debasis Majumdar, *Powder Diffr.*, 2013, **28**, 68–71.

33 L. J. Cote, R. Cruz-Silva and J. Huang, *J. Am. Chem. Soc.*, 2009, **131**, 11027–11032.

34 L. Peng, Z. Xu, Z. Liu, Y. Wei, H. Sun, Z. Li, X. Zhao and C. Gao, *Nat. Commun.*, 2015, **6**, 5716.

35 Y.-Z. Liu, Y.-F. Li, F.-Y. Su, L.-J. Xie, Q.-Q. Kong, X.-M. Li, J.-G. Gao and C.-M. Chen, *Energy Storage Mater.*, 2016, **2**, 69–75.

36 Y. Tao, X. Xie, W. Lv, D.-M. Tang, D. Kong, Z. Huang, H. Nishihara, T. Ishii, B. Li, D. Golberg, F. Kang, T. Kyotani and Q.-H. Yang, *Sci. Rep.*, 2013, **3**, 2975.

37 Y. Zhang, F. Wang, H. Zhu, L. Zhou, X. Zheng, X. Li, Z. Chen, Y. Wang, D. Zhang and D. Pan, *Appl. Surf. Sci.*, 2017, **426**, 99–106.

38 C. Yang, H. Jin, C. Cui, J. Li, J. Wang, K. Amine, J. Lu and S. Wang, *Nano*

Energy, 2018, **54**, 192–199.

39 C. Hu, S. Zheng, C. Lian, Q. Hu, S. Duo, R. Zhang and F. Chen, *Appl. Surf. Sci.*, 2015, **335**, 92–98.

40 T. Wang, L. X. Wang, D. L. Wu, W. Xia and D. Z. Jia, *Sci. Rep.*, 2015, **5**, 1–9.

41 M. Borghei, N. Laocharoen, E. Kibena-Põldsepp, L. S. Johansson, J. Campbell, E. Kauppinen, K. Tammeveski and O. J. Rojas, *Appl. Catal. B Environ.*, 2017, **204**, 394–402.

42 V. M. Gaikwad, K. K. Yadav, Sunaina, S. Chakraverty, S. E. Lofland, K. V. Ramanujachary, S. T. Nishanthi, A. K. Ganguli and M. Jha, *J. Magn. Magn. Mater.*, 2019, **492**, 165652-7.

43 T. Purkait, G. Singh, M. Singh, D. Kumar and R. S. Dey, *Sci. Rep.*, 2017, **7**, 15239.

44 G. Z. Chen, *Prog. Nat. Sci. Mater. Int.*, 2013, **23**, 245–255.

45 M. Liu, L. Liu, Y. Yu, H. Lv, A. Chen and S. Hou, *Front. Mater. Sci.*, 2019, **13**, 156–164.

46 K. Gopalsamy, J. Balamurugan, T. D. Thanh, N. H. Kim and J. H. Lee, *Chem. Eng. J.*, 2017, **312**, 180–190.

47 L. Yin, Y. Chen, D. Li, X. Zhao, B. Hou and B. Cao, *Mater. Des.*, 2016, **111**, 44–50.

48 A. Jain and S. K. Tripathi, *Mater. Sci. Eng. B Solid-State Mater. Adv. Technol.*, 2014, **183**, 54–60.

49 L. Sun, C. Tian, M. Li, X. Meng, L. Wang, R. Wang, J. Yin and H. Fu, *J. Mater. Chem. A*, 2013, **1**, 6462.

50 M. Zhang, Y. Li, H. Si, B. Wang and T. Song, *Int. J. Electrochem. Sci.*, 2017, **12**, 7844–7852.

51 Z. Lu, X. Xu, Y. Chen, X. Wang, L. Sun and K. Zhuo, *Green Energy Environ.*, 2019, **5**, 69–75.

52 M. Karuppannan, Y. Kim, Y. E. Sung and O. J. Kwon, *J. Appl. Electrochem.*, 2019, **49**, 57–66.

53 S. Yaglikci, Y. Gokce, E. Yagmur and Z. Aktas, *Environ. Technol.*, 2019, **0**, 1–13.

54 J. Liang, Y. Jiao, M. Jaroniec and S. Z. Qiao, *Angew. Chemie Int. Ed.*, 2012, **51**, 11496–11500.

55 A. O. Lobo, S. C. Ramos, E. F. Antunes, F. R. Marciano, V. J. Trava-Airoldi and E. J. Corat, *Mater. Lett.*, 2012, **70**, 89–93.

56 P. Dulyaseree, V. Yordsri and W. Wongwiriyapan, *Jpn. J. Appl. Phys.*, 2016, **55**,

02BD05-5.

57 D. Hulicova, M. Kodama and H. Hatori, *Chem. Mater.*, 2006, **18**, 2318–2326.

58 M. Ahmad, S. S. Lee, X. Dou, D. Mohan, J.-K. Sung, J. E. Yang and Y. S. Ok, *Bioresour. Technol.*, 2012, **118**, 536–544.

59 W. Wu, S. Liang, L. Shen, Z. Ding, H. Zheng, W. Su and L. Wu, *J. Alloys Compd.*, 2012, **520**, 213–219.

60 K. S. Kumar, S. Pittala, S. Sanyadanam and P. Paik, *RSC Adv.*, 2015, **5**, 14768–14779.

List of Publications

1. **Krishna K. Yadav**, M. Sreekanth, Ankush, S. Ghosh, Menaka Jha. New Process for Stabilization of Vertically Aligned GdB_6 nanorods and their Field Emission Properties. *CrystEngComm*, **2020,** 22, 5473-5480.
2. **Krishna K. Yadav**, M Sreekanth, S Ghosh, Ashok K Ganguli, Menaka Jha. Excellent Field Emission from Ultrafine Vertically Aligned Nanorods of NdB_6 on Silicon Substrate. *Appl. Surf. Sci.*, **2020**, 526, 146652.
3. **Krishna K. Yadav**, Ritika Wadhwa, Nausad Khan, Menaka Jha. Efficient metal-free supercapacitor based on graphene oxide derived from waste rice. *Curr. Opin. Green Sustain. Chem.*, **2021**, 4, 100075.
4. **Krishna K. Yadav**, Harish Singh, Supriya Rana, Sunaina, Heena Sammi, S.T. Nishanthi and Menaka Jha. Utilization of waste coir fibre architecture to synthesize porous graphene oxide and their derivatives: An efficient energy storage material. *J. cleaner prod.*, **2020,** 276, 124240.
5. **Krishna K. Yadav**, M Sharma, Menaka Jha. Extraction of nanostructured sodium nitrate from industrial effluent and their thermal properties. *Water Environ. Res.*, **2020**. 92, 1123–1130.
6. **Krishna K. Yadav**, Sujit Kumar Guchhait, CM Hussain, Ashok K. Ganguli, Menaka Jha. Synthesis of zirconium diboride and its application in the protection of stainless steel surface in harsh environment. *J. Solid State Electr.*, **2019**, 23 (12), 3243-3253.
7. **Krishna K. Yadav**, A Gupta, M Sharma, N Dabas, AK Ganguli, M Jha. Low temperature synthesis process of stabilization of cubic yttria stabilized zirconia spindles: an important high temperature ceramic material. *Mater. Res. Express*., **2017**, 4 (10), 105044.
8. Ankush, **Krishna K. Yadav**, Sujit Kumar Guchhait, Supriya Rana, Menaka Jha. Excellent hydrogen generation from ultrathin nanosheets of cobalt cyclotetraphosphate. *Mat. Sci. Eng. B-Adv***, 2021,** 265, 114983.
9. Ritika Wadhwa, **Krishna K. Yadav**, Tanmay Goswami, Ankush, Sujit Kumar Guchhait, Sunaina, S.T. Nishanthi, Hirendra N. Ghosh, Menaka Jha. Black Gold decorated Zirconia: An efficient electrocatalyst for ethanol oxidation. *ACS Appl. Mater. Interfaces*, **2021**, 13, 8, 9942–9954.
10. ST Nishanthi, **Krishna K. Yadav**, A Baruah, AK Ganguli, M Jha.New sustainable and

environmental friendly process of synthesis of highly porous Mo_2S_3 nanoflowers in cooking oil and their electrochemical properties. *Electrochim. Acta*, **2019**, 300, 177-185.

11. N Dabas, **Krishna K. Yadav,** Ashok K Ganguli, Menaka Jha. New process for conversion of hazardous industrial effluent of ceramic industry into nanostructured sodium carbonate and their application in textile industry. *J. Envir. Manag.*, **2019**, 240, 352–358.
12. ST Nishanthi, **Krishna K. Yadav,** A Baruah, K Vaghasiya, RK Verma, AK Ganguli, Menaka Jha. Nanostructured silver decorated hollow silica and their application in the treatment of microbial contaminated water at room temperature; *New J. Chem*., **2019**, 43 (23), 8993-9001.
13. Supriya Rana, **Krishna K. Yadav**, Sujit Kumar Guchhait, S. T. Nishanthi, S. K. Mehta, Menaka Jha. Insights of enhanced oxygen evolution reaction of nanostructured cobalt ferrite surface. *J. Mater. Sci.*, **2021**, 56, 8383–8395**.**
14. Supriya Rana, **Krishna K. Yadav**, Kritika Sood, Ankush, S. K. Mehta, Menaka Jha. Low Temperature Hydrothermal Method for Synthesis of Fe_2O_3 and their Oxygen Evolution Performance. *Electroanalysis***, 2020,** 32, 1-8**.**
15. Yang Gao, Fangru Xing, Menaka Jha, **Krishna K Yadav**, Ranjana Yadav, and Avtar S. Matharu. Towards Novel Biocomposites from Unavoidable Food Supply Chain Wastes and Zirconia. *ACS Sustain Chem Eng*., **2020,** 37, 14039–14046.
16. Sujit Kumar Guchhait, Heena Sammi, **Krishna K. Yadav**, Supriya Rana, Menaka Jha. New Hydrometallurgical Approach to Obtain Uniform Antiferromagnetic Ferrous Chloride Cubes from Waste Tin Cans. *J. Mater. Sci: Mater. Elect.* **2021**, 32, 2965–2972.
17. H Singh, Sunaina, **Krishna K. Yadav,** VK Bajpai, Menaka Jha. Tuning the bandgap of m-ZrO_2 by incorporation of copper nanoparticles into visible region for the treatment of organic pollutants. *Materials Research Bulletin*, **2020**, 123, 110698.
18. VM Gaikwad, **Krishna K. Yadav,** S Chakraverty, SE Lofland, KV Ramanujachary, ST Nishanthi, Ashok K Ganguli, Menaka Jha Design of process for stabilization of La_2NiMnO_6 nanorods and their magnetic properties. *J. Magn. Magn. Mater*, **2019**, 492, 165652.
19. Vishwajit M. Gaikwad, **Krishna K. Yadav**, S. E. Lofland, Kandalam V. Ramanujachary, Suvankar Chakraverty, Ashok K. Ganguli, Menaka Jha. New low-temperature process for stabilization of nanostructured La_2NiMnO_6 and their

magnetic properties. *J. Magn. Magn. Mater.*, **2019**, 471, 8-13.

20. Sunaina, **Krishna K. Yadav**, SK Guchhait, K Sood, SK Mehta, AK Ganguli, Menaka Jha. Mechanistic insights of enhanced photocatalytic efficiency of SnO_2-SnS_2 heterostructures derived from partial sulphurization of SnO_2. *Sep. Puri. Tech.*, **2020**, 242, 116835.
21. ST Nishanthi, A Baruah, **Krishna K. Yadav**, D Sarker, S Ghosh, AK Ganguli, Menaka Jha. New low temperature environmental friendly process for the synthesis of tetragonal MoO_2 and its field emission properties. *Appl. Surf. Sci.*, **2019**, 467, 1148-1156.
22. Ankush, **Krishna K. Yadav**, Sujit Kumar Guchhait, Menaka Jha. Surface phopsphorization of nickel oxalate nanosheets to stabilize ultrathin nickel cyclotetraphosphate nanosheets for efficient hydrogen generation. *Mater. Res. Bull.*, **2021,** DOI: 10.1016/j.materresbull.2021.111275**.**

List of conferences/workshop attended

- Presented Poster entitled "**Synthesis of nanostructured iron-cobalt oxide and their electro-catalytic properties**" in **CRIKC Nano Science day 2016** organized by Institute of Nano Science and Technology, Mohali, Punjab.
- Participated in "**10th CRSI-RSC Joint Symposium**" held on 4th February 2016 and "**18th CRSI National Symposium in Chemistry**" held from February 5th-7th,2016, organized by Institute of Nano Science and Technology and Punjab University.
- Attend a workshop on X-ray **entitled "X'Radiate "Workshop on Powder, Nano and Thin Film Characterization Using X-Ray Diffraction"** from 15-16 December 2016 organised by PSGTECHS COE INDUTECH in Collaboration with PANalytical India and The Office of Textile Commissioner, Ministry of Textiles, Govt. of India.
- Poster entitled "**Extraction of valuable nanostructured materials from industrial waste"** presented in **9th Bangalore India Nano** from 7-9 December 2017 and own **Best poster** prize.
- Poster entitled "**Excellent field emission from ultrafine vertically aligned nanorods of NdB_6 on silicon substrate"** presented in ICONSAT 2018, organised by Centre for Nano and Soft Matter Sciences, Bengaluru, India.
- Participated in the workshop "**The Full Agenda of DST and ACS workshop**" held on 20 Nov 2019 at Institute of Nano Science and Technology, Mohali, India.
- Poster entitled "**Synthesis of zirconium diboride and its application in the protection of stainless-steel surface in harsh environment**" presented in Electrochemistry in Industry, Health and Environment (EIHE-2020) held at DAE Convention Centre, Bhabha Atomic Research Centre, Mumbai, India in Collaboration with Indian Society for ElectroAnalytical Chemistry (ISEAC).
- Poster entitled "**Design of process to stabilize metal- zirconia heterostructure and their application"** presented in **International Conference** on"**Nanotechnology for Better Living** NBL -2019" from 7-11 April 2019 held at NIT Srinagar, India in Collaboration with IIT Kharagpur, India
- Participated in the workshop "**National Workshop on Catalysis for the Clean Energy and Safe Environment**" held on 16th Nov 2019 at Punjab University, Chandigarh, India